

Iron Oxide Based Magnetic Nanocomposites: Removal of Inorganic and Organic Water Contaminants and Antimicrobial Properties

JITENDRA KUMAR SAHOO



**DEPARTMENT OF CHEMISTRY
NATIONAL INSTITUTE OF TECHNOLOGY
ROURKELA-769008, ODISHA, INDIA**

Iron Oxide Based Magnetic Nanocomposites: Removal of Inorganic and Organic Water Contaminants and Antimicrobial Properties

Thesis submitted in partial fulfilment of the requirements for the degree of

DOCTOR OF PHILOSOPHY

By

Jitendra Kumar Sahoo

Roll No: 514CY6011

Under the supervision of

Dr. Harekrushna Sahoo

&

Dr. Priyabrat Dash



**DEPARTMENT OF CHEMISTRY
NATIONAL INSTITUTE OF TECHNOLOGY
ROURKELA-769008, ODISHA, INDIA**



September 2019

Certificate of Examination

Roll Number: **514CY6011**

Name: **Jitendra Kumar Sahoo**

This is to certify that the thesis entitled “**Iron Oxide Based Magnetic Nanocomposites: Removal of Inorganic and Organic Water Contaminants and Antimicrobial Properties**” being submitted by Sri Jitendra Kumar Sahoo to the National Institute of Technology, Rourkela, India, for the award of the degree of Doctor of Philosophy is a record of bonafide research work carried out by him under my supervision and guidance. I am satisfied that the thesis has reached the standard for fulfilling the requirements of the regulations relating to the nature of the degree. To the best of my knowledge, the matter embodied in the thesis has not been submitted to any other University/Institute for the award of any Degree or Diploma.

Harekrushna Sahoo
Principal Supervisor

Priyabrat Dash
Co-supervisor

Raj Kishor Patel
Member (DSC)

Himanshu Bhushan Sahu
Member (DSC)

Arvind Kumar
Member (DSC)

Suneel Kumar Srivastava
External Examiner

Garudadhvaj Hota
Chairman (DSC)

Rupam Dinda
Head of the Department



Department of Chemistry
National Institute of Technology Rourkela

Dr. Harekrushna Sahoo

Assistant Professor

September 2019

Supervisors Certificate

This is to certify that the work presented in this dissertation entitled “**Iron Oxide Based Magnetic Nanocomposites: Removal of Inorganic and Organic Water Contaminants and Antimicrobial Properties**” by “*Mr. Jitendra Kumar Sahoo*”, Roll Number - **514CY6011**, is a record of original research carried out by him under my supervision and guidance in partial fulfilment of the requirements for the degree of *Doctor of Philosophy in Chemistry*. Neither this dissertation nor any part of it has been submitted for any degree or diploma to any institute or university in India or abroad.

Dr. Harekrushna Sahoo
Principal Supervisor

Dr. Priyabrat Dash
Co-Supervisor

Dedicated

To

*All the pioneers who explored nanochemistry in
environmental applications*

Declaration of Originality

I, **Jitendra Kumar Sahoo**, Roll Number - **514CY6011** hereby declare that this dissertation entitled **“Iron Oxide Based Magnetic Nanocomposites: Removal of Inorganic and Organic Water Contaminants and Antimicrobial Properties”** represents my original work carried out as a doctoral student of NIT Rourkela and, to the best of my knowledge, it contains no material previously published or written by another person, nor any material presented for the award of any other degree or diploma of NIT Rourkela or any other institution. Any contribution made to this research by others, with whom I have worked at NIT Rourkela or elsewhere, is explicitly acknowledged in the dissertation. Works of other authors cited in this dissertation have been duly acknowledged under the section "Bibliography". I have also submitted my original research records to the scrutiny committee for evaluation of my dissertation.

I am fully aware that in the case of any non-compliance detected in future, the Senate of NIT Rourkela may withdraw the degree awarded to me on the basis of the present dissertation.

September 2019

NIT Rourkela

Jitendra Kumar Sahoo

Acknowledgment

I take this opportunity to express my deep sense of gratitude and indebtedness to my research supervisor **Prof. Harekrushna Sahoo**, for providing his excellent guidance, support, encouragement, and inspiration throughout my research work. It has been a great opportunity to work with him with his vast scientific knowledge and analytical approach. I greatly feel fortunate enough for his patience to assist me, which he devoted from his busy schedule. Without his expertise and guidance, this work would not have been accomplished. I feel so lucky to have spent my research work under the guidance of an intelligent, forgiving, open-minded, honest and beloved person like him. I am also very much thankful to his family members for their hospitality, love, and encouragement.

I would also like to acknowledge **Prof. Priyabrat Dash**, my co-supervisor for providing his outstanding technical support, caring and valuable suggestions, which helped me making this research work a success.

My special thanks are to Prof. S. K. Sarangi, Ex-Director, and Prof. A. Biswas, Director, National Institute of Technology, Rourkela for giving all the facilities to successfully complete my Ph.D. work

I am thankful to all my Doctoral Scrutiny Committee members **Prof. G. Hota** (chairman), **Prof. R. K. Patel** (member), **Prof. H. B. Sahu** (member), and **Prof. A. Kumar** (member) for their valuable suggestions throughout my research career.

I would also like to express my deep sense of gratitude to **Prof. N. Panda** (Ex-HOD), **Prof. S. Chatterjee** (Ex-HOD), and **Prof. R. Dinda**, HOD, Department of Chemistry, and NIT Rourkela for allowing me to avail the experimental facilities.

I wish to express my sincere thanks to **the faculty members of Chemistry Department** (NIT, Rourkela) for suggestions and useful discussions during my research work.

I am very much thankful to **Prof. S. K. Srivastava** (Indian institute of Technology, Kharagpur) and **Prof. Yixin Zhang** (Technical University Dresden, Germany) for reviewing my PhD thesis.

I have had the pleasure to be a part of collaborative projects with groups from life science. I express my sincere thanks to **Prof. M. Mishra** from Life Science Department National Institute

of Technology, Rourkela, Odisha, India for giving me the opportunity to work collaboratively on antibacterial activity of novel composite. I also take this opportunity to thank Sanjeev Kumar Paikra from the same department, for helping me to do the antibacterial activity in presence of synthesized nanocomposite.

I have had the pleasure to be a part of collaborative projects with groups from other institutes. I express my sincere thanks to **Miss. Juhi Rath** from Hydro & Electrometallurgy Department, Institute of Minerals and Materials Technology, Bhubaneswar, Odisha, India for helping me with Atomic adsorption spectroscopy analysis for this work and also continuous support and guidance in my whole Ph.D. life.

Above all, I am very much thankful and indebted to the **National Institute of Technology, Rourkela** for selecting me as a Ph. D. scholar.

I acknowledge BRNS, DAE, and SERB, DST sponsored me financially throughout the research program.

I am very much grateful to the Department of Physics, Mining, Ceramic, Life science, Metallurgical and Chemical Engineering, NIT Rourkela, for providing various characterization techniques.

I would like to extend thanks to my dear lab mates (Satish Bhai, Sabera didi, Monidipa, and Suchismita) for their support and help in the laboratory and for providing a most pleasant working environment. I would also like to thank all of my seniors and juniors Aniket Bhai, Lipika didi, Basanti didi, Balmiki Bhai, Satish Bhai, Pratap and Bapun who supported me in writing and incited me to strive towards my goal. My special thanks to Uttam, Shraban, Rakesh, Chandini and Manoj Bhai for their companionship, emotional support, and entertainment, which helped me a lot to get through the difficult times during my work. Words cannot express how grateful I am to my mother (Bou) and father (Bapa) for all of the sacrifices that they have made on my behalf. I would like express appreciation to my grandfather, elder brothers (Rajani Bhai), loving sister Bishnu didi, younger brother Papa and Bhauja for their love inspiration, mental support, and encouragement.

September 2019
NIT Rourkela

Jitendra Kumar Sahoo
Roll Number: 514CY6011

Abstract

In the current scenario, most of the researcher try to prepared novel and cost-effective nanomaterials for wastewater treatment especially discharge from industrial and domestic water, drinking water and contaminated water. A worldwide growing population is one of the major sources of water pollution. The overall thesis demonstrates an extensive view of the use of nanomaterials in water purification using functionalized iron oxide nanomaterials by adsorption of inorganic and organic contaminants.

In the present work, we have prepared iron oxide nanoparticles (Fe_3O_4) and iron oxide-based nanomaterials such as Fe_3O_4 -TSPED-Tryptophan, Fe_3O_4 -GG, Fe_3O_4 -APTES-EDTA and $\text{GO-Fe}_3\text{O}_4$ -APTES of various morphology using precipitation methods. The synthesized nanomaterials were analyzed using FT-IR, XRD, TEM, FE-SEM, VSM, BET surface area, TGA, Zeta potential, Raman and UV-Vis Spectroscopy techniques and were used as effective adsorbent towards heavy metal ions and organic dyes from aqueous solution.

In the first project, we use amino acid (Tryptophan) functionalized iron oxide nanomaterial and TSPED act as a linking agent in between them. The results revealed that the Fe_3O_4 -TSPED-Tryptophan shows greater affinity towards Congo Red (CR) dye adsorption and antibacterial properties. The adsorption efficacy of the dye is assessed by varying various parameters such as pH, dye concentration, adsorbent dose and time. The adsorption isotherm is found to follow Langmuir isotherm model and the rate of adsorption well fitted to pseudo-second-order kinetics. We further checked the antibacterial activity of the dye against gram-negative (*Escherichia coli*) and gram-positive (*Bacillus subtilis*) bacterial strain. FTT nanocomposite responds positively towards antibacterial activity.

In the same direction, the second project, functionalized Guar-gum (GG) on the surface of iron oxide (Fe_3O_4) nanoparticles were synthesized via conventional co-precipitation method. The efficiency of the nanocomposite was investigated towards the adsorption of different dyes such Congo red (CR), Malachite green (MG), Methylene blue (MeB), Methyl orange (MO), Eriochrome Black T (EBT), Methyl blue (MB) and Rhodamine B (Rhb). Among which CR dye shows adsorption efficiency of 97% using the prepared nanocomposite. The presence of $-\text{NH}_2$ in the CR dye is responsible for the efficient adsorption, as it easily forms hydrogen bonding with

the surface hydroxyl group of Fe₃O₄-GG. The optimum condition for dye removal efficiency using Fe₃O₄-GG has been investigated by varying different factors such as the influence of pH, the initial concentration of dye, adsorbent dose and influence of contact time. Moreover, the adsorption procedure was studied with various adsorption isotherms (Langmuir, Freundlich, Temkin, Dubinin-Radushkevich, and Elovich isotherm). Among all isotherm model, Langmuir isotherm model is best fit for CR adsorption. The CR dye adsorption limit was found to be, $q_m=60.24$ mg/g. The dye adsorption rate follows the pseudo-second-order kinetic model.

For the removal of inorganic contaminants, in the third project advancement of an efficient and cost-effective method for heavy metal removal from contaminated water utilizing Fe₃O₄-APTES-EDTA nanocomposite, a productive reusable adsorbent, is explained in this study. The novel Fe₃O₄-APTES-EDTA nanocomposite was prepared by three-step process such as (a) firstly Fe₃O₄ nanoparticle was prepared by chemical co-precipitation method, (b) secondly, the silane coating on the surface of magnetic Fe₃O₄ cores using linking agent APTES was done which provide amino group (-NH₂) for linking with the EDTA molecule and (c) finally, EDTA molecules functions as inclusion sites and a selective containers for trapping different heavy metal ions. Fe₃O₄-APTES-EDTA is found to be a good adsorbent for Pb²⁺, Cd²⁺, Ni²⁺, Co²⁺ and Cu²⁺ removal with a higher adsorption capacity. The maximum adsorption capacity of Pb²⁺, Cd²⁺, Ni²⁺, Co²⁺, Cu²⁺ are found to be 11.31, 13.88, 7.64, 4.86 and 78.67 mg/g, respectively. The adsorption and desorption cycle was studied for five cycles with minimal loss of efficiency.

In the fourth project, amino silane magnetic nanocomposite decorated on graphene oxide (GO-Fe₃O₄-APTES) was successfully prepared by organic transformation reaction followed by co-precipitation method. GO-Fe₃O₄-APTES material was highly selective for Chromium (VI) removal from aqueous solution. About 91 % of Chromium (VI) was removed at pH 3, 160 rpm of shaking speed, 0.3 g/L of adsorbent dose and 10 hours of contact time. The adsorption process of Chromium (VI) on GO-Fe₃O₄-APTES follows Pseudo-second-order kinetic and Langmuir isotherm model because of the high correlation coefficient value ($R^2=0.99$). The maximum adsorption capacity (q_m) of GO-Fe₃O₄-APTES was observed at 60.53 mg/g. The synthesized material was desorbed with 0.5 M NaOH and recycled up to five cycles. After five cycles, the removal efficiency of chromium (VI) possesses high efficacy towards-Fe₃O₄-APTES. Mechanistically, adsorption of Chromium (VI) follows strong electrostatic attraction between adsorbate and adsorbent. GO-Fe₃O₄-APTES has potential adsorbent for the adsorption of

chromium (VI) in wastewater treatment. Furthermore, the Fe₃O₄-APTES were tested for antibacterial properties against gram-negative (*Escherichia coli*) and gram-positive (*Bacillus subtilis*) bacterial strain. The synthesized material responds positively towards antibacterial activity.

Kew Words: Organic dye, Heavy metals, Antibacterial activity, Adsorption, Iron oxide nanoparticle, Nanocomposite materials.

List of Figures

1.1	Distribution of water bodies on earth.	2
1.2	Sources of water pollution (Graphic Courtesy: Central Pollution Control Board India).	6
1.3	Schematic illustration of removal of inorganic water contaminants by reverse osmosis process. (Graphic Courtesy: Water products).	8
1.4	Removal of inorganic contaminants using ion-exchange process.	10
1.5	Coagulation process for removal of inorganic contaminants.	11
1.6	Phytoremediation process for removal of inorganic contaminants (Graphic Courtesy: National Institute for Biotechnology and Genetic Engineering)	11
1.7	The TEM image of magnetite (Fe_3O_4) nanoparticles at different temperature (A) 90 °C with its SAED pattern, (B) 75 °C, (C) 33 °C and (D) HR-TEM of 33 °C (Ghosh et al. 2014).	20
1.8	XRD pattern of magnetite nanoparticles (Compeán-Jasso et al., 2008).	20
1.9	Mossbauer spectrum of magnetite (Compeán-Jasso et al., 2008).	21
1.10	Overview of the research work	22
2.1	Schematic illustration of the synthetic procedure for Fe_3O_4 -TSPED-Tryptophan nanocomposite	26
2.2	Schematic illustration of the synthetic procedure for Fe_3O_4 -APTES.	27
2.3	Schematically detailed synthetic mechanism of Fe_3O_4 -APTES.	28
3.1	FTIR spectra of (a) Fe_3O_4 , (b) Fe_3O_4 -TSPED and (c) Fe_3O_4 -TSPED-Tryptophan.	38
3.2	XRD patterns for (a) Fe_3O_4 , (b) Fe_3O_4 -TSPED and (c) Fe_3O_4 -TSPED-Tryptophan.	39
3.3	(a) TEM image of FTT, (b) SAED pattern of FTT and (c) EDX spectra of FTT nanocomposite.	40
3.4	Magnetization curve of Fe_3O_4 , Fe_3O_4 -TSPED and Fe_3O_4 -TSPED-Tryptophan nanocomposite.	41
3.5	(a) N_2 adsorption-desorption isotherm of Fe_3O_4 , Fe_3O_4 -TSPED and Fe_3O_4 -TSPED-Tryptophan nanocomposite, Pore size distribution of (b) Fe_3O_4 , (c) Fe_3O_4 -TSPED and (d) Fe_3O_4 -TSPED-Tryptophan.	42
3.6	TGA curve of Fe_3O_4 , Fe_3O_4 -TSPED and Fe_3O_4 -TSPED-Tryptophan nanocomposite.	42
3.7	(a) Effect of adsorbent dosage on CR adsorption (b) the removal of CR at different concentrations (c) Effect of time on adsorption of CR and (d) Effect of pH on the removal efficiency	43
3.8	(a) Langmuir isotherm plot and (b) Freundlich isotherm plot for CR dye adsorption.	45

3.9	(a) Pseudo-first order model and (b) Pseudo-second order model for CR adsorption on Fe ₃ O ₄ -TSPED-Tryptophan nanocomposite.	46
3.10	Reusability test of Fe ₃ O ₄ -TSPED-Tryptophan adsorbent for removal of CR.	47
3.11	(A) Antibacterial activity by disc diffusion method (a) shows the zone of inhibition when <i>E.coli</i> treated with the 160 µg/ml of FTT (b,c,d) Shows the zone of inhibition when <i>E.coli</i> treated with 80 µg/ml, 40 µg/ml, 20 µg/ml respectively where zone of inhibition is not clearly visible. (e) At middle shows the zone of inhibition, when <i>E.coli</i> treated with standard drug Gentamicin. (B) Antibacterial activity by disc diffusion method (a) shows the zone of inhibition when <i>B. subtilis</i> treated with the 160 µg/ml of FTT (b) Shows the zone of inhibition when <i>B. subtilis</i> treated with 80 µg/ml. (c) At middle shows the zone of inhibition, when <i>B. subtilis</i> treated with standard drug Gentamicin.	48
3.12	Graph representing the antibacterial activity of FTT with varying concentration against, <i>E. coli</i> and <i>B. subtilis</i> by showing the percentage loss in bacterial cell viability.	49
3.13	Growth kinetics of (a) <i>E. coli</i> and (b) <i>B. subtilis</i> in presence as well as absence of FTT. The experiment performed in triplicate and result showed as the Mean ± SEM.	49
3.14	Fe ₃ O ₄ -TSPED-Tryptophan induced ROS generation in (a) <i>E. coli</i> and (b) <i>B. subtilis</i> . Fluorescence intensity shows the ROS generation at different concentration of Fe ₃ O ₄ -TSPED-Tryptophan.	50
4.1	Schematic illustration of the adsorption process for the CR using Fe ₃ O ₄ -GG.	55
4.2	(A) FT-IR Spectra of (a) Fe ₃ O ₄ , (b) GG and (c) Fe ₃ O ₄ -GG nanocomposite (B) X-ray diffraction patterns of (a) Fe ₃ O ₄ and (b) Fe ₃ O ₄ -GG nanocomposite.	55
4.3	Field emission scanning electron microscopy (FE-SEM) images of (a) Fe ₃ O ₄ (b) Fe ₃ O ₄ -GG nanocomposite (c) EDX spectra of Fe ₃ O ₄ -GG nanocomposite (d,e,f) EDS data of Fe ₃ O ₄ -GG nanocomposite.	58
4.4	(a) TEM of Fe ₃ O ₄ nanoparticles and (b) SAED pattern of Fe ₃ O ₄ nanoparticles.	58
4.5	Histogram of the particle size distribution of Fe ₃ O ₄ .	59
4.6	The TEM image of (a) Fe ₃ O ₄ -GG nanocomposites, (b) SAED pattern of Fe ₃ O ₄ -GG nanocomposites and (c) EDS mapping analysis of Fe ₃ O ₄ -GG nanocomposites.	59
4.7	FigHistogram of the particle size distribution of Fe ₃ O ₄ -GG nanocomposite.	60
4.8	(a) N ₂ adsorption-desorption isotherm of Fe ₃ O ₄ , Fe ₃ O ₄ -GG nanocomposite (b) Magnetization curve of Fe ₃ O ₄ , Fe ₃ O ₄ -GG nanocomposite, (c) Zeta potential versus P ^H of Fe ₃ O ₄ , Fe ₃ O ₄ -GG nanocomposite and (d) Preferential adsorption efficiency of different dyes on Fe ₃ O ₄ -GG nanoparticles.	60
4.9	(a) The removal of CR at different concentrations, (b) Effect of pH on the removal efficiency, (c) Effect of adsorbent dosage on adsorption CR and (d) Effect of time on adsorption of CR.	63
4.10	Kinetic model parameters of CR on Fe ₃ O ₄ -GG (a) Pseudo-first order kinetic model and (b) Pseudo-second order kinetic model.	64
4.11	(a) Langmuir isotherm plot, (b) Effect of the initial concentration for CR adsorption on Fe ₃ O ₄ -GG, (c) Freundlich isotherm plot, (d) Temkin isotherm plot, (e) Dubinin-	65

Radushkevich isotherm plot and (f) Elovich isotherm plot of CR on Fe₃O₄-GG.

4.12	Reusability of the adsorbent.	67
5.1	(A) XRD patterns for (a) Fe ₃ O ₄ , (b) Fe ₃ O ₄ -APTES and (C) Fe ₃ O ₄ -APTES-EDTA (B) FTIR spectra of (a) Fe ₃ O ₄ , (b) Fe ₃ O ₄ -APTES and (C) Fe ₃ O ₄ -APTES-EDTA.	71
5.2	TEM of (a) Fe ₃ O ₄ , (b,c) Fe ₃ O ₄ -APTES-EDTA, (d) SAED pattern and (e) EDX analysis	72
5.3	EDS mapping analysis of Fe ₃ O ₄ -APTES-EDTA.	73
5.4	(A)Vibrating sample magnetometer (VSM) supermagnetization curves of (a) Fe ₃ O ₄ (b) Fe ₃ O ₄ -APTES and (C) Fe ₃ O ₄ -APTES-EDTA. (B) N ₂ adsorption-desorption isotherms of (a) Fe ₃ O ₄ (b) Fe ₃ O ₄ -APTES and (C) Fe ₃ O ₄ -APTES-EDTA. (C) Zeta potential of (a) Fe ₃ O ₄ (b) Fe ₃ O ₄ -APTES and (c) Fe ₃ O ₄ -APTES-EDTA nanocomposite. (D) Reusability of the adsorbent.	74
5.5	Pore size distribution curves of Fe ₃ O ₄ , Fe ₃ O ₄ -APTES, and Fe ₃ O ₄ -APTES-EDTA nanocomposite.	75
5.6	TGA curves of Fe ₃ O ₄ and Fe ₃ O ₄ -APTES-EDTA.	76
5.7	(a) Effect of pH, (b) Effect of adsorbent dosage, (c) Effect of the initial concentration of heavy metal ions and (d) Effect of contact time for heavy metal ions on to Fe ₃ O ₄ -APTES-EDTA nanocomposite.	78
5.8	(a) Pseudo-first order and (b) Pseudo-second order kinetic models for heavy metal ions adsorption on Fe ₃ O ₄ -APTES-EDTA nanocomposite.	79
5.9	(a) Langmuir isotherm plot, (b) Freundlich isotherm plot, (c) Temkin isotherm plot and (d) Elovich isotherm plot for heavy metal ions on to Fe ₃ O ₄ -APTES-EDTA nanocomposite.	82
5.10	Schematic illustration of the synthetic procedure for Fe ₃ O ₄ -APTES-EDTA nanocomposite.	83
6.1	FT-IR spectra of (a) GO, (b) Fe ₃ O ₄ , (c) Fe ₃ O ₄ -APTES and (d) GO-Fe ₃ O ₄ -APTES.	88
6.2	X-ray diffraction patterns of (a) GO, (b) Fe ₃ O ₄ , (c) Fe ₃ O ₄ -APTES and (d) GO-Fe ₃ O ₄ -APTES.	89
6.3	FE-SEM image of (a) Fe ₃ O ₄ -APTES, (b) GO and (c) GO-Fe ₃ O ₄ -APTES	90
6.4	(a) The TEM image of Fe ₃ O ₄ -APTES, (b) The particle size distribution of Fe ₃ O ₄ -APTES, (c,d) TEM image of GO-Fe ₃ O ₄ -APTES (200 and100 nm resolution) and (e-g) HRTEM micrograph with interplanar spacing of GO-Fe ₃ O ₄ -APTES.	91
6.5	(a) SAED pattern of GO- Fe ₃ O ₄ -APTES, (b-h) EDS elemental mapping of GO-Fe ₃ O ₄ -APTES and (i) EDX spectrum of GO-Fe ₃ O ₄ -APTES.	92
6.6	Raman spectra of (a) GO and (b) GO-Fe ₃ O ₄ -APTES.	93
6.7	Hysteresis loop of Fe ₃ O ₄ , Fe ₃ O ₄ -APTES, and GO-Fe ₃ O ₄ -APTES at room temperature. The bottom inset: aqueous solution of GO-Fe ₃ O ₄ -APTES (left), separated particles of GO-Fe ₃ O ₄ -APTES by an external magnet (right).	94
6.8	N ₂ adsorption-desorption isotherm of GO, Fe ₃ O ₄ , and GO-Fe ₃ O ₄ -APTES.	95
6.9	(a) the removal of Cr (VI) at different concentrations, (b) Effect of adsorbent dosage on Cr (VI) adsorption, (c) Effect of time on adsorption of Cr (VI) and (d) Effect of pH on the removal efficiency.	96

6.10	Zeta potential plot of GO-Fe ₃ O ₄ -APTES.	97
6.11	Effect of shaking speed on adsorption of Cr (VI) onto-Fe ₃ O ₄ -APTES.	98
6.12	(a) Pseudo-first-order kinetic model, (b) Pseudo second-order kinetic model and (c) Intraparticle diffusion model for the adsorption of chromium (VI) on GO-Fe ₃ O ₄ -APTES.	99
6.13	(a)Langmuir, (b)Freundlich, (c) Temkin, (d) Elovich and (e) Dubinin-Radushkevich adsorption of Chromium (VI) on GO-Fe ₃ O ₄ -APTES.	100
6.14	Effect of co-existing anions.	103
6.15	Regeneration and reusability of GO-Fe ₃ O ₄ -APTES.	103
6.16	Plausible mechanisms for Chromium (VI) removal.	104
6.17	Image (A) shows the antibacterial activity of GO-Fe ₃ O ₄ -APTES against the E.coli at concentration 160 µg/ml (a) with a clear zone of inhibition but the zone of inhibition is not clearly visible at 80, 40, 20 µg/ml shown in b,c,d respectively. Image (B) shows the antibacterial activity of GO-Fe ₃ O ₄ -APTES against B. subtilis at concentration 160 µg/ml (a) and 80 µg/ml (b) with clear zone of inhibition but the zone of inhibition is not clearly visible at 40, 20 µg/ml shown in c,d respectively. At middle shows the clear zone of inhibition for gentamicin against both the bacteria	105
6.18	Shows the Concentration-dependent effect of GO-Fe ₃ O ₄ -APTES, when 10, 20, 40, 80, 160 µg/ml of GO-Fe ₃ O ₄ -APTES was incubated with <i>E.coli</i> and <i>B. subtilis</i> for 6 hours. Percentage viability of bacteria at varying concentration of GO-Fe ₃ O ₄ -APTES was measured.	105
6.19	Growth of <i>E. coli</i> and <i>B. subtilis</i> in the presence of GO-Fe ₃ O ₄ -APTES at concentration 160 and 80 µg/ml in varying interval of time.	106
6.20	GO-Fe ₃ O ₄ -APTES induced ROS generation in (a) <i>E.coli</i> and (b) <i>B. subtilis</i> . Fluorescence intensity shows the ROS generation at different concentration of GO-Fe ₃ O ₄ -APTES. Higher fluorescence intensity indicates the excess generation of ROS.	107

List of Figures in Appendices

A1	DTA and DTG curve of Fe_3O_4 , Fe_3O_4 -TSPED, and Fe_3O_4 -TSPED-Tryptophan	136
A2	The FT-IR spectrum of FTT after CR adsorption.	136
A3	FE-SEM image of FTT nanocomposite (a) before adsorption and (b) after CR adsorption.	136
A4	Figure A5 FE-SEM micrograph showing the alteration in bacterial cell membrane morphology where (a) represent the <i>B.subtilis</i> control image and (b) represent the EDX spectrum of bacterial surface (c) represent the FTT treated <i>B. subtilis</i> and (d) shows the EDX spectrum of FTT treated <i>B.subtilis</i> .	137
A5	FE-SEM micrograph showing the alteration in bacterial cell membrane morphology where (a) represent the <i>B.subtilis</i> control image and (b) represent the EDX spectrum of bacterial surface (c) represent the FTT treated <i>B. subtilis</i> and (d) shows the EDX spectrum of FTT treated <i>B.subtilis</i> .	137
A6	The FT-IR spectrum of GO- Fe_3O_4 -APTES after Cr (VI) adsorption	138
A7	FE-SEM image of after adsorption of Chromium (VI) (a) 1000 nm, (b) 500 nm resolution and (c) EDS mapping.	138
A8	Antibacterial activity of GO- Fe_3O_4 -APTES against <i>E.coli</i> , where (a) is FESEM image of <i>E.coli</i> , (b) is the <i>E.coli</i> treated with GO- Fe_3O_4 -APTES, (c) is the EDS analysis showing the elements in bacteria and (d) is the element deposited in bacteria after GO- Fe_3O_4 -APTES treatment.	139
A9	Antibacterial activity of GO- Fe_3O_4 -APTES against <i>B. subtilis</i> , where (a) is FESEM image of <i>B. subtilis</i> , (b) is the <i>B. subtilis</i> treated with GO- Fe_3O_4 -APTES, (c) is the EDS analysis showing the elements in bacteria and (d) is the element deposited in bacteria after GO- Fe_3O_4 -APTES treatment.	139

List of Tables

1.1	Major water pollutants and its sources.	3
1.2	The maximum contamination levels of toxic inorganic pollutants.	5
1.3	Common sources releasing inorganic contaminants into water.	7
1.4	List of some inorganic contaminants and their health problems.	9
3.1	Isotherm parameters for adsorption of CR on Fe ₃ O ₄ -TSPED-Tryptophan nanocomposite.	45
3.2	Adsorption capacity (q_{\max}) values for the removal of CR on various adsorbents.	46
3.3	Kinetic model parameters and constant with statistical data.	47
4.1	BET surface area, pore volume and pore size of Fe ₃ O ₄ , Fe ₃ O ₄ -GG nanocomposite.	61
4.2	Kinetics parameters for CR dye adsorption on Fe ₃ O ₄ -GG.	64
4.3	Isotherm parameters for the adsorption of CR on to Fe ₃ O ₄ -GG at room temperature (300k) and initial dye concentration 40 mg/L	66
4.4	Comparison of adsorption capacity of Fe ₃ O ₄ -GG nanocomposite for removal of Congo red dye with different adsorbents.	66
5.1	BET surface area pore size and the pore volume of Fe ₃ O ₄ , Fe ₃ O ₄ -APTES, and Fe ₃ O ₄ -APTES-EDTAnanocomposite.	75
5.2	Kinetic parameters for heavy metal ions sorption on Fe ₃ O ₄ -APTES-EDTA nanocomposite	79
5.3	Isotherm parameters for the adsorption of heavy metal on to Fe ₃ O ₄ -APTES-EDTA at room temperature (25°C).	81
6.1	Kinetic parameters for Chromium (VI) adsorption on GO-Fe ₃ O ₄ -APTES powder.	99
6.2	Isotherm parameters for the adsorption of chromium (VI) on to GO-Fe ₃ O ₄ -APTES powder at room temperature (25 °C).	101
6.3	Comparison of performance of the proposed method with some previously reported Chromium (VI) adsorption systems.	102

Acronyms

APTES	(3-aminopropyl)triethoxysilane
FA	Fe ₃ O ₄ -APTES
TSPED	N-[3-(Trimethoxysilyl)propyl]-ethylenediamine
FT	Fe ₃ O ₄ -TSPED
FTT	Fe ₃ O ₄ -TSPED-Tryptophan
FAE	Fe ₃ O ₄ -APTES-EDTA
CR	Congo red
<i>E. coli</i>	<i>Escherichia coli</i>
<i>B. subtilis</i>	<i>Bacillus subtilis</i>
MeB	Methylene blue
MG	Malachite green
MB	Methyl blue
MO	Methyl orange
EBT	Eriochrome Black T
Rhb	Rhodamine B
FT-IR	Fourier-transform infrared spectroscopy
FESEM	Field emission scanning electron microscopy
FCS	Fluorescence correlation spectroscopy
XRD	X-ray powder diffraction
TEM	Transmission electron microscope
EDX	Energy dispersive X-ray
SEM	Scanning electron microscope
VSM	Vibrating sample magnetometer
BET	Brunauer-Emmett-Teller surface area analysis
TGA	Thermogravimetric analysis
GO	Graphene oxide
GOFA	GO- Fe ₃ O ₄ -APTES
<i>M. luteus</i>	<i>Micrococcus luteus</i>
GG	Guar-gum
pH	Potential of Hydrogen

UV/Vis	Ultraviolet/Visible
Cr (VI)	Chromium (VI)
Pb	Lead
Cd	Cadmium
Ni	Nickel
Co	Cobalt
Cu	Copper
U	Uranium
Th	Thorium
AAS	Atomic absorption spectroscopy

Table of Contents

Page No.

Certificate of Examination	ii
Supervisors' Certificate	iii
Dedication	iv
Declaration of Originality	v
Acknowledgment	vi
Abstract	viii
List of Figures	xi
List of Figures in Appendices	xv
List of Tables	xvi
Abbreviations	xvii
Contents	
CHAPTER 1 Introduction	1
1.1 Research motivation	1
1.2 Background of water pollution	2
1.3 Inorganic pollutant in water and its sources	3
1.3.1 Health hazardous of inorganic pollutants	5
1.3.2 Removal methods available for inorganic contaminants from wastewater	6
1.3.2.1 Reverse osmosis process	6
1.3.2.2 Ion-exchange	7
1.3.2.3 Chemical precipitation	8
1.3.2.4 Bio-sorption	9
1.3.2.5 Coagulation and flocculation	10
1.3.2.6 Phytoremediation	10
1.3.2.7 Adsorption	10
1.3.3 Materials available for removal of inorganic contaminants	12
1.4 Organic pollutant in water	12

1.4.1	Source of organic contaminants	12
1.4.2	Health hazard	13
1.4.3	Removal technique available for organic contaminants	13
1.4.3.1	Electrocoagulation process	13
1.4.3.2	Adsorption	14
1.4.3.3	Photo catalytic degradation	14
1.4.4	Materials are available for removal of organic contaminants.	14
1.5	Bacteria in water pollution	15
1.5.1	Nanocomposite material in water purification and its impact on bacteria	16
1.6	Background on Nanomaterials	16
1.6.1	Metal oxide Nanomaterials	17
1.6.1.1	Iron oxide nanoparticles	17
1.6.1.2	Iron oxide based composite materials	18
1.6.1.3	Synthesis route of iron oxide nanoparticles	18
1.6.1.4	Precipitation method	19
1.6.1.5	Characterization techniques	19
1.7	Research gap	21
1.8	Research objective	21
1.9	Overview of thesis	22
CHAPTER 2 Materials and Methods		24
2.1	Reagent and chemicals	24
2.2	Synthesis of iron oxide (Fe ₃ O ₄) nanoparticles	25
2.3	Synthesis of Fe ₃ O ₄ -TSPED (FT)	25
2.4	Synthesis of Fe ₃ O ₄ -TSPED-Tryptophan (FTT)	25
2.5	Synthesis of Fe ₃ O ₄ -GG nanocomposite	25
2.6	Preparation of Fe ₃ O ₄ -APTES nanocomposite.	26
2.7	Preparation of Fe ₃ O ₄ -APTES-EDTA nanocomposite	27
2.8	Preparation of Graphene oxide (GO)	27
2.9	Preparation of GO-Fe ₃ O ₄ -APTES	27

2.10	Characterization techniques	29
2.10.1	FTIR spectroscopy	29
2.10.2	X-ray powder diffraction	29
2.10.3	Scanning electron microscope (SEM) and energy dispersive X-ray (EDX)	29
2.10.4	Field emission scanning electron microscope (FE-SEM)	29
2.10.5	Transmission electron microscope (TEM)	29
2.10.6	N ₂ adsorption-desorption isotherm	30
2.10.7	Vibrating Sample Magnetometer (VSM)	30
2.10.8	Raman spectrometer	30
2.10.9	Zeta potential	30
2.10.10	UV-visible spectroscopy	30
2.10.11	Atomic adsorption spectroscopy (AAS)	30
2.10.12	Fluorescence	30
2.10.13	pH analysis	31
2.10.14	Thermogravimetric analysis	31
2.11	Adsorption behavior	31
2.11.1	Adsorption kinetics	31
2.11.2	Adsorption isotherm	32
CHAPTER 3 Amine functionalized magnetic iron oxide nanoparticles: Synthesis, antibacterial activity and rapid removal of Congo red dye		34
3.1	Introduction	34
3.2	Batch adsorption experiment	36
3.3	Antibacterial activity of FTT	36
3.3.1	Cultivation of bacteria	36
3.3.2	Disc diffusion method	36
3.3.3	Concentration and time-dependent antibacterial activity	37
3.3.4	Examination of bacterial cell morphology under FE-SEM	37
3.3.5	Assessment of reactive oxygen species (ROS) generation	37
3.4	Result and discussion	37

3.4.1	Characterisation of magnetic nano adsorbent	37
3.4.2	Impact of the different parameter on adsorption	43
3.4.3	Adsorption isotherm	45
3.4.4	Adsorption kinetics	46
3.4.5	FT-IR and FE-SEM analysis of after adsorption of Congo red dye	47
3.4.6	Reusability of adsorbent	48
3.4.7	Antibacterial activity	48
3.5	Summary	51
CHAPTER 4 Guar-gum coated iron oxide nanocomposite as an efficient adsorbent for Congo red dye		52
4.1	Introduction	52
4.2	Batch adsorption experiment	54
4.3	Result and discussion	55
4.3.1	Characterisation of magnetic nano adsorbent	55
4.3.2	Preferential adsorption of different dyes	61
4.3.3	Impact of different parameters on the adsorption	61
4.3.4	Adsorption kinetics	63
4.3.5	Adsorption isotherm	64
4.3.6	Comparative study of adsorption capacity with different adsorbents	65
4.3.7	Regeneration of dye-loaded adsorbent	65
4.4	Summary	67
Chapter 5 An investigation of heavy metals adsorption by hexadentate ligand modified magnetic nanocomposite		68
5.1	Introduction	68
5.2	Batch adsorption study	69
5.3	Results and discussion	70
5.3.1	Adsorbent characterizations	70
5.3.2	Impact of the different parameter on adsorption	76
5.3.3	Adsorption kinetics	78

5.3.4	Adsorption isotherm	79
5.3.5	Desorption and reusability	80
5.3.6	Adsorption mechanism	82
5.4	Summary	83
Chapter 6 Surface functionalization of graphene oxide using amino silane magnetic nanocomposite for Cr (VI) removal and bacterial treatment.		84
6.1	Introduction	84
6.2	Adsorption experiment	86
6.3	Antibacterial activity	87
6.3.1	Bacterial culture	87
6.3.2	Antibacterial activity of GO-Fe ₃ O ₄ -APTES	87
6.3.3	Analysis of bacterial damage under FE-SEM	87
6.3.4	Detection of ROS production	87
6.4	Result and discussion	88
6.4.1	Characterization of the adsorbent	88
6.4.2	Impact of the different parameter on adsorption	95
6.4.3	Adsorption kinetics	98
6.4.4	Adsorption isotherm	100
6.4.5	Influence of co-existing ion	100
6.4.6	Reusability of adsorbent	101
6.4.7	Adsorption mechanism	103
6.4.8	Antibacterial activity	104
6.5	Summary	107
CHAPTER 7 Conclusions and Scope of Future Work		108
6.1	Conclusions	108
6.2	Scope of Future Work	109
Bibliography		110
Appendices		136
Dissemination		140
Vitae		142

Chapter 1

Introduction

Chapter summary

In this chapter, we focused on the water contamination and its environmental effects followed by their purification process. The overall thesis emphasizes about inorganic and organic contaminants and the source of these contaminants along with and their effects on the health of aquatic life. Due to hazardous effect of these contaminants, it is necessary to remove them with the available methods. The various removal techniques are discussed in details using synthesized iron oxide-based nanocomposite. Furthermore, the antibacterial activity of synthesized iron oxide-based magnetic nanomaterials was thoroughly investigated.

1.1 Research motivation

The worldwide demand for freshwater is increasing due to population growth. Out of the total available water, 2.7 % is freshwater while remaining 97.3 % of water remains in ocean. This 2.7 % freshwater was contributed by groundwater, river, lakes, polar, ice and glacier (distribution graph is presented in Fig. 1)[1]. In the current scenario, lots of industries are coming up to make our life simpler but we are missing ‘how to utilize the wastewater from the industries in better way’ and in addition to that, we are dispensing industrial effluents into the water bodies, which in later stage affect the drinking water sources[2]. Per day, around 2 million tons of chemicals, industrial waste and agricultural wastes are being disposed into water system[3]. In literature, it has been reported that due to water-related contamination, every day more than 14000 people lose their life [4]. From literature survey we know that the higher percentage of diseases is caused by use of polluted water and around 500 children below the age of five die due to diarrhea only. According to Central Pollution and Control Board (CPCB) of India, 80 % of drinking water comes from river but half of the river in India is polluted and not suitable for drinking purposes. In India two rivers Ganga and Yamuna are now being added in the list of top 10 dirtiest rivers in the world [5]. Waste water contains several toxic contaminants like organic dyes, heavy metal ions, inorganic compounds, pesticides, pharmaceutical waste and many other complex compounds [6-8]. Among all toxic substances heavy metals and dyes are highly carcinogenic. Thus, it is necessary to prevent the harmful effects of toxic substances and keep the environment safe and improve the human living condition. The present work focuses on the novel synthesis of magnetic materials for remediation of water pollutants before discharging into water bodies.

Global Water Scenario

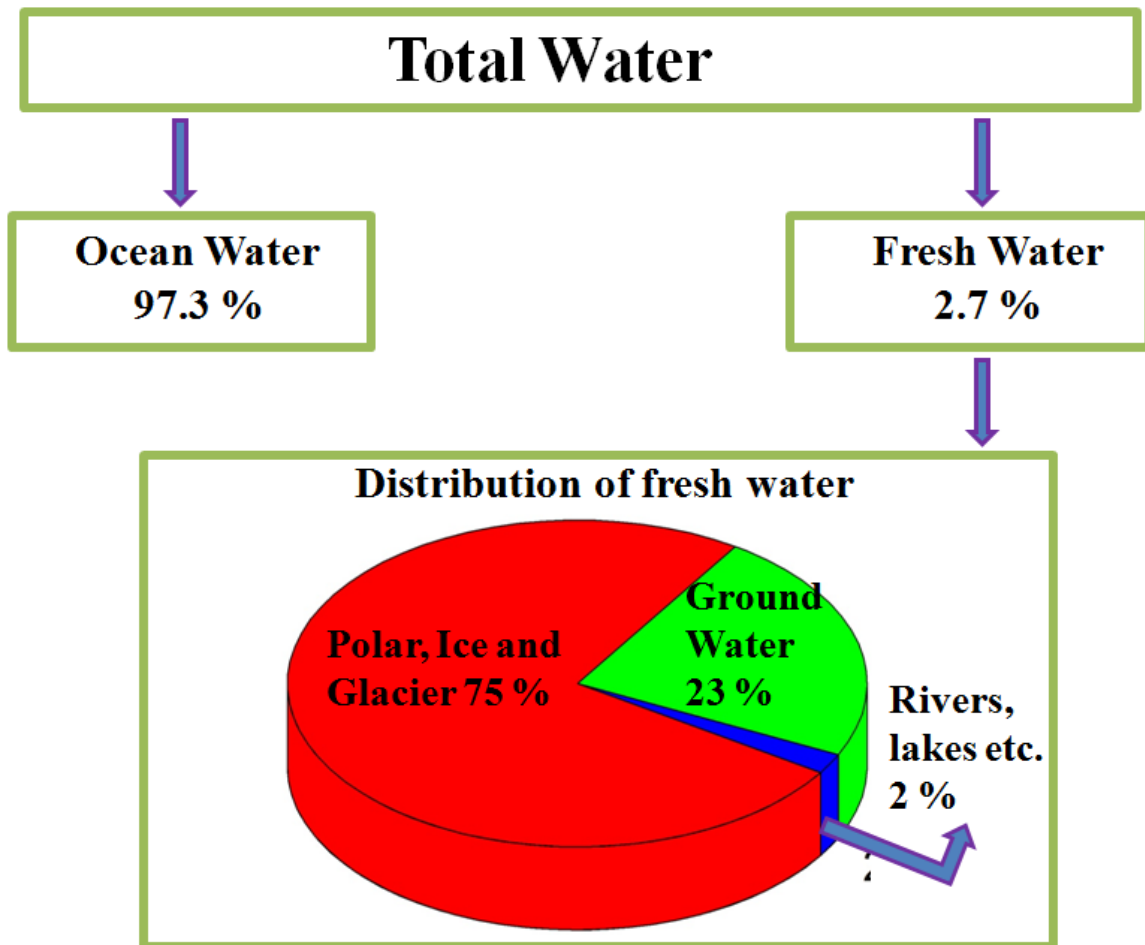


Figure 1.1 Distribution of water bodies on Earth.

1.2 Background of water pollution

Environmental pollution is a serious problem because of developing technology and industrialization. It is the preamble of toxic or poisonous substances into the natural environment. The same can also be defined as the discharge of unwanted materials, overuse, misuse, and mismanagement of natural resources in the environment to fulfill the ever-growing need and greed of human activities. The pollution levels are high in developed cities because of large population, which produces more contaminated water with inadequate waste management. Now, the time has come to implement necessary steps to address these environmental issues. The Environmental Protection Agency, scientific communities and countries across world are thinking about developing technology towards the eradication of environmental pollution. Environmental pollution arises at various levels; soil, water, air, radioactive, sound, thermal, light, etc. Every type of pollution has two sources of occurrence; the non-point and point sources. The non-point sources are hard to control, whereas the point sources are easy to identify, monitor and control. Among all environmental pollutions, water pollution is of greater interest, as water is the backbone of life and pure water is the elixir of

life. Furthermore, water is universal liquid and it is equally essential for all living organisms on Earth. Water pollution affects surface water such as lakes, rivers, and oceans. Polluted water is analyzed for the presence of chemical, physical and biological substances that interfere with the quality of water and renders it unsuitable for drinking purpose. We know that freshwater is colorless, odorless and transparent but the symptoms of polluted water are basically bad taste or smell. However, some water pollutants are invisible and have no smell or taste such as chemicals like's pesticides and pathogenic micro-organism are mixed with freshwater but at later stage it affects living organism. We can't use contaminated water for drinking, washing or agriculture purpose because it can affect our body in various ways, depending on the concentration and type of pollutant. For biological pollutants main groups are bacteria, viruses and protozoa are affecting the freshwater. Chemically, water pollution is due to heavy metals, pesticides, colouring substances, organic chemicals, fertilizers etc. Some major water pollutants and their sources are shown in Table1.1.

Table1.1 Major water pollutants and its sources.

Category	Pollutants	Sources
Organic	Dyes, pesticides, plastic, phenol and it's derivative, detergents, oil, gasoline, etc.	Industries, sewage, agriculture, household
Inorganic	heavy metals, salts, fluoride, nitrate, sulphate, etc.	Industrial effluents, household, surface runoff, agriculture, sewage
Bio	Bacteria, viruses, parasites, etc.	Sewage, pharmaceuticals, human and animal excreta
Radioactive materials	Uranium, thorium, cesium, iodine, radon, etc.	Mining and processing of ores power plant, weapons production, natural resources.

1.3 Inorganic pollutant in water and its sources

The inorganic contamination present in water bodies creates a serious environmental concern in current time. Among inorganic pollutant, heavy metals, trace elements, acids, inorganic salts, cyanide, sulphate, etc. have gained attention, due to their toxic nature. These are non-biodegradable and hence persist in environment for longer time period. The major sources of inorganic pollutant released into environmental segment are domestic and agricultural wastes along with industrial effluent. The most toxic common inorganic pollutants are discussed below.

Metals: The amount of metal present in water depends on the sources of water. The concentration of various metals depends on the type of mining units, industrial units, and agricultural practices. Heavy metals are metallic element having comparatively high specific gravity and high density, almost five times greater than the specific gravity of water[9, 10]. The list of toxic heavy metals includes Mercury (specific gravity 13.54), Arsenic (5.7), Chromium (7.19), Cadmium (8.65), Zinc (7.13), Cobalt (8.74), Nickel (8.8), Lead (11.35) and Iron (7.9), etc.[11, 12] These toxic inorganic metals are divided into three categories such as precious metals (like Pt, Au, Ag, Pd, Ru, etc.), radioactive metals (like Th, U, Am, Ra, etc.) and carcinogenic metals (As, Hg, Cr, Zn, Co, Ni, Cu, Cd etc.). Heavy metals enter into our body via drinking water, air, and food. Some metals like selenium, copper, and zinc are important in trace quantities to maintain the vital metabolic processes in humans; however if the concentration increases it shows reverse effect on living organism.

Fluorides: Fluorine is the most reactive and highly electronegative element in the periodic table. Fluorides originate from different minerals like fluor spar (CaF_2), Fluorapatite ($\text{Ca}_5(\text{PO}_4)_3\text{F}$) sellaite (MgF_2) and cryolite (Na_3AlF_6). They are basically found in rocks, soil, plants, animals and human beings. Many industries such as ceramic production, brick and iron factories, electroplating, aluminum, smelters, semiconductor manufacturing, and beryllium extraction plants are highly responsible for fluorides contamination in surface water[13]. Almost, 10 to 1000 mg/L of fluoride contaminants are present in industrial wastewater. According to WHO guideline, 1.5 mg/L is the permissible limit of fluoride in drinking water, it exceeds the limit, then it is harmful to live organisms. It is reported that more than 200 million people consume drinking water with fluoride concentration beyond the permissible limit[14]. Fluoride contamination creates multiple effects on human health including arthritis, mottling of teeth, neurological disorder, embrittlement of bones, thyroid disorder, and it also interferes with DNA synthesis, gastro-intestinal tract, carbohydrates, lipids, vitamins, proteins and mineral metabolism[15].

Sulfate: It is another inorganic pollutant present in water that is caused as a result of leaching from sulfur deposits in Earth's crust and other human activities. The permissible limit of sulfate in drinking water is 250 mg/L.

Nitrate: Nitrate pollutant enters the water via fertilizers and from human or animal wastes. The concentration level of nitrate in drinking water is 45 mg/L. Beyond the permissible limit it causes methemoglobinemia (blue baby disease)[16]. Table 1.2 shows widely observed toxic inorganic pollutant and their permissible limit[17].

Table 1.2 The maximum contamination levels of toxic inorganic pollutants.

Heavy metals	Water permissible limits (mg/L)
Arsenic	0.010
Mercury	0.002
Chromium	0.100
Nickel	0.100
Cobalt	0.002
Thallium	0.002
Nitrate	1.000
Cyanide	0.200
Barium	2.000
Beryllium	0.004
Antimony	0.006
Fluoride	1.500
Asbestos	0.010
Nitrite	1.000
Selenium	0.050

Inorganic contaminants mainly arise from the industrial effluent discharged by industries dealing with electronic equipment manufacturing, electroplating, and chemical processing plants. Figure 1.3 represents some of the common industrial units releasing toxic metal ions into water.

Paper mills and Fertilizer industries are release effluents such as various cyanides, ammonia, alkalis, and heavy metals into the water bodies[18]. Additionally, the considerable amount of heavy metal ions is originated from wastewater of various dyes and pigment industries, metal cleaning, galvanometry, leather and mining industries, which further improve the environmental contamination. A different inorganic pollutant and their sources are represented in Table 1.3. Among all represented inorganic pollutant arsenic, lead, chromium, mercury, cobalt, Nickel, copper are extremely carcinogenic heavy metals of widespread use in many industries. In current time, heavy metal pollution is important issue towards ecological consequence.

1.3.1 Health hazardous of inorganic pollutants.

Elements such as iron, copper, cobalt, manganese, zinc, and molybdenum play a key role in living organism. However, they are toxic at higher concentration. Inorganic contaminants are

non-biodegradable so it can easily enter into the bodies because of their high solubility in water and later stage it creates health problem in living system[19-21]. Some toxic metals and their impacts are summarized in the Table 1.4. Excessive consumption of heavy metal contaminants creates a number of illness such as kidney damage, liver damage, brain disorders, diarrhea, lungs damage, nausea, renal dysfunctions, damaged central nervous system and cancer[22]. Thus, it is important to control metal-contaminated effluents before they are discharged into aquatic systems[23].



Figure 1.2 Sources of water pollution (Graphic Courtesy: Central Pollution Control Board India)

1.3.2 Removal methods available for inorganic contaminants from water

Several removal methods have been reported to reduce the load of inorganic contaminants present in water and to make it suitable for human use and consumption. The important methods and techniques employed are reverse osmosis, ion-exchange, chemical precipitation, bio-sorption, coagulation and flocculation, phytoremediation, adsorption, etc.[24]. The general criteria of all the techniques are described briefly.

1.3.2.1 Reverse osmosis process

In reverse osmosis (RO), the solute molecules are separated from solution through a semi-permeable membrane using pressure, which retains the solute on one side while the solvent molecules are passed to the other side (Figure. 1.3)[25]. The semi-permeable membranes are

generally based on synthetic and natural polymers (polysulfone, polyamide, cellulose, cellulose acetate, etc.). For removal of inorganic pollutants, reverse osmosis process is considered as potential technique where the pollutants are separated by semi-permeable membrane at a high pressure (i.e. greater than osmotic pressure) caused by the solutes present in polluted water. RO is one of the most useful methods for water purification, it has some limitations like cost-effectiveness, drinking water obtained after reverse osmosis treatment is devoid of useful minerals, membranes are clogged after prolonged use and, hence, it requires periodical replacement.

Table 1.3 Common sources releasing inorganic contaminants into water

Contaminates	Sources
Arsenic	Automobile exhaust/industrial dust, wood preservatives, dyes, etc.
Lead	Petrol based materials, leaded gasoline, pesticides, mobile batteries, etc.
Chromium	Electroplating industry petrol refining, textile manufacturing, leather, tanning, pulp processing unit, etc.
Cadmium	Batteries, pesticides, electroplating industries, polyvinyl, copper refineries, phosphate fertilizers, paint pigments, detergents, refining petroleum products, etc.
Mercury	Electric/Light bulb, leather, tanning, wood preservatives, thermometers, ointments, paint, etc.
Cobalt	the power plant, nuclear reactor, etc
Nickel	Batteries, electroplating industries, etc.
Copper	Waste incinerators, coal-fired power stations, sewage treatment process, metal production, agricultural chemicals, etc.
Fluorides	Semiconductor processing, pharmaceuticals, ceramic production, fluoride

1.3.2.2 Ion-exchange

The ion-exchange process involves the reversible chemical reactions for removal of inorganic contaminants from wastewater by replacing them with other similarly charged ions[26]. Some positively and negatively charged inorganic pollutants are exchanged with ions held by electrostatic forces on the exchange resin (Figure 1.4). Ion-exchange resins are very small polymer matrix. Based on their functional groups attached on polymer matrix, the ion exchange resins are classified as two types such as cation and anion exchange resins. In a cation exchange process, positively charged pollutants are replaced with positively charged ion-exchange resin surface. Similarly, in anion-exchange process, negatively charged

pollutants are replaced with negatively charged ion-exchange matrix. Typically, the exchange medium consists of solute phase (synthetic resin or zeolites) having a transportable ion attached to an immovable functional of base or acid group. Transportable ions are exchanged with solid ions having greater attraction towards functional group. Inorganic pollutants like mercury, chromium, arsenic, nitrate, etc. can be removed by anion resins.

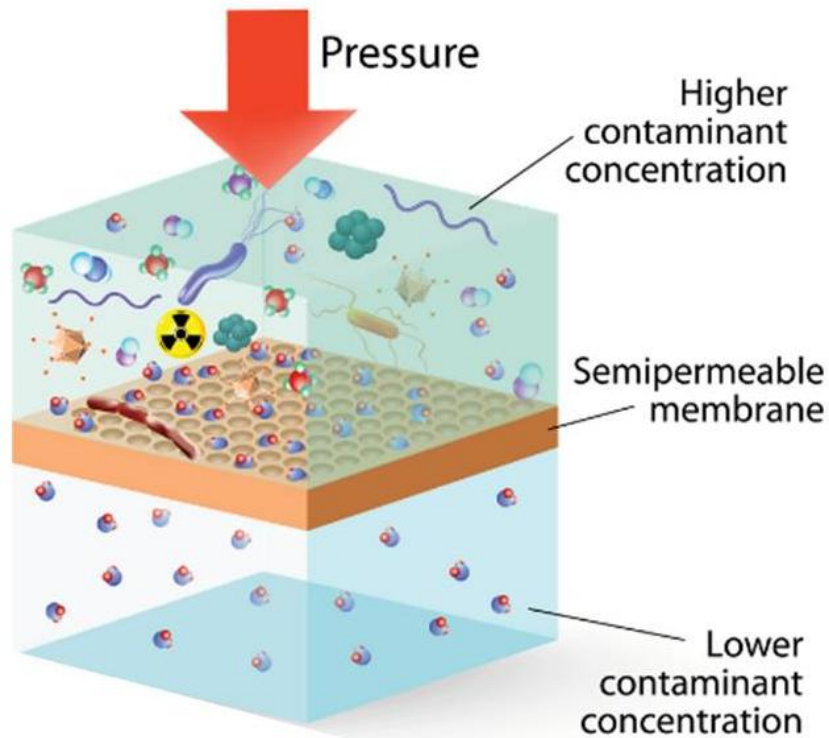


Figure 1.3 Schematic illustration of the removal of inorganic water contaminants by reverse osmosis process. (Graphic Courtesy: Water products)

Advantages of ion exchange process include easy removal of contaminants (anions and cations) from wastewater, recovery of materials from industrial waste, capability to handle hazardous wastes, etc. However, the limitations are ion-exchange resin cannot for the diet requiring low sodium intake because ion-exchange resin-treated water that contains sodium, it cannot remove biological pollutants and organic compound, high cost and partial removal of certain ions.

1.3.2.3 Chemical precipitation

Chemical precipitation technique is widely used for separation of inorganic contaminants from wastewater. In this process some precipitant such as lime, alum, iron salts and other organic polymers are converted to soluble carcinogenic ions and transferred as insoluble solid phase[27]. However, the treated contaminated water is unable to meet the permissible limit for inorganic pollutants for drinking purpose as per different agencies like US EPA, WHO,

etc. Thus, it is necessary for subsequent treatments using different physio-chemical process to improve the quality of drinking water by remembering the precipitate which produces the greater amount of sludge containing harmful compounds, which make it unsuitable for wastewater treatment.

Table 1.4 List of some inorganic contaminants and their health problems.

Inorganic contaminants	Diseases
Arsenic	Gastrointestinal upsets, dermatitis, muscle cramps, , bronchitis, convulsions, etc.
Lead	Acute or chronic damage to the nervous system, effects on the kidneys, anemia, gastrointestinal tract, joints and reproductive system, weight loss, headache, fatigue, cognitive dysfunction and decreased coordination, nerve conductions, memory loss, etc.
Cadmium	Renal dysfunction, Hypertension or high blood pressure, lung cancer, lung disease, osteomalacia, liver damage, osteoporosis, shortened lifespan, etc.
Mercury	Depression, anxiety, confusion, irritability, fatigue, insecurity, etc.
Chromium	Eye irritation, asthma, liver damage, perforated eardrums, respiratory irritation, edema, pulmonary congestion, upper abdominal pain, respiratory cancer, nose irritation, etc.
Cobalt	Effects on the lungs, including asthma, pneumonia, and wheezing.
Nickel	Dermatitis (a type of skin rash), hand eczema, effects in their blood (increased red blood cells), kidneys (increased protein in the urine), chronic bronchitis, reduced lung function, and lung cancer and nasal sinus
Copper	Nausea, diarrhea, Brain damage, chest pain, irritation of the respiratory tract and kidney problem, etc.
Fluorides	Thyroid, dementia, dental, diabetes, skeletal and sometimes neurological disorder etc.

1.3.2.4 Bio-sorption

The bio-sorption process involves the use of biological systems such as bacteria, algae, yeasts, and fungi to accumulate inorganic pollutants from contaminated water through Physico-chemical pathways[28, 29]. The limitation of bio-sorption process is longer time for removal of waste from contaminated water.

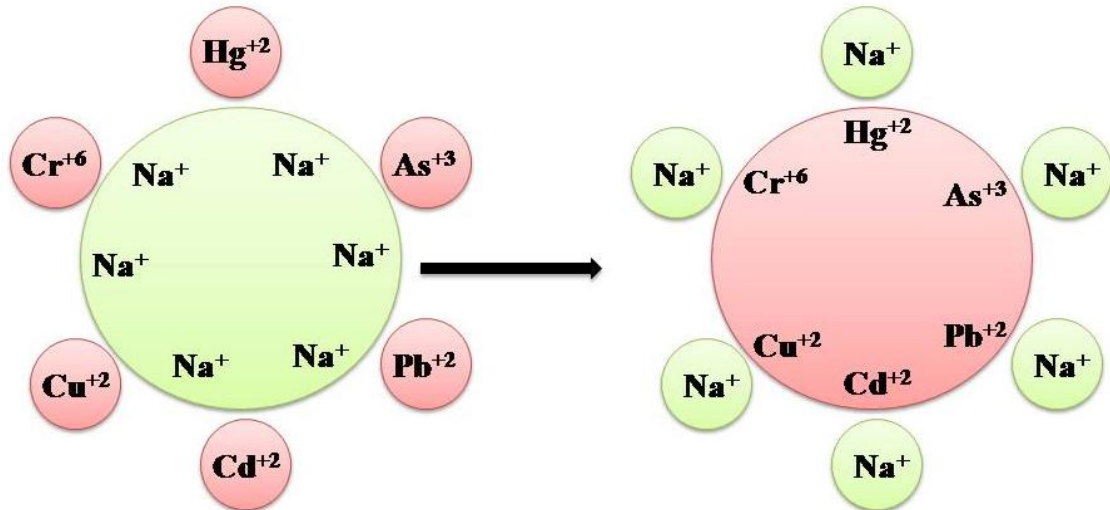


Figure 1.4 Removal of inorganic contaminants using ion-exchange process.

1.3.2.5 Coagulation and flocculation

Coagulation and flocculation are physical techniques used to purify contaminated water. The method includes filtration followed by sedimentation to separate inorganic pollutant from wastewater (Figure 1.5)[30-32]. Coagulation is a chemical process and flocculation is a physical process; however, coagulation involves the neutralization of charge while flocculation does not involve any such process. Many coagulants such as iron and aluminum salts are widely used in wastewater treatment. This removal technique is effective for inorganic impurities by charge neutralization of particles. This method has two major limitations like continuous supply of huge chemicals and operational cost is too high.

1.3.2.6 Phytoremediation

Phytoremediation is an environmentally friendly media that uses living plants to separate pollutants from water sources as shown in (Figure 1.6)[33, 34]. Though, it is a greener way to remove inorganic pollutants from wastewater. Two major limitations of this process involve longer time for removal of inorganic pollutants and regeneration of the plants for further use.

1.3.2.7 Adsorption

The adsorption process is a prominent technique for removal of inorganic pollutants from contaminated water. In this process, solid phase is used as adsorbent to separate solid from aqueous phase (Figure 1.7)[23, 35-37]. The substance which adsorbs the solid medium is called adsorbate and on which it is being adsorbed is called adsorbent. Among all removal processes, adsorption is prominent due to low cost, no sludge formation, high removal efficiency, simple to handle and safe operation. In this process, the adsorbent can recycle by suitable desorption process for re-use. Some parameters affect the adsorption process such as

type of adsorbent and adsorbate, amount of adsorbent, initial adsorbate concentration, temperature, pH of the solution and other impurities in the solution. The parameters which affect the removal efficiency of inorganic pollutants can be optimized for the best performance. The adsorbate attaches onto the adsorbent surface via two different ways such as physical adsorption (physisorption) and chemical adsorption (chemisorption)

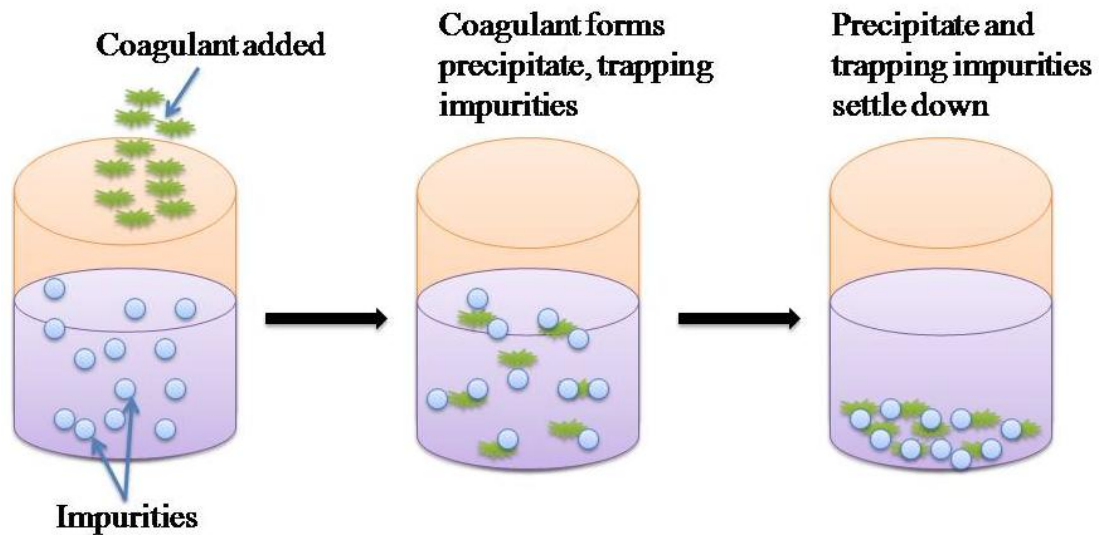


Figure 1.5 Coagulation process for removal of inorganic contaminants.



Figure 1.6 Phytoremediation process for removal of inorganic contaminants. (Graphic Courtesy: National Institute for Biotechnology and Genetic Engineering)

In the physisorption process, weak Vander wall interaction occurs between adsorbate and adsorbent surface. Depending upon the nature of adsorbent, the adsorbent surface is monolayer or multilayer. Physisorption is a very fast process that means interaction between

adsorbent and adsorbate requires very less activation energy i.e. 5-20 kJ/mol[38]. In chemisorption process, a strong chemical bond or strong force of attraction is involved between adsorbate and adsorbent. The strong chemical bonding is due to electrostatic interaction, ion exchange, chelation, complex formation, etc. Here, high amount of energy (i.e. 40-400 kJ/mole) is required to break the chemical bond between adsorbate and adsorbent surface.

1.3.3 Materials available for removal of inorganic contaminants

Adsorbents play an important role in the removal of inorganic contaminants. Some of materials such as zeolite, activated carbon, activated alumina, metal oxide, iron oxide, silica, clay, etc. have been already reported as an adsorbent for removing inorganic contaminants[39-45]. However, the adsorbent used in heavy metal removal depends on various parameters such as selectivity, adsorption capacity, non-toxicity, adsorption kinetics reusability and regeneration, and low operational cost. The preparation of adsorbents is an interesting research field to explore. Looking towards the advantages of adsorption processes the nanocomposite based adsorbents are in demand because of their uniform pore size distribution, high surface area, high pore volume, high thermal stability, and mechanistic properties.

1.4 Organic pollutant in water

In water pollution, organic contaminants are playing a vital role as inorganic contaminates. Most of the organic pollutants include pesticides, and plant and animal tissues, and are usually expected to cause adverse impact on the environment. The trace amount of organic contaminant found in water, soil, air, and sometimes in food, which might cause various type of environmental problem[46]. The list of organic pollutants includes different dyes such as Congo red, malachite green, methyl blue, methyl orange, Rhodamin B, Eriochrome black T, etc., and aliphatic compounds (trichloroethylene, chloroform, etc.), chlorinated aromatic (chlorobenzene, dichlorobenzene, 4-chlorophenol, etc.), organic solvents and pesticides. Due to their vast use, endocrine disruptors (like bisphenol A, atrazine), pharmaceuticals (like ibuprofen, flumequine, carbamazepine), synthetic musk and fragrances (like musk xylene and galactoside), personal care products (like oxybenzone and parabens), dyes (Congo red, malachite green, safranin-O and methylene blue), pesticides (like isoproturon and endosulfan) and other toxic substances are found in larger amount in contaminated drinking water and surface water[47-49]. Among all substances, most of them are used in our daily life; it is difficult to eliminate them. However, it is necessary to control completely, so it is required to remove through chemical/physical/mechanical or other processes.

1.4.1 Sources of organic contaminants

There are several ways through which organic pollutants enter into the aquatic systems[50, 51]. The sources are summarized below:

- Impurities from wood preservatives
- Incomplete combustion of fossil fuels.
- Organic dyes discharged from textile industries.
- Waste products from cooking food that is discharged from domestic sources.
- Compounds mobilized by volatilization from the soil.
- Contaminants discharge from industrial/domestic process.
- Residues from detergents.
- Compounds from antibiotics, pharmaceuticals, synthetic steroids, and hormones.
- Solvents, flame retardants
- Compounds from the various above groups with endocrine-disrupting potential.

1.4.2 Health Hazard

In the current scenario, the environmental effect due to organic contaminants received greater attention from researchers worldwide. The contamination of the aquatic life has become an important concern because contaminated water creates multiple diseases among aquatic animals. Many studies revealed the abnormalities observed in aquatic organisms like abnormal ratio of testosterone and estrogen in juvenile alligators and disturb the reproductive tissues, sexual abnormalities in fish, etc[52-55].

1.4.3 Removal technique available for organic contaminants

There are several techniques available for the treatment of contaminated water. They include biological, physical and chemical processes. Most of the removal methods have both advantages and disadvantages. A number of processes are not considered for large scale purification owing to their high cost, secondary toxic side products, and sludge disposal problems, etc. There are several physio-chemical methods available such as filtration, electrocoagulation, photocatalytic degradation, ion-exchange, adsorption, membrane separation are being used to treat[56, 57]. All removal processes are simple yet they possess some limitations like high cost, low removal efficiency, huge amount of sludge production, making these removal processes are unsuitable for treating the contaminated water. However, a brief description and limitations associated with each physio-chemical processes are described below.

1.4.3.1 Electrocoagulation process

Electrocoagulation is an electrochemical method developed for contaminated water treatment. It is a simple and reliable process to separate organic pollutants from contaminated water[58-62]. In this process a direct current is applied between metal electrodes immersed in contaminated water. The metal electrode is made up of aluminum or iron. Electrocoagulation process passes through several consecutive steps such as removal of colloidal pollutants on coagulants or removal of suspended particles, electrolytic reaction at metal electrode surfaces, and formation of wide range of coagulated species in an aqueous phase, which further adsorb by flotation or sedimentation process.

1.4.3.2 Adsorption

The adsorption process is a prominent method for purifying the contaminated water and produces pollutant-free water by removing various kinds of organic contaminants [63-67]. This process is economically feasible, effective, eco-friendly and simple to operate. This process is advantageous in terms of its hydrophobic interactions for adsorbing organic contaminants, especially non-polar contaminants. The efficiency of nano adsorbents is usually limited by the active sites, surface area, the lack of selectivity, and the adsorption kinetics. Due to lack of advantages, adsorption process is best method for removing both organic and inorganic contaminants in wastewater.

1.4.3.3 Photocatalytic degradation

Photocatalytic degradation is the advance oxidation method for degradation of organic contaminants in wastewater. In photocatalytic degradation, the light energy or photons is to create hole (h^+) and electrons (e^-), which play a part in redox reactions to degrade the organic pollutants[68-70]. This process has some limitations like high temperature, formation of by-products, long-time period, etc.

1.4.4 Materials available for removal of organic contaminants

The removal process is widely used for the treatment of wastewater from organic contaminants and received attention from the researchers. In current years, various low-cost adsorbents agricultural waste, natural materials, industrial waste, clay minerals, fly ash, metal hydroxide sludge, wood powder, etc are available but they have some limitations like contaminated binding sites[71-79]. One of the key driving forces for the use of nanoparticle in the removal of organic contaminants is its unique physicochemical properties as compared to bulk materials. Most of the researchers have great interest to prepare different types of activated carbon, metal oxide and graphene-based adsorbents for the removal of organic contaminants. A significant volume of researchers showed the inhibition of the aggregation produced by highly active nanoparticles. In this direction, the blending of porous

nanoparticles and nanocomposites are interesting areas in the field of wastewater treatments. The following section deals with bare metal oxide and its functionalization along with its synthesis techniques.

1.5 Bacteria in water pollution

Water pollution is not only restricted to chemical contamination but also to different microorganism and pathogens, which are also capable of polluting the water. A variety of sources can contribute to the contamination of water, bacteria is one of them. Biological sources of pollution are the crucial components of water pollution[80]. A small amount of bacterial contaminants is enough to pollute the entire water body and to make it unhygienic for human health. Water contamination by bacteria is a global health issue [81] which leads to different water-borne disease like meningitis, hepatitis, gastroenteritis, dysentery, and salmonellosis[82]. Coliform bacteria (*E.coli*) is the marker organism to detect the fecal contamination of potable water[83]. Presence of *E.coli* in water indicates the fecal contamination[84]. *E.coli* is the extraintestinal pathogenic bacteria which may found in the drinking water system due to contamination of water resources[85]. Some other *coli* form bacteria include the member of genera *Escherichia*, *Klebsiella*, *Enterobacter*, and *Citrobacter*. *Bacillus subtilis* as a water-polluting microorganism was identified in the tap water[86]. It shows resistance to chromium and sensitive to silver, cadmium, and mercury[86]. The presence of *B. subtilis* is also identified in the surface water in the rivers and drinking water sources[87]. Most common treatment method available so far to remove bacillus spores are chlorination and filtration. These spores can also be removed by using the bipolar electrochemical method [88]. *Micrococcus luteus* is present in dust, soil, water and as human skin flora. Apart from these three bacteria other different micropollutants and cyanobacteria are found to be a threat to human health by contaminating drinking water [89]. To remove the bacteria from polluted water there is number of techniques which is being used are oxidation process, chemical precipitation, filtration, adsorption, and UV irradiation, etc[90]. Besides these strategies, several nanocomposites material has been discovered which have propensity to kill *E.coli*, *B.subtilis* and *M. luteus*. These nanocomposites material are implemented in water treatment, for example, micro/mesoporous nanomaterial[91], polyoxometalate-modified magnetic nanocomposites material [92], Iron oxide nanomaterial[93], biogenic nanomaterial[94], polymer/carbon nanotubes mixed matrix membrane[95], charged cellulose nanocrystal[96], mesoporous carbon-based enzyme biocatalyst [97], graphene oxide [98], magnetic graphene-based material [99], graphene polysulfone mixed matrix[100] and magnetic nanoparticles [101] are already investigated for the treatment of water.

1.5.1 Nanocomposite material in water purification and its impact on bacteria

Nanocomposite material with magnetic properties acts as an adsorbent for the removal of the different microbial organism. It alters the structure of bacterial cell membrane and sometimes it causes the leakage of cytoplasmic contents. It has unique property to inactivate the bacteria. These materials are bacteriostatic as well as bactericidal in nature depend on surface modification. Graphene-based nanocomposite materials have monolayer of closely packed carbon atom which inhibits the growth of microorganism like (*E. coli* and *B. subtilis*). Bacterial cells eventually died over a period of time when it comes in contact with graphene-based materials. Three common mechanisms have been identified which causes bacterial death such as bacterial membrane stress, oxidative stress and leakage of cytoplasmic contents [102]. The most probable mechanism behind the bacterial death is the physical contact of thin sheet of graphene (having sharp edge), which pierce the bacterial cell membrane[103] and causes the loss in cell membrane integrity. Nanofabrication of graphene-based material with iron oxide enhances its propensity to kill the bacteria. Further the oxidative stress on bacteria causes the oxidation of lipid, protein and nucleic acid contents and it induces the cell membrane destruction and inhibition of cellular growth. Including all these, the generation of hydroxyl radicals, superoxide radicals, peroxide radicals and reactive oxygen species disrupt the cellular components in bacteria.

1.6 Background on Nanomaterials

Nanomaterials include the study of chemical substances or materials with very small scale i.e. approximately 1-100 nm[104]. At these sizes, nanomaterials can show unique behaviors based on sub-domain (overlapping double layer in fluids and superparamagnetism) or quantum phenomena (quantum entanglement, near field-optical methods, electron confinement ballistic transport and electron tunneling)[105]. In current scenario, nanomaterials considered as one of the advances and interdisciplinary research area in bioscience, material engineering, chemistry, physics[106]. Nanomaterials permit unique chemical, physical, mechanical, electrical and optical properties to provide wide range as compared to conventional materials. Nanomaterials basically used in commercially purpose such as drug carries, photocatalysts, fillers, semiconductors, cosmetics, adsorbents, catalysts, microelectronics, storage of hydrogen, antifriction coating, energy storage, and much other application [107, 108]. Furthermore, nanomaterials have multiple applications in various research fields like treatment of wastewater, sensing, and energy production. From literature study, we know how the novel nanomaterials can used to address the major wastewater treatment[109].

In past decades, most of the researcher focused on theoretical and experimental approaches of novel synthesis, characterization, and application of various inorganic nanostructures like nanocomposite materials, ceramics and metal oxides that have resulted in mature and multidisciplinary research field. Among different inorganic nanoparticles, metal oxide has very much attention from science and engineering point of view. Duo to the small size and higher density, metal oxide nanomaterials demonstrate unique physical and chemical properties[110]. Metal oxide has a large application in different fields such as wastewater treatment like adsorption and degradation, sensors and catalysis[111].

1.6.1 Metal Oxide Nanomaterials

The metal oxide is shown to have several structural geometries with an electronic structure with metallic, insulator or semiconductor character because metals are formed various type of oxide compounds. Metal oxide has various properties like fuel cells, photoelectrochemical, mechanical, magnetic, optical, thermal, optoelectronic, electrochemical, and catalytic properties[112]. Metal oxides are small scale nanomaterials, which increase the surface area to volume ratio and enhance novel properties, compare to other bulk materials[113]. However, metal oxide nanoparticles have been in wide application towards wastewater treatment. Some of the metal oxides such as magnesium oxide (MnO_2), copper oxide (CuO), zirconium oxide (ZrO_2), cerium oxide (CeO_2), iron oxide (Fe_2O_3 , Fe_3O_4) and titanium oxide (TiO_2) have been widely used in waste water treatment and many other purpose.

1.6.1.1 Iron oxide nanoparticles

In the current scenario, most of the researcher attracted towards iron oxide nanoparticles because of its excellent magnetic character, high surface area compare to volume ratio, excellent multivalent oxidation state, character, easy separation from aqueous solution using external magnetic field, small size, comparatively low cost, low toxicity and environmental friendly nature[114, 115]. The iron oxide has different phases in nature including oxides, hydroxides, and oxy-hydroxides. Most of them are FeO , Fe_3O_4 , Fe_4O_5 , Fe_4O_3 , $Fe(OH)_3$, $FeOOH$, polymorphs of Fe_2O_3 (α - Fe_2O_3 , and γ - Fe_2O_3) and so on. Among various phases of iron oxide, three main phases such as hematite (α - Fe_2O_3), maghemite (γ - Fe_2O_3) and magnetite (Fe_3O_4) are charming interest due to their electrical, optical, magnetic properties. These phases are practically applicable in optical devices, gas sensing, color imaging, magnetic strong media, ferrofluid technology, magnetocaloric refrigerant and drinking water treatment [116-118]. Under ambient condition, hematite (α - Fe_2O_3) possesses stable iron oxide but it shows weak magnetic properties or antiferromagnetic in nature because of its n-type semiconducting properties due to its bandgap 2.3 eV. Hematite has rhombohedral

structure, which is the most common form and basically apply in photocatalyst which can driven by visible light up to 600 nm[119, 120]. Maghemite ($\gamma\text{-Fe}_2\text{O}_3$) show magnetic properties in all conditions and possess cubic structure with bandgap 2.0 eV[121]. Meghemite has large application in the field of electronic devices, fabrication of biocompatible magnetic fluids, magnetic resonance imaging, and magnetic recording media. The $\gamma\text{-Fe}_2\text{O}_3$ has $21\frac{1}{3}$ Fe^{3+} ions, 32 O^{2-} ions and $21\frac{1}{3}$ vacancy sites are present. Magnetite (Fe_3O_4) assumes to have cubic spinel structure and exists in two oxidation states with a stoichiometric ratio of Fe^{2+} and Fe^{3+} is 1/2 and hence, shows very interesting properties. Fe_3O_4 can act as both p-type and n-type semiconductor with band gap 0.1 eV. The Fe_3O_4 have lot of impact on water remediation like easy and fast production, high adsorption capacity, easy separation, rapid uptake, etc.[122]. The separation of Fe_3O_4 in aqueous solution is easy by external magnetic field after adsorption of toxic substance [123-126]. Therefore, most of the researcher use Fe_3O_4 for removal of inorganic and organic contaminants from wastewater.

1.6.1.2 Iron oxide based composite materials

Iron oxide functionalized materials have been found to exhibit unique physicochemical properties suitable for many applications such as adsorbent for removal of inorganic and organic contaminants, catalyst, magnetic-optical materials, biomedical, sensors, and much more application. Compared to bare iron oxide, functionalized iron oxide nanocomposite are potential materials towards removal of inorganic and organic contaminants from wastewater[127]. Iron oxide has some limitations like low adsorption capacity, slow kinetics, and leaching problem in low pH. Therefore, current research has modified some chief, non-toxic and environmental friendly material on the surface of iron oxide and to make ideal adsorbent[128]. This modification is due to increase the active sites of adsorbent and the active sites used for high adsorption capacity towards water contamination.

1.6.1.3 Synthesis route of iron oxide nanoparticles

The iron oxide nanoparticles are prepared by different physical-chemical and biological processes. Among three processes, chemical process is excellent because of bulk material is formed with tunable sizes, shapes and desire morphology with effective scientific properties. During the synthesis, the researcher always tries to preparer suitable size of monodisperse particles not only in experimental condition but also in the purification step likes ultracentrifugation, filtration and size exclusion chromatography. So the prepared nanoparticles are not containing any homogeneous composition and thereby, increase its potential[129]. There are several synthetic methods of iron oxide are available such as precipitation, hydrothermal, microemulsion, electrochemical process, sonochemical

synthesis, sol-gel method, laser pyrolysis and thermal decomposition process[130-136]. In our study we have followed precipitation methods for synthesis of iron oxide nanoparticles because of simple operation, large scale production, less time to prepare and good yield. Brief description of chemical co-precipitation of iron oxide is as follows.

1.6.1.4 Precipitation method

Precipitation method is the simplest way of iron oxide nanoparticles preparation, which attracts significant interest in industries because of inexpensive and cost-effective, temperature and bulk production. In precipitation method, precipitation of solids from a solution with metal ions is required to pH adjustment. Particle size, shape, and crystallinity of the nanoparticles depend on the reaction kinetics. The various parameters are involved in precipitation method such as temperature, concentration, the pH of the solution, the mixing process and adding of the reactants[137], which can affect the efficiency spherical iron oxide (Fe_3O_4) nanoparticles synthesized by precipitation method using ferrous (Fe^{2+}) and ferric (Fe^{3+}) ions as a precursor, NH_4OH as a precipitation agent and temperature should maintain in between 60-100°C[138]. The successful synthesis of iron oxide follows washing with ethanol and distilled water[138].

1.6.1.5 Characterization techniques

Basic techniques such as FT-IR, X-ray photoelectron microscopy, atomic force microscopy (AFM), XRD, TEM, FE-SEM, and VSM are used to confirm the formation of Iron oxide nanoparticles[139]. Ghosh et al. and the co-workers synthesized magnetite Fe_3O_4 core-shell nanostructure through aqueous route via co-precipitation method[140]. In this synthetic method they varied different temperatures but kept the precursor concentration constant. They characterized using TEM analysis and found high crystalline spherical magnetite particles in the size 8.2-12.5 nm range (Figure 1.7). Deng et al. synthesized iron oxide in magnetite phase by forced hydrolysis method, controlling the oxidation with a nitrogen atmosphere. They reported approximately diameter 15 nm and characterized by XRD and Mossbauer spectroscopy techniques[141]. From XRD analysis, they got 7 intense peaks at around 25-70 °C (Figure 1.8). Since the XRD patterns of magnetite and maghemite have very similar, they performed Mossbauer spectroscopy technique to distinguish the oxidation state of iron as magnetite contain Fe^{+2} oxidation state and maghemite contain Fe^{+2} and Fe^{+3} oxidation states. The obtained Mossbauer spectrum data were fitted into two sextets patterns corresponding to the Fe^{+3} tetrahedral and octahedral site of iron (Fe^{+2} and Fe^{+3}) (hyperfine field were 433.6 KOe and 471.3 KOe finally), which corroborates the presence of magnetite. The sextets with quadruple splitting, hyperfine field, and isomer shift of one are 0.019 mm/s, 433.6 KOe,

and 0.317 mm/s respectively, and the other 0.001 mm/s, 471.3 T, and 0.228 mm/s relative to the iron metal, suggesting the existence of two iron with different oxidation states considered as ferrimagnetic magnetite (Figure 1.9).

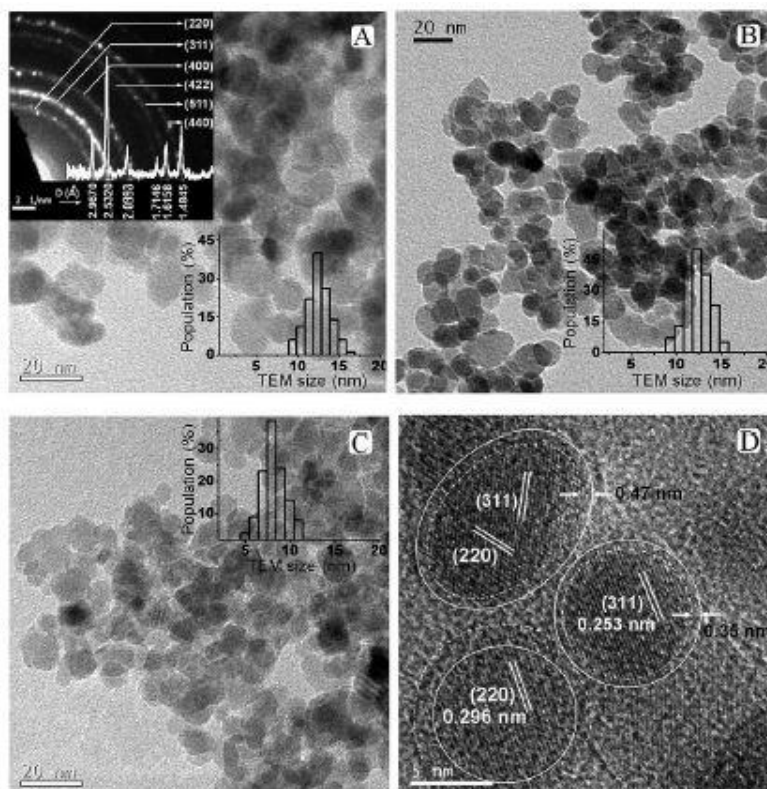


Figure 1.7 TEM image of magnetite (Fe_3O_4) nanoparticles at different temperature (A) 90 °C with its SAED pattern (B) 75 °C (C) 33 °C (D) HR-TEM of 33°C (Ghosh et al. 2014).

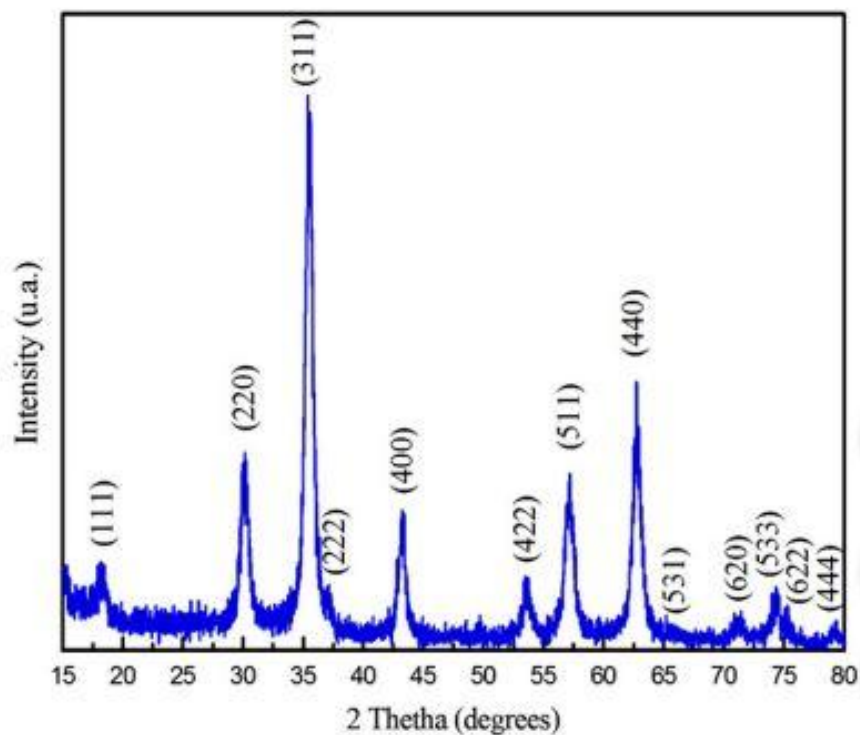


Figure 1.8 XRD pattern of magnetite nanoparticles (Compeán-Jasso et al., 2008).

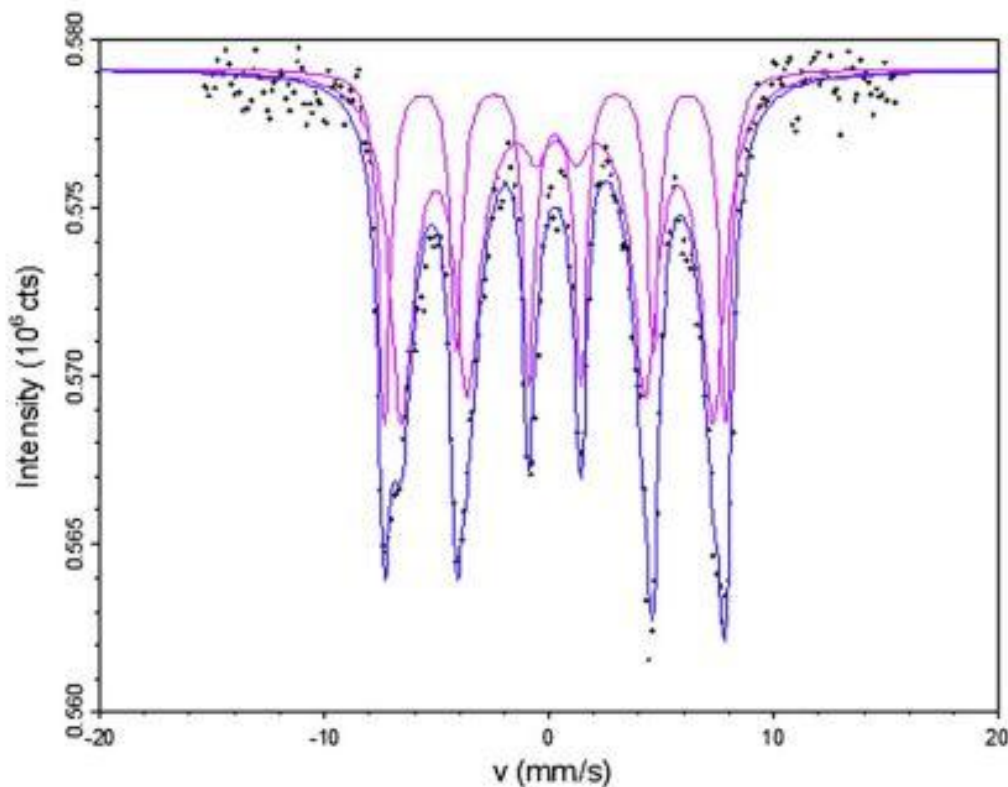


Figure 1.9 Mossbauer spectrum of magnetite (Compeán-Jasso et al., 2008).

1.7 Research gap

At the start of my research work, there was no report on the use of carbohydrate, amino acid, and chelating ligand functionalize magnetic nanocomposites for wastewater treatment. Though several nanocomposites are investigated for the adsorption of heavy metals and organic dyes contaminates, most of them are carcinogenic in nature, less efficient, expensive, long time duration, and separation process is too difficult in aqueous solution. In this direction number of functionalized materials are invented and use in wastewater treatment. However, the carbohydrate, amino acid, and chelating ligand functionalize magnetic nanocomposites has not been in detail study for wastewater treatment. So there is a knowledge gap existing in this field. Moreover, antibacterial activity has drawn a little attention.

1.8 Research objective

Keeping the above-mentioned facts in mind, we have tried to develop some functionalized novel magnetic adsorbent for wastewater treatment. The main objective of research work is as follows:

1. To synthesize iron oxide nanoparticles via chemical co-precipitation method.

2. To synthesize potential adsorbent with active groups like amino acid (Tryptophan), carbohydrate (guar-gum), chelating ligand (EDTA) and amino silane (APTES) functionalization on the surface of iron oxide nanoparticles.
3. To characterize the above nanocomposite using techniques such as FT-IR, XRD, FE-SEM, TEM, Raman spectroscopy, VSM, N₂ adsorption-desorption isotherm, Zeta-potential, UV-visible spectroscopy.
4. To study the environmental application for heavy metals (Pb²⁺, Cd²⁺, Ni²⁺, Co²⁺, Cr⁺⁶, and Cu²⁺) and organic dye (Congo red) removal from contaminated water.
5. To check the anti-bacterial activity (Gram-positive and Gram-negative) of the synthesized nanocomposite.

1.9 Overview of the thesis

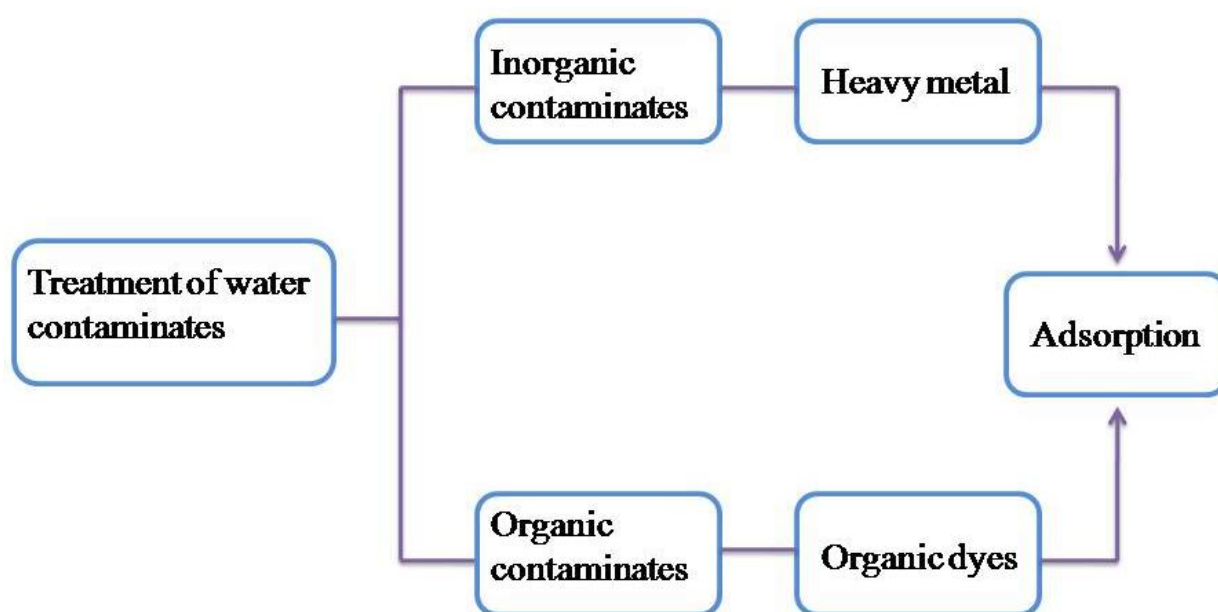


Figure 1.10 Overview of the research work.

This Ph.D. thesis is focused on the synthesis of different functionalized magnetic nanocomposites for removal of heavy metal and organic dye and also check the antibacterial activity. The thesis is divided into seven chapters. The present chapter (chapter-1) contains the introduction of water pollution as a function of inorganic and organic contaminants antibacterial activity and treatment with nanomaterials, nanocomposite materials, metal oxide nanoparticles, iron oxide nanoparticles. Chapter-2 represents the materials and experimental procedure which are embraced for the synthesis of adsorbent materials. The details of analytical technique which are used to confirm the synthesis of adsorbent and removal of contaminants are presented briefly. Chapter-3 indicates the application of amine-functionalized magnetic iron oxide nanoparticles for rapid removal of Congo red dye and its antibacterial activity. Chapter-4 represents Guar-gum coated iron oxide nanocomposite as an

efficient adsorbent for Congo red dye. Chapter-5 represents an investigation of heavy metals (Pb^{2+} , Cd^{2+} , Ni^{2+} , Co^{2+} , and Cu^{2+}) adsorption by hexadentate ligand modified magnetic nanocomposite. Chapter 6 indicates Surface functionalization of graphene oxide using amino silane magnetic nanocomposite for Chromium (VI) removal and bacterial treatment. Chapter 7 includes conclusion obtained from the above work along with scope of future work.

Chapter 2

Materials and Methods

Chapter summary

This chapter illustrates the reagent, chemicals, and other materials are used in the time of experimental work. The total synthetically procedure was conducted during research work was Thorley investigated. The detail of all the synthesise materials for removal of organic and inorganic contaminants are described. The analytical techniques which are used for nanocomposite materials characterization were also discussed in the chapter.

2.1 Reagent and chemicals

Sodium hydroxide (NaOH), Lead chloride (PbCl₂), cadmium chloride anhydrous (CdCl₂), L-Tryptophan, Luria Bertani broth and Luria Bertani Agar, Guar-gum, ethylenediaminetetraacetic acid (C₁₀H₁₆N₂O₈), sodium fluoride (NaF), Ferrous chloride anhydrous, (3-aminopropyl)triethoxysilane (APTES) aqueous ammonia solution (NH₄OH), Sodium chloride (NaCl) and Thionyl Chloride (SOCl₂) were purchased from HI media. Copper nitrate pentahydrate (Cu(NO₃)₂ · 5H₂O), cobalt nitrate (Co(NO₃)₂) and nickel nitrate (Ni(NO₃)₂) were purchased from SDFCL company. The pH of the solution was preserved by the addition of required amount of 0.1 M HCl and 0.1 M NaOH. N-[3-(Trimethoxysilyl)propyl]-ethylenediamine (TSPED) and 2',7'-Dichlorofluorescein diacetate was purchased by Sigma Aldrich. Congo red (CR) were provided by Central Drug House (P) Ltd. Ferric chloride anhydrous, N, N-Dimethyl formamide (DMF) and Methanol (CH₃OH) were procured from Finar Limited Company. *E. coli* and *B. subtilis* (MTCC10110) were obtained from the Microbial Type culture collection (MTCC), Chandigarh, India. Triethylamine (Et₃N) were purchased from SDFCL Company and Ethanol (C₂H₅OH) was purchased from Jiangsu Huaxi International Trade Co. Ltd. Hydrogen chloride (HCl), Sulphuric acid (H₂SO₄), Sodium nitrate (NaNO₃), Hydrogen peroxide (H₂O₂, 30%), 1,5-diphenylcarbazide (DPC), Ethanol (C₂H₅OH), sodium sulfate (Na₂SO₄) and Acetone (CH₃COCH₃) were purchased from Merck life science (India). sodium carbonate (Na₂CO₃), sodium bicarbonate (NaHCO₃) was purchased from Fisher scientific. Potassium dichromate (K₂Cr₂O₇) was supplied by Spectrochem, India. Potassium permanganate (KMnO₄) was supplied from Avra chemical, India. Graphite powder was purchased from Loba Chemie, India. All reagents used were of analytical grade

and used without any further any purification. All solutions were prepared with distilled water.

2.2 Synthesis of iron oxide (Fe₃O₄) nanoparticles

Iron oxide (Fe₃O₄) was prepared using previously reported chemical co-precipitation method with some modification[142]. Briefly, 4 g of anhydrous FeCl₂ and 12 g of anhydrous FeCl₃ were dissolved in 50 ml of 0.1 M HCl solution. Further, the mixture was added slowly to 500 ml of 1.5 M NH₃ solution until reaches pH 11, afterward, stirred for 2 hours at the temperature 40 °C. A black precipitate of Fe₃O₄ magnetic nanoparticle was formed after stirring for 2 hours, which was collected by centrifugation and washed three times with distilled water and two times with ethanol, and then dried at 60 °C.

2.3 Synthesis of Fe₃O₄-TSPED (FT)

The synthesis of Fe₃O₄-TSPED was done following the previously reported method[143]. Freshly prepared 1.77 g of Fe₃O₄ nanoparticle was dispersed in 200 ml of distilled water in a round bottom flask. Then it was allowed for ultrasonication for 30 minutes followed by the addition of 180 ml of 62 % methanol at room temperature. The above solution was stirred for 24 hours in the presence of argon atmosphere and TSPED was added slowly while stirring, followed by centrifugation at 6000 rpm. Then the solution was washed with distilled water until the pH of the water reaches around ~7. Finally centrifuged at 6000 rpm and dried at 80 °C for 24 hours.

2.4 Synthesis of Fe₃O₄-TSPED-Tryptophan (FTT)

20 ml of N, N-Dimethyl formamide (DMF) and 0.15 ml of thionyl chloride (SOCl₂) are taken in a round bottom flask and the solution was stirred followed by addition of Tryptophan (400 mg). The stirring was continued under reflux condition for 24 hours at room temperature. Fe₃O₄-TSPED (1 g) and Et₃N (0.28 ml) were added to the solution and the solution was stirred and kept under reflux condition for 72 hours. The solution was centrifuged at 6000 rpm and washed with ethanol and water until the pH of the solution becomes 7. Then it was dried at 80 °C for 24 hours. Synthesis of FTT was shown in Figure 2.1.

2.5 Synthesis of Fe₃O₄-GG nanocomposite

Firstly we have taken 250 mg of GG powder and 50 ml of isopropyl alcohol in a round bottom flask then continuous stirring for 1 hour under 60 °C to facilitate the formation of a viscous gel. After the appearance of a completely homogeneous solution, then added 2.0 gm of Fe₃O₄ nanoparticles was stirred for 1h at 60 °C under N₂ atmosphere then add 0.5 ml

glutaraldehyde 25 % was added into the mixture as a crosslinker. After completion of the reaction, the pH 9-11 in the solution was adjusted to 1.0 mol/L NaOH. The mixture was stirred 3 h and heated 60 °C then after followed by washing with distilled water (centrifuged at 6,000 rpm for 10 min) to remove any free particles. Finally, the obtained composite was dried at 80 °C so as to obtain a dry powder of Fe₃O₄-GG nanocomposite, which was stored in desiccators.

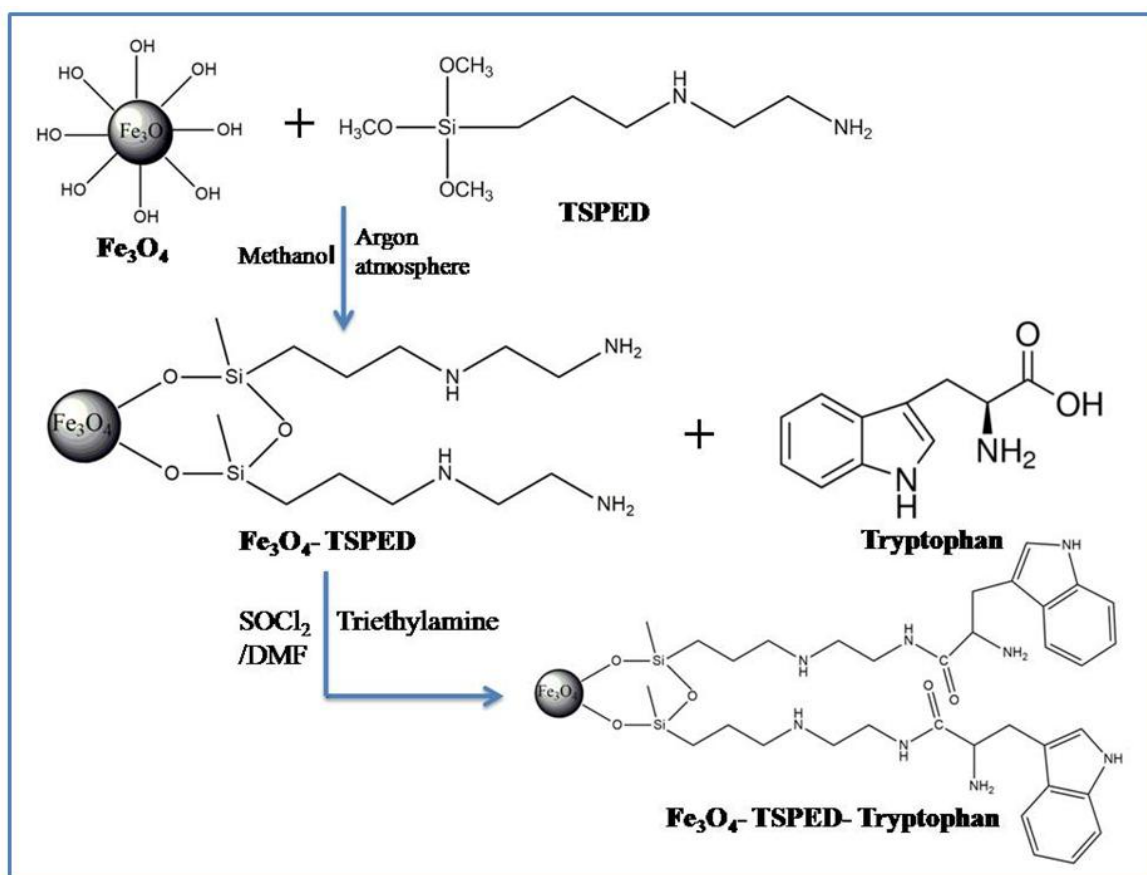


Figure 2.1 Schematic illustration of the synthetic procedure for Fe₃O₄-TSPED-Tryptophan nanocomposite

2.6 Preparation of Fe₃O₄-APTES nanocomposite.

The APTES modified Fe₃O₄ magnetic nanoparticles (FA) was synthesized based on our previously established method with small modification[144]. Firstly, a solution mixture was prepared using 1gm of Fe₃O₄ and 100ml of ethanol in a round bottom flask. In order to disperse the Fe₃O₄ nanoparticles, the solution was ultrasonicated for 30 mins. Then the resulting dispersion was bubbled with argon gas for 30 min, and then added 1 ml of APTES by a syringe under mechanical stirring. The reaction was then maintained at room temperature for 24 hours. The reaction was incubated at room temperature for 24 hours. Finally, the obtained solid product was collected with the help of a magnet and repeatedly

washed with ethanol. The obtained FA nanocomposite was dried in a muffle furnace at 60 °C (Figure 2.2).

2.7 Preparation of Fe₃O₄-APTES-EDTA nanocomposites

APTES modified Fe₃O₄ (0.5 g) was added to 188 ml (acetic acid /Ethanol) mixture by (1:1 volume). Next, the freshly 0.3 g EDTA anhydride was added to this mixture and was refluxed for 16 hours at 80 °C. Finally, the solid was recovered by vacuum filtration, washed with excess acetone and distilled water, and dried at 60 °C.

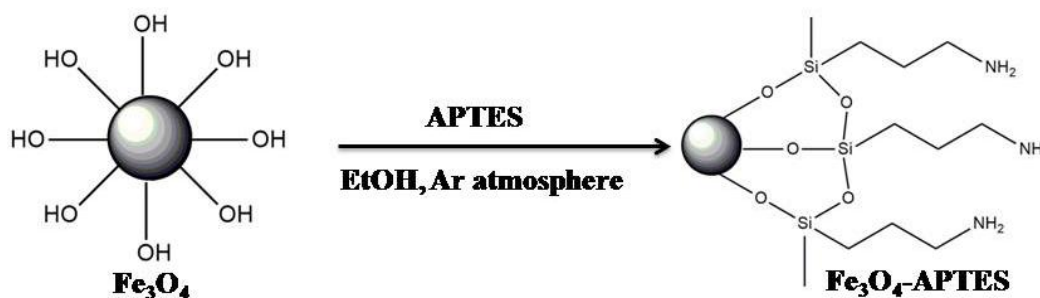


Figure 2.2 Schematic illustration of the synthetic procedure for Fe₃O₄-APTES.

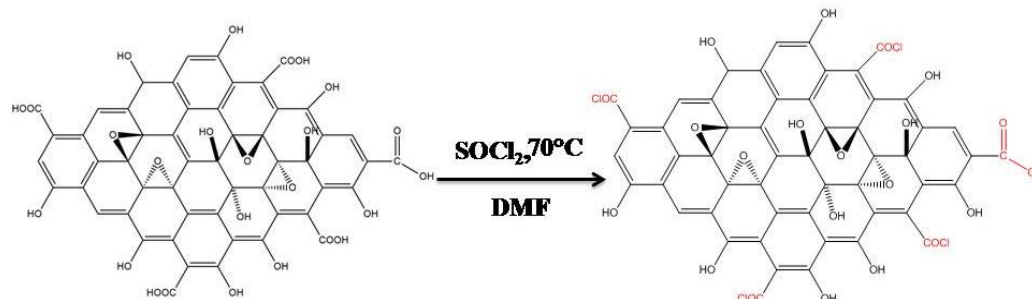
2.8 Preparation of graphene oxide (GO)

Graphene oxide (GO) was prepared according to reported work via modified hummers method[145]. In a typical synthesis, 1 g of graphite powder was suspended in 25 ml of H₂SO₄ (98%) and ultrasonicated for 20 min. After which, 100 mg of NaNO₃ was added to the above solution and stirred for 34 hours at room temperature. The obtained mixture was kept in an ice bath to cool down 5 °C followed by the slow addition of 3 g of KMnO₄ with constant stirring, by keeping in mind the temperature should not rise above 20 °C. The stirring was continued for 4 hours at the same condition. Then the ice bath was removed and kept the reacting mixture at room temperature and 250 ml distilled water was added dropwise. The stirring was continued for another 45 min and 50 ml of warmed distilled water to terminate the reaction 5 ml of H₂O₂ (30 %) was added dropwise to the contents and stirred for 12 hours. Bright yellow color indicates the complete oxidation of graphite to GO. The yellow suspension was centrifuged and washed three times with HCl (10 %) to remove the metal ions and then several times with distilled water to maintain the pH 7. Then the solution was dried at 60° C and grind to get desire GO powder

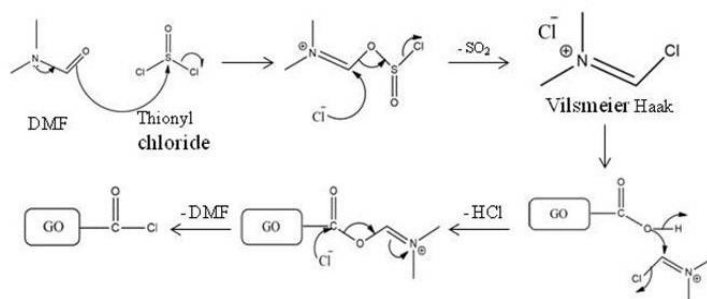
2.9 Preparation of GO-Fe₃O₄-APTES

Firstly 300 mg of GO powder was dispersed in 20 ml of DMF in 250 ml capacity of round bottom flask followed by the addition of 0.25 ml of SOCl₂ and the reaction was left to proceed for 24 hours with constant stirring at 70 °C. SOCl₂ is a strong reducing agent, it can convert less reactive -COOH group of GO into much reactive -COCl group (Figure 2.3a).

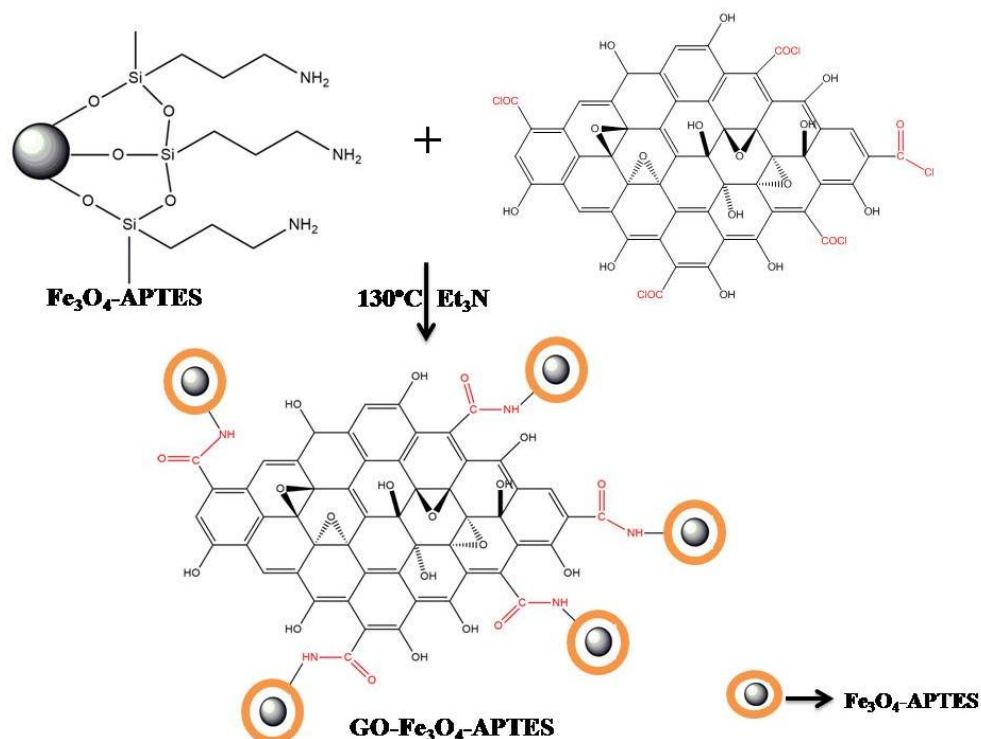
Solvents like DMF is used for surface coating and it facilitates Vilsmeier-Haack reaction which is used to formylate aromatic compounds are suitable catalyst to speed up the reaction. Then 600 mg of Fe_3O_4 -APTES was added to the reacting mixture followed by addition of 10 ml of DMF and 0.38 ml of Et_3N . The temperature of the following mixture was kept up to 130°C , then stirred and refluxed for next 72 hours. In the following method–COCl group



Mechanism



(a) Preparation of GO-COOH to GO-COCl.



(b) Preparation of GO- Fe_3O_4 -APTES

Figure 2.3 Schematically detailed synthetic mechanism of GO- Fe_3O_4 -APTES.

react with $-NH_2$ group of Fe_3O_4 -APTES to form an amide bond. The solid residue was separated by centrifugation followed by washing using distilled water. The residue was dried at $80^\circ C$ for 12 hours to form desired product. The detailed synthetic mechanism was represented in Figure 2.3.

2.10 Characterisation techniques

2.10.1 FTIR spectroscopy

The FT-IR spectra were carried out to know the functional group present in synthesized material and after adsorption. FT-IR spectra of the synthesized nanocomposite were performed with KBr discs in the range 4000 to 400 cm^{-1} on Perkin Elmer (95277) FT-IR Spectrometer Spectrum RX-I. Nearly 3-4 mg of the sample was mixed completely with 30 mg dried KBr and made into pallets.

2.10.2 X-ray powder diffraction (XRD)

X-ray diffraction (XRD) tells about the various phase, composition, and more information about unit cell dimensions of the all prepared materials. XRD measurements (Rigaku Dmax-2000 diffractometer using $Cu\ K\alpha$ radiation source ($\lambda=0.15418\text{ nm}$)) with the range of 2θ angle 10 - 80° with scanning rate $5^\circ/\text{min}$.

2.10.3 Scanning electron microscope (SEM) and energy dispersive X-ray (EDX)

The surface properties and morphology of the materials were examined using SEM microgram (JEOL model JSM-6390LV) and the elemental mapping and composition of the materials were explained by corresponding EDX. The synthesized materials were kept on carbon tape and coated for 2 min with vacuum current strength of 50 mA. After coating we can take required images.

2.10.4 Field emission scanning electron microscope (FE-SEM)

FE-SEM technique was also similar to SEM instrument with a difference that it gives a clean image. The sample preparation was same as that of sample preparation of SEM instrument. The prepared sample was run in FE-SEM instrument (NOVA NANO SEM 450) which was operated at setting voltage of 15-20 kilovolts.

2.10.5 Transmission electron microscope (TEM)

TEM (HRTEM, JEM-2100, and Japan) microscopic technique was used for the atomic-level analysis of materials and was operated at 200 kV. The TEM provides texture, structure, size, and shape of the materials. Here the sample was prepared by dispersing the material in ethanol for 90 min and the dropped in a carbon-coated grid. The elemental mapping and

composition were studied by EDX analyzer (Oxford INCA) fitted with TEM. Raman Spectrometer (LABRAM-010) having the range of wave number 500-2500 cm^{-1} was used to get the structural information.

2.10.6 N₂ adsorption-desorption isotherm

N₂ adsorption-desorption technique was used to determine the surface area using 77 K on a Quantachrome Autosorb 3-B apparatus (model no-ASIQM0000-4). The Barret-Joyner-Halenda (BJH) method was used to determine the pore size distribution and pore-volume.

2.10.7 Vibrating Sample Magnetometer (VSM)

The VSM (VSM-7410) technique was used to test the magnetic properties of iron-based materials at room temperature. The material first weighed and kept in Teflon then directly placed in the instrument for analysis.

2.10.9 Raman spectrometer

Raman spectrometer was used to determine the rotational, vibrational, chemical composition of the materials and other states in a molecular system. Raman Spectrometer (LABRAM-010) having the range of wave number 500-2500 cm^{-1} .

2.10.9 Zeta potential

To determine the surface charge of the prepared materials, Zeta potential measurement was investigated. This technique was analyzed by Nano-ZS 90, MALVERN, UK instruments. For the study, 1 mg of the sample was dispersed in distilled water in a quartz cube container by adjusting at different pH (2-12) with the addition of 0.1 M HCl and 0.1 M NaOH.

2.10.10 UV-visible spectroscopy

The UV-visible Spectrophotometer (UV-SHIMADZU 2450, Malaysia) was used to determine the concentration of Chromium (VI) present in solution by using the method 1, 5-diphenylcarbazide (DPC) and the concentration of organic dyes in a particular wavelength.

2.10.11 Atomic adsorption spectroscopy (AAS)

AAS (Elico SL 176, India) technique was used to analyze the concentration of heavy metal in solution. To calibrate the instrument using appropriate concentration prepared from the stock solution.

2.10.12 Fluorescence

To check the fluorescence intensity of nanomaterials treated bacteria in conjunction with the DCFDA dye, Spectrofluorometer, Fluoromax-4 (Horiba Scientific, Japan) with a quartz cell having path lengths of 1.0 cm were used. To perform these studies bacteria were treated with

varying concentrations (10, 20, 40, 80, 160 micrograms per ml) of nanomaterials and 1 micromolar of DCFDA dye.

2.10.13 pH analysis

To maintain different pH of the solution using a digital pH meter (Sartorius Mechatronics India Pvt. Ltd).

2.8.14 Thermogravimetric analysis

Thermogravimetric analysis or thermal gravimetric analysis is a method of thermal analysis in which changes in the weight of a material can be measured either as a function of increasing temperature or as a function of time. The thermal behavior of the synthesized material was characterized by differential scanning calorimeter and thermogravimetric analysis by taking samples of about 7 mg by weight, under nitrogen flow (50 mL min⁻¹) at heating rate of 10 °C min⁻¹, (NETZSCH STA 449C, Germany).

2.11 Adsorption behavior

2.11.1 Adsorption kinetics

To understand the mechanism of adsorption process well on contact time, we investigate adsorption kinetics. Three models were introducing to simulate the predictable data such as Pseudo first-order kinetic theory, Pseudo second-order kinetic theory, and Intra particle diffusion model.

The Pseudo first-order kinetic equation is expressed as follows.

$$\log(q_e - q_t) = \log q_e - \frac{K_1 t}{2.303} \quad (2.1)$$

Here q_e = Adsorbed amount of adsorbate at equilibrium concentration (mg/g), q_t = Adsorbed amount of adsorbate at equilibrium time, K_1 = Pseudo first-order rate constant. The values of K_1 , q_e and R^2 were calculated from the slope & intercept of the plot $\log(q_e - q_t)$ vs t .

The Pseudo second-order kinetic equation is expressed as follows.

$$\frac{t}{q_t} = \frac{1}{K_2 q_e^2} + \frac{t}{q_e} \quad (2.2)$$

Here K_2 = Pseudo second-order rate constant. The values of q_e , K_2 and R^2 were calculated from the slope and intercept of the plot t/q vs t .

The intra particle diffusion model is expressed by using the following equation.

$$q_t = k_p \times t^{0.5} + C \quad (2.3)$$

Here k_p is the intraparticle diffusion constant ($\text{mg/g min}^{0.5}$) and C is the boundary layer thickness constant (mg/g). The values of k_p , C and R^2 were calculated from the plot q_t vs $t^{0.5}$.

2.11.2 Adsorption isotherm

The adsorption isotherm models such as Langmuir, Freundlich, Temkin, Dubinin-Radushkevich (D-R) and Elovich were selected to define the adsorption process.

Langmuir isotherm is used for assuming the adsorption of adsorbate on homogeneous planes by monolayer adsorption. The mathematical expression for Langmuir isotherm is written as follows.

$$\frac{c_e}{q_e} = \frac{1}{bq_m} + \frac{c_e}{q_m} \quad (2.4)$$

Here c_e represents the adsorbate concentration (mg/L) at equilibrium, q_e is the capacity of equilibrium adsorption (mg/g), q_m is the maximum adsorption capacity (mg/g) and b is the Langmuir constant. The values of q_m , b and R^2 was calculated by using the slope and intercept of the plot $\frac{c_e}{q_e}$ versus c_e .

The value of R_L which is the dimensionless constant can also be considered to know the favourability or unfavourability of the process of adsorption. R_L can be evaluated by using the following equation.

$$R_L = \frac{1}{1+bc_0} \quad (2.5)$$

The calculated value of R_L was found to be less than 1 (<1). This designates that the adsorption process of adsorbate was favorable for this isotherm.

Freundlich isotherm is utilized for assuming the adsorption of adsorbate on heterogeneous planes by multilayer adsorption. This isotherm model can be expressed as follows,

$$\ln q_e = \ln K_F + \frac{1}{n} \ln c_e \quad (2.6)$$

Here q_e is the adsorbed amount of adsorbate per unit weight of adsorbent (mg/g) at equilibrium, n is the density of adsorption. c_e is the concentration of Chromium (VI) in solution at equilibrium time (mg/L). The values of K_F (Freundlich constant), n and R^2 was determined by using the slope and intercept of the plot $\ln q_e$ versus $\ln c_e$.

The electrostatic force of attraction between the adsorbent and the adsorbate were shown by Temkin isotherm. The Temkin isotherm is written as follows,

$$q_e = B_1 \ln K_T + B_1 \ln C_e \quad (2.7)$$

$$B_1 = \frac{RT}{B} \quad (2.8)$$

Here, B_1 is The Temkin constant which is related to the adsorption of heat, K_T is the isotherm constant, R is the gas constant and T is the absolute temperature. The parameters like B_1 , K_T , R^2 are evaluated by plotting the graph between q_e versus $\ln c_e$.

Elovich isotherm model suggested multilayer adsorption. The mathematical expression for Elovich isotherm is expressed as follows, which depend on the kinetic principle presuming that the adsorption side exponentially increases with adsorption.

$$\ln \frac{q_e}{c_e} = \ln K_E q_m - \frac{q_e}{q_m} \quad (2.9)$$

Here q_m is the maximum capacity of adsorption (mg/g), K_E is the Elovich constant. The values of q_m , K_E and R^2 was calculated by using the plot between $\ln(\frac{c_e}{q_e})$ versus q_e .

Dubinin- Radushkevich isotherm model is used to express the mechanism of adsorption onto a heterogeneous surface with a energy distribution. This isotherm model is fitted in the intermediate range of concentrations as well as solute activities. The equation for this model is,

$$\ln q_e = \ln q_m - K_{DR} \varepsilon^2 \quad (2.10)$$

Here, q_e is the equilibrium concentration of adsorbate on the adsorbent, q_m shows the saturation capacity of theoretical isotherm, K_{DR} is the constant for Dubinin-Radushkevich model, ε is the isotherm constant for the Dubinin-Radushkevich model.

The value of epsilon (ε) can be derived by applying the following equation.

$$\varepsilon = RT \ln(1 + \frac{1}{c_e}) \quad (2.11)$$

Here, R is the gas constant and T is the absolute temperature

The value of E can be computed by using the formula,

$$E = \frac{1}{\sqrt{-2K_{DR}}} \quad (2.12)$$

Chapter 3

3. Amine functionalized magnetic iron oxide nanoparticles: Synthesis, antibacterial activity and rapid removal of Congo red dye

3.1 Introduction

Disposal of chemical contaminants through wastewater from industries, i.e., paper, plastics, cosmetics, leather, pharmaceuticals and textiles which use dyes for colouring their products[146, 147], is one of the major problems for aquatic environment, because such effluents contain a number of highly toxic and carcinogenic substances such as dye[9, 148-150]. Dyes usually have complex aromatic molecular structures which make them more stable and difficult to biodegrade[151, 152]. Furthermore, many dyes are toxic to several microorganisms and may cause direct destruction or inhibition of their catalyst properties. Most of the dyes represent acute problems to the ecological system as they considered as toxic and they have the carcinogenic properties [153-155]. Dyes can have acute or chronic effects on exposure to an organism depending on concentration. The ability of dyes to absorb/reflect sunlight entering the water has a drastic impact on the growth of bacteria and upsets their biological activity. Dyes in wastewater undergo chemical and biological changes, and consume dissolved oxygen from the stream and thereby, destroy aquatic life. Out of several dyes, Congo Red (CR) is an anionic or acidic dye and has a wide application which includes in the field of aquaculture, commercial fish hatchery and animal husbandry as an antifungal therapeutic agent, as well it is used as antiseptic and fungicidal[152, 156-158]. Also, CR causes kidney and heart diseases on human health and create disease like amyloidosis caused by the accumulation of proteins in the form of abnormal, insoluble fibers, known as amyloid fibrils, within the extracellular space in the tissues of the body[159]. In the international scenario, due to its health hazard concerns, CR is banned in Europe, the United States and Canada[160].

So far, various physical and chemical treatment methods have been reviewed for the removal of dyes such as biological degradation[161], ion exchange, adsorption[162], membrane filtration[163], ultra chemical filtration[164], coagulation and flocculation[165], etc. However, these treatment processes have their limitations such as high cost, generation of toxic sludge, etc. Adsorption has been observed to be better than other different methods for wastewater treatment as far as introductory cost, effortlessness for configuration, the

simplicity in operation and insensitivity towards hazardous substances. In past decades, the various low cost adsorbent such as clay minerals[71, 166], fly ash[167-171], bark wastes[172, 173], peat[174, 175], industrial waste products[176], wood powder[149, 157], coffee grounds[177], metal hydroxide sludge[76], hydrotalcite[178], biodegradable waste[77], agricultural waste[78] and dolomitic sorbents[79] are used for removal of dyes from wastewater. Along with, a number of non-conventional adsorbents have been reported in the literature supporting the removal of CR from aqueous solutions, such as guar-gum coated iron oxide nanocomposite[179], chitosan/montmorillonite nanocomposite[180], magnetically modified fodder yeast cell[181], chitosan-coated magnetic iron oxide[182], palm kernel seed coat[183] and activated carbon (prepared from coir pith, an agricultural solid waste, bamboo dust carbon, rice husk carbon coconut shell carbon and straw carbon)[184, 185]. Looking towards the biocompatibility and efficiency of the nanocomposites, we designed a Fe_3O_4 nanocomposite with a tryptophan covering on the surface using TSPED as a cross-linker.

Fe_3O_4 nanoparticles have several advantages in the field of adsorption. Some of them include (a) magnetic separation of contaminate from aqueous solution, (b) high surface area and (c) high superparamagnetic behavior. TSPED is selected as the silane-coupling agent that provides both hydrophilic and hydrophobic in nature[186]. Silane polymer also increases the removal efficiency and plays an important role in the adsorption of dyes[186]. Tryptophan, an essential amino acid, is functionalized on FT surface. The coating has no significant effect on magnetic properties[187]. Tryptophan contains an active binding site (after binding to TSPED) in terms of a protonated amino group, which assumed to play a key role on adsorption. Adsorption process using FTT has been preferred for the treatment of dye-pollutant water due to its simple design and easy operation, less energy intensiveness, not affected by toxic substances and high quality of the treated effluents particularly for well-designed sorption processes.

In this work, a magnetic nano-adsorbent (Fe_3O_4 -TSPED-Tryptophan) is prepared for the adsorption of organic dyes (such as CR) along with its antibacterial activity towards gram-negative and positive bacteria. To study the antimicrobial potential of the material, we have chosen gram-negative bacteria (*Escherichia coli*) and gram-positive bacteria (*Bacillus subtilis*) for the screening purpose. Adsorbents possessing antibacterial activity have wide application in improving public health. The characteristic properties like solubility, particle size, and dispersion rate influence the antibacterial properties[188, 189]. Physicochemical properties of iron oxide nanoparticles also impart antimicrobial activity[190, 191]. Iron oxide

nanoparticle itself has biomedical applications due to its magnetic properties and biocompatibility[192].

3.2 Batch adsorption experiment

For the adsorption experiments, 100 mg of FTT was added to the 100 ml CR dye solution of the desired concentration and pH of dye solution was adjusted with 0.1 N HCl and NaOH using pH meter. The mixture was continuously stirred using a magnetic stirrer to reach the equilibrium under the desired experimental condition. At 2 min time intervals the adsorbent was removed by centrifugation. The supernantsolution was used to determine concentration by UV-Visible spectrophotometer at wavelength 500 nm, where the absorbance is maximum. The amount of CR dye adsorbed onto FTT was determined by subtracting the final solution concentration from the initial of the dye solution.

$$\% \text{Adsorption} = \frac{C_o - C_e}{C_o} \times 100 \quad (3.1)$$

And the equilibrium uptake was calculated using Eq. (3.2):

$$q_e = (C_o - C_e) \times \frac{V}{W} \quad (3.2)$$

Here q_e indicates equilibrium capacity of dye on the adsorbent (mg g^{-1}), C_e is equilibrium concentration of dye solution (mg L^{-1}), C_o indicates initial concentration of dye solution (mg L^{-1}), V indicates volume of dye solution used (L) and W is the weight of adsorbent (g) used. All the batch experiments were carried out in triplicate and results represented as there average readings.

3.3 Antibacterial activity of FTT

3.3.1 Cultivation of bacteria

E.coli DH5 α and *B.Subtilis* were grown in LB media at 37 °C. To observe the impact on checking the antibacterial activity bacterial cell suspension were diluted to obtain cell samples having 10^6 to 10^7 cfu/ml.

3.3.2 Disc diffusion method

Antibacterial activity of FTT was tested against gram-negative bacteria *E.Coli* and gram-positive *B. subtilis*. Different concentration of FTT (10, 20, 40, 80, 160 $\mu\text{g/ml}$) were prepared for the study. To perform the disc diffusion test *E.coli* and *B. Subtilis* bacteria (10^6 to 10^7 cfu/ml) were spread on an LB agar plate. The equal-sized disc was dipped in different concentration of FTT solution and then placed at Petri plate. Plates were incubated for 12 hours at 37 °C and then used to measure the zone of inhibition.

3.3.3 Concentration and time-dependent antibacterial activity

Different concentrations of FTT (10, 20, 40, 80, 160 µg/ml) was repared by dispersing in LB broth by sonication for 2 hours. Effect of nanoparticle on bacterial growth was checked by colony counting method to observe the loss of viability. Bacterial culture of an appropriate concentration was further treated with the FTT and incubated for 12 hours at 37 °C under 120 rpm shaking speed to observe the time-dependent growth of both the bacteria. At different time points we have collected the bacterial cell suspension from the treatment group and optical density of the collected cell suspension was measured at 595 nm using the ELISA plate reader (Biobase-EL10A Elisa reader, Shandong Co.Ltd).

3.3.4 Examination of bacterial Cell morphology under FESEM

To examine the bacterial cell morphology *E.coli* and *B.subtilis* cells were treated with 160 µg/ml of FTT dispersion for 6 hours. One group without the nanoparticles treatment were taken as control which only contains bacteria having concentration 10^6 cfu/ml. The cell suspension from the treated as well as the non-treated group was washed with 0.9 % sodium chloride to avoid the media component. Cells were further fixed with 4 % paraformaldehyde at 4 °C for overnight. After fixation, it was washed with PBS and then dehydrated by sequential exposure to 30, 50, 70, 90, and 100 % alcohol for 15 mins. The dehydrated cells were fixed on a clean glass slide which is further sputter-coated with gold for FESEM analysis. We have also done the EDX analysis to check the element deposited in the bacterial body.

3.3.5 Assessment of Reactive oxygen species (ROS) generation

To quantify the amount of ROS produced 1 µM of 2',7'-Dichlorofluorescein diacetate (DCFDA) were taken as a fluorescent dye. It penetrates the bacterial cell membrane and reacts with the ROS produced inside as well as outside of the cells which impart the green fluorescence[193]. To carry out the quantification of ROS, both gram-negative and gram-positive bacteria were treated with different concentration of FTT (10, 20, 40, 80, 160 µg/ml) for 8 hours. Afterward the normal cells as well as treated cells were incubated with DCFDA dye for 1 hour at 37 °C and then analyzed under Fluorescence spectrophotometer to check the fluorescence intensity.

3.4 Result and discussion

3.4.1 Characterisation of magnetic nano adsorbent.

The surface functionalization on iron oxide nanoparticles is characterized by using Fourier-transform infrared (FT-IR) spectroscopy. FT-IR spectra of (a) Fe₃O₄, (b) Fe₃O₄-TSPED and (c) Fe₃O₄-TSPED-Tryptophan are shown in figure (Figure 3.1). The peak at 583 and 628 cm⁻¹ was observed for all three materials; which corresponds to the Fe-O bond of bulk magnetite

phase [194-196]. After coating TSPED on the surface of Fe_3O_4 nanoparticles, the additional peak at 983 cm^{-1} assigned to the Si-O-Si groups, 1625 and 3411 cm^{-1} can be ascribed to the NH_2 bending mode of free NH_2 group and N-H stretching vibration, respectively[197, 198]. The peaks at 2924 and 2862 cm^{-1} (two small adsorption bands) ascribe to the C-H stretching vibration. Figure 3.1(c) refers to tryptophan coated FT nanocomposite. The tryptophan functionalization is confirmed from the appearance of C-O stretching at 1439 cm^{-1} and 1650 cm^{-1} , which are ascribed to the formation of an amide bond ($-\text{NHCO}$)[199-204]. The peak at 1127 and 1042 cm^{-1} correspond to the SiO-H and aliphatic C-N stretching. The peak at 983 cm^{-1} is observed in both FT and FTT. From these changes shown in IR spectra, it can be reasonably concluded that Fe_3O_4 nanoparticles have successfully coated with TSPED and tryptophan.

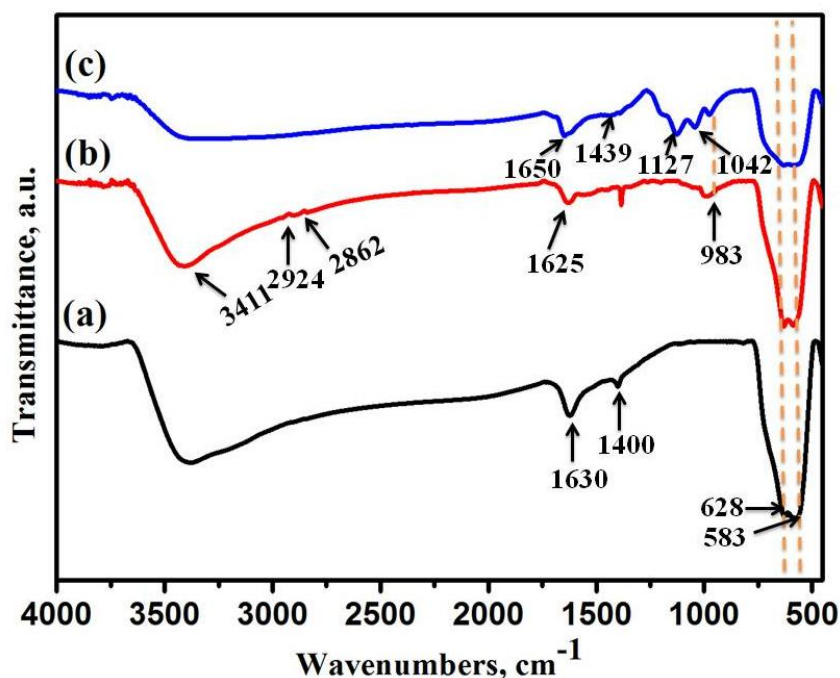


Figure 3.1 FTIR spectra of (a) Fe_3O_4 , (b) Fe_3O_4 -TSPED and (C) Fe_3O_4 -TSPED-Tryptophan.

The crystal structure of synthesized Fe_3O_4 , FT and FTT were analyzed by XRD (Figure 3.2). The XRD pattern of Fe_3O_4 shows six diffraction lines and the characteristic peaks are $2\theta = 30.3^\circ$ (220), 35.6° (311), 43.4° (400), 53.4° (422), 57.9° (511), and 62.7° (440), which agree well with the XRD pattern of JCPDS file no (65-3107)[203, 205]. The diffraction peaks reveal that the Fe_3O_4 nanoparticles are pure and spinel structure, indicating that the TSPED and tryptophan coating does not result in the phase change of Fe_3O_4 [179, 195, 206, 207]. The XRD shows high crystallinity of FTT. The average core size can be evaluated from the XRD result by Scherrer formula:

$$D = \frac{0.94\lambda}{B \cos \theta}$$

Where D is the average crystalline diameter, 0.94 is the Scherrer constant, λ is the X-ray wavelength, B is the angular line width of half-maximum intensity and θ is the Bragg's angle in degree. Here, the peak (311) with highest intensity was picked to evaluate the particle diameter of Fe_3O_4 , FT and FTT, and the D was calculated as 25.5 nm, 32.5 nm, and 48.17 nm, respectively.

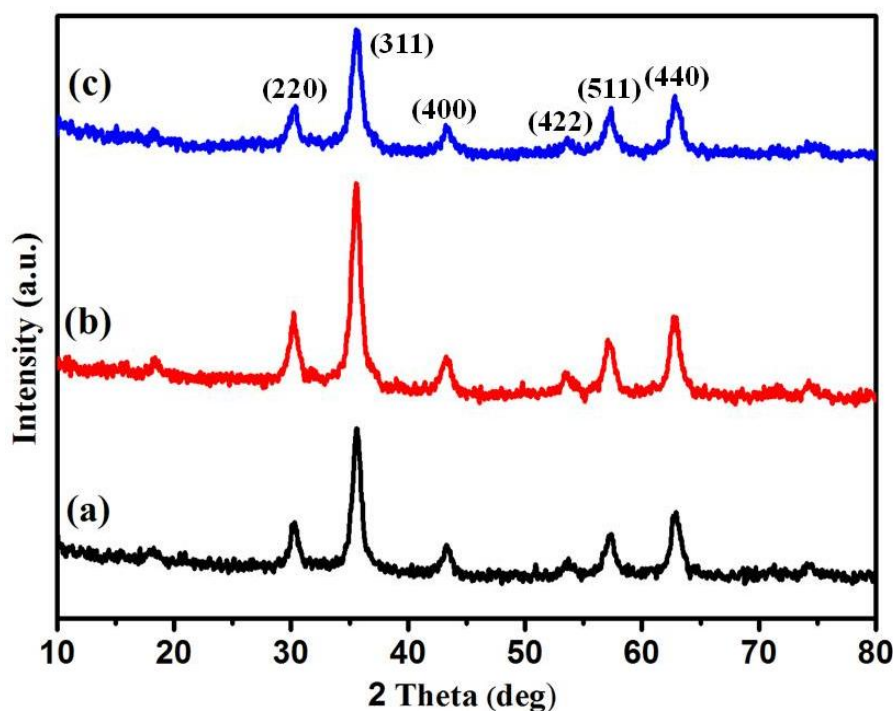


Figure 3.2 XRD patterns for (a) Fe_3O_4 , (b) Fe_3O_4 -TSPED and (c) Fe_3O_4 -TSPED-Tryptophan.

The morphology of the FTT nanocomposite was characterized using a transmission electron microscope (TEM) (Figure 3.3). TEM images reveal FTT composite are monodisperse and has an average size of of 47 nm, and spherical in shape (Figure 3.3a). The selected area electron diffraction (SAED) pattern of FTT shows the ring-like structure clearly indicating the existence of crystalline nature (Figure 3.3b). EDX spectrum of FTT shows the strong peaks for Fe, C, O, N and Si (Figure 3.3c). The quantitative analysis indicated the molar presence of iron (52.50%), carbon (20.16 %), oxygen (32.65%), nitrogen (3.66 %) and silicon (1.21 %) in the nanocomposite.

The magnetic properties of Fe_3O_4 , FT and FTT were investigated by vibrating sample magnetometer (VSM). At room temperature the hysteresis loop of bare Fe_3O_4 , TSPED coated Fe_3O_4 and FTT (Figure 3.4) shows superparamagnetic behavior at room temperature with negligible remanence and coercivity. The obtained magnetic saturation (M_s) value of Fe_3O_4 ,

FT and FTT were 71, 52 and 39 emu/g, respectively. The magnetic saturation value FT and FTT are significantly smaller than bare Fe₃O₄ nanoparticles. These phenomena may be explained by the addition of nonmagnetic substance or high molecular weight of TSPED and tryptophan [179, 208, 209]. According to Ma's study, the magnetic saturation value 16.3 emu/g is enough for magnetic separation from aqueous solution by using an external magnetic field [210]. This result suggested that FTT could be easily separated and collected with a magnetic field.

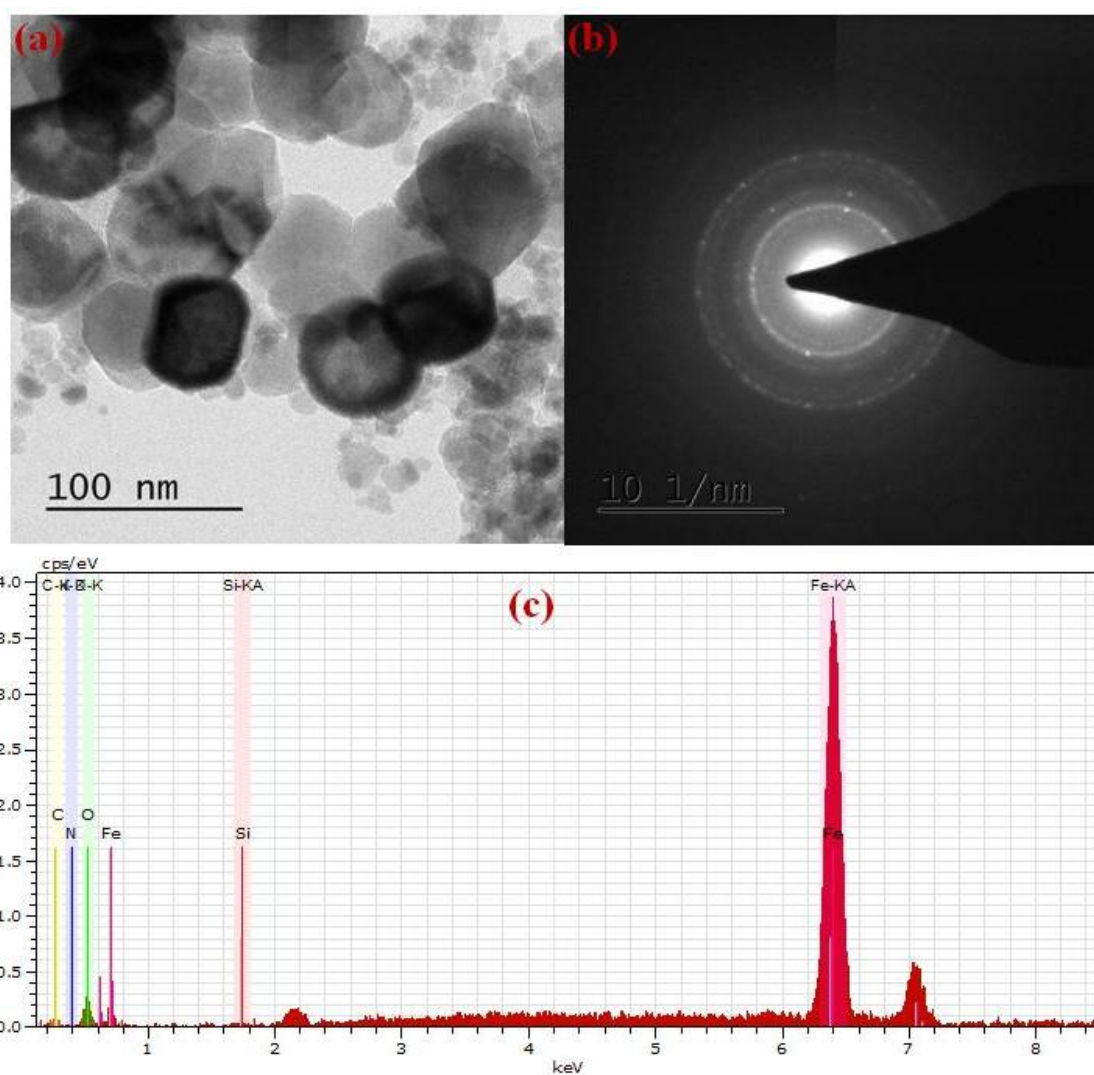


Figure 3.3 (a) TEM image of FTT (b) SAED pattern of FTT (c) EDX spectra of FTT nanocomposite.

N₂ adsorption/desorption analysis at 77 K was undertaken for Fe₃O₄, FT and FTT to reveal their texture properties. Figure 3.5a shows the N₂ adsorption/desorption isotherms of Fe₃O₄, FT and FTT. All three samples exhibit a type IV isotherm, with relative pressure between 0 and 1, which corresponds to mesoporous structure [211, 212]. The Brunauer-Emmett-Teller (BET) specific surface area of Fe₃O₄, FT and FTT was determined to be 223.83, 216.08, 138.7 m²/g. These results indicate that after coating TSPED and Tryptophan on the surface of

Fe_3O_4 , the surface area significantly decreases. This may be because of the large number of TSPED and tryptophan which occupy the surface of Fe_3O_4 nanoparticles and reduces the surface area[212, 213]. The pore size distribution was determined by the Barret, Joyner, and Halenda (BJH) method using the desorption isotherm, which shown in Figure3.5 (b-d). The result indicates that the pore size of Fe_3O_4 , FT and FTT are 1.84, 1.67 and 1.61 nm, respectively. The total pore volume of Fe_3O_4 , FT and FTT are 0.439, 0.495 and 0.617 cc/g.

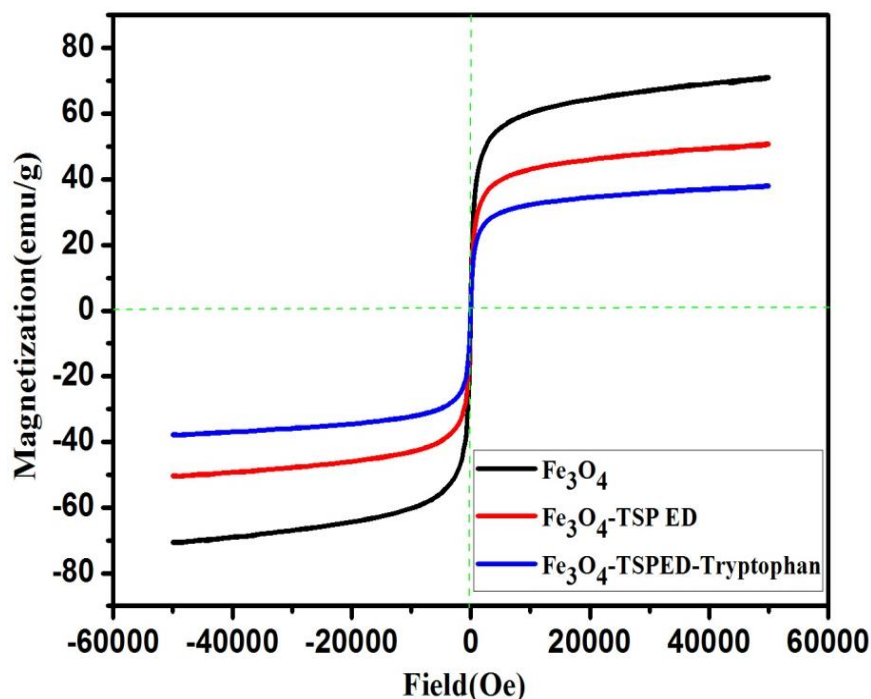


Figure 3.4 Magnetization curve of Fe_3O_4 , Fe_3O_4 -TSPED, and Fe_3O_4 -TSPED-Tryptophan nanocomposite.

For thermal stability of the nanocomposite, thermogravimetric (TGA) analysis was carried out. The typical TGA curve of Fe_3O_4 , FT and FTT is shown in Figure 3.6. The TGA curve of Fe_3O_4 nanoparticles shows a 7.15 % weight loss between 32-150 °C because of physically adsorb water, followed by further weight loss around 1.68 % between 150-500 °C, a slow decrease about 0.9 % in between 525-600 °C was attributed to loss of moisture which tightly bound, and after 600 °C there is no loss of mass was observed. The TGA curve of Fe_3O_4 -TSPED (FT) indicates weight loss 7.5 % between 34-589 °C, which can be ascribed to the escape of physically adsorbed water, the decomposition of amine group, the complete oxidation of carbon but in case of FTT, it show a 9.6 % weight loss in between the range 37-609 °C, which might be due to the decomposition of the amine group and carboxylate group of the tryptophan, respectively. Therefore the weight loss in FTT (9.6 %) which is higher than FT (7.5 %) verifies that tryptophan was modified successfully on the surface of FT. The DTA curve of Fe_3O_4 showed the presence of an exotherm at 334 °C and 524 °C, whereas FT showed the presence of an exotherm at 345 °C and 666 °C and FTT showed at 346 °C and

668 °C (Figure A1a) compared to others. The DTA result specifies the loss of water molecules and decomposition of organic moiety, respectively. The peaks are shown in DTG curve also enlighten the decomposition of constituent organic moieties at specific temperature as in Figure A1b. The DTA and DTG curve supports the TGA findings.

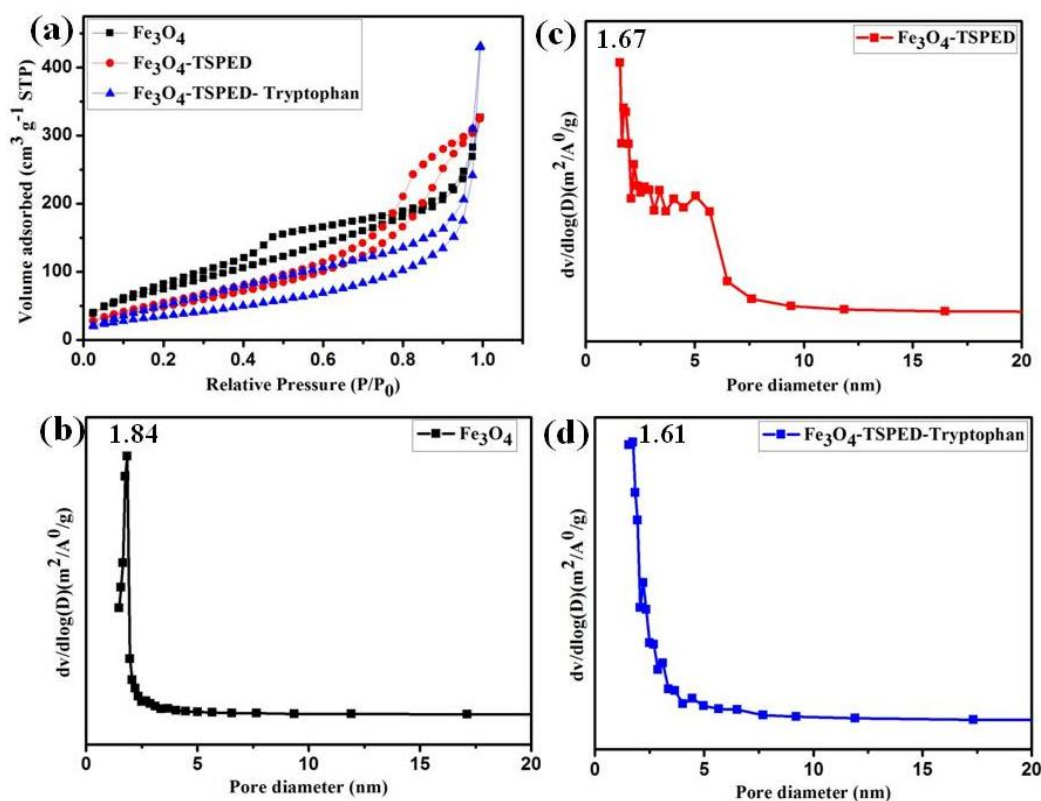


Figure 3.5 (a) N₂ adsorption-desorption isotherm of Fe₃O₄, Fe₃O₄-TSPED, and Fe₃O₄-TSPED-Tryptophan nanocomposite. The pore size distribution of (b) Fe₃O₄, (c) Fe₃O₄-TSPED and (d) Fe₃O₄-TSPED-Tryptophan.

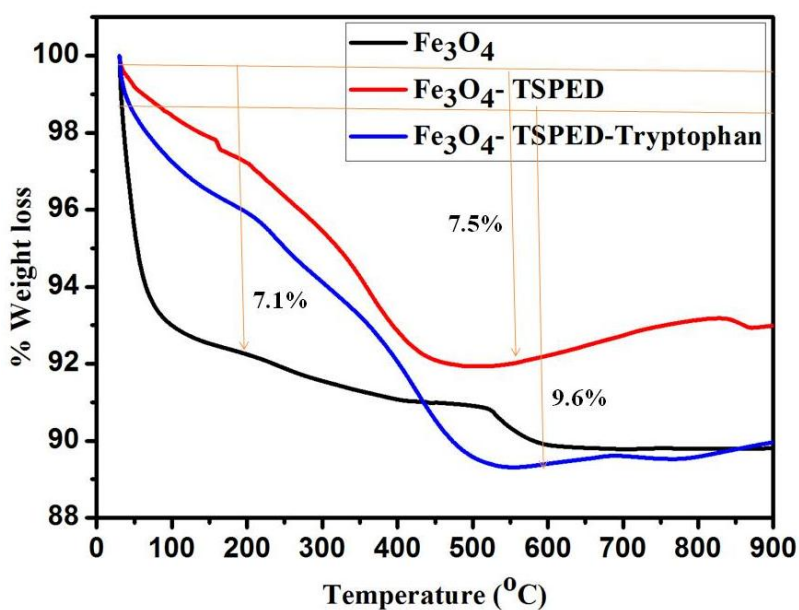


Figure 3.6 TGA curve of Fe₃O₄, Fe₃O₄-TSPED, and Fe₃O₄-TSPED-Tryptophan nanocomposite.

3.4.2 Impact of the different parameter on adsorption

Adsorbent dosage is an important parameter in the adsorption process. It significantly influences the removal of adsorbate species. The effects of FTT dosage on the adsorption of CR were examined at room temperature by varying the amount of adsorbent from 20 mg to 200 mg, keeping other parameters constant such as dye concentration 60 mg/L, pH 3 and time 10 min. The increasing in adsorbent dosage, dye removal efficiency also increases due to the higher number of active binding site (Figure 3.7a). With further increase in the adsorbent dosage, adsorption capacity (q_e) significantly decreases, while the removal efficiency of CR shows a steady trend. Also, Fig 7a shows the equilibrium state for CR removal efficiency.

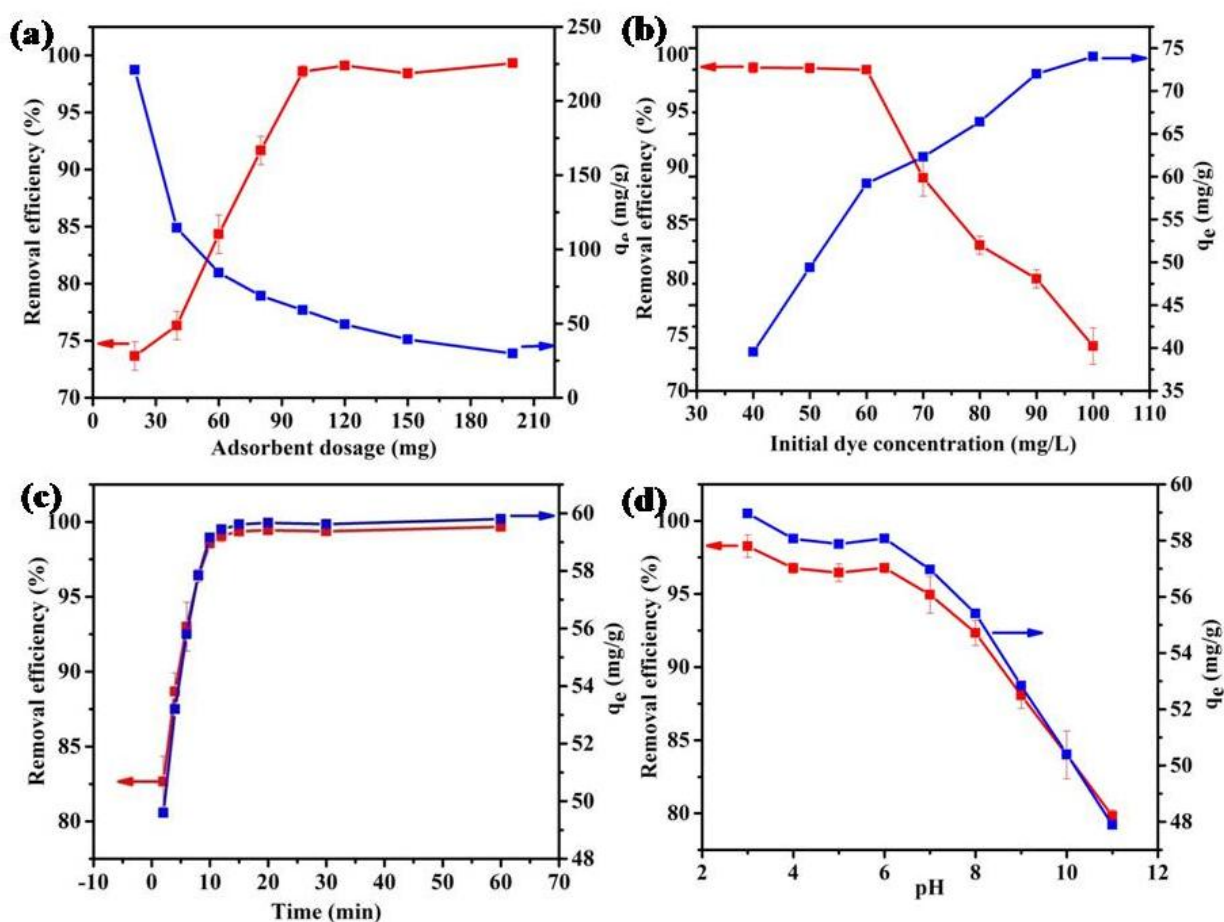


Figure 3.7 (a) Effect of adsorbent dosage on CR adsorption, (b) the removal of CR at different concentrations, (c) Effect of time on adsorption of CR and (d) Effect of pH on the removal efficiency.

The effect on adsorption efficiency with initial CR concentrations is shown in Figure 3.7b. The concentration of CR dye varied from 40 to 100 mg/L at room temperature, keeping other parameters constant such as adsorbent dosage (100 mg), pH (3), time (10min). The removal percentage of CR dye which decreases with the increase in CR concentration is depicted in Figure 3.7b. This decreasing trend is due to the saturation with the available active binding

sites and surface area. From the graph, it is clearly seen that the dye removal efficiency nearly same between 40 mg/L and 60 mg/L, but after significantly decreases. The increase in dye concentration up to 100 mg/L resulted in increase in adsorption capacity (q_e) (from 39.54 mg/g to 74.01mg/g).

The removal efficiency of CR dyes from wastewater increases with increase in adsorption time (Figure 3.7c). It attained the equilibrium of 99% in 10 minutes for CR removal. After 10 min to 60 min, the removal efficiency was found to be nearly same. Due to comparatively larger surface area and abundant active binding sites of the nanocomposite, the rate of removal of CR dye is high. Overall, the adsorption capacity (q_e) increases with increase in time.

The impact of pH on the removal of CR from aqueous solution was observed in a range of pH (3-11), as shown in Figure 3.7d. At neutral pH (around 7), the color of the CR dye is solid red, which remains same at alkaline pH (10-11) but the color changes to dark blue at strong acidic pH (3-5). In addition, it is observed that the solubility decreases at pH 2 compared to higher pH[214]. In the present work, the maximum removal percentage of CR was observed at acidic medium (at pH 3) and gradually decreases in basic medium. The CR removal was nearly the same over the pH range 3-6, after pH 6 the removal efficiency slightly decreases. At pH 3, a significant high electrostatic attraction exists between positive charge surface of adsorbent and anionic dye, which makes the strong interaction between them. At higher pH, the number of positive sites decreases and negative sites increases, that causes the electrostatic repulsion between negative charge adsorbent and anionic dye. Moreover, the adsorption capacity (q_e) decreases with increase in pH. Furthermore, there was a competition between excess of OH^- ions with anionic dye towards the adsorption sites. It has been reported that the solution at a pH below the zero point charge (pH_{zpc}) makes the adsorbent surface positive and can interact with the negative charge of the dye in solution. The pH_{zpc} of the sample was analyzed by potentiometric titration method (Data not shown). The point of zero charges (pH_{zpc}) value of FTT nanocomposite was found to be 6.5. Therefore, below 6.5, most of the free amino groups are protonated in the case of FTT samples[215]. The protonated amino group of adsorbent are attracted towards the doubly negatively charged SO_3^- groups in CR dye molecules. So, an electrostatic interaction plays a vital role in adsorption between adsorbent and adsorbate. Including the above mechanism, one can expect π - π stacking interactions between aromatic rings of CR and tryptophan. This dispersion interaction is also important parameter for CR adsorption as reported earlier[216]. A similar

result was reported earlier for the removal of CR on orange peel waste[150], Biogas waste slurry [217] and activated carbon [184].

3.4.3 Adsorption isotherm

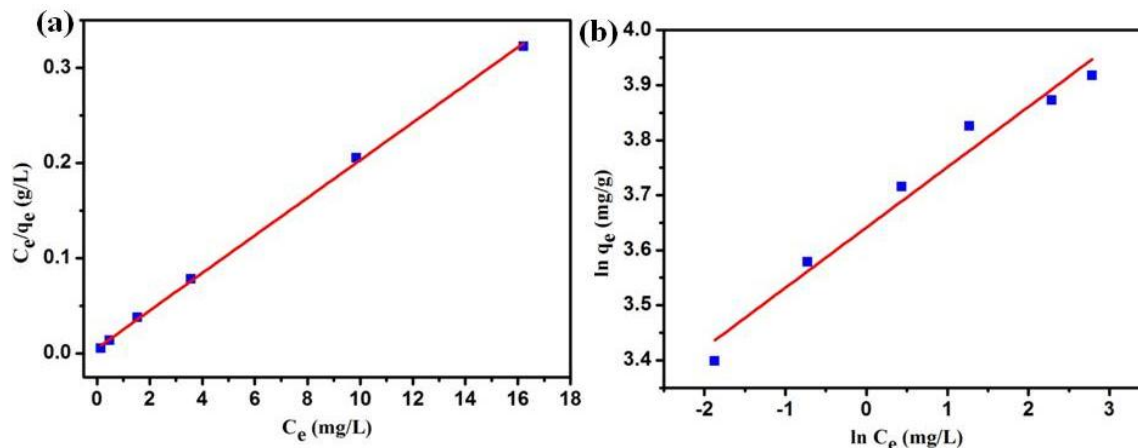


Figure 3.8 (a) Langmuir isotherm plot and (b) Freundlich isotherm plot for CR dye adsorption.

In this study, we perform Langmuir and Freundlich isotherm model. Both of the above isotherms are shown graphically in Figure 3.8 and the isotherm parameters are listed in Table 3.1. It is clear from Figure 3.9 that the Langmuir isotherm data fit better than Freundlich isotherm. Besides it can be seen from Table 1 that the value of R^2 for the Freundlich isotherm ($R^2 = 0.96$), which is less than of the Langmuir isotherm ($R^2 = 0.99$), showing the applicability of Langmuir isotherm. Therefore the adsorption of CR dye is regarded as monolayer adsorption on the homogeneous surface. The R_L value of CR adsorption onto FTT is 0.0045 for initial concentration of 60 mg/L respectively. Table 3.2 shows maximum adsorption capacity (q_{max}) of FTT is 183.15 mg/g for CR, which is significantly higher than that various adsorbent reported in the literature. From the Freundlich isotherm, the value of n is 9.11, which represents favorable adsorption.

Table 3.1 Isotherm parameters for adsorption of CR on Fe_3O_4 -TSPED-Tryptophan nanocomposite.

Langmuir isotherm Parameter	CR
q_m (mg/g)	183.1
b (mg/g)	3.62
R^2	0.99
Freundlich isotherm parameters	CR
K_f (L/g)	38.1
n	9.11
R^2	0.96

3.4.4 Adsorption kinetics

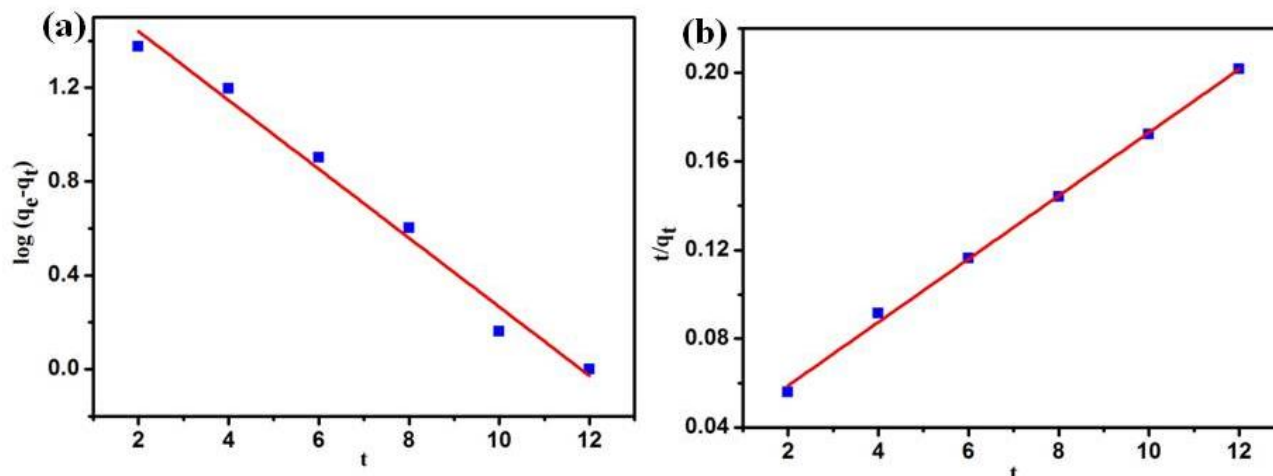


Figure 3.9 (a) Pseudo-first order model and (b) Pseudo-second order model for CR adsorption on Fe₃O₄-TSPED-Tryptophan nanocomposite.

Table 3.2 Adsorption capacity (q_{\max}) values for the removal of CR on various adsorbents.

Adsorbent	q_{\max} (mg/g)	Reference
M-cell/ Fe ₃ O ₄ /ACCs	66.09	[218]
CTS powder	74.73	[180]
Bamboo dust carbon	101.9	[185]
Ground nut shell carbon	110.8	[185]
Magnetically modified fodder yeast cell	49.7	[181]
Chitosan/montmorillonite nanocomposite	54.52	[180]
Activated carbon prepared from coir pith, an agricultural solid waste	6.72	[184]
Chitosan coated magnetic iron oxide	42.62	[182]
Waste orange peel	22.4	[150]
Palm Kernel seed Coat	66.23	[183]
Fe ₃ O ₄ -GG nanocomposite	60.	[179]
Waste red mud	4.05	[219]
Rice hull ash	171.0	[220]
Fe ₃ O ₄ -TSPED-Tryptophan	183.15	This Study

Figure 3.9 shows the pseudo-first-order and pseudo-second-order kinetic model and the parameters are listed in Table 3.3. The linear fits of the kinetics results reflect that pseudo-second-order model exhibits higher R^2 value, compared to the pseudo-first-order model. This specifies that adsorption kinetics process follows pseudo-second-order kinetics and is dependent on the amount of solute adsorbed on the surface of nanocomposite as well as amount adsorbed at equilibrium. The above results supported that the adsorption was due to chemisorptions which involved valence forces between dye anion and adsorbent.

Table 3.3 Kinetic model parameters and constant with statistical data.

dye Concentration	$(C_0,$ mg/L)	$q_{e, \text{exp}}$ (mg/ g)	Pseudo-first-order			Pseudo-second-order		
			$q_{e, \text{cal}}$ (mg/g)	K_1	R^2	$q_{e, \text{cal}}$ (mg/g)	K_2	R^2
Congo Red	60	59.502	5.663	0.3362	0.98	70.42	0.0066	0.99

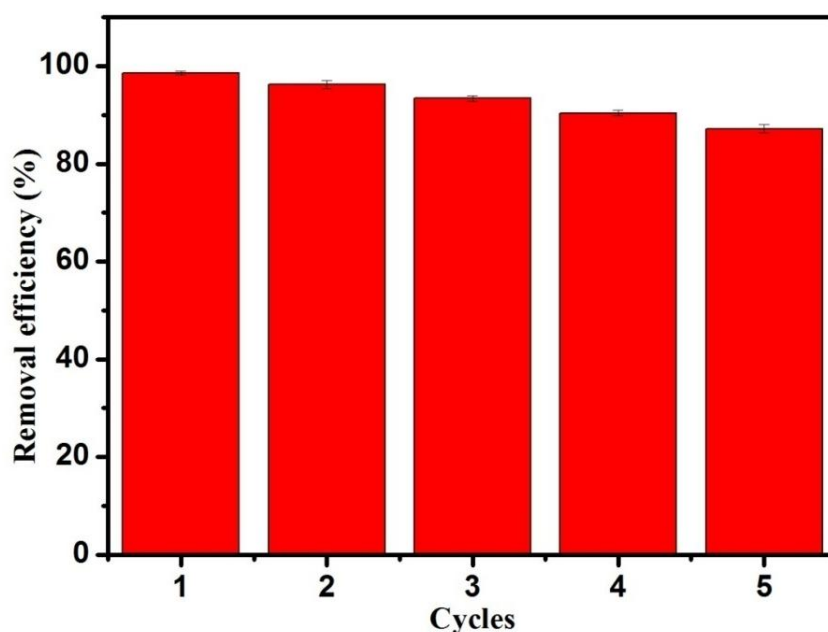


Figure 3.10 Reusability test of Fe₃O₄-TSPED-Tryptophan adsorbent for removal of CR.

3.4.5 FT-IR and FE-SEM analysis of after adsorption of Congo red dye

Native FT-IR peaks were already discussed in section 3.1. Figure A2 after CR dye adsorbed on FTT, where the peaks were slightly shifted higher with values 584, 633, 984, 1026, 1128, 1442, 1652 cm^{-1} . The shifting of peaks may correspond to the formation of a chemical bond between adsorbate and adsorbent. The morphology of FTT before and after adsorption of CR is analyzed by FE-SEM and is shown in Figure A3. From the Figure A3a and A3b, before adsorption of FTT shows the particles are spherical in shape and homogeneously distributed

but after adsorption, some aggregation took place on the spherical particle due to the attachment of CR dye on the surface of FTT which are shown in Figure A3b.

3.4.6 Reusability of adsorbent

The reusability of adsorbent is one of the important parameters of the adsorption process from the economy and environmental point of view. To check the desorption study using methanol, ethanol, chloroform, and acetone; ethanol was found to be good desorption efficiency. The dye loaded on adsorbent was washed with ethanol after that the adsorbent was dried using the oven to remove the ethanol. Thus, the used adsorbent could be further used for adsorption of CR. As shown in Figure 3.10, five consecutive cycles were examined, after five cycles the CR removal efficiency of the adsorbent is 87.2 %. This shows that the high regeneration capability of Fe_3O_4 - TSPED-Tryptophan and its good reusability of CR removal.

3.4.7 Antibacterial activity

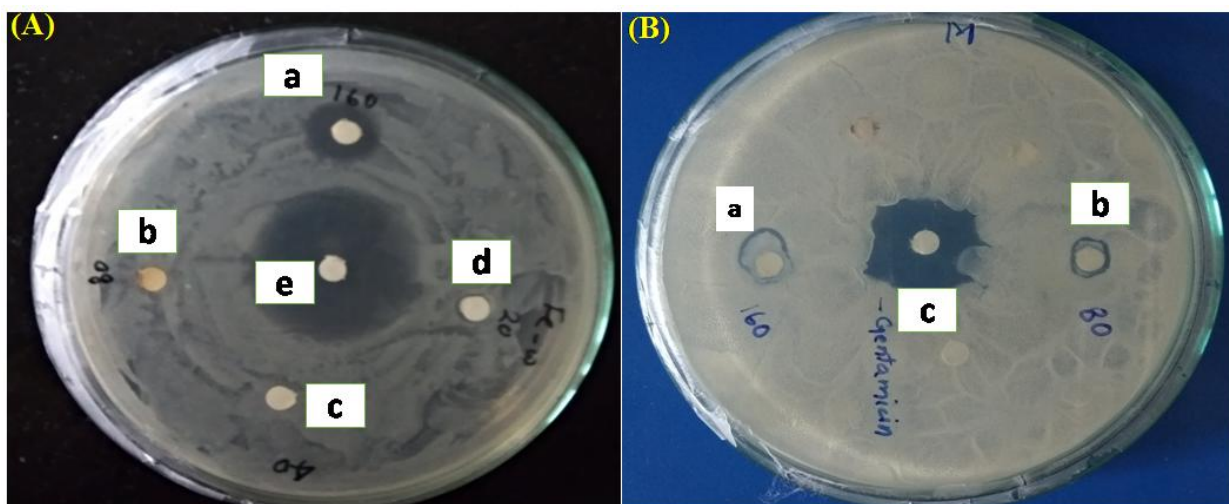


Figure 3.11 (A) Antibacterial activity by disc diffusion method (a) shows the zone of inhibition when *E.coli* treated with the 160 $\mu\text{g}/\text{ml}$ of FTT (b,c,d) Shows the zone of inhibition when *E.coli* treated with 80 $\mu\text{g}/\text{ml}$, 40 $\mu\text{g}/\text{ml}$, 20 $\mu\text{g}/\text{ml}$ respectively where zone of inhibition is not clearly visible. (e) At middle shows the zone of inhibition, when *E.coli* treated with standard drug Gentamicin. (B) Antibacterial activity by disc diffusion method (a) shows the zone of inhibition when *B.subtilis* treated with the 160 $\mu\text{g}/\text{ml}$ of FTT (b) Shows the zone of inhibition when *B. subtilis* treated with 80 $\mu\text{g}/\text{ml}$. (c) At middle shows the zone of inhibition, when *B.subtilis* treated with standard drug Gentamicin.

Disc diffusion method was performed to check the antimicrobial potential of the adsorbent material. Cell viability test of *E. Coli* and *B. Subtilis* with FTT were done by using the colony counting method. Bacterial growth kinetics was studied in presence of the FTT as well as in absence. FESEM analysis was done to check the effect of FTT on bacterial cell

morphology.EDX analysis was further done to check the element deposited in the bacterial body. Concentration and Time-dependent antibacterial activity of nanomaterial was also carried out.Antibacterial activity of FTT was determined by the interaction of *E.coli* and *B. subtilis* with the FTT by using a varying range of the concentration. To determine its propensity of killing bacteria, disc diffusion assay has been performed and antibacterial activity was observed at concentration 160 $\mu\text{g/ml}$ and 80 $\mu\text{g/ml}$. We have observed the clear zone of inhibition at the concentration 160 $\mu\text{g/ml}$ for FTT in *E.coli* and *B.Subtilis* (shown in Figure 3.11).

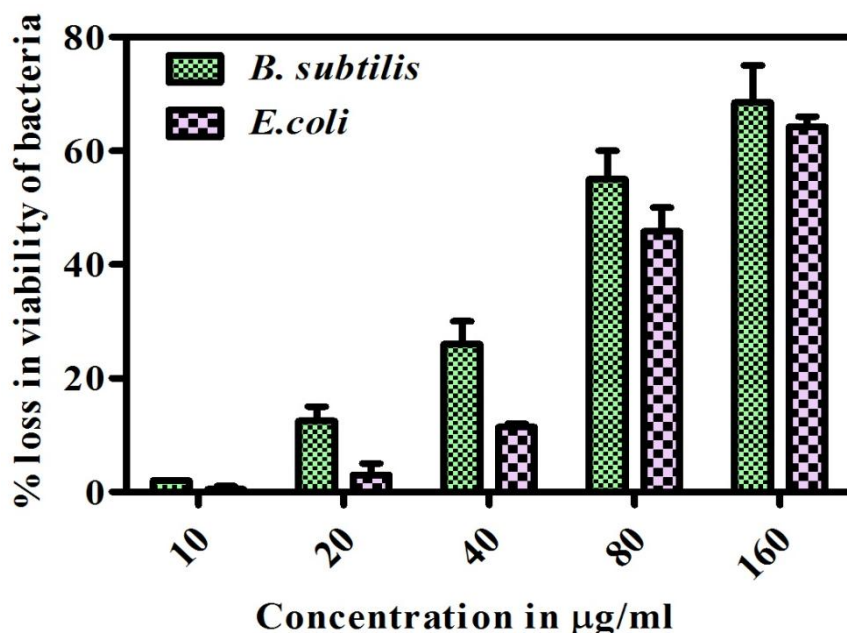


Figure 3.12 Graph representing the antibacterial activity of FTT with varying concentration against, *E. coli* and *B. subtilis* by showing the percentage loss in bacterial cell viability.

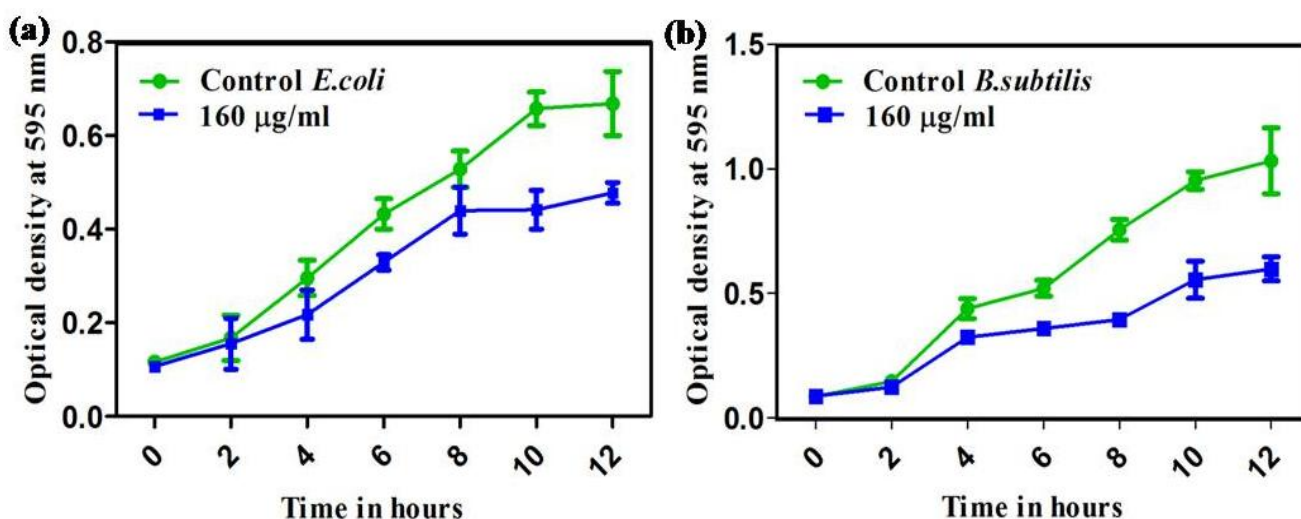


Figure 3.13 Growth kinetics of (a) *E. coli* and (b) *B. subtilis* in presence as well as the absence of FTT. The experiment performed in triplicate and the result showed as the Mean \pm SEM.

Zone of Inhibition also observed at 80 $\mu\text{g/ml}$ but it was not clear. At low concentration zone of inhibition was not predominantly seen. Concentration-dependent activity of FTT was again examined by colony counting method, maximum inhibition observed at 160 $\mu\text{g/ml}$ and it gradually decreases with decreasing concentration (shown in Figure 3.12). Bacterial growth kinetics were studied in presence as well as the absence of FTT (Figure 3.13). We found that the stationary phase in bacterial growth can be observed at an early stage when bacteria treated with FTT at concentration 160 $\mu\text{g/ml}$. Bacterial growth inhibition is shown in the curve in comparison to control one. Production of reactive oxygen species due to oxidative stress induced by FTT is considered as the possible mechanism behind the antibacterial activity of FTT. To quantify the amount of ROS generated in the influence of FTT is measured by an assay employing the use of DCFDA dye is followed. DCFDA have the potential to penetrate the bacterial cell membrane and then gets hydrolyzed inside bacteria. The hydrolyzed product gives the green fluorescence in presence of reactive oxygen species like singlet oxygen, superoxide radical, hydroxyl radical, peroxide and hydroperoxide radical. The fluorescence intensity is directly proportional to the presence of reactive oxygen species. More the amount of ROS, more the fluorescence intensity. The concentration-dependent effect of FTT on ROS generation in *E.coli* and *B.subtilis* has been depicted in

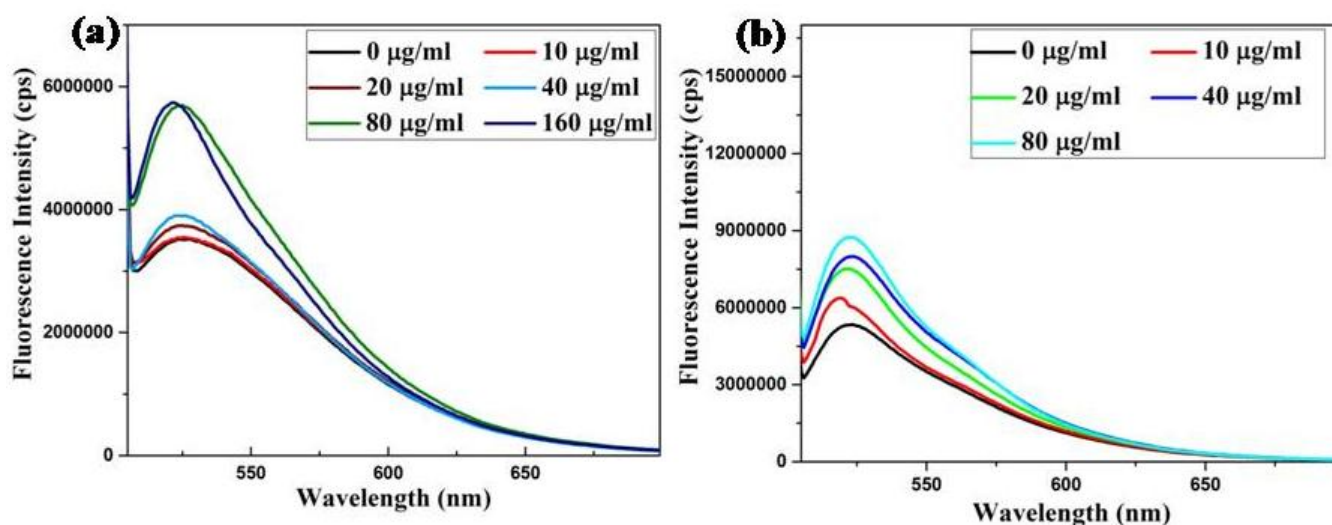


Figure 3.14 Fe₃O₄-TSPED-Tryptophan induced ROS generation in (a) *E.coli* and (b) *B. subtilis*. Fluorescence intensity shows the ROS generation at different concentration of Fe₃O₄-TSPED-Tryptophan. Higher fluorescence intensity indicates the excess generation of ROS.

Figure 3.14 ROS production could also be observed in the absence of FTT treatment but it is less prominent in comparison to the treated one. Bacterial death was further characterized by alteration in normal morphology of bacteria which was done by FE-SEM shown in (Figure A4 and Figure A5), EDX analysis was also done, by which we detected the presence of silicon and iron in the bacterial body. We have chosen tryptophan as a coating material to

modify the surface properties of iron oxide nanoparticle, which inflect the functional group and surface potential of the material. The amino group of tryptophan has a strong binding affinity toward the paramagnetic FTT by the help of hydrogen bonding or electrostatic force of interaction between the molecules. This tryptophan tagged FTT comprises of the carboxylic group which carries OH group which directly interact with the water molecule by hydrogen binding force of interaction to form the colloidal dispersion of FTT.

This colloidal dispersion facilitates the interaction with the bacteria. Substantial interaction also increases ROS production due to iron oxide[221]. It is well known that tryptophan is found in its zwitterions form which imparts the positive or negative surface potential which supports the Coulomb repulsion among the iron oxide nanoparticle which again enhances dispersivity of particles[222]. It is already reported that the iron oxide is capable of inducing the reactive oxygen species (ROS) generation which increases the oxidative stress[223, 224] and then bacterial death. The electrostatic force of interaction with bacteria also alters membrane integrity [225]. The above-shown result has shown that the current nanoparticles have the potential to kill bacteria in dose-dependent as well as concentration-dependent manner.

3.5 Summary

In summary, we report the increased adsorption efficiency and antibacterial properties of FTT nanocomposite. The FTT nanocomposite was successfully prepared using the simple and economic method and further analyzed to confirm the chemical and physical structure. When employed as Nanoadsorbent, FTT nanocomposites were found with increase adsorption efficiency as compared to alone Fe_3O_4 and FT. The adsorption of Congo red onto FTT nanocomposites followed pseudo-second-order kinetics and Langmuir model of adsorption isotherm. The maximum adsorption capacity (q_{max}) for FTT nanocomposite was calculated as 183.15 mg/g which was quite significant. In addition FTT nanocomposites were examined for better antimicrobial activity towards *E. coli* and *B. subtilis*. Further understanding the mechanism of cell death, FE-SEM micrographs were captured and ROS generation was observed. To further investigate the toxicity profile of FTT, *In vivo* studies need to be performed. Surface chemistry and magnetic properties of FTT strongly support its distribution profile to get interact with the bacteria. Thus, with excellent adsorption capacity and adequate antibacterial properties, such nanocomposites are truly a potential and promising adsorbent in the future water treatment and purification.

Chapter 4

4. Guar-gum coated iron oxide nanocomposite as an efficient adsorbent for Congo red dye

4.1 Introduction

Nowadays the disposal of dyes and organic contaminants generated from the industries are the major source of water pollution that became a worldwide environmental concern. Industries such as paper, printing, cosmetics, plastics, leather, textile and petroleum release different types of dyes into the aquatic environment which causes water pollution[226, 227]. These pollutant dyes and organic compounds are reported as toxic, carcinogenic and mutagenic in nature. Even with a few dyes discharged into the water system can affect the aquatic ecosystem and possess a serious problem to living organisms. Thus the removal of dye from the wastewater is necessary and important before it discharged into the environment[228]. Most of these dyes are frequently used in various industries such as Congo red (CR), Malachite green (MG), Methylene blue (MeB), Methyl orange (MO), Eriochrome Black T (EBT), Methyl blue (MB) and Rhodamine B (Rhb), etc. Among them Congo red (CR) dye, benzidine-based anionic bis azo dye is most frequently used for various applications. This dye is responsible for several diseases like human cancer and a potential threat to bioaccumulation and unfavorably susceptible issues[229]. Here, CR has been picked as a model dye in view of its complex structure, restricted biodegradability, soundness towards the light and high dissolvability in watery arrangement[230], so it is required to remove them during treatment. Till date, most of the techniques such as photodegradation[231], adsorption[232], solvent extraction[233], coagulation[234], membrane filtration[235], oxidizing agents[236], are used to take off poisonous chemicals from the dissolved aqueous solution. Among these, adsorption is a classical technique, because of its efficiency, economy and high level of effectiveness[237].

In past decades, the various low-cost adsorbent such as palm kernel seed coat[238], magnetic alginate beads[239], chitosan[240], bagasse fly ash[241], clay mineral[71], biodegradable waste[242], agricultural waste[78] and industrial waste products[243] have effective adsorbent for adsorption of carcinogenic dyes from different water body. A number of literature has also been reported towards the adsorption of Congo red on various adsorbent

*Jitendra Kumar Sahoo, Aniket Kumar, Juhi Rath, Tanuja Mohanty, Priyabrat Dash, Harekrushna Sahoo** *Desalination and Water Treatment*, 2017, 95, 342-354.

surfaces. Moreover, Kannan and Meenakshisundaram have used activated carbon for removal of congo red[244]. Additionally, biogas waste has also been employed for the removal of congo red from aqueous solution[245]. During the past decade, iron oxide has attracted much attention due to its wide range of applications such as biosensor development[246], biomedical engineering[247], drug delivery[248], bioseparation technologies[249] and other developments. Among various applications, iron oxides have frequently used as adsorbent because of its several advantages like low cost, extensive availability, good adsorption capacity and thermal stability[250, 251]. Moreover, Fe_3O_4 have large specific surface areas, reactive surfaces and easy magnetic separation after adsorption process. Therefore the Fe_3O_4 nanoparticles can be a good selection for the adsorption of different dyes. The adsorption capacity of the Fe_3O_4 nanoparticle can be further improved by modifying it with various polysaccharides. There is some literature available where polysaccharides modified magnetic nanoparticles have been reported such as adsorption of reactive black dye using modified with graphite oxide magnetic chitosan nanocomposite[252], cobalt ferrite/activated carbon/alginate composite beads for adsorption of methyl blue[253], removal of methylene blue dye using chitosan-g-poly (acrylic acid)/vermiculite hydrogel composites[254] etc.

Among all available polysaccharides, Guar gum (GG) is the most important class of polysaccharide that can be a promising supporting material for adsorption due to its thermal stability and higher solubility. So we have explored the grafting of GG on to the surface of Fe_3O_4 nanoparticles to improve the hydrophilicity of Fe_3O_4 [255-258]. Therefore, the combined properties of both GG and Fe_3O_4 nanoparticle can be used for adsorption of toxic dyes. Till now GG modified Fe_3O_4 nanoparticle has not been studied thoroughly for the adsorption of various toxic dyes.

It is assumed that cross-linking of Fe_3O_4 nanoparticles with GG occurs via the 3,4-cis-hydroxy moiety, and thereby the formation of a three-dimensional network responsible for the gelation (the mechanism is illustrated in Fig. 1a). Besides of having previous reports on the mechanistic points, which says that the active sites of GG are responsible for the cross-linking with Fe_3O_4 , till date the mechanism is not clear[259]. The author observed that entirely two different mechanisms; (a) a condensation reaction of OH groups on Fe_3O_4 nanoparticles and surface OH groups on GG and (b) An esterification reaction between Fe_3O_4 compounds and a hydroxyl group on GG. These two mechanisms do not impose any actual and clear mechanism. Therefore, it is still commonly believed that the formation of these nanoparticles only represents an undesired side reaction which actually reduces the

activity of the cross-linker[260]. Thus, generally, the cross-linking mechanism is based on the ligand exchange reaction between Fe₃O₄nanoparticles and GG[261].

Keeping this in mind our aim is to synthesize an efficient and active GG coated Fe₃O₄nanocompositeadsorbent and to study its activity towards the adsorption of various dyes. The enhanced adsorption efficiency is due to the presence of multiple numbers of hydrogen bonding selective binding site of Fe₃O₄-GG nanocomposite with the CR dye. The optimum experimental condition such as pH, contact time, adsorbent dose and initial dye concentration was demonstrated in order to give knowledge about adsorption kinetics, isotherm, thermodynamics and reusability of the prepared adsorbent (i.e. Fe₃O₄-GG). The present study showed that Fe₃O₄-GG nanocomposite could perform challenging adsorbent for dyes removal at large scale and low cost.

4.2 Batch adsorption experiment

CR dye uptake study was performed by using batch adsorption experiment on a magnetic stirrer (REMI 5MLH plus, Kolkata, India). An amount of 150 mg of the Fe₃O₄-GG nanocomposite with 100 ml of dye solution of the required concentration was taken in a 250 ml of conical flask and pH of the solution were adjusted by adding NaOH (0.1M) or HCl (0.1M) as required then the mixture was stirred. The concentration of CR dye was analyzed by using UV-Vis (SHIMADZU-2450) spectrophotometer by monitoring the absorbance (495.7 nm). To get the optimum condition, the experiments were performed by varying adsorbent dose 10 mg to 200 mg, initial dye concentration 20 mg/L to 100 mg/L and pH 2 to 12 and the solutions were taken out at a different time interval during the adsorption. From the above experimental data, we get the optimum condition i.e. adsorbent dose of 150 mg, dye concentration 60 mg/L at pH 6 shows the highest efficiency in 5 min. Later on, Fe₃O₄-GG nanoparticles were separated from the solution by exposing to magnet Shown in Figure 4.1.

The percentage of dye removal was calculated using Eq. (4.1)

$$\text{Percentage of removal} = \frac{C_o - C_e}{C_o} \times 100 \quad (4.1)$$

And the equilibrium uptake was calculated using Eq. (4.2):

$$q_e = (C_o - C_e) \times \frac{V}{W} \quad (4.2)$$

Where C₀ is the initial concentration of the dye (mg/L), C_e is the final dye concentration (mg/L), q_e is equilibrium adsorption capacity (mg/g), w and V represents the weight of adsorbent (g) and the volume of dye solution used (L) respectively. All the batch experiments

were carried out in triplicate and the results represented here are the average readings[262].

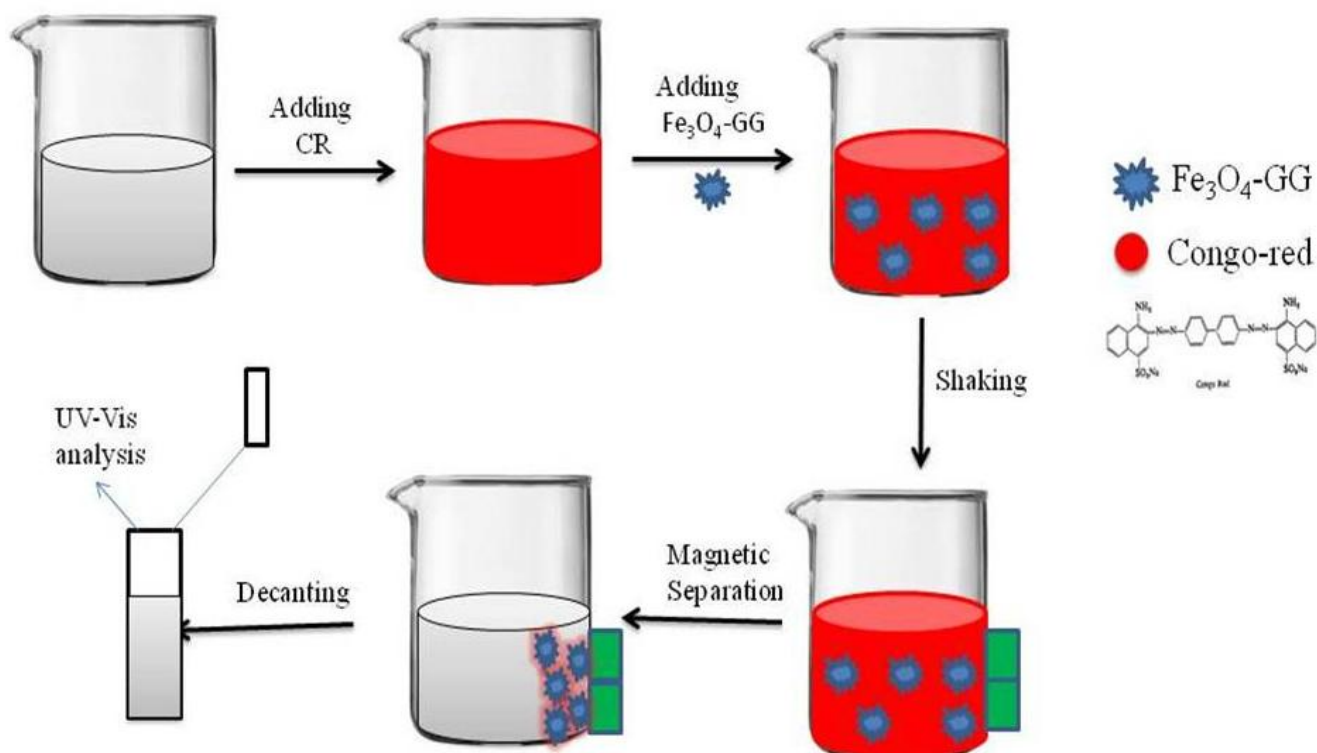


Figure 4.1 Schematic illustration of the adsorption process for the CR using $\text{Fe}_3\text{O}_4\text{-GG}$.

4.3 Results and discussion

4.3.1 Characterisation of magnetic nano adsorbent

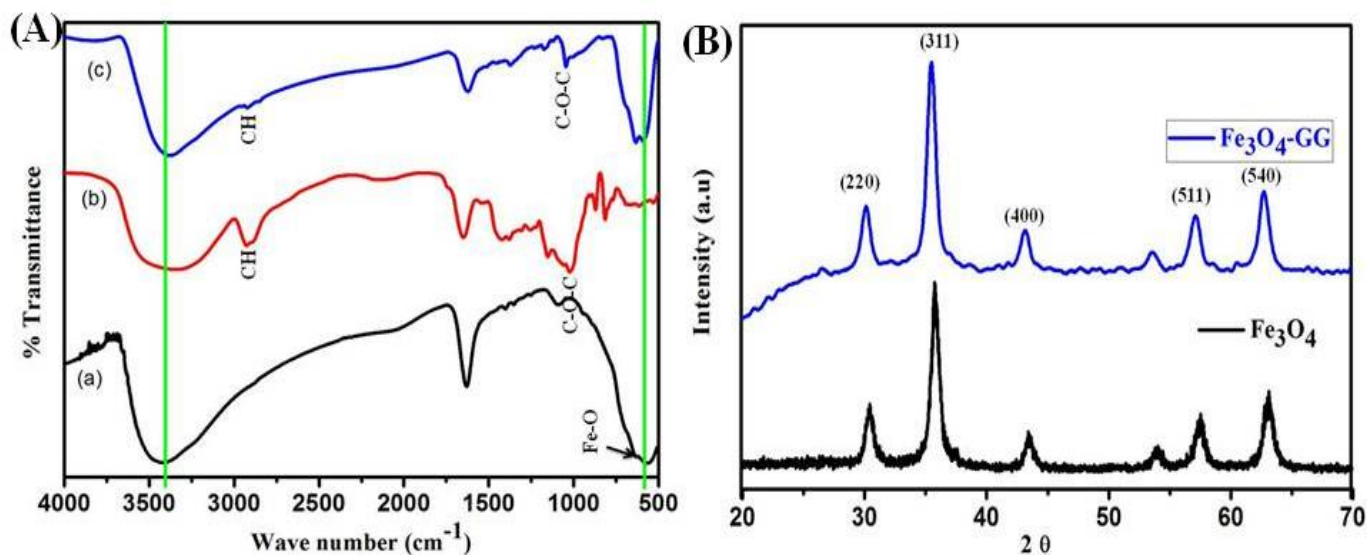


Figure 4.2 (A) FT-IR Spectra of (a) Fe_3O_4 and (b) GG (c) $\text{Fe}_3\text{O}_4\text{-GG}$ nanocomposite (B) X-ray diffraction patterns of (a) Fe_3O_4 and (b) $\text{Fe}_3\text{O}_4\text{-GG}$ nanocomposite.

FTIR spectra of Fe_3O_4 , GG & $\text{Fe}_3\text{O}_4\text{-GG}$ nanocomposite are presented in Figure 4.2A. In the case of Fe_3O_4 , the peak at 569 cm^{-1} relates to Fe-O group[263, 264], whereas GG exhibits the characteristic adsorption band at 3383 cm^{-1} due to -OH stretching vibration of the polymer

and water involved in hydrogen bonding[265]. The peak observed in the spectra at 800 and 1200 cm^{-1} , represents the highly coupled C-OH and C-O-C stretching mode of polymer backbone[266]. The peak 1654 cm^{-1} attribute due to ring stretching of galactose and mannose. The weak bands around 770 cm^{-1} , indicate the ring stretching and ring deformation of β -D-(1-4) and α -D-(1-6) linkages. The peak at 2897 cm^{-1} and the marked bands at 1059-1033 cm^{-1} ascribed to C-H stretching and C-O stretching of Guar-gum, which indicated the formation of covalent bond between -OH groups of GG and Fe_3O_4 . All these findings suggest that CR on Fe_3O_4 -GG is held by chemical activation or chemisorptions[256, 267].

To determine the crystal structure and phase purity, the Fe_3O_4 and Fe_3O_4 -GG nanocomposite were investigated by X-ray diffractometer shown in Figure 4.2B. The XRD patterns shows the characteristic peaks identified at $2\theta = 30.09^\circ$, 35.42° , 43.05° , 56.94° and 62.51° , which are marked by their indices (220), (311), (400), (511), and (440), which agree well with the XRD pattern of JCPDS file no (65-3107) respectively[268-270]. The diffraction peaks of Fe_3O_4 -GG are similar to the Fe_3O_4 nanoparticles, which reveal the crystal structure of high purity of Fe_3O_4 is well-maintained after the coating of GG. The average crystallite size was calculated using the Debye–Sherrer formula.

$$D = \frac{0.94\lambda}{B \cos \theta} \quad (4.3)$$

Where D is the average crystalline diameter, 0.94 is the Scherrer constant, λ is the X-ray wavelength, B is the angular line width of half-maximum intensity and θ is the Bragg's angle in degree. Here, the (311) peak of the highest intensity was picked out to evaluate the particle diameter of Fe_3O_4 and Fe_3O_4 -GG. The D was calculated to be 4.2 and 6.8 nm, which is basically in accordance with the transmission electron micrographs discussed later

The shape of the nanocomposite was investigated by FE-SEM and results are shown in Figure 4.3. Figure 4.3a,b shows that the FE-SEM micrograph of Fe_3O_4 and Fe_3O_4 -GG nanocomposite, which has a nearly uniform and spherical shape with homogeneous dispersed. In both micrograph size of the nanoparticles almost same while some smaller and bigger size of the nanoparticles is also seen in images. To overcome this problem, later on, we are investigating TEM analysis for determining the size of the nanoparticles. In FE-SEM analysis, the magnetic nanoparticles were characterized using energy dispersive X-ray (EDX) analysis in order to identify the elemental components of the sample. Figure 4.3c shows the EDX spectrum of Fe_3O_4 -GG, which shows that various compositions were recorded. The effect illustrates strong peaks for Fe, C and O. The quantitative analysis indicated the molar presence of carbon (72.81%), oxygen (9.09%) and iron (18.08%) in the nanocomposite. Figure 4.3(d-f) shows energy dispersive study Fe_3O_4 -GG nanocomposite indicates the

distribution of different element in different colour. That confirms well distributed of the element present in the nanocomposite.

From the TEM analysis, we confirm the particles size and morphology of nanocomposite. Figure 4.4 shows the TEM analysis of Fe_3O_4 nanoparticles and Figure 4.6. Shows GG coated Fe_3O_4 nanocomposite. As we can see from the obtained micrograph, the prepared Fe_3O_4 nanoparticles and Fe_3O_4 -GG nanocomposite are spherical in nature and some particles agglomerate, which is due to their high density and high specific surface area. The average particle size of Fe_3O_4 is 3.4 nm shown in Figure 4.5 whereas, Figure 4.7 shows the distribution analysis for Fe_3O_4 -GG and found to be 6.1 nm. After coating GG on the surface of Fe_3O_4 , the particle size increases, and aggregation of particles reduces. Figure 4.4b and Figure 4.6b show selected area electron diffraction study (SAED) of Fe_3O_4 and Fe_3O_4 -GG nanocomposite. In both, the case predicts a well-determined set of rings with bright spots. Which indicates both Fe_3O_4 and GG coated Fe_3O_4 nanocomposites are nanocrystalline in nature [271]. Figure 4.6c shows the Energy-dispersive study (EDS) micrographs of Fe_3O_4 -GG nanocomposite indicating the distribution of different elements like carbon, oxygen, and iron. Figure 4.6d demonstrate the distribution of all the element together and Figure 4.6(e-g) shows the element maps of Iron (Fe), carbon (C) and oxygen (O) individually. The elemental mapping confirms all the elements are well arranged.

The nitrogen sorption technique was performed to investigate the textural properties of Fe_3O_4 nanoparticles and Fe_3O_4 -GG nanocomposite. In this analysis, we found that the BET surface area, pore volume and pore size of the Fe_3O_4 nanoparticles is $220 \text{ m}^2/\text{g}$, $0.99 \text{ cm}^3/\text{g}$ & 6.5 nm and $158 \text{ m}^2/\text{g}$, $0.398 \text{ cm}^3/\text{g}$ & 15.5 nm for Fe_3O_4 -GG nanocomposite. In Figure 4.8a shows, the nanocomposite has type IV isotherm (According to IUPAC classification). As we can see from the Table 4.1 the surface area decrease after coating GG on the surface of Fe_3O_4 because large number of GG occupy the Fe_3O_4 nanoparticles surface and lower in surface area can attribute the increase in crystal size of the nanoparticles by applying the Scherrer formula [272-275]. The result shows the immobilization of GG on the surface of Fe_3O_4 nanoparticles. The BET surface area and BJH pore size distribution data confirm our prepared nanocomposite having mesoporous in nature and high surface area, these two properties having potential application in adsorption.

The magnetic property of Fe_3O_4 and Fe_3O_4 -GG nanocomposite were analyzed by vibrating sample magnetometer (VSM). Figure 4.8b shows the typical room temperature (298K) the saturation magnetization curves of bare Fe_3O_4 nanoparticles and Fe_3O_4 -GG can reach 51.95, 22.73 emu/g, (magnetic field $\pm 5000 \text{ G}$). As we can see from Figure 4.8b these two samples

show no remanence and coercivity. This indicates that the magnetic nanocomposites are paramagnetism in nature. However, the magnetic saturation value of the Fe_3O_4 -GG nanocomposite became lower as compare to Fe_3O_4 nanoparticles, because of its higher molecular weight of GG[254]. When an outside magnet was added, the Fe_3O_4 -GG nanocomposite was attracted rapidly to the place close to the magnet in a few minutes and the solution almost purified (inset in Figure8b). The result suggested that Fe_3O_4 -GG has good removal properties and could be easily separated from aqueous solution by using a magnetic field[276]

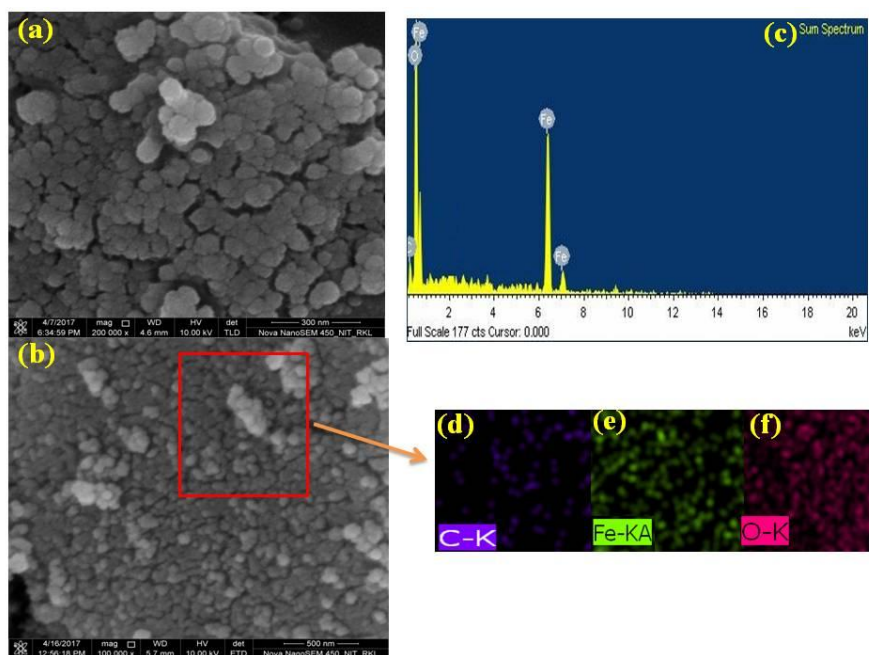


Figure 4.3 Field emission scanning electron microscopy (FE-SEM) images of (a) Fe_3O_4 , (b) Fe_3O_4 -GG nanocomposite, (c) EDX spectra of Fe_3O_4 -GG nanocomposite and (d,e,f) EDS data of Fe_3O_4 -GG nanocomposite.

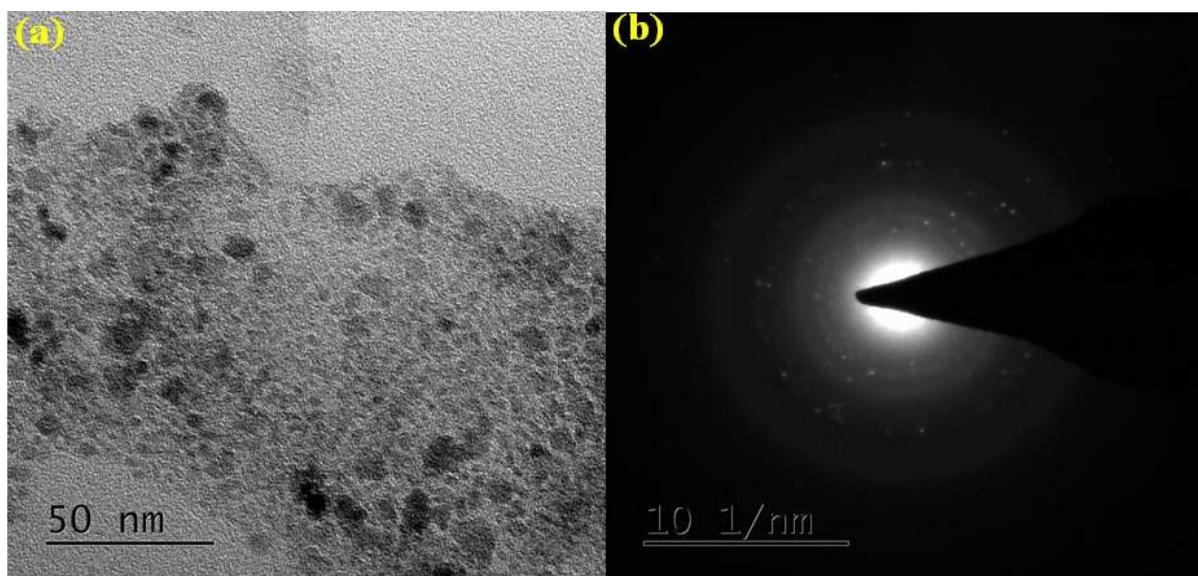


Figure 4.4 (a) TEM of Fe_3O_4 nanoparticles and (b) SAED pattern of Fe_3O_4 nanoparticles.

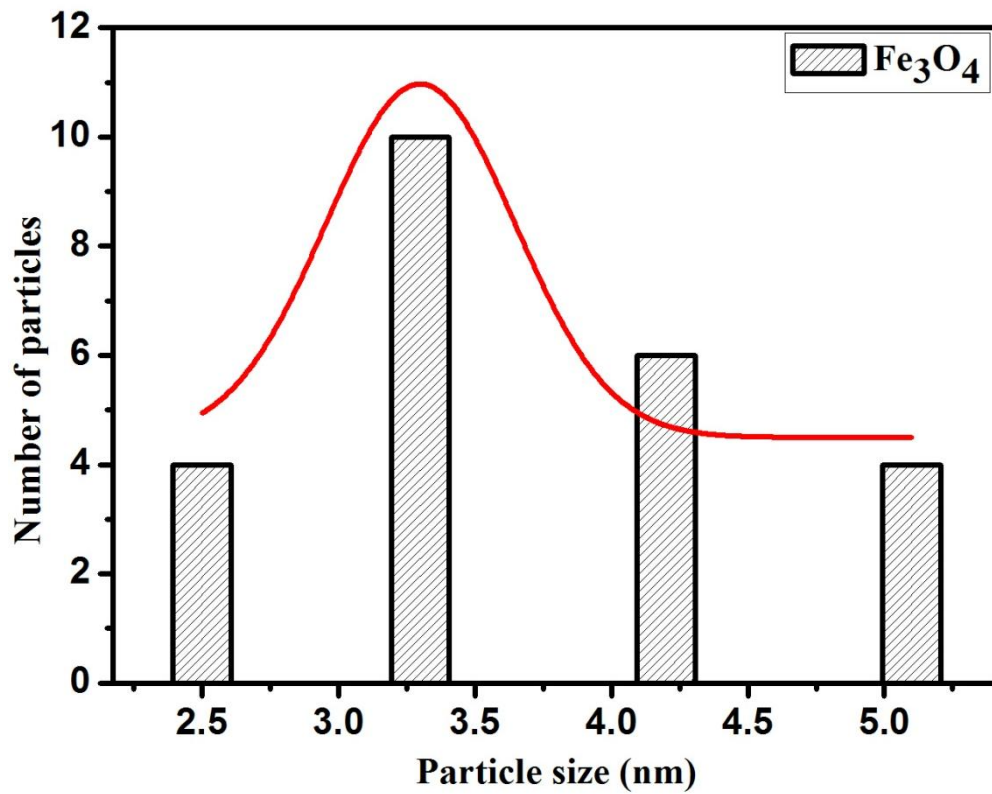


Figure 4.5 Histogram of the particle size distribution of Fe₃O₄.

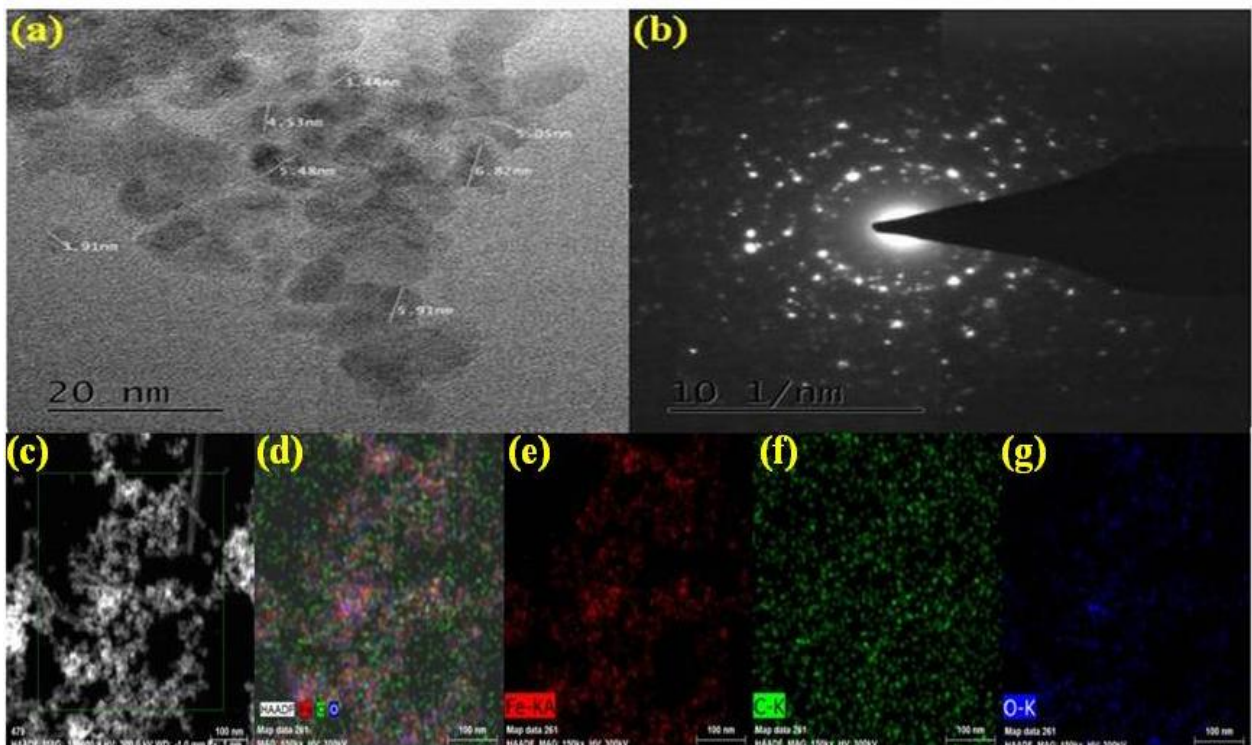


Figure 4.6 (a)TEM image of Fe₃O₄-GG nanocomposites, (b) SAED pattern.of Fe₃O₄-GG nanocomposites and (c) EDS mapping analysis of Fe₃O₄-GG nanocomposites.

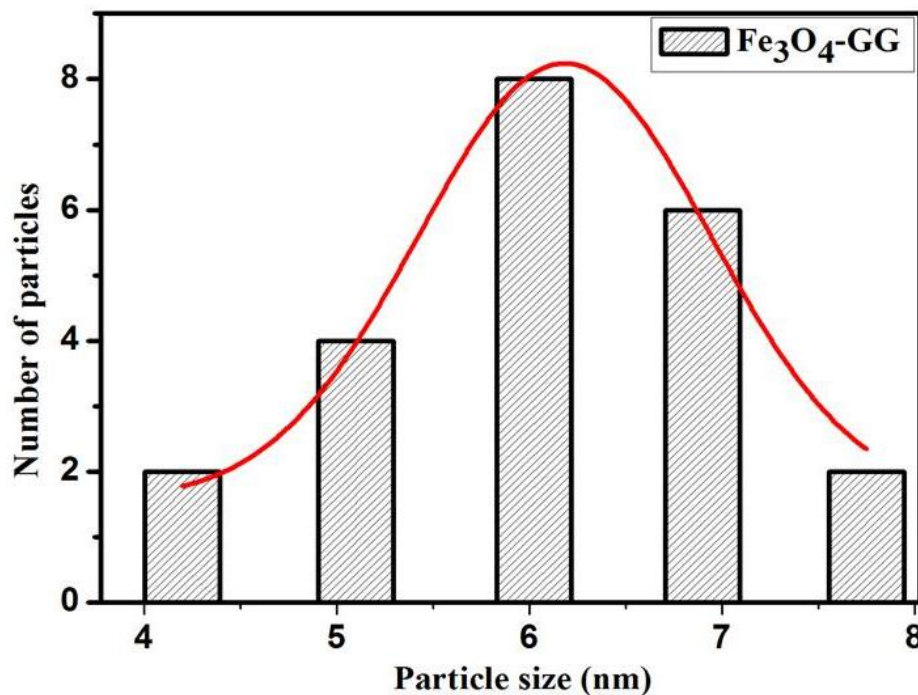


Figure 4.7 Histogram of the particle size distribution of Fe₃O₄-GG nanocomposite.

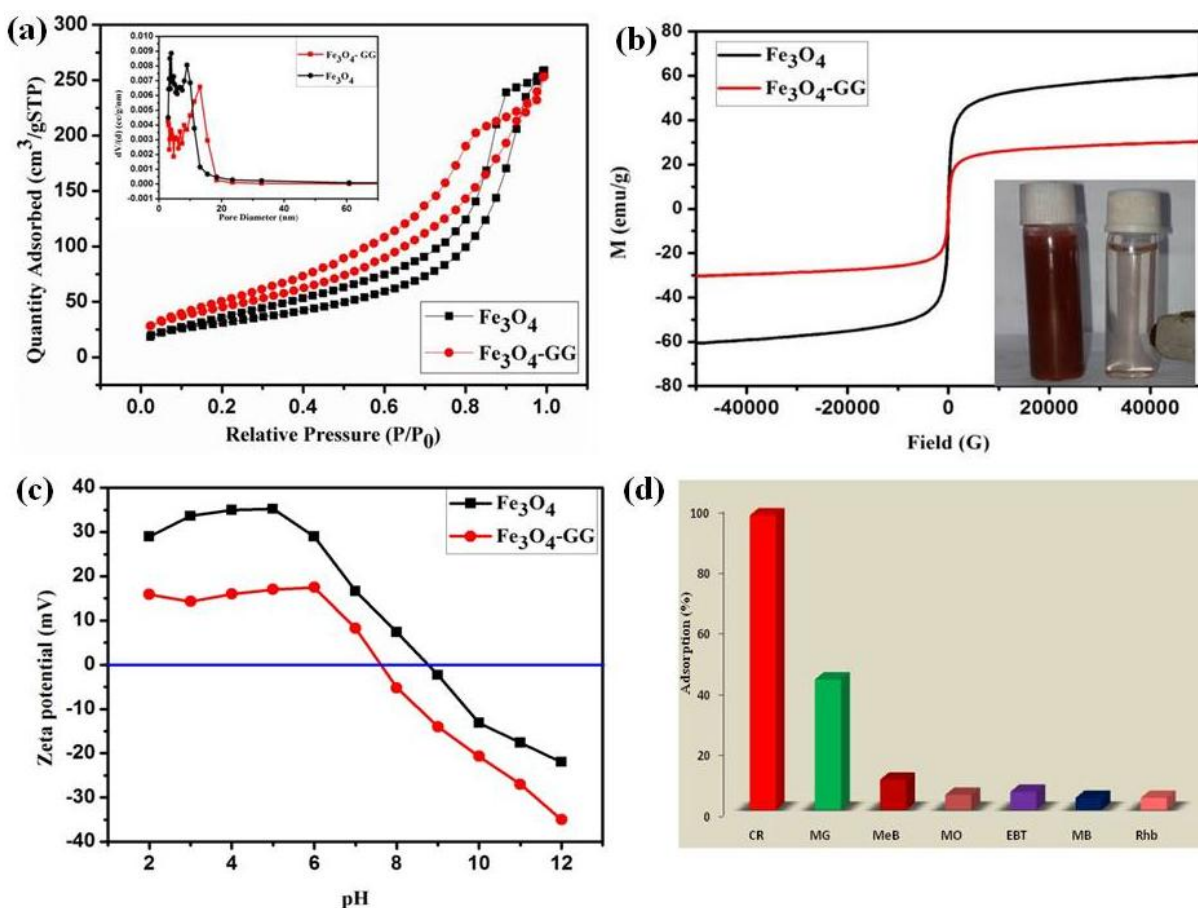


Figure 4.8 (a) N₂ adsorption-desorption isotherm of Fe₃O₄, Fe₃O₄-GG nanocomposite, (b) Magnetization curve of Fe₃O₄, Fe₃O₄-GG nanocomposite, (c) Zeta potential versus P^H of Fe₃O₄, Fe₃O₄-GG nanocomposite and (d) Preferential adsorption efficiency of different dyes on Fe₃O₄-GG nanoparticles.

Table 4.1 BET surface area, pore volume and pore size of Fe₃O₄ and Fe₃O₄-GG nanocomposite.

Sample	BET Surface Area (m ² /g)	Pore Volume (cm ³ /g)	Pore Size (nm)
Fe ₃ O ₄	220	0.99	6.5
Fe ₃ O ₄ -GG	158	0.398	15.5

Zeta potential measurement as a function of pH has been performed to confirm the surface charge properties. The Zeta potential data of Fe₃O₄ and Fe₃O₄-GG at different pH is shown in Figure 4.8c. The Fe₃O₄ magnetic nanoparticles have a positive charge at lower pH which decreases with increase in pH and became negative after its isoelectric point. The isoelectric point of the Fe₃O₄ and Fe₃O₄-GG nanocomposite are found to be 8.8 and 7.5, respectively.

4.3.2 Preferential adsorption of different dyes.

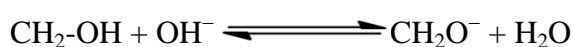
The removal efficiency of various dyes (40 mg/L) by Fe₃O₄-GG nanocomposite (150 mg adsorbent dose) is shown in Figure 4.8d. The observation indicates the preferential adsorption of the dyes containing the amino group (-NH₂) group such as Congo red (CR), which adsorbed with higher efficiency (~97% for CR) as compared to other available dyes like Malachite green (MG) (~43%), Methylene blue (MeB) (~11%), Methyl orange (MO) (~5%), Erichrome Black T (EBT) (~4%), Methyl blue (MB) (~5%) and Rhodamine B (Rhb) (~4%) on the magnetic nanocomposite surface. Fe₃O₄-GG nanocomposite contain surface hydroxyl group that can be easily bonded to the dyes (i.e., CR and MG) containing -NH₂ group can form hydrogen electrostatic bonding with the surface hydroxyl group of the prepared Fe₃O₄-GG nanocomposite, which leads to improvement of the adsorption efficiency of discussed dyes as compare to other dyes, without -NH₂ group. The most dominating mechanism for adsorption of organic dyes on polymer-coated Fe₃O₄ nanocomposite surface is due to the surface complexation via electrostatic interaction under solution conditions [277, 278].

4.3.3 Impact of different parameters on adsorption

Five various concentrations i.e. 20, 40, 60, 80, 100 mg/L to examine the effect of the initial concentration of CR dye onto adsorbent, and the result obtained at adsorbent dose 150mg, pH 6 and 25 °C (room temperature) are shown in Figure 4.9a. From this figure, it was observed that the percentage removal of CR 20 mg/L and 40 mg/L is approximately same but after increasing the concentration of the dye 40 mg/L to 100 mg/L, the removal efficiency decreased from 97.45 % to 51.49 % because the numbers of active binding sites were

saturated and the removal efficiency decrease[279]. The optimum dye concentration was an initiate to be 40 mg/L.

pH assumes as an important parameter to control the removal efficiency of CR dyes by the Fe₃O₄-GG nanocomposite. From Figure 4.9b, it is observed that about 97.58 % of CR (initial concentration 40 mg/L) is removed at pH 6. The isoelectric point of the Fe₃O₄-GG nanocomposite was found to be 7.5. The Fe₃O₄-GG nanocomposite has positive surface charge at pH < 7.5 and electrostatic interaction has occurred between the positive charge nanocomposite and negatively charged CR dyes. But pH > 7.5 the surface charge becomes more negative due to the presence of excess OH⁻ ions on the adsorbent surface as shown in the following equation.



Hence, there is a repulsive force existing in between the adsorbent surface and the negatively charged CR dye resulting in the reduction of the adsorption efficiency. Hence in acidic condition, anionic complexes are formed between anionic dye (CR) molecules and the cationic polymer functionalized magnetic adsorbent surface.

The effect of Fe₃O₄-GG adsorbent dose on the removal of CR dyes from aqueous solution is illustrated in Figure 4.9c. The maximum CR dye removal efficiency for 40 mg/L solutions are 61.3 %, 74.2 %, 81.6 %, 97.4 % and 97.5 % with different adsorbent dose 10mg, 50 mg, 100mg, 150 mg and 200 mg after 5 min, respectively. As shown in the graph the optimum adsorbent dose 150 mg, after which it reached equilibrium. The obtained results confirm that on increasing the amount of adsorbent dose, dye adsorption efficiency was also increased due to the availability of more adsorbent surface area [258, 262].

The effect of Fe₃O₄-GG adsorbent dose on the removal of CR dyes from aqueous solution is illustrated in Figure 4.9c. The maximum CR dye removal efficiency for 40 mg/L solutions are 61.3 %, 74.2 %, 81.6 %, 97.4 % and 97.5 % with different adsorbent dose 10 mg, 50 mg, 100 mg, 150 mg and 200 mg after 5 min, respectively. As shown in the graph the optimum adsorbent dose 150 mg, after which it reached equilibrium. The obtained results confirm that on increasing the amount of adsorbent dose, dye adsorption efficiency was also increased due to the availability of more adsorbent surface area [258, 262].

Contact time is one of the essential factors in the design of an economical adsorption system. Figure 4.9d reveals that dye uptake initial rate increase sharply with time and attained equilibrium (97.5 %) within 5 min for CR dyes. This phenomenon shows that monolayer

exposure of dye molecule at the external interface of then a composite is formed during the adsorption process. The initial higher rate of removal is due to the larger surface area as well as the abundant active binding site of the nanocomposite[280, 281]. After maximum removal, the adsorption rate was controlled by the rate of dye transport from external to internal pores of the nanocomposite materials.

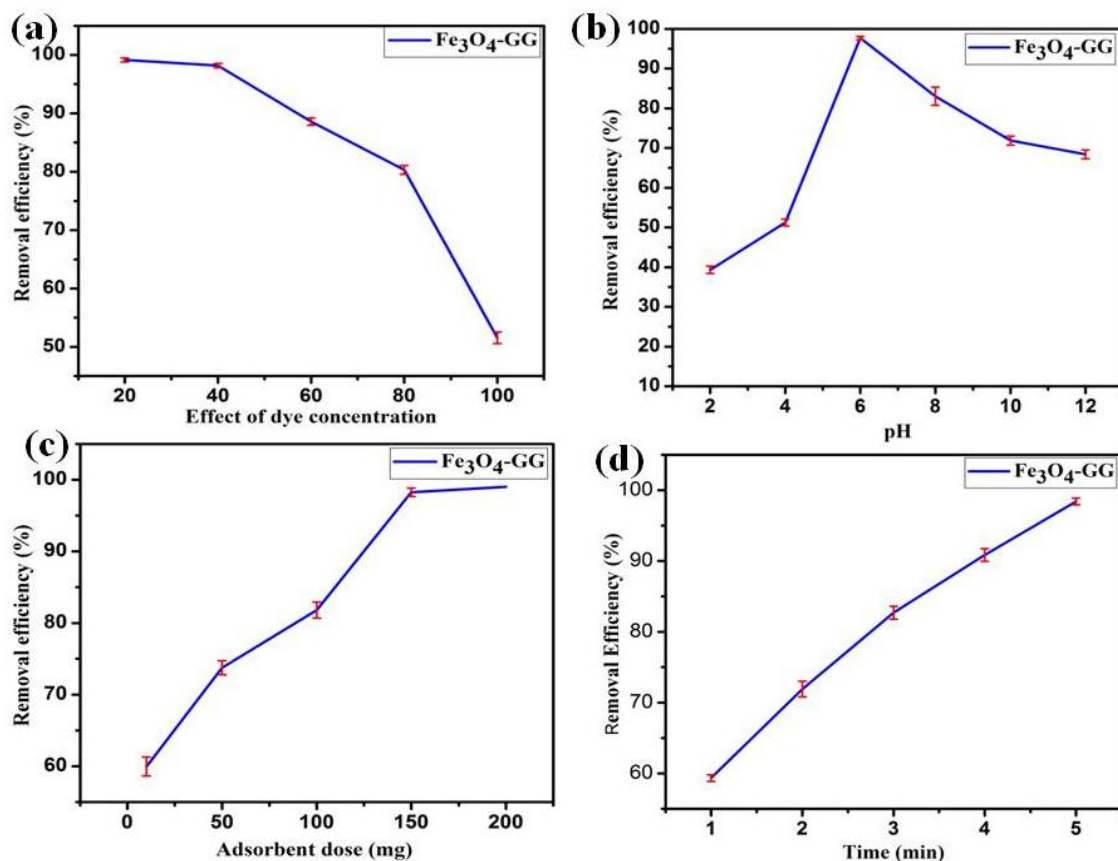


Figure 4.9 (a) The removal of CR at different concentrations (b) Effect of pH on the removal efficiency. The concentration of the adsorbent was 150 mg and the initial concentration of dye solution was 40 mg/L. (c) Effect of adsorbent dosage on adsorption CR. (d) Effect of time on adsorption of CR.

4.3.4 Adsorption Kinetics

It investigates to understand the mechanism of adsorption process well on contact time. Two kinetic models (pseudo-first-order and pseudo-second-order) are illustrated in Figure 4.10 and the parameters are listed in Table 4.2. The kinetic models well fit with the pseudo-second-order model because due to higher R^2 value as compare to pseudo-first-order model. Our adsorption process follows pseudo second-order model and is dependent on the amount of dye adsorbed on the surface of Fe₃O₄-GG nanocomposite at equilibrium. Generally, the pseudo-first-order is applicable to initial stage of adsorption that's why this model does not well fit with the whole range of contact time[262, 282]. From the above the kinetic data, we

confirm the adsorption process is due to chemisorptions which involved valence forces between dye anion and adsorbent.

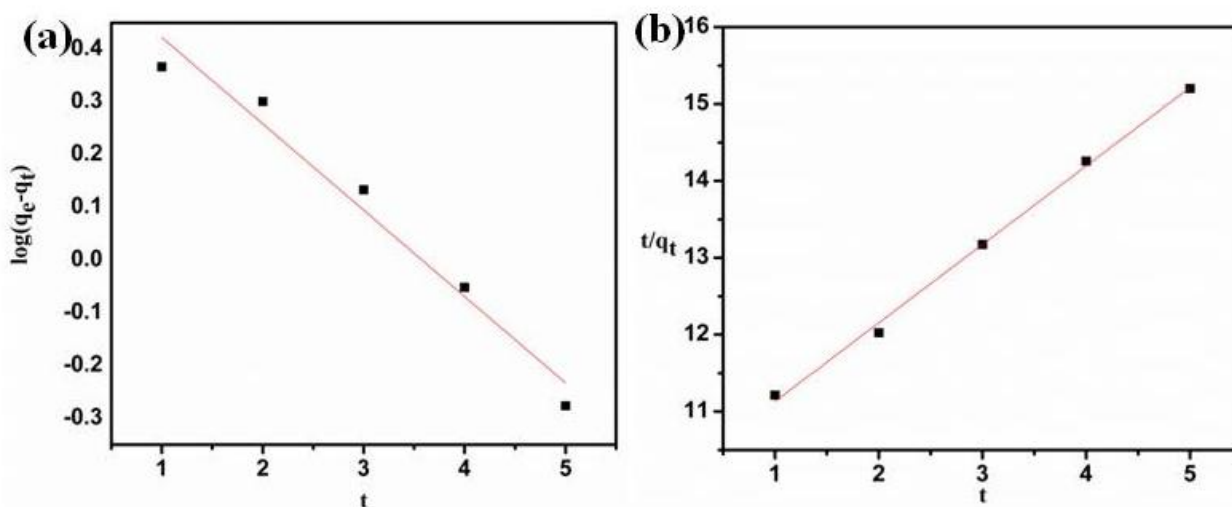


Figure 4.10 Kinetic model parameters of CR on Fe₃O₄-GG (a) Pseudo first-order kinetic model and (b) Pseudo second-order kinetic model.

Table 4.2 Kinetics parameters for CR dye adsorption on Fe₃O₄-GG.

Initial dye concentration (mg/L)	Pseudo 1 st kinetic order			Pseudo 2 nd kinetic order		
	q_e mg/L	K_1	R^2	q_e mg/L	K_2	R^2
40 mg/L	3.85	0.07	0.95	5.26	2.71	0.99

4.3.5 Adsorption Isotherm

Five adsorptions isotherm model, Langmuir, Freundlich, Temkin, D-R plot and Elovich isotherm models are illustrated graphically in Figure 4.11 and the isotherm parameters are listed in Table 4.3. From the obtained R_L value within the range 0 to 1, which confirm the adsorption process of CR on Fe₃O₄-GG was favorable at the condition being studied. However, the initial concentration increases from 20 to 100 mg/L as the R_L value decreases (Fig. 11b.). From the Freundlich isotherm, the values of $1/n$ less than 1 represent favorable adsorption[283]. The smaller value of the Temkin constant (B_1) suggested that adsorption of CR on Fe₃O₄-GG is favorable. The highest Coefficient of correlation (R^2) value regarded as the well fit of isotherm model. The comparison of coefficients indicates that the Langmuir isotherm fit more precisely ($R^2 = 0.98$) than the Freundlich isotherm ($R^2 = 0.96$), Temkin isotherm ($R^2 = 0.92$) Elovich isotherm (0.91) and Dubinin–Radushkevich isotherm ($R^2 = 0.97$). The Langmuir adsorption isotherm model assumes that monolayer formation in between CR on the surface of Fe₃O₄-GG nanocomposite[284].

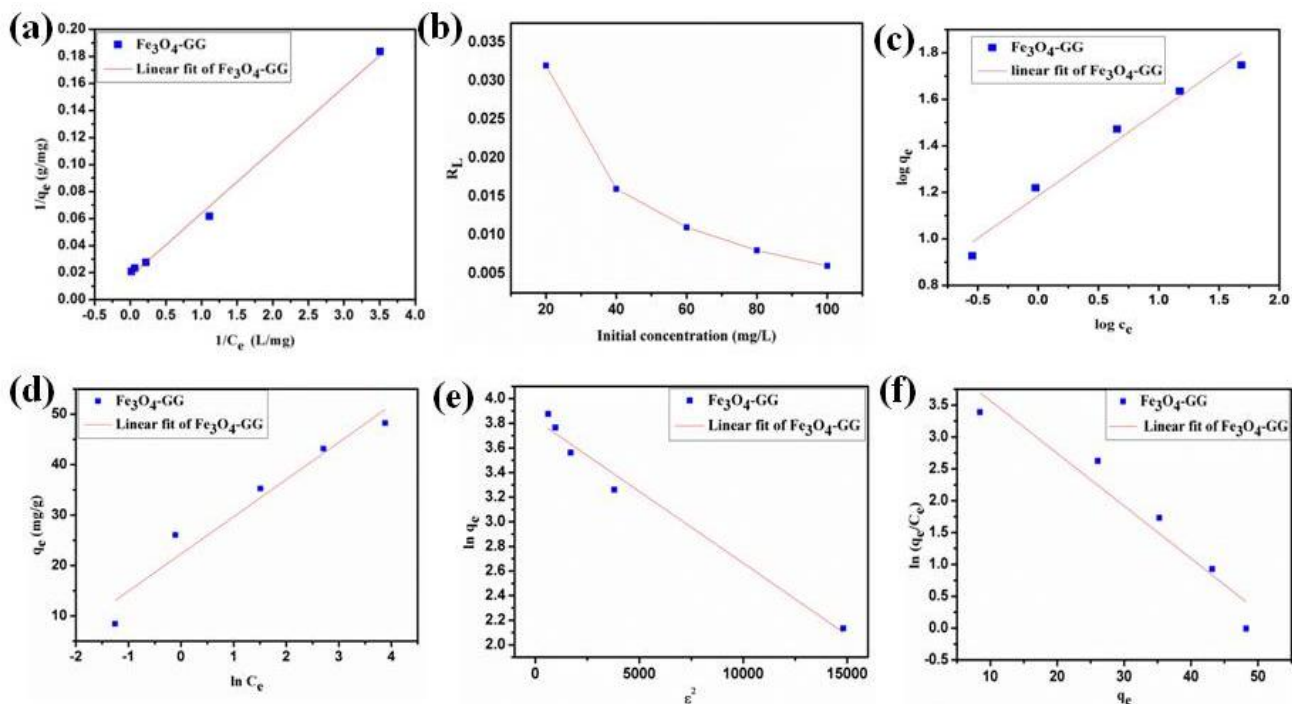


Figure 4.11 (a) Langmuir isotherm plot, (b) Effect of the initial concentration for CR adsorption on $\text{Fe}_3\text{O}_4\text{-GG}$, (c) Freundlich isotherm plot, (d) Temkin isotherm plot (e) Dubinin-Radushkevich isotherm plot and (f) Elovich isotherm plot of CR on $\text{Fe}_3\text{O}_4\text{-GG}$.

4.3.6 Comparative study of adsorption capacity with different adsorbents

The comparison study of highest adsorption limit of $\text{Fe}_3\text{O}_4\text{-GG}$ nanocomposite with reported adsorbents has been examined to understand the effectiveness of the prepared nanocomposite as an adsorbent for the removal of anionic CR dye from aqueous solution. Table 4.4 reflects that q_{max} of synthesized $\text{Fe}_3\text{O}_4\text{-GG}$ (60.24 mg/g for CR) is substantially higher than that of other reported adsorbents toward CR dye. This result indicates that $\text{Fe}_3\text{O}_4\text{-GG}$ nanocomposite can be considered as a better adsorbent for the uptake of CR dyes from aqueous solution. As stated above in Table 4.4, CR has a higher adsorption rate with Palm Kernel seed coating material but the disadvantage of the material is that it cannot be regenerated for multiple applications. Whereas, overcoming the said disadvantage, our GG-based Fe_3O_4 nanocomposite can be regenerated for several cycles with an almost similar efficiency that can show in Figure 4.8d [182, 239, 285, 286].

4.3.7 Regeneration of dye-loaded adsorbent

The reusability of the nanocomposite ($\text{Fe}_3\text{O}_4\text{-GG}$) was loaded with 40 mg/L CR dye solution (pH=6) mixed with 150 mg of $\text{Fe}_3\text{O}_4\text{-GG}$ nanocomposite for 5 min. The dye-loaded sample was filtered and dried completely. Afterward, the adsorbent was washed with ethanol and several times with deionized water [287]. Five successive adsorption-desorption cycles were performed to find out the repeated use of the adsorbent as an efficient adsorbent as shown in Figure 4.12.

Table 4.3 Isotherm parameters for the adsorption of CR on to Fe₃O₄-GG at room temperature (300 K) and initial dye concentration 40 mg/L

Isotherm Model	Parameters
Langmuir	q_m (mg/g) = 60.24
	b (L/mg) = 1.47
	R_L = 0.016
	R^2 = 0.99
Freundlich	K_f = 15.13
	n = 2.77
	R^2 = 0.96
Temkin	K_T (L/mg) = 20.58
	B_1 = 7.373
	R^2 = 0.92
Dubinin-Radushkevich	q_m (mg/g) = 46.08
	K (mol ² K/ J ²) = -1.1674×10^{-4}
	E = 65.93
	R^2 = 0.97
Elovich	K_E = 6.63
	q_m = 12.19
	R^2 = 0.91

Table 4.4 Comparison of adsorption efficiency of Fe₃O₄-GG nanocomposite for removal of Congo red dye with different adsorbents.

Dye	Adsorbent	q_{max} (mg/g)	Reference
Congo red	Magnetically modified fodder yeast cell	49.7	[239]
Congo red	Chitosan/montmorillonite nanocomposite	54.52	[281]
Congo red	Chitosan coated magnetic iron oxide	42.62	[182]
Congo red	Palm Kernel seed Coat	66.23	[286]
Congo red	Fe ₃ O ₄ -GG nanocomposite	60.24	Present Study

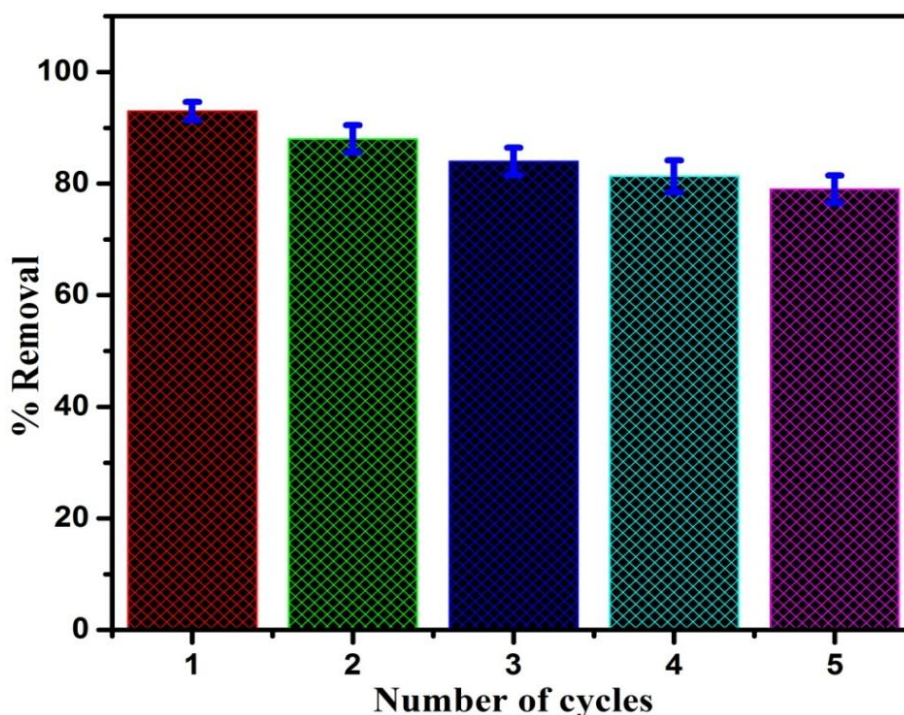


Figure 4.12 Reusability of the adsorbent

4.4 Summary

A simple method has been developed for covalently coating GG on to the surface of Fe_3O_4 nanoparticles by using low-toxic and cost-effective precursors. The dye CR was adsorbed in much higher amounts as compared to MG, MeB, MO, EBT, MB, and Rhb. The preferential adsorption phenomena could attribute to the presence of $-\text{NH}_2$ groups present in CR dye, which can bind easily with the surface hydroxyl groups of GG coated magnetite nanoparticles. The optimum concentration of Fe_3O_4 -GG nanocomposite is 150 mg/L, while the initial dye concentration 40 mg/L at pH 6. Due to the paramagnetic behavior of prepared nanocomposite, the magnetic adsorbent can be easily separated dye by using a small magnet. The result indicates the removal of CR is over 97 %. There are several advantages of the nanocomposite plays a crucial role for dye adsorption such as higher surface area, easy separation by exposing magnet, hydrodynamic volume, and controlled growth of guar-gum coated Fe_3O_4 nanocomposite as well as multiple numbers of H-bonding sites of nanocomposite with dye molecules. The optimum concentration of Fe_3O_4 -GG is 150 mg/L, while the initial concentration of CR is 40 mg/L at pH 6. The result indicates the removal of CR is over 97 %. In addition, the adsorption capacity can be affected by ionic strength. The equilibrium data were found to be better fits with the pseudo-second-order kinetics and Langmuir adsorption isotherm model. Finally, the cycling performance of adsorbent contributes a significant accomplishment toward sustainable improvement towards the dye-polluted water.

Chapter 5

5. An investigation of heavy metals adsorption by hexadentate ligand modified magnetic nanocomposite.

5.1 Introduction

Water contamination arises because of the aimless removal of toxic metal ions and organic contaminants, which is currently a rising concern in environmental science. For example, industrial units based on metallurgical, mining and chemical are the main source of wastewater as they discharge toxic entities[9, 288]. For environmental safety, it is required to remove these metal contaminants from the toxic contaminated water before releasing into the aquatic environment[289]. Disposal of toxic contaminants from the wastewater not only protect the environment but also stop in entering the food chains. Up to now, Traditional techniques have been developed for the removal of toxic metal ions from wastewater such as co-precipitation[290], membrane filtration[291], ion exchange[292], biosorption[293], electro-coagulation[294], electrodialysis[295] and adsorption[232]. Among all these established, adsorption is a promising process for removal of heavy metals from contaminated water. A few adsorbents that have been examined for metal removal including activated carbon(AC)[296], zeolite[297], resins[298] and inorganic materials[299, 300]. However, these adsorbents have been suffering from demerits like low adsorption capacities or low efficiencies. Therefore, a serious effort has been made to seek novel adsorbents and acquire new methods with passage of time. Nanotechnology and nanomaterials have gradually been investigated permanently in this aspect.[301-304] The ease of the use of nanomaterials are concentrated around improved reactivity, higher surface area and sequestration characteristics. So far, an array of nanomaterials are employed in research and development and each displaying an unique attribute that have perspective application in the purification of industrial discharge, ground water, drinking water and surface water[305].

Magnetic nanoparticles particularly Fe_3O_4 has been in focus due to its magnetic segregation properties and potential application in different research areas, such as supercapacitor electrode materials[14, 306-313], heavy metal adsorption[314], catalytic oxidation of alcohols[315], magnetic carriers for protein separation[316] and wastewater treatment[317-319]. Moreover, Fe_3O_4 nanoparticles with different morphologies may show unique physical

Jitendra Kumar Sahoo, Aniket Kumara, Lipeeka Rout, Juhi Rath, Priyabrat Dash and Harekrushna Sahoo* Separation Science and Technology, 2017, 53, 863-876.*

and chemical properties, such as a specific surface area and unique lattice plane[320], Still, diverse Fe₃O₄ nanoparticles with miscellaneous morphologies, including sphere, cube, wire, tube, polyhedron, core-shell structure, and ring have been synthesized[321-325]. For example, Bayou Geng et al. synthesized single-crystalline Fe₃O₄ nanotubes maneuvering egg albumin as a nanoreactor[326], Kok Chung Chin et al. synthesized Fe₃O₄ nanosheets by oxidizing Fe substrates in a low pH solution on a hot plate[327]. Xiyan Li et al. prepared single-crystalline triangular Fe₃O₄ nano prisms via a hydrothermal route and also porous flower-shaped[328].

Silica gel, inorganic materials are used for water treatment, which can be modified chemosynthetically by incorporating functional groups following silanization method to improve its removal efficiency. In addition, other advantages of silica gel are local availability, high surface area of about 600 m²/g and high thermal resistance[329, 330]. Although modified silica gels effectively can remove trace elements such as Cu, Zn, Fe, Cd, Pb, and Mn from polluted water[329, 330]. However, all of the silica-bound ligands could not reverse the metal binding and the regeneration of spent adsorbent became complicated[331, 332].

Linking agents, for example, ethylene diamine tetraacetic acid (EDTA), are widely used as extractive reagents for heavy metals removal[333]. Due to its low cost and strong metals linking ability, EDTA has been used to functionalized variety of materials such as chitosan[334], mercerized cellulose and sugarcane bagasse[335], polystyrene[336], silica gel[337], polyamine composites[338] ker's yeast biomass[339] and rice husk[340]. Keeping an eye on the above difficulties, in the current study, silica gel was functionalized with metal chelating agents such as ethylene diamine tetraacetic acid (EDTA) prior to their use as adsorbents. The chelating agents are presumed to have the ability to form stable complex or interaction with target metals and reverse the metal-binding after being treated chemically. The aim of this study was to investigate the performance of FAE nanocomposite for the removal of heavy metal ions (Pb²⁺, Cd²⁺, Ni²⁺, Co²⁺, and Cu²⁺) from contaminated water. Effect of pertinent factors such as adsorbent dosage, pH, contact time and initial metal ions concentration were studied. The Langmuir, Freundlich, Temkin and Elovich models were employed to simulate their adsorption isotherm. The adsorption mechanism of metal ions removal by adsorbent and reusability of the nanocomposite are also presented.

5.2 Batch adsorption study

Batch experiments were carried out at room temperature (25 °C) under the optimum condition of all adsorption parameters such as adsorbent dosage, pH, initial heavy metal ions

concentration, and contact time. All the experiments were conducted by taking under consideration different concentration of heavy metals (Pb^{2+} , Cd^{2+} , Ni^{2+} , Co^{2+} , and Cu^{2+}) in a series of 200 mL poly-lab plastic bottles fitted with cap. The reaction bottles were incubated at 25 ± 5 °C in a thermostatic shaker (SELEC RC5100) at 250 rpm. Adsorbent dose for different heavy metals is not constant. Distilled water was used throughout the experiment. After adsorption, the adsorbents are separated by External magnetic field. The concentration of heavy metals in the residual solution is analyzed by atomic absorption spectroscopy. The percentage removal and uptake capacity of heavy metal ions are evaluated by using the following equation:

$$\% \text{ Adsorption} = \frac{C_o - C_e}{C_o} \times 100 \quad (5.1)$$

And the equilibrium uptake was calculated using Eq. (5.2):

$$q_e = (C_o - C_e) \times \frac{V}{W} \quad (5.2)$$

Where C_o is the initial concentration of dye solution (mg/L), q_e is the equilibrium capacity of dye on the adsorbent (mg/g), C_e is the equilibrium concentration of dye solution (mg/L), W is the weight of adsorbent (g) used and V is the volume of dye solution used (L). All experiments have been done in triplicates and the results are represented as average readings.

5.3 Results and discussion

5.3.1 Adsorbent characterizations

XRD patterns showing the phase purity of Fe_3O_4 , Fe_3O_4 -APTES, and Fe_3O_4 -APTES-EDTA nanocomposite are indicated in Figure 5.1A. All detected diffraction are indexed with the standard XRD pattern of face-centered cubic (fcc), Fe_3O_4 (JCPDS no 65-3107), which indicates the high purity of Fe_3O_4 . The main peaks for Fe_3O_4 nanoparticles observed at $2\theta = 30.09^\circ$, 35.42° , 43.05° , 56.94° , and 62.51° . The diffraction peaks for Fe_3O_4 -APTES and Fe_3O_4 -APTES-EDTA are similar to the Fe_3O_4 nanoparticles, which reveal the crystal structure of Fe_3O_4 is well-maintained after the coating of APTES and EDTA [206, 341, 342]. The absence of peaks at 110 ($2\theta=21.22$) and 104 ($2\theta=33.15$) indicate that both goethite and hematite α - Fe_2O_3 are not formed in the prepared samples [343]. The XRD pattern for Fe_3O_4 -APTES and Fe_3O_4 -APTES-EDTA revealed that after coating with APTES and EDTA, the phase of Fe_3O_4 did not change. Moreover, it was identified that the coating process was insufficient to seed growth and thus didn't affect the physical properties of the magnetite particles. The XRD data indicated towards high crystallinity of Fe_3O_4 -APTES-EDTA

nanocomposite. The average core size can be evaluated from the XRD result by Scherrer formula:

$$D = \frac{0.94\lambda}{B \cos \theta} \quad 5.3$$

Where D is the average crystalline diameter, 0.94 is the Scherrer constant, λ is the X-ray wavelength, B is the angular line width of half-maximum intensity and θ is the Bragg's angle in degree. Here, the (311) peak of the highest intensity was picked out to evaluate the particle diameter of Fe_3O_4 , $\text{Fe}_3\text{O}_4\text{-APTES}$, and $\text{Fe}_3\text{O}_4\text{-APTES-EDTA}$, and the D was calculated to be 8.15 nm, 18.24 nm, and 38.17 nm.

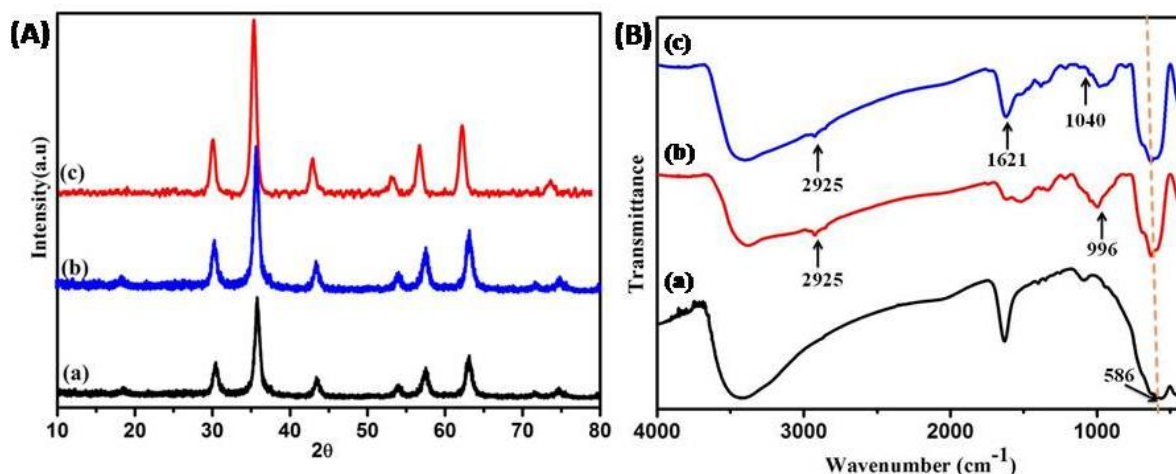


Figure 5.1 (A) XRD patterns for (a) Fe_3O_4 , (b) $\text{Fe}_3\text{O}_4\text{-APTES}$ and (C) $\text{Fe}_3\text{O}_4\text{-APTES-EDTA}$ (B) FTIR spectra of (a) Fe_3O_4 , (b) $\text{Fe}_3\text{O}_4\text{-APTES}$ and (C) $\text{Fe}_3\text{O}_4\text{-APTES-EDTA}$.

The surface characteristic of a functional group present on Fe_3O_4 magnetic nanoparticle is characterized by using Fourier-transform infrared (FTIR) spectroscopy. Figure 5.1B shows the FT-IR spectra of Fe_3O_4 , $\text{Fe}_3\text{O}_4\text{-APTES}$, and $\text{Fe}_3\text{O}_4\text{-APTES-EDTA}$ magnetic nanocomposite. In Figure 5.1B, the strong IR band at 586 cm^{-1} is the characteristic absorption of Fe-O bond, which confirms that magnetite nanoparticle [342, 344]. In Figure 2b, we observe 2925 cm^{-1} , 996 cm^{-1} , 1040 cm^{-1} , 1302 cm^{-1} , and 3360 cm^{-1} ascribe to the asymmetric stretching vibrations of CH_2 in alkyl chain, Si-O-Si group, C-N stretching, Free -NH_2 but after modification EDTA on $\text{Fe}_3\text{O}_4\text{-APTES}$ (Figure 2c), we observe two new peaks around 1621 cm^{-1} and 2925 cm^{-1} corresponds C=O stretching vibration of -COOH and C-H stretching respectively, indicating the existence of EDTA [305, 345-351]. From these changes shown in IR spectra, it can be reasonably concluded that Fe_3O_4 nanoparticles have been successfully modified with APTES and EDTA.

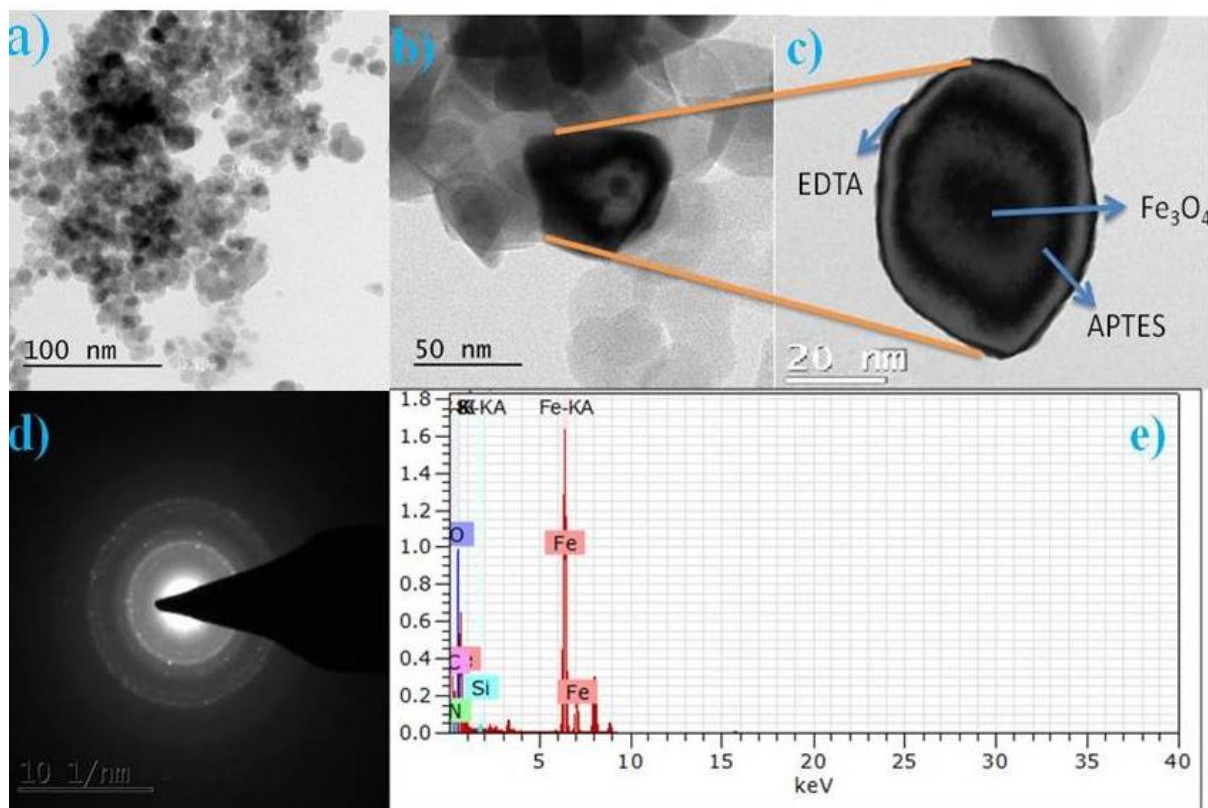


Figure 5.2 TEM of (a) Fe_3O_4 , (b,c) Fe_3O_4 -APTES-EDTA, (d) SAED pattern Fe_3O_4 -APTES-EDTA and (e) EDX analysis.

The morphology of the Fe_3O_4 and Fe_3O_4 -APTES-EDTA is characterized using a transmission electron microscope (TEM) presented In Figure 5.2a, it is visualized that Fe_3O_4 particles are monodisperse and average size about 12.15 nm, with an approximately spherical shape. After modification with APTES and EDTA, the TEM micrograph as shown in Figure 5.2b and, the obtained particle size was found to be 50 nm. Figure 5.2c shows the TEM image of a single Fe_3O_4 -APTES-EDTA particle with a core-shell structure. Moreover, the TEM images with higher resolutions (Figure 5.2c) reveal that the EDTA coating is relatively rough with sizes of 20 nm range. From TEM analysis we found that APTES and EDTA coating reduces the aggregation and simultaneously improves the particle distribution. In Figure 5.2c, we clearly observe there is three-layer of spherical particles we assume that the first layer is Fe_3O_4 and second layer is APTES and the third layer is EDTA. The Selected area electron diffraction (SAED) pattern shows the ring-like structure clearly indicates that our composite having crystalline nature (Figure 5.2d). From TEM analysis, the magnetic nanoparticles were analyzed using energy dispersive X-ray (EDX) in order to identify the elemental components. Figure 5.2(e) display the EDX spectrum of Fe_3O_4 -APTES-EDTA, which shows strong peaks for Fe, C, O, Si and N. The quantitative analysis indicated the molar presence of different composition i.e. iron (39.83 %), oxygen (35.17 %), carbon (11.37 %), silicon (9.73 %) and nitrogen (3.90 %) in the nanocomposite. Figure 5.3 shows the EDS mapping images of

Fe_3O_4 -APTES-EDTA nanocomposite indicating the spatial distribution of iron, oxygen, silicon, carbon, and nitrogen. Figure 5.3(a) represents the TEM image of the APTES and EDTA coated Fe_3O_4 nanocomposite which is to be analyzed in EDS mapping. Figure 5.3(b) displays the elemental mapping of all of different elements together, and Figure 5.3(c–g) display the elemental analysis of Fe, N, O, C, and Si individually. The elemental mapping results show that all elements were well arranged.

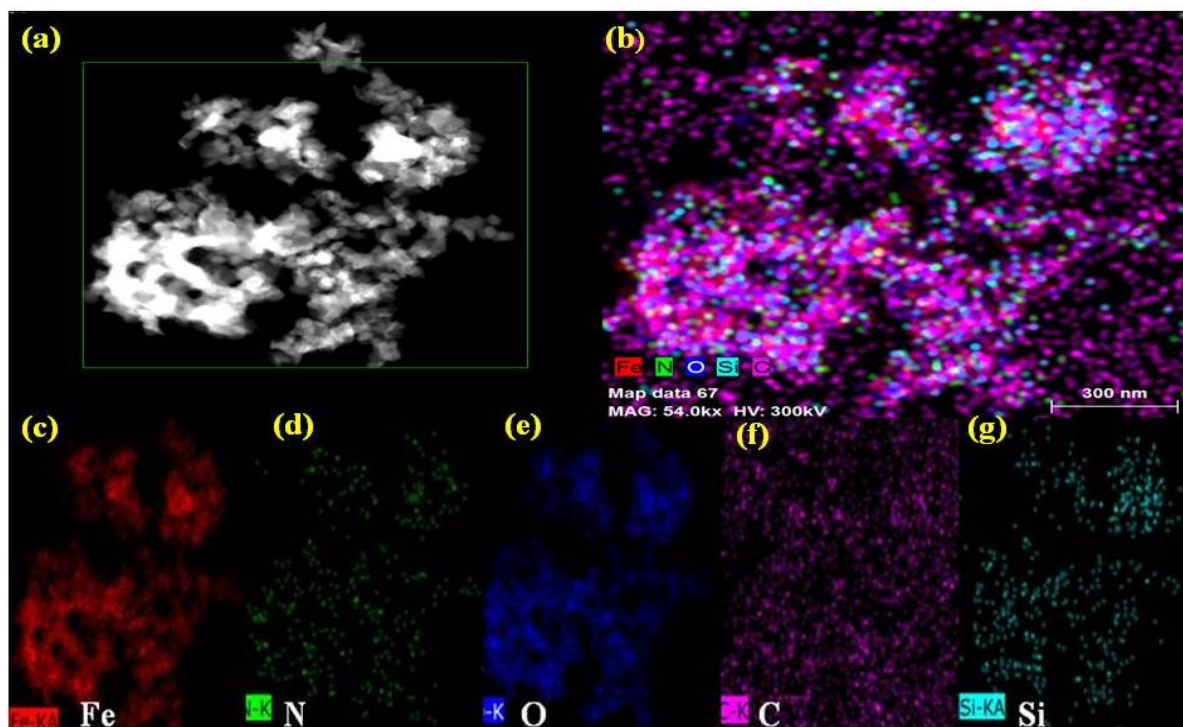


Figure 5.3 EDS mapping of Fe_3O_4 -APTES-EDTA.

The magnetic properties of Fe_3O_4 , Fe_3O_4 -APTES, and Fe_3O_4 -APTES-EDTA nanocomposite are analyzed by Vibrating sample magnetometer (VSM). Figure 5.4 shows the supermagnetization curves of Fe_3O_4 , Fe_3O_4 -APTES, and Fe_3O_4 -APTES-EDTA at room temperature with negligible coercivity and remanence. Maximum saturation super magnetizations from the hysteresis loop for the Fe_3O_4 , Fe_3O_4 -APTES, and Fe_3O_4 -APTES-EDTA nanoparticles were 55, 43 and 36 emu/g, respectively. Although the attachment of APTES and EDTA non-magnetic portion resulted in a decline in saturation of supermagnetizations in Fe_3O_4 nanoparticles, the obtained Fe_3O_4 -APTES-EDTA have a high saturation supermagnetization of 36 emu/g. According to Ma's study, a value of 16.3 emu/g supermagnetization is enough for magnetic separation with a magnet from solution.[352-356] These imply that Fe_3O_4 -APTES-EDTA adsorbents can be dispersed into water solution readily and the magnetic sorbent loaded with analytes can be isolated from

the matrix conveniently by using an external magnet. Once the external magnetic field is taken away, these sorbents can re-disperse rapidly.

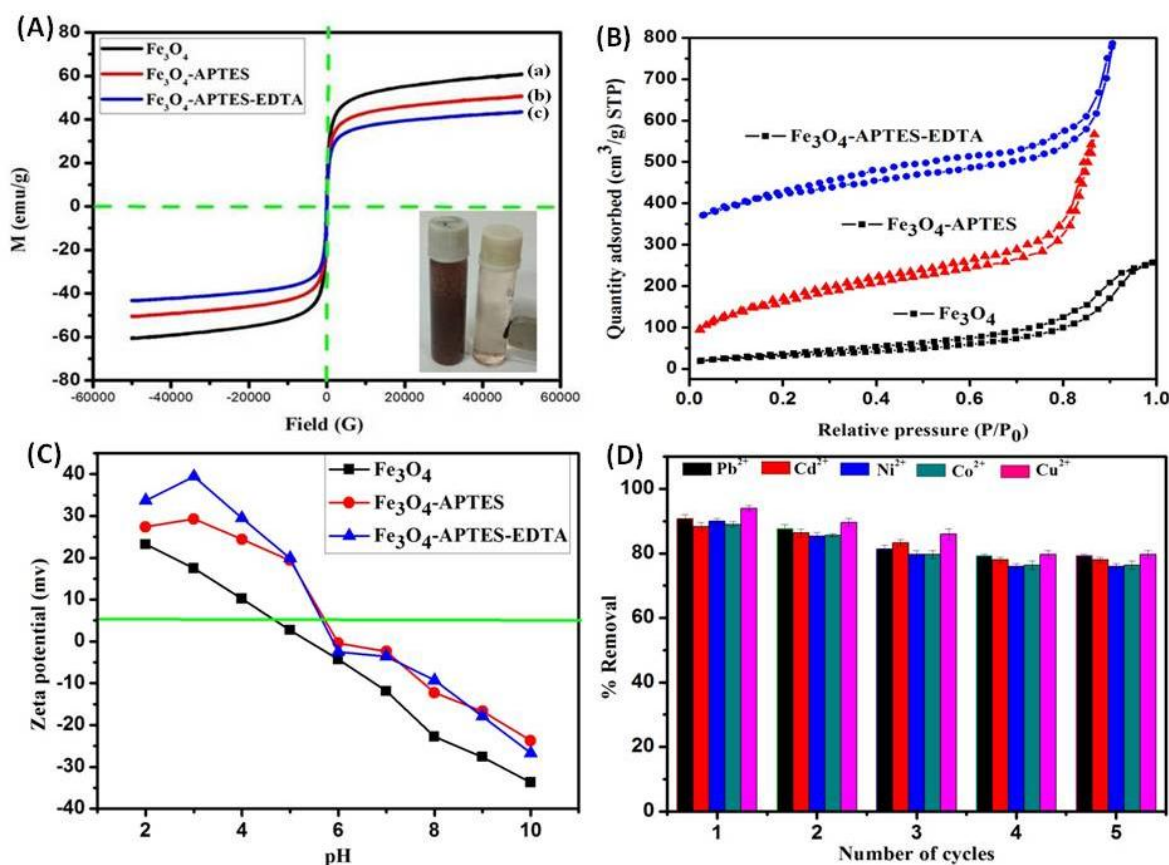


Figure 5.4 (A) Vibrating sample magnetometer (VSM) supermagnetization curves of (a) Fe_3O_4 , (b) Fe_3O_4 -APTES and (C) Fe_3O_4 -APTES-EDTA. (B) N_2 adsorption-desorption isotherms of (a) Fe_3O_4 , (b) Fe_3O_4 -APTES and (C) Fe_3O_4 -APTES-EDTA. (C) Zeta potential of (a) Fe_3O_4 , (b) Fe_3O_4 -APTES and (c) Fe_3O_4 -APTES-EDTA nanocomposite. (D) Reusability of the adsorbent.

Figure 5.4B represents the porous properties of the Fe_3O_4 , Fe_3O_4 -APTES, and Fe_3O_4 -APTES-EDTA were studied by N_2 adsorption-desorption method. It can be seen that the samples have type IV isotherms (as per IUPAC classification). The Brunauer-Emmett-Teller (BET) surface area of Fe_3O_4 , Fe_3O_4 -APTES, and Fe_3O_4 -APTES-EDTA was found to be 165, 105 and 67.2 m^2/g , respectively. As it can be observed from Table 5.1 that after coating APTES and EDTA on the surface of Fe_3O_4 , the surface area decreases that can be attributed to increase in the crystal size of the nanoparticles calculated by applying the Scherrer formula.[357]. Then the total pore size and volume were determined by the Barret, Joyner, and Halenda (BJH) method using desorption isotherms.[358] The result indicates that the Fe_3O_4 , Fe_3O_4 -APTES and Fe_3O_4 -APTES-EDTA powder have the total pore volume of 0.195, 0.398 and 0.475 cm^3/g and the total pore sizes were 2.4, 4.6 and 5.2 nm are displayed in Figure 5. The BET specific surface area and BJH pore size distribution analysis confirm our nano-composites having

mesoporous in nature and these higher surface areas and mesoporous have potential application in adsorption.

Table 5.1 BET surface area pore size and the pore volume of Fe₃O₄, Fe₃O₄-APTES, and Fe₃O₄-APTES-EDTAnanocomposite.

Sample	BET Surface Area (m ² g ⁻¹)	Pore Volume (cm ³ g ⁻¹)	Pore Size (nm)
Fe ₃ O ₄ -APTES-EDTA	67.2	0.475	5.2
Fe ₃ O ₄ -APTES	105	0.398	4.6
Fe ₃ O ₄	165	0.195	2.4

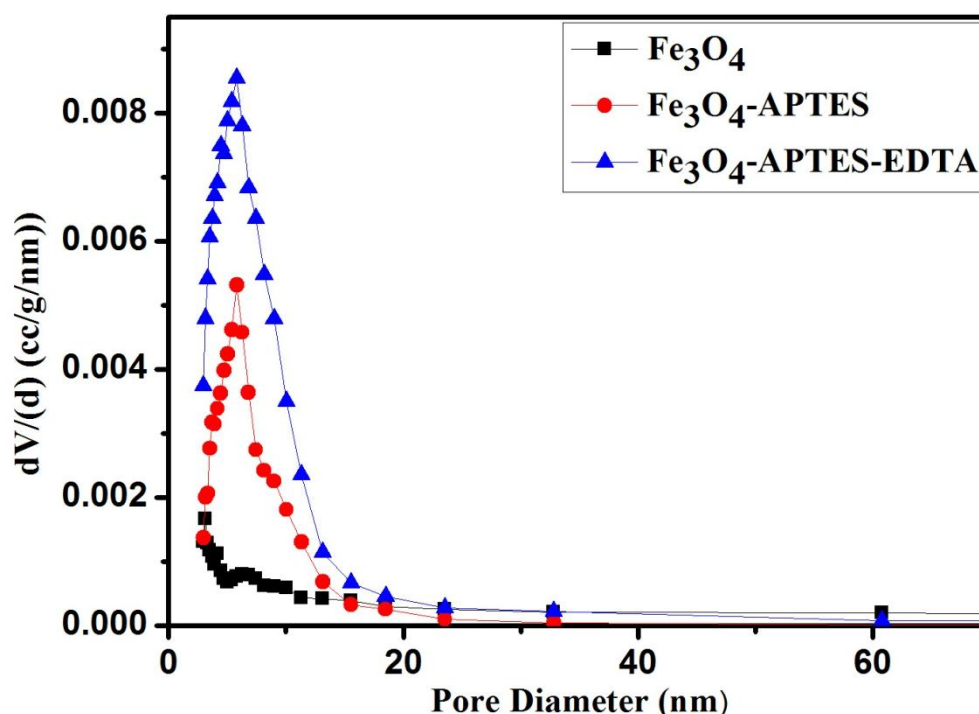


Figure 5.5 Pore size distribution curves of Fe₃O₄, Fe₃O₄-APTES, and Fe₃O₄-APTES-EDTAnanocomposite.

The TGA analysis of Fe₃O₄ and Fe₃O₄-APTES-EDTA nanocomposite is done in argon atmosphere as shown in Figure 5.6. The TGA curves of Fe₃O₄nanoparticles show a 3% weight loss up to 60-100 °C, followed by a further weight loss around 3.8% at 300 °C, and a slow decrease 1.3% in between 600 °C to 800 °C. These indicate loss of moisture, some of it more tightly bound. The curve for Fe₃O₄-APTES-EDTA, three weight loss steps at about 272, 395 and 610 °C, as demonstrated in the derivative curve, which can be ascribed to the decomposition of an amine group, the decomposition of EDTA and the complete oxidation of carbon respectively. The weight percentage of EDTA attached to Fe₃O₄-APTES can be

determined by the difference of initial and final mass of the sample in the TGA curve (Figure. 5.6) and was approximately 9% of the total mass of Fe₃O₄-APTES-EDTA. The high fraction of EDTA and porous surface structure possible many active binding sites for metal ion removal.[359] As a consequence, this nanocomposite can be effectively used for the adsorption purpose because a majority of adsorption experiments are mostly carried out below 35 °C.

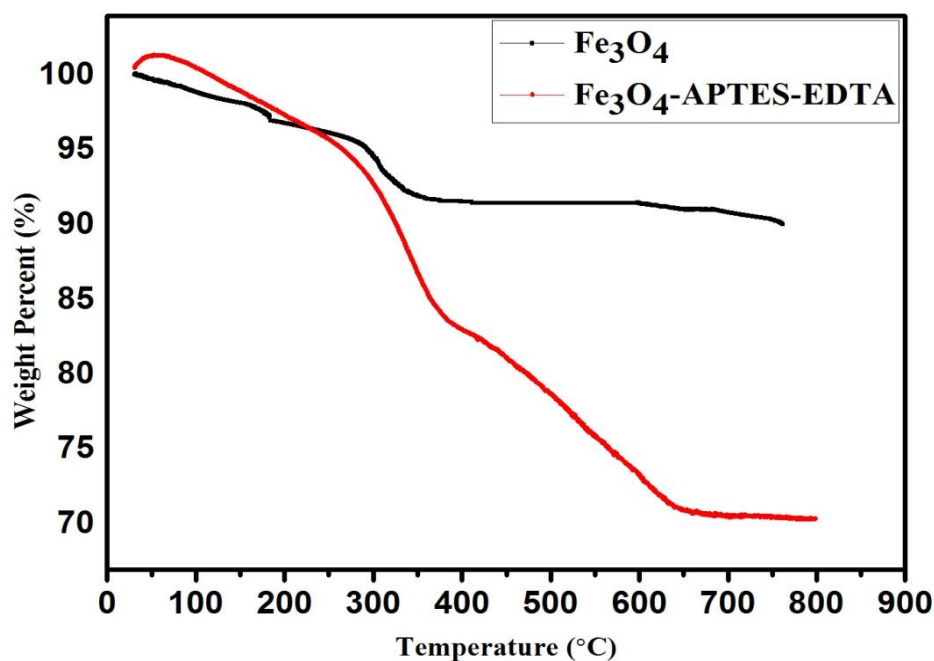


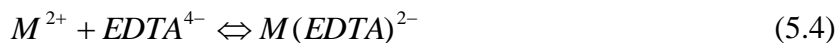
Figure 5.6 TGA curves of Fe₃O₄ and Fe₃O₄-APTES-EDTA.

Zeta potential measurement as a function of pH has been accomplished to confirm the surface charge properties. Figure 5.4c shows that the surface charges of Fe₃O₄, Fe₃O₄-APTES, and Fe₃O₄-APTES-EDTA at different pH. The Fe₃O₄ magnetic nanoparticles have positive potential at lower pH (2-5) range and negative potential at higher pH (6-10) range and the isoelectric point is 5.3, while the Fe₃O₄-APTES and Fe₃O₄-APTES-EDTA are positively charged at lower pH and negatively at higher pH with isoelectric points (IEP) of 5.5 and 5.7, respectively. The difference in charge properties can be attributed to the ionization of the functional groups, i.e., -COOH and -NH₂ at different pH[360].

5.3.2 Impact of the different parameter on adsorption

In water treatment, pH is a key operational parameter, as it can influence both the adsorbent structure and the distribution of pollutant species. The uptake efficiency in the pH range was examined with initial concentrations of 10 mg/L for each heavy metals (Pb²⁺, Cd²⁺, Ni²⁺, Co²⁺, and Cu²⁺). Effect of pH on the adsorption of heavy metals (Pb²⁺, Cd²⁺, Ni²⁺, Co²⁺, and Cu²⁺) on FAE nanocomposite shown in Fig. 4(a). The adsorption of heavy metals (Pb²⁺, Cd²⁺, Ni²⁺, Co²⁺, and Cu²⁺) on the FAE nanocomposite surface is a surface reaction. It is well

known that the pH plays an important role in the adsorption of particular metal ions onto adsorbent surface. The pH of the solutions was varied in between 3 to 10. No significant difference in heavy metal removal efficiency was found between pH 3 and 7, because in this range heavy metal forms stable complex with EDTA and binds the corresponding metals ions ($M = \text{Pb}^{2+}, \text{Cd}^{2+}, \text{Ni}^{2+}, \text{Co}^{2+}, \text{and Cu}^{2+}$). This can be explained as follows;



But with increase in pH, the metal hydroxide formation increases and reduce the formation of $M(\text{EDTA})^{2-}$ and $M(\text{HEDTA})^-$, which leads to decreased the adsorption of metal ions on the $\text{Fe}_3\text{O}_4\text{-APTES-EDTA}$ surface. A similar type of results was observed by Zirino et al[361].

As shown in Fig. 4(b), with a rise in the adsorbent dosages, the percentage removal efficiency of heavy metal ($\text{Pb}^{2+}, \text{Cd}^{2+}, \text{Ni}^{2+}, \text{Co}^{2+}, \text{and Cu}^{2+}$) simultaneously increases. This behavior is expected as a surge in the amount of sorbent will enhance the number of active binding sites and are available for the adsorption and more metal ions will be removed. Since the composite possesses functional groups like carboxyl, hydroxyl, amine, and carbonyl, they have a vital role in heavy metal adsorption. The removal efficiency of $\text{Pb}^{2+}, \text{Cd}^{2+}, \text{Ni}^{2+}, \text{Co}^{2+}$ and Cu^{2+} ions for 10mg/L solution are 95%, 96%, 96%,97% and 97% with optimum adsorbent dosages 125, 150, 150, 170 and 200 mg respectively.

The initial metal ion concentrations play a significant effect on their removal from aqueous solutions. In Fig. 4(c) shows the removal efficiency of heavy metals ($\text{Pb}^{2+}, \text{Cd}^{2+}, \text{Ni}^{2+}, \text{Co}^{2+}$ and Cu^{2+}), which increases from 0.63 to 18.42 mg/L for Pb^{2+} , 0.64 to 21.19 for Cd^{2+} , 0.46 to 13.71 for Ni^{2+} , 0.53 to 16.16 for Co^{2+} and 0.77 to 26.97 Cu^{2+} when the initial metal ion concentration changes from 1 mg/L to 50 mg/L. For the different adsorbent dosage of $\text{Fe}_3\text{O}_4\text{-APTES-EDTA}$, an upsurge in the metal ion concentration indicates a decline in the removal efficiency as the number of active binding sites is insufficient to bind metal ion. Higher initial metal ion concentrations resulted in higher mass gradient pressures between the aqueous solution and nanocomposite, which may provide a driving force in overcoming the mass transfer resistance between the aqueous and solid phases[362].

The effect of contact time on heavy metal ($\text{Pb}^{2+}, \text{Cd}^{2+}, \text{Ni}^{2+}, \text{Co}^{2+}, \text{and Cu}^{2+}$)removal from aqueous solution is shown in Fig. 4(d). For all heavy metal ions, the optimum maximum removal rate is reached at contact time 150 min, 120 min, 120 min, 220 min, and 220 min. At

this contact time, the removal rates of Pb^{2+} , Cd^{2+} , Ni^{2+} , Co^{2+} and Cu^{2+} ions reach 98 %, 97 %, 98 %, 98 %, and 96 %, respectively. Fig. 4(d) depicts the increase in efficiency with change in time. This is based on the fact that a large number of vacant active surface sites are occupied by the adsorbed metal suggesting the nature of the adsorbent and availability of adsorption sites.

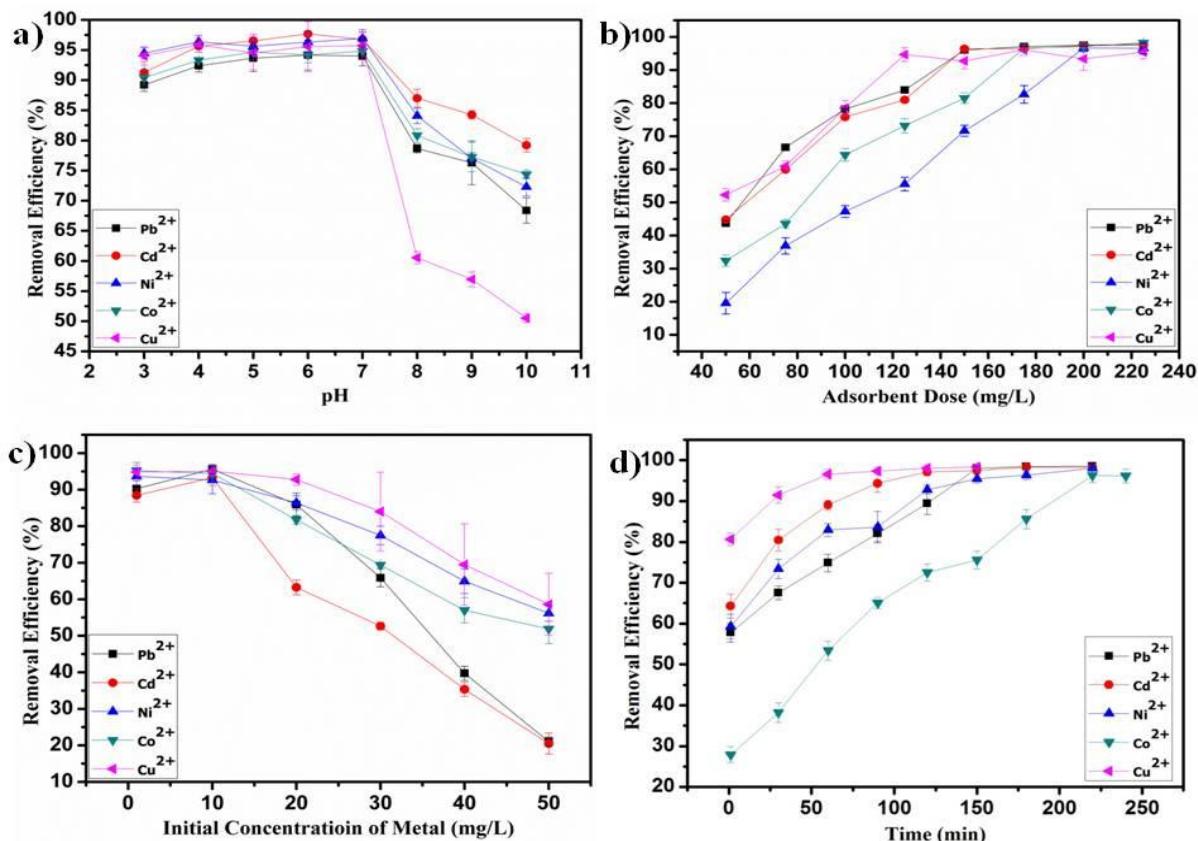


Figure 5.7 (a) Effect of pH, (b) Effect of adsorbent dosage, (c) Effect of the initial concentration of heavy metal ions and (d) Effect of contact time for heavy metal ions on to Fe_3O_4 -APTES-EDTA nanocomposite.

5.3.3 Adsorption Kinetics

From First-order kinetics plot, we calculated q_e , K_1 , and the corresponding linear regression coefficient of determination R^2 values are shown in Table 5.2. The low correlation coefficients indicate that the pseudo-first-order model does not predict the kinetics of the heavy metal ions (Pb^{2+} , Cd^{2+} , Ni^{2+} , Co^{2+} , and Cu^{2+}) adsorption on to nanocomposite surface. The plot of t/q_t versus t (In Figure 5.8b) with second-order kinetics shows a linear relationship. Values of K_2 is the rate constant of pseudo-second-order adsorption and equilibrium adsorption capacity q_e and the corresponding linear regression the coefficient of determination (R^2) were calculated from the intercept and slope of the plots[363-365]. The coefficient of determination for the second-order kinetics model (R^2) are greater than 0.99,

indicating the applicability of this kinetics equation and the second-order nature of the adsorption process of metal ions (Pb^{2+} , Cd^{2+} , Ni^{2+} , Co^{2+} , and Cu^{2+}) on to nanocomposite surface. Comparing to all the determination coefficients (R^2) and above analysis, it can be concluded that the pseudo-second-order is the more suitable kinetic model for adsorption, which also suggests that the adsorption process is controlled by chemical adsorption.

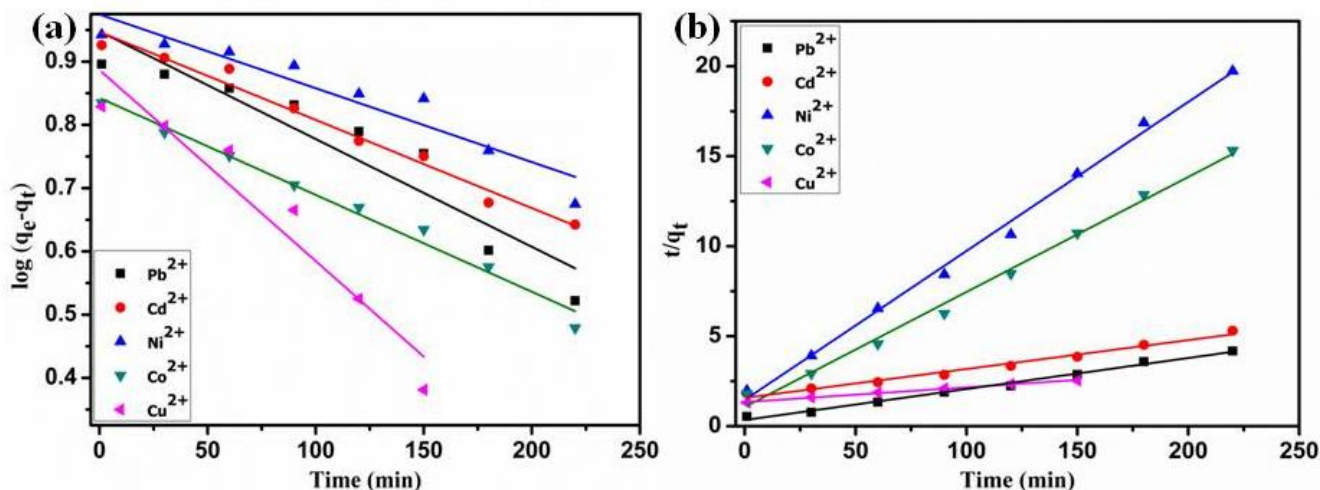


Figure 5.8 (a) Pseudo-first order and (b) Pseudo-second order kinetic models for heavy metal ions adsorption on Fe₃O₄-APTES-EDTA nanocomposite.

Table 5.2 Kinetic parameters for heavy metal ions sorption on Fe₃O₄-APTES-EDTA nanocomposite

Metal ions	(C ₀ , mg L ⁻¹)	q _{e, exp} (mg g ⁻¹)	Pseudo-first-order			Pseudo-second-order		
			q _{e, cal} (mg g ⁻¹)	K ₁	R ²	q _{e, cal} (mg g ⁻¹)	K ₂	R ²
Pb ²⁺	10	6.57	2.542	0.034	0.95	6.631	0.040	0.99
Cd ²⁺	10	6.54	2.482	0.033	0.88	5.393	0.019	0.99
Ni ²⁺	10	4.91	2.617	0.012	0.95	2.783	0.048	0.99
Co ²⁺	10	5.33	2.617	0.014	0.94	3.369	0.033	0.99
Cu ²⁺	10	7.94	2.791	0.307	0.90	4.076	0.245	0.99

5.3.4 Adsorption isotherm

The isotherms are shown graphically in Figure 5.9 and the isotherm parameters are listed in Table 5.3. From the Freundlich isotherm, the values of $1/n$ less than 1 represent favourable adsorption[366, 367]. The smaller value of the Temkin constant (B_1) suggested that adsorption of heavy metals on Fe₃O₄-APTES-EDTA is feasible. The comparison of coefficients indicates that the data fits well with Langmuir isotherm ($R^2 = 0.99$) than the other isotherm model. The basic assumption of the Langmuir adsorption isotherm is based on the monolayer coverage of the adsorbate on the surface of adsorbent. Based on this fact, the adsorption of heavy metal onto Fe₃O₄-APTES-EDTA generates a monolayer formation.

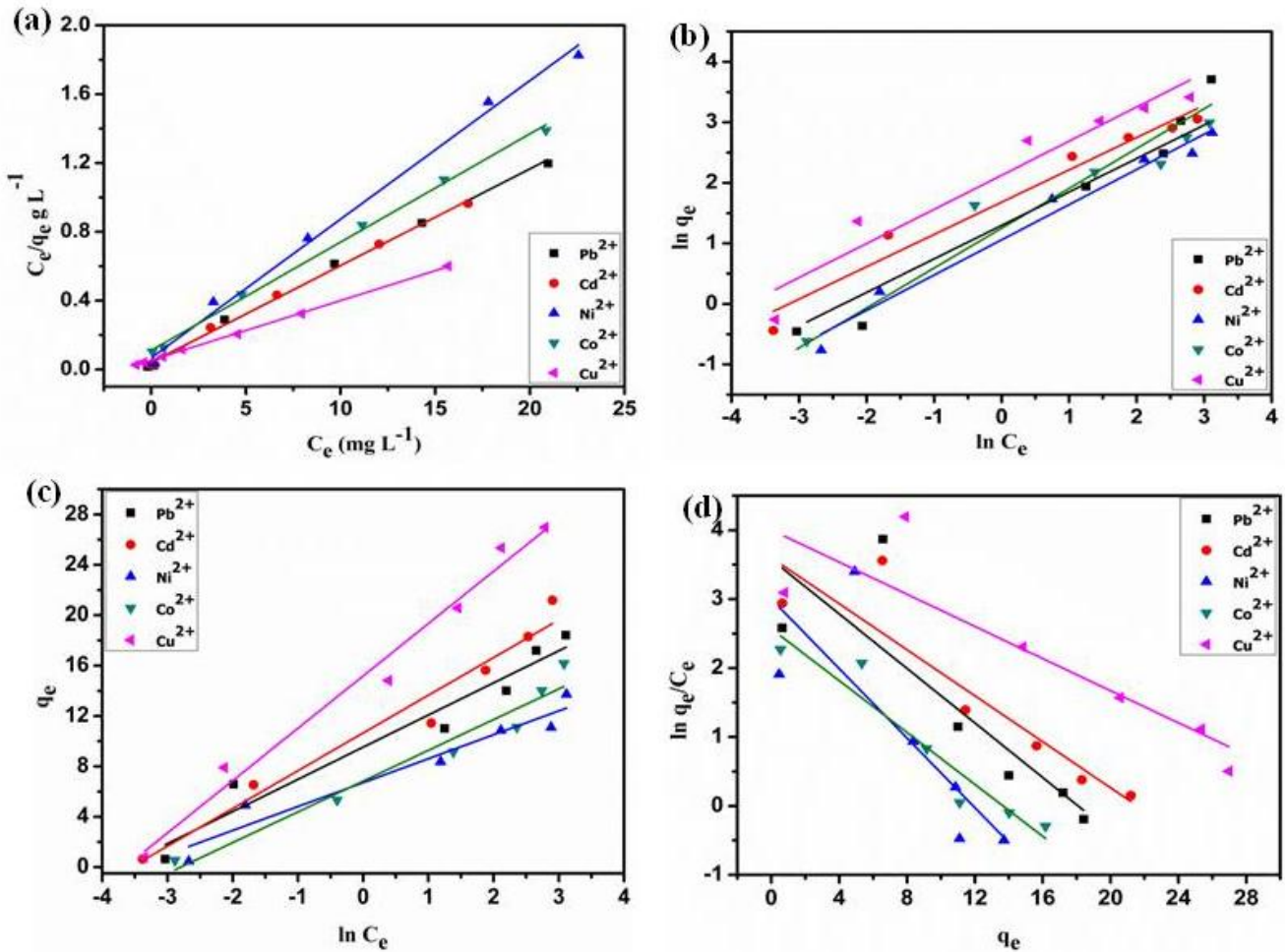


Figure 5.9 (a) Langmuir isotherm plot, (b) Freundlich isotherm plot, (c) Temkin isotherm plot and (d) Elovich isotherm plot for heavy metal ions on to Fe₃O₄-APTES-EDTA nanocomposite.

5.3.5 Desorption and reusability

Regeneration and reusability studies give knowledge regarding the nature of adsorption. The regeneration of the adsorbent may be imperative for holding the methodology expenses down and recovering the metals extracted from the liquid phase. Desorption experiments were performed to validate the mechanism of sorption in three different stripping solutions (*pH*2, *pH*7, and *pH*10). Out of three solutions, maximum % desorption was observed in acidic environment (*pH* = 2, 91.21 % for Pb²⁺, 87.18 % for Cd²⁺, 92.07 % for Ni²⁺, 89.87 % for Co²⁺ and 94.45 % for Cu²⁺) and minimum % desorption was observed in basic environment (*pH* = 10, 42.54 % for Pb²⁺, 39.61 % for Cd²⁺, 43.25.07 % for Ni²⁺, 41.27 % for Co²⁺ and 45.83 % for Cu²⁺). In Figure 5.4D shows that percentage of regeneration occurs at *pH*=2 for heavy metals, respectively on the grounds that under acidic conditions the adsorbent surface is protonated by H₃O⁺ particles to make conceivable desorption of positively charged metal particles from the adsorbent surface. Desorption studies of heavy metal ions were studied using 1.0 M HCl. At low *pH* conditions the surface –OH and

–COOH groups become more protonated, becoming positively charged and hence leading to desorption of the positively charged ions. The reusability of the adsorbent was studied by taking number of cycle (cycles 1–5) in Figure 5.4D. There was small considerable variation in adsorption and desorption values until four cycles, after four cycles the removal efficiency remains constantly and no difference in desorption capacity is observed during these adsorption-desorption cycles. The reusability of the adsorbent was studied with *pH* 2 aqueous solution. It has been found that 89.12 % for Pb^{2+} , 84.57 % for Cd^{2+} , 88.43 % for Ni^{2+} , 83.91 % for Co^{2+} and 89.06 % for Cu^{2+} was desorbed after 4th cycle. These results show that Fe_3O_4 -APTES-EDTA nanocomposite is very good adsorbent with good adsorption and desorption capabilities under acidic pH conditions. The results also confirm the regeneration and reusability of the adsorbent by following a simple desorption process.

Table 5.3 Isotherm parameters for the adsorption of heavy metal on to Fe_3O_4 -APTES-EDTA at room temperature (25°C).

Langmuir isotherm Parameter	Pb²⁺	Cd²⁺	Ni²⁺	Co²⁺	Cu²⁺
q_m (mg/g)	11.31	13.88	7.64	4.86	78.67
b (mg/g)	0.58	0.52	0.59	0.27	1.95
R^2	0.99	0.99	0.99	0.99	0.99
Freundlich isotherm Parameter					
K_f (L/g)	3.952	5.032	2.975	3.935	6.500
n	1.74	1.94	1.79	2.00	1.86
R^2	0.91	0.92	0.93	0.92	0.92
Temkin isotherm Parameter					
K_T (L/mg)	41.77	34.52	45.80	38.96	31.11
B_1	2.55	2.90	1.82	2.15	3.88
R^2	0.93	0.93	0.93	0.91	0.94
Elovich isotherm Parameter					
K_E	3.23	2.03	2.13	7.09	3.34
q_m	5.49	6.45	6.36	6.36	5.98
R^2	0.87	0.86	0.93	0.78	0.92

5.3.6 Adsorption mechanism

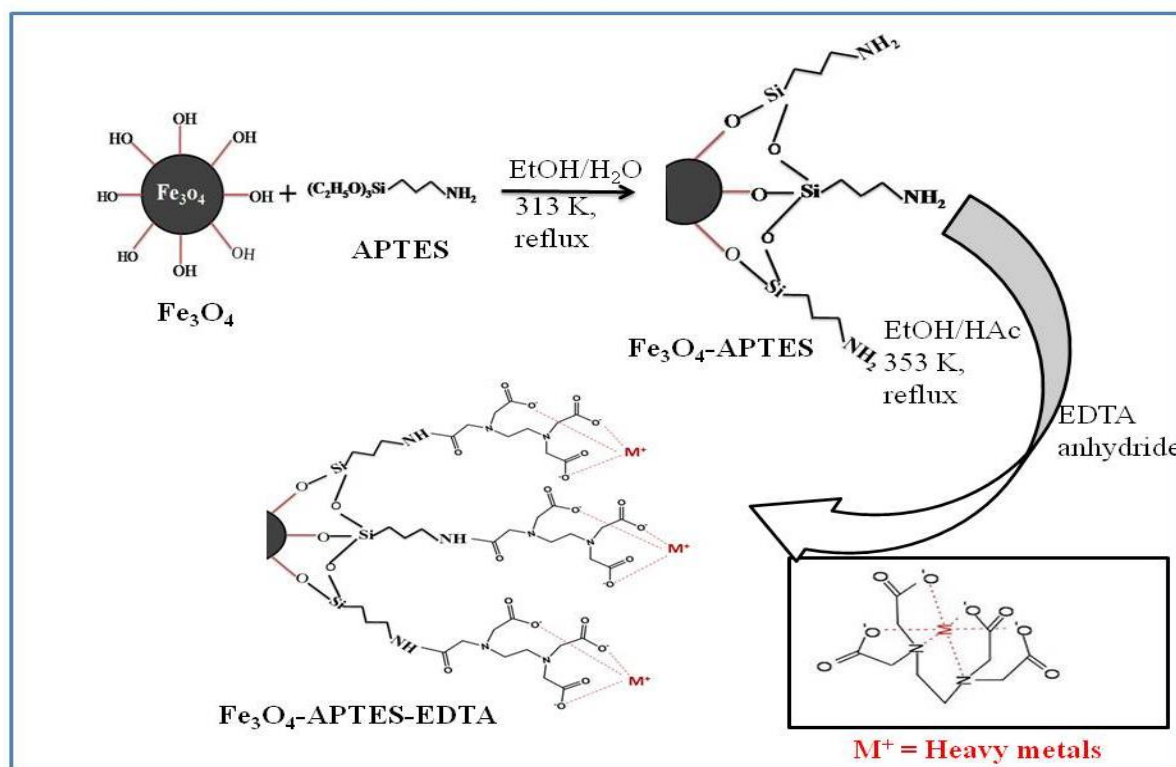


Figure 5.10 Schematic illustration of the synthetic procedure for Fe₃O₄-APTES-EDTA nanocomposite.

The synthesis of Fe₃O₄ nanoparticles can introduce a huge amount of -OH functional groups onto the surface of the nanoparticle, which induces hydrophilicity in Fe₃O₄ nanoparticles. The synthesis of EDTA functionalized Fe₃O₄ nanocomposite comprises of two steps, schematically represented in Figure 5.10. In first step, the Fe₃O₄ nanoparticles are made to react with APTES in order to deposit amino trialkoxy groups of silane on the surface of the Fe₃O₄ nanoparticles. Following step 1, hydrolysis was performed in which, the alkoxide group (-OC₂H₅) of APTES were replaced by hydroxyl groups to form reactive silanol (-Si-OH) groups. This silanol functional group condensed with other silanol groups to introduce siloxane bonds (Si-O-Si) and generates silane polymer. Then, this polymer coated with Fe₃O₄ nanoparticles is then finally reacted with EDTA which attaches covalently on the Fe₃O₄-APTES surface[368]. EDTA which is attached covalently to particles is possible by the formation of amide bonds between the carboxylic acid group of the complexing agent and amino groups provided by the APTES coating[369-372]. The metal adsorption on the surface of the EDTA functionalized nanocomposite was attributed to columbic forces between the positive charge of the heavy metal and the negative charge surface of the adsorbent (illustrated in Figure 5.10). Based on the electrostatic interaction between the electron-donating nature of the oxygen and nitrogen-containing functional groups on the surface of the

adsorbent (Lewis base) and the electron-accepting nature of the heavy metal ions (Lewis acid), the active interaction between the heavy metal ions such as Pb^{2+} , Cd^{2+} , Ni^{2+} , Co^{2+} and Cu^{2+} with the functionalized EDTA molecules play a key role in the overall adsorption process and Fe_3O_4 is used as magnetic separation from aqueous solution and APTES is used as cross-linker in between Fe_3O_4 and EDTA.

5.4 Summary

The inclusion of EDTA groups on the Fe_3O_4 nanoparticle surface through silanization process can significantly increase the adsorption efficiency towards different toxic heavy metals. The EDTA modified Fe_3O_4 nanoparticle is found to be an excellent adsorbent for the removal of toxic heavy metals (Pb^{2+} , Cd^{2+} , Ni^{2+} , Co^{2+} , and Cu^{2+}) in aqueous solution. Our nanocomposite has high surface area and paramagnetic behavior, which made the separation process quite easier and magnetically separated under an external magnetic field. The adsorption of heavy metal ions by the EDTA functionalize Fe_3O_4 nanocomposite fits the Langmuir adsorption isotherm model and follow pseudo-second order kinetic model. On the other hand, the desorption behavior of metals on the FAE nanocomposite surface suggests that the nanocomposite high stability and good reusability up to five consecutive cycles. The experimental investigations demonstrate Fe_3O_4 -APTES-EDTA nanocomposite as an effective adsorbent for removal of toxic heavy metals in moderate concentrations.

Chapter 6

6. Surface functionalization of graphene oxide using amino silane magnetic nanocomposite for Cr (VI) removal and bacterial treatment

6.1 Introduction

The water contamination throughout the world occurs by toxic heavy metals (Cr, As, Pb, Hg, and Cd) above their permissible limit are a serious problem for living organism[373]. Among various toxic metal ions, Chromium (Cr) is one of the highly toxic heavy metal and often discharges to water from wood preservatives, electroplating, textile industries, metal refining and plant producing industrial inorganic chemicals and pigments[374, 375]. A very low concentration of chromium creates serious health problem like stomach cancer, bronchial asthma, kidney damage, anemia, liver damage, and hepatotoxicity in human[376, 377]. Chromium exists in water both Chromium (III) and Chromium (VI) states, Chromium (VI) is highly contaminant because of high solubility, smaller size and large mobility[378-382]. As compare to Chromium (VI), Chromium (III) is less toxic and also used as an essential micronutrient for sugar, protein and fat metabolism in mammals[383, 384]. Hence, Chromium (VI) can be converted to Chromium (III) as an alternative way to reduce the toxicity[385]. In current year, the photocatalytic reduction is considered a prominent method to reduce the toxicity of Chromium (VI) to Chromium (III) but their initial and operational cost is very high[386]. There are several methods available to remove Chromium from contaminated water. Those methods are ion exchange[387, 388], ultra-filtration[389], reverse osmosis[390, 391], electro dialysis[392-394], biosorption, adsorption and chemical precipitation[395]. Among all the removal methods, adsorption is one of the most commonly used methods for Chromium (VI) removal because of its low cost, less energy, less chemical requirement, easy to operate, high regeneration capacity and removal efficiency[396]. A number of naturally occurring adsorbents such as almond shells, olive cake, wool, charcoal used tyres, cactus leaves, soot, coconut shell charcoal, banana peel, pine needles, sawdust, dead fungal biomass, and green algae have been used for the removal of Chromium[397-400]. Among all the naturally available adsorbents, most of them are slow process kinetics and have low adsorption capacity. Hence, it is necessary to prepare novel and innovative adsorbents useful for both the environment safety and industry.

Jitendra Kumar Sahoo, Sanjeev Kumar Paikra, Archana Baliarsingh, Debashis Panda, Sourav Rath, Monalisa Mishra, Harekrushna Sahoo (Under Review)*

Due to high surface-area-to-volume ratio, excellent magnetic character, surface property, great biocompatibility, reusability, easy separation by external magnetic field and comparatively low cost, iron oxide (Fe_3O_4) have already been investigated as excellent adsorbents for different heavy metal ions[114, 401, 402]. Iron oxide nanoparticle has several applications in various research areas such as catalytic oxidation of alcohol[403], magnetic carrier for protein separation[404], supercapacitor electrode materials[405-409], wastewater treatment[410-412]and heavy metal adsorption[413].In recent years, most of the researchers are interested in chemical modify Fe_3O_4 to enhance their adsorption capacity. Also aerosol-based iron-carbon nanocomposites synthesized for Chromium (VI) adsorption[414]. Another pioneering work shows iron oxide decorated PEDOT:PSS used for cancer biosensor[415]. Keeping the above information in mind, we modified Fe_3O_4 on graphene oxide (GO) surface using (3-aminopropyl) triethoxysilane (APTES) as a cross-linker.

GO is very commonly used adsorbent because of high surface area, aromatic sp^2 domains and high functionality (containing hydroxyl, epoxy, and carboxyl functional groups) and low manufacturing cost that make GO as a potential adsorbent for heavy metal adsorption. Many researchers have been focused on the preparations of metal oxide modified GO based nano adsorbent for heavy metal removal[416]. Wide ranges of metal oxide modified GO such as $\text{ZnO-ZnFe}_2\text{O}_4$ decorated on GO for adsorption of chromium, $\text{Co/MnFe}_2\text{O}_4$ magnetic nanohybrids for adsorption of As and Pb from water and nickel ferrite, iron and aluminium decorated GO surface for fluoride removal and RGOFe_3O_4 nanocomposite for Pb(II), Cr(IV) adsorption[417]. In order to further improve the adsorption percentage, current researchers have been interested to synthesize by grafting new functional group on GO surface[418]. Apart from this, GO has one limitation in terms of difficulty in like no easy separation from aqueous solution. However, separation of adsorbent after adsorption from contaminated water still challenging work. To overcome this limitation, iron oxide is the best modification on GO surface because of superparamagnetic nature, which can be easily separated because of its magnetic nature.

Metallic nanoparticle on GO matrix has a lot more biomedical importance[419]. The antibacterial property of graphene and GO is reported from various studies [420, 421]. Graphene sheet acts as a substrate for adhesion of cells or any other microorganism[422]. Graphene-based nanomaterial has multifunctional application including photoluminescence, cellular imaging, as a vehicle for gene delivery and as a drug carrier for advanced drug delivery system[423-425]. Antibacterial activity of graphene nanomaterial is due to loss of membrane integrity. The sharp edge of graphene nanosheet damage the cell membrane of

bacteria and leads to the leakage of cellular component i.e. RNA or protein contents of bacteria[426]. Various physical, as well as a chemical factor of graphene, is responsible for its antimicrobial property [427]. Graphenenanocomposite increases the cellular oxidative stress which disturbs the metabolic activity in bacteria resulting bacterial cell death[428]. Fabrication of silver nanoparticle with graphene oxide acts as a carrier for the efficient delivery of the water-insoluble drug into the cells [421, 424, 429-432]. Besides this it's peculiar electrical conductivity and paramagnetic property allows to be used in various biomedical application [432, 433]. Chemical modification of graphene sheet can be easily dispersed with the polymeric matrix[434]or inorganic material matrix [435]. The smooth surface of GO enables the bacteria to adhere to the surface.The oxygen-containing a functional group of GO provides a new dimension to trap the radioactive impurity from the water [436].

Therefore, in this paper we reported Fe₃O₄-APTES functionalize on GO surface for Chromium (VI) removal from aqueous solution by varying the adsorbent dosage, initial Chromium (VI) concentration, immersion time and pH, which plays an important role for adsorption. To evaluate the experimental data statistical analysis done to make a predict model and to test its viability.

6.2 Adsorption Experiment

All the batch adsorption experiments were carried out in 200 ml capacity of polypropylene bottles by considering the various concentration of Chromium solution. For the adsorption studies, 0.3 g of GO-Fe₃O₄-APTESwas added in 20 mg/L of Chromium solution at pH 3. The reaction bottles were shaken using an incubator shaker (RC 5100) at shaking rate 200 rpm at room temperature. After 10 hours, the adsorbent was separated out by Whatman-42 (mm) filter paper. The remaining concentration of Chromium was analyzed by UV-Visible spectrophotometer using 1,5-diphenyl carbazide (DPC) method at the wavelength of 540 nm[437]. The impact of various parameters like pH (2-12), adsorbent dosage (0.15-0.35 g), time (2-10 hours) and room temperature (25°C) influencing the removal of Chromium ion was examined separately by keeping the others constant, so as to optimize the adsorption process. The adsorbed amount of chromium ion and the removal efficiency (%) was determined using the subsequent equations.

$$q_e = \frac{C_0 - C_e}{W} \times V \quad (6.1)$$

$$\% \text{ of adsorption} = \frac{C_0 - C_e}{C_0} \times 100 \quad (6.2)$$

From the above equation, q_e shows the adsorbed amount of Chromium (VI). C_0 is the initial concentration of chromium (VI) (mg/L), C_e is the final concentration of chromium ion (mg/L), V is the volume of Chromium (VI) solution and W is the mass of adsorbent. All experiments were repeated for 3 times.

6.3 Antibacterial activity

6.3.1 Bacterial culture

E.coli and *B.subtilis* were grown in Luria-Bertini (LB) broth. For colony counting purpose LB agar was taken and plates were prepared in Petri dishes.

6.3.2 Antibacterial activity of GO-Fe₃O₄-APTES

Assessment of antibacterial activity of GO-Fe₃O₄-APTES was checked against gram-negative bacteria, *E.coli* and gram-positive bacteria *B. subtilis*. For the evaluation of antibacterial activity both the bacteria were grown in LB broth and an appropriate concentration of bacteria was taken for the antimicrobial assay. The bacteria were inoculated on the LB agar plate and the antimicrobial activity of GO-Fe₃O₄-APTES was checked by using the disc diffusion method[438]. To check the concentration-dependent activity of GO-Fe₃O₄-APTES, the bacteria (*E.coli* and *B.subtilis*) were grown in LB media with different concentration of GO-Fe₃O₄-APTES (10, 20, 40, 80, 160 µg/ml) and then it is incubated for 8 to 12 h at 37 °C at 120 rpm. Bacterial growth was examined by measuring the optical density at 595nm using the ELISA plate reader (Bio-base-EL10A Elisa reader) obtained from Bio-based Bio-industry (Shandong) Co. Ltd. Bacterial growth kinetics was studied by varying interval of time with and without GO-Fe₃O₄-APTES treatment.

6.3.3 Analysis of bacterial damage under field emission scanning electron microscopy (FE-SEM)

Bacterial damage was analyzed by field emission scanning electron microscopy (FESEM). This experiment helps us to visualize the fine structure of bacterial cells before and after GO-Fe₃O₄-APTES treatment. Treated and untreated cells were washed properly with 0.9% sodium chloride and then fixed with 4% Paraformaldehyde. After fixation, it was washed with phosphate-buffered saline (PBS) and then dehydrated by using graded series (30, 50, 70, 90 and 100 %) of alcohol. Afterward it was fixed on a clean glass slide and gold sputtering was done before taking the images. For detection of different elements deposited in the bacterial cells EDX analysis was done.

6.3.4 Detection of ROS production

Assessment of ROS generation by bacteria was checked by using the 2,7-Dichlorofluorescein diacetate (DCFDA) dye. It is a peroxy nitrile indicator which confirms the generation of different reactive oxygen species (nitric oxide or hydrogen peroxide)[439]. Bacterial cells treated with and without GO-Fe₃O₄-APTES were exposed to DCFDA dye (1 μM) and then its fluorescence intensity was measured at emission wavelength 529 nm with an excitation of 495 nm by using the fluorescence spectrophotometer.

6.4. Result and discussion

6.4.1 Characterisation of the adsorbent

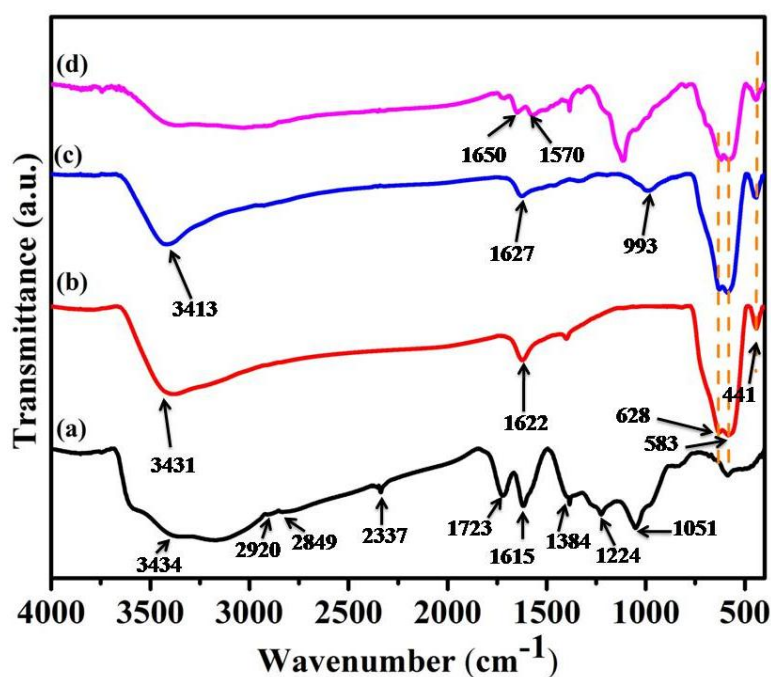


Figure 6.1 FT-IR spectra of (a) GO, (b) Fe₃O₄, (c) Fe₃O₄-APTES and (d) GO-Fe₃O₄-APTES.

In order to study the presence of functional groups in GO-Fe₃O₄-APTES, FTIR measurement was carried out. Figure 6.1 shows the comparison FT-IR data of GO, Fe₃O₄, Fe₃O₄-APTES, and GO-Fe₃O₄-APTES. In the spectrum of GO, the presence of peaks at 1051 cm⁻¹ (C-O-C stretching vibration of epoxide group), 1224 cm⁻¹ (C-OH), 1384 cm⁻¹ (C-O asymmetric stretching vibration of carboxylic group), 1615 cm⁻¹ (C=C in the carbon skeletal network), 1723 cm⁻¹ (C=O stretching vibration of carboxylic group), 2337 cm⁻¹ (CO₂), 2849 cm⁻¹ (CH bending vibration), 2920 cm⁻¹ (CH stretching vibration) and the strong peak around 3434 cm⁻¹ can ascribe to the O-H stretching mode of water molecules[440-442]. In the spectrum of Fe₃O₄, the existence of peaks at 441 cm⁻¹ ascribed to the shifting of the ν₂ band of the Fe-O bond of bulk magnetite, two strong peaks at 583 cm⁻¹ and 628 cm⁻¹ ascribe to the presence of Fe-O and two peaks at 1622 cm⁻¹ and 3431 cm⁻¹ ascribe to the O-H bending and stretching frequency of water molecules[443, 444]. The existence of silica network on Fe₃O₄ was

confirmed by Fe-O-Si bonds, this peak cannot show in the FT-IR spectrum because it appears at 584 cm^{-1} and therefore 583 cm^{-1} peak of Fe_3O_4 overlaps [445, 446]. So, the presence of silane polymer on Fe_3O_4 was confirmed by the peak at 993 cm^{-1} assign to Si-O-Si groups. The two broad peaks at 1627 cm^{-1} and 3413 cm^{-1} can be ascribed to NH_2 bending mode of free NH_2 and N-H stretching vibration [447, 448]. Comparing to the FT-IR data of GO and Fe_3O_4 -APTES with GO- Fe_3O_4 -APTES, the peaks of GO- Fe_3O_4 -APTES are similar with GO and Fe_3O_4 -APTES but two new peaks at 1570 cm^{-1} and 1650 cm^{-1} were observed, this peak corresponds to N-H bending and amide bond ($-\text{NHCO}-$) formation in between free NH_2 group of Fe_3O_4 -APTES and $-\text{COOH}$ group of GO. These observed data were also compared with other published data [439, 449-451].

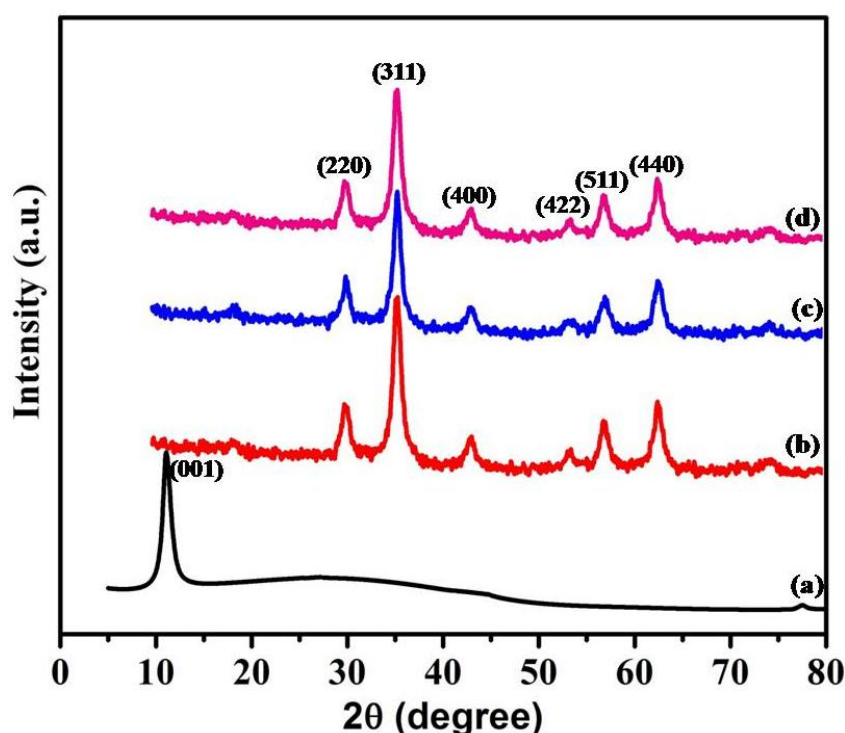


Figure 6.2 X-ray diffraction patterns of (a) GO, (b) Fe_3O_4 , (c) Fe_3O_4 -APTES and (d) GO- Fe_3O_4 -APTES.

Figure 6.2 represents the XRD patterns of GO, Fe_3O_4 , Fe_3O_4 -APTES, and GO- Fe_3O_4 -APTES. In the XRD peak of GO, the strongest peak at $2\theta = 11.4^\circ$ was observed which corresponds to (001) crystal plane. This 011 plane can confirm the formation of GO [452]. The XRD patterns of Fe_3O_4 , Fe_3O_4 -APTES, and GO- Fe_3O_4 -APTES were found to be similar. The crystalline peaks at $2\theta = 30.3^\circ$ (220), 35.7° (311), 43.5° (400), 53.9° (422), 57.5° (511) and 63.0° (440) corresponds to the structure of Fe_3O_4 according to the JCPDS no- 019-0629 [453]. The XRD patterns of Fe_3O_4 -APTES on GO surface, GO peaks might be absence because Fe_3O_4 -APTES nanoparticles decorated on GO surface that prevents the restacking of the GO layer [455]. It

can conclude by XRD pattern of the GO-Fe₃O₄-APTES material that there is no change in the characteristic peaks of Fe₃O₄ after modification of APTES and GO [454, 455].

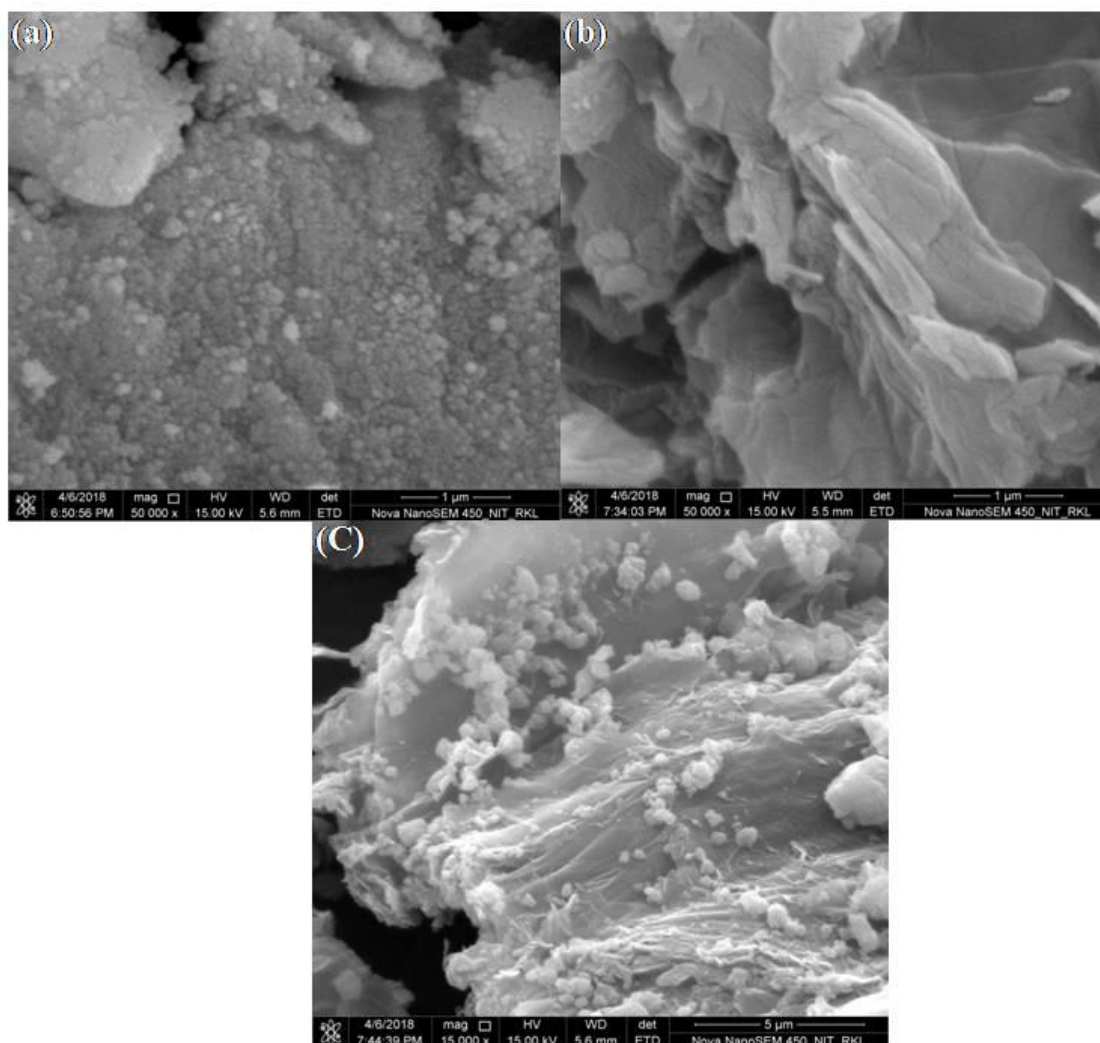


Figure 6.3 FE-SEM images of (a) Fe₃O₄-APTES, (b) GO and (c) GO-Fe₃O₄-APTES.

Techniques such as FE-SEM and TEM were used to explore the surface morphology of the synthesized material. Figure 6.3a shows the FE-SEM image of the Fe₃O₄-APTES. It is observed that the shape of Fe₃O₄-APTES was nanosized spherical shape and homogeneously distributed. The FE-SEM image of GO (Figure 6.3b) shows the layer type structure. Figure 6.3c illustrates the FE-SEM image of GO-Fe₃O₄-APTES, which indicates the formation of nanospheres on GO layer. The structure and morphology of Fe₃O₄-APTES and GO-Fe₃O₄-APTES were further examined by TEM analysis. Figure 6.4a shows the TEM image of Fe₃O₄-APTES and Figure 6.4b shows the particle size distribution of Fe₃O₄-APTES. From TEM image, it is clearly seen that the Fe₃O₄-APTES having fine spherical particles and the histogram of Fe₃O₄-APTES shows the average particle size 8 nm. The average particle size was calculated by measuring the diameters of 53 nanoparticles by Image J software. Figure 6.4c and 6.4d represent the TEM image of GO-Fe₃O₄-APTES with various resolutions (200

and 100 nm resolution). These images clearly have shown that the 8 nm-sized spherical particles are successfully modified on GO layer. The HRTEM image of GO-Fe₃O₄-APTES was given

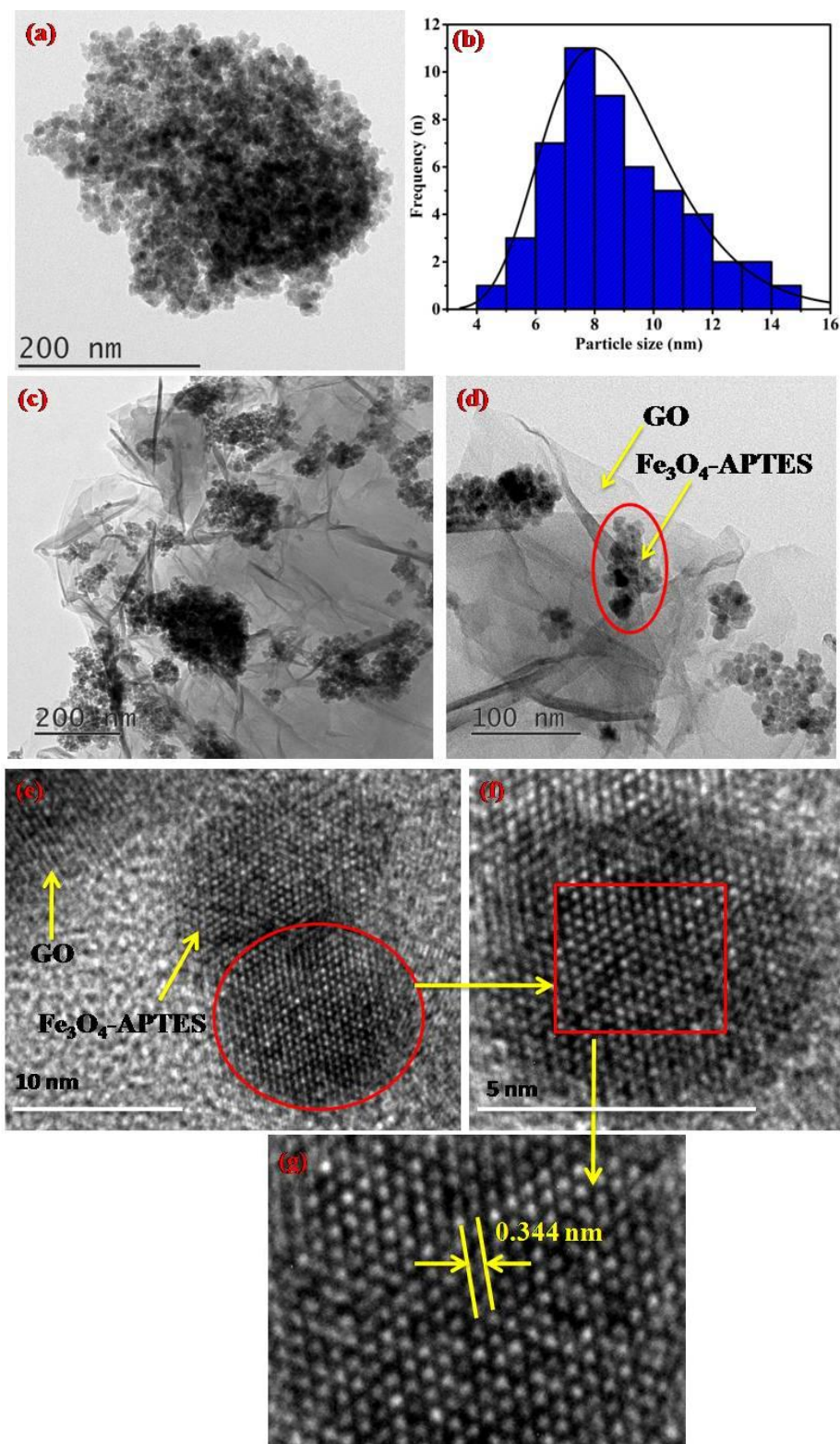


Figure 6.4 (a) TEM image of Fe₃O₄-APTES, (b) The particle size distribution of Fe₃O₄-APTES, (c,d) TEM image of GO-Fe₃O₄-APTES (200 and 100 nm resolution) and (e-g) HRTEM micrograph with an interplanar spacing of GO-Fe₃O₄-APTES.

in Figure 6.4e, 6.4f and 6.4g, respectively. Figure 6.4e shows two different lattice fringes, which ascribe the crystalline nature of GO and Fe₃O₄-APTES. From Figure 6.4g, we confirm the d-spacing 0.344 nm attribute to the (111) lattice plane of Fe₃O₄. The above results were also similar to RD data in JCPDC files for Fe₃O₄. The SAED pattern of GO-Fe₃O₄-APTES is shown in Figure 6.5a. The ring-like shape of SAED pattern shows the crystalline nature of the material. The elemental mapping (EDS) of GO-Fe₃O₄-APTES (Figure 6.5(b-h)) represents the presence of elements like Fe, C, O, N and Si with different colors. Again EDX spectrum confirms the synthesized material contains iron (Fe), carbon (C), oxygen (O), nitrogen (N) and silicon (Si) elements with 16.4, 65.8, 9.5.4 and 3.4 atomic percentages (Figure 6.5i), respectively. The elemental mapping and EDX result shows there is no impurity peak found in GO-Fe₃O₄-APTES material.

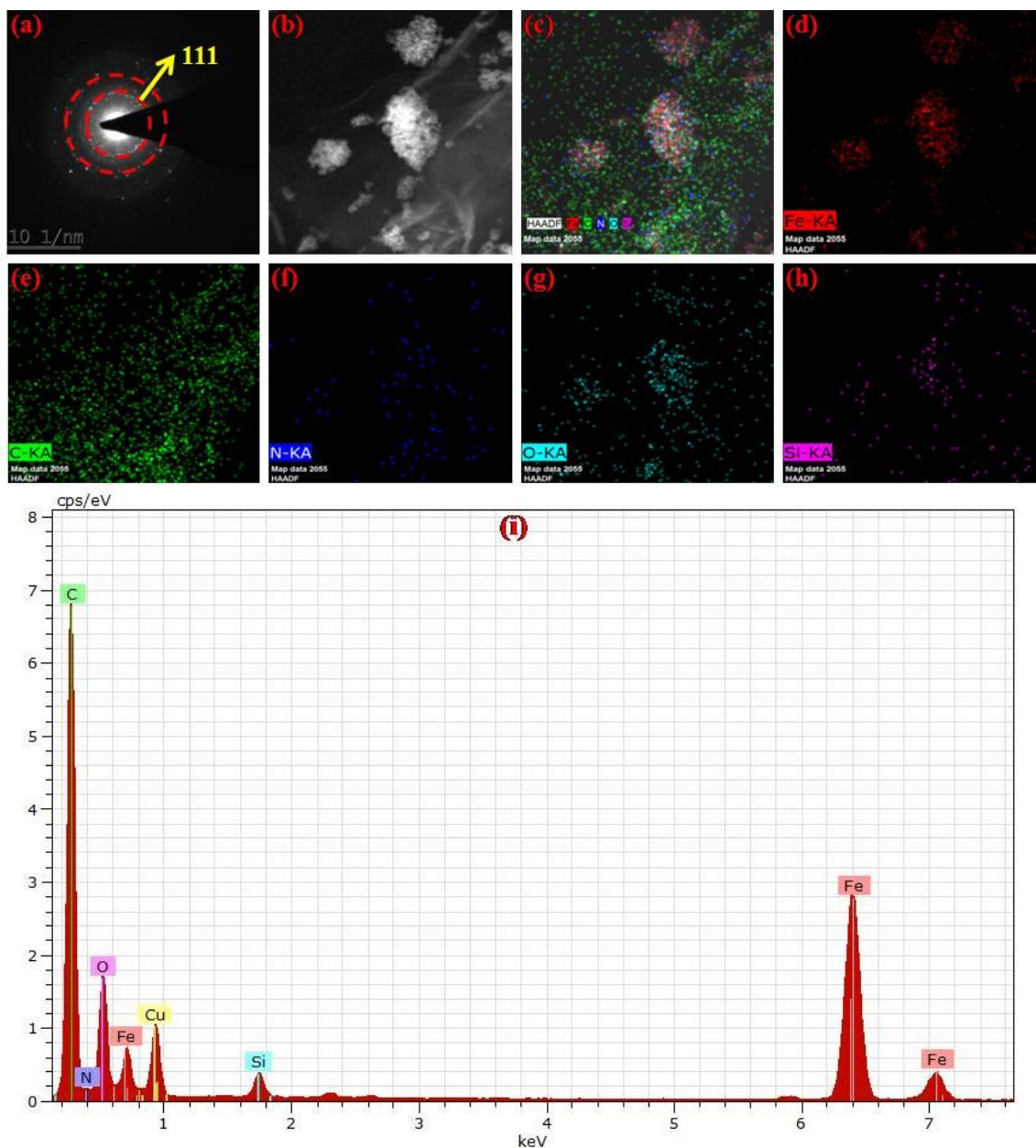


Figure 6.5 (a) SAED pattern of GO-Fe₃O₄-APTES, (b-h) EDS elemental mapping of GO-Fe₃O₄-APTES and (i) EDX spectrum of GO-Fe₃O₄-APTES.

The Raman spectroscopy was carried out to study the structural configuration of GO and GO-Fe₃O₄-APTES during the process of adsorption and the data was shown in Figure 6.6. The Raman spectrum of GO shows two strong peaks one is D band at 1353 cm⁻¹ due to the disorder of GO arising from imperfection linked with vacancies, amorphous carbon species, and grain boundaries and other is G band at 1607 cm⁻¹ which specifies the E_{2g} phenomenon of Sp² hybridized carbon in a 2- dimensional hexagonal lattice[456]. After the modification of Fe₃O₄-APTES on the surface of GO, the intensity of D and G band became higher than pristine GO. In case of GO-Fe₃O₄-APTES, it is observed that two strong bands at 1350 cm⁻¹ and 1588 cm⁻¹ are found. The D and G band of GO-Fe₃O₄-APTES was slightly shifted by 3 cm⁻¹ and 19 cm⁻¹ as compared to pristine GO. This Raman shift of D and G band for GO-Fe₃O₄-APTES sheet demonstrates that the charge transfer occurs between the sheets of GO and Fe₃O₄-APTES. It exhibits a strong interaction between GO and Fe₃O₄-APTES nanocomposite. The intensity ratio I_D/I_G of GO and GO-Fe₃O₄-APTES was calculated to be 1.00 and 1.12, respectively. However, the intensity ratio I_D/I_G of GO-Fe₃O₄-APTES was higher than pure GO, which was due to the defects arises by the interaction between Fe₃O₄-APTES and GO[457, 458].

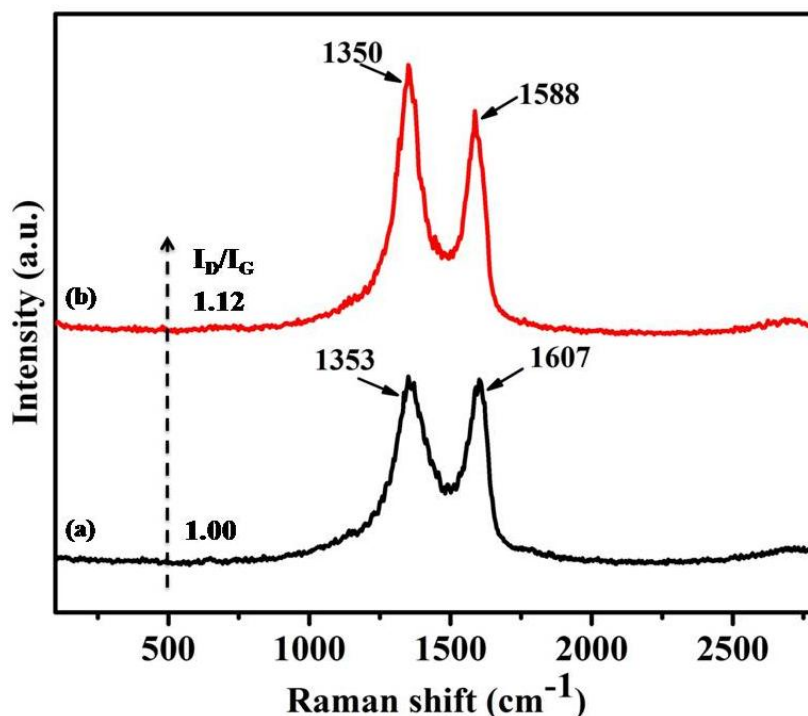


Figure 6.6 Raman spectra of (a) GO and (b) GO-Fe₃O₄-APTES.

Vibrating sample magnetometer (VSM) analysis was carried out to know the magnetic properties of prepared Fe₃O₄, Fe₃O₄-APTES, and GO-Fe₃O₄-APTES. Magnetization curve of Fe₃O₄, Fe₃O₄-APTES, and GO-Fe₃O₄-APTES are shown in Figure 6.7. The magnetic

saturation (M_s) value of Fe_3O_4 , Fe_3O_4 -APTES, and $GO-Fe_3O_4$ -APTES are 52.8 emu/g, 47.4 emu/g, and 30.6 emu/g. The magnetic saturation value decreases, after modifying APTES and GO on Fe_3O_4 [452]. These modifications on the surface of Fe_3O_4 nanoparticles are non-magnetic and their shielding effect resulted in the decrease of magnetic property of Fe_3O_4 nanoparticles. The S-like magnetization of all the samples shows superparamagnetic in nature at room temperature because of negligible coercivity and remanence. The right inset of Figure 6.7. shows that $GO-Fe_3O_4$ -APTES is attracted by an external magnet and the clear solution can be easily removed pipette.

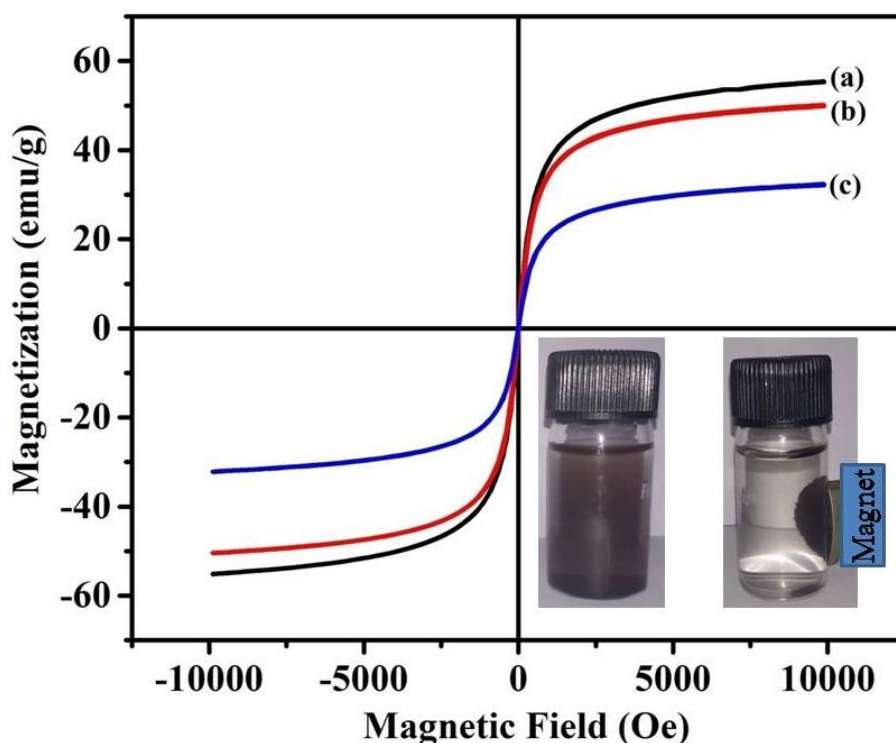


Figure 6.7 Hysteresis loop of (a) Fe_3O_4 , (b) Fe_3O_4 -APTES, and (c) $GO-Fe_3O_4$ -APTES at room temperature. The bottom inset: aqueous solution of $GO-Fe_3O_4$ -APTES (left), separated particles of $GO-Fe_3O_4$ -APTES by an external magnet (right).

The N_2 adsorption-desorption isotherm is carried out to calculate the specific surface area of the synthesized material. Figure 6.8 shows BET isotherm plot curve of GO, Fe_3O_4 , and $GO-Fe_3O_4$ -APTES. The surface area of GO, Fe_3O_4 , and $GO-Fe_3O_4$ -APTES was found to be 35.3, 48.2, and 57.9 m^2/g respectively. The isotherm curve of $GO-Fe_3O_4$ -APTES exhibit typical type IV with comparatively high surface area. Similar observations were also reported by other researcher groups[457, 459]. The surface area of $GO-Fe_3O_4$ -APTES increases after modification of Fe_3O_4 -APTES on GO. The higher surface area is further improving the adsorption capacity toward the removal of Chromium (VI)

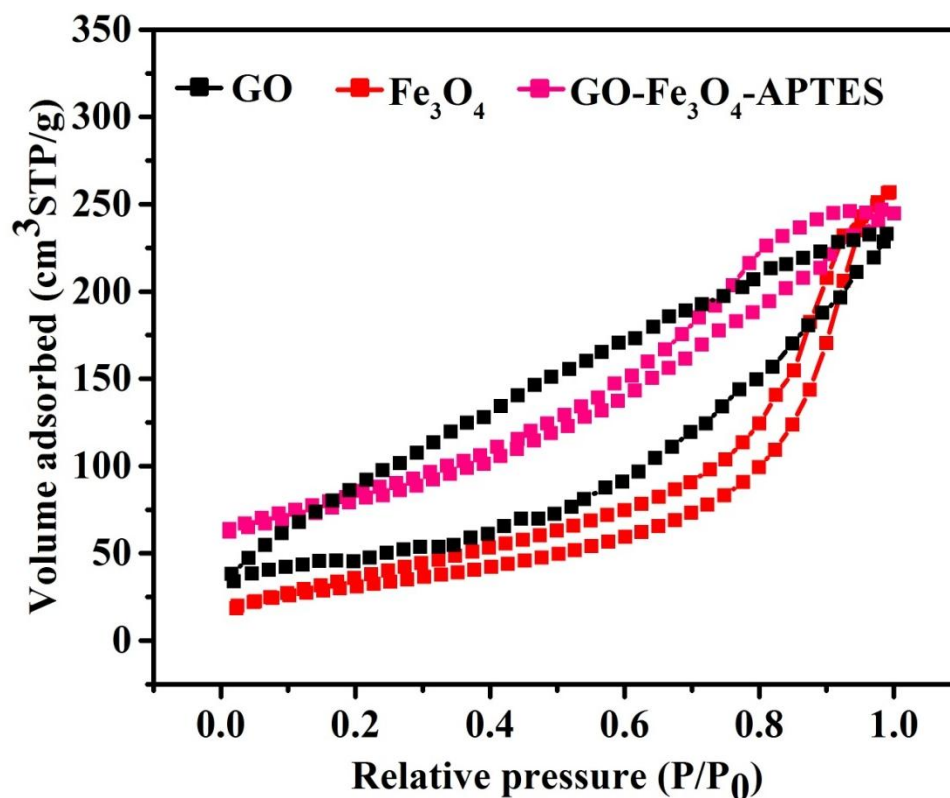


Figure 6.8 N₂ adsorption-desorption isotherm of GO, Fe₃O₄, and GO-Fe₃O₄-APTES.

6.4.2 Impact of a different parameter on adsorption

The initial concentration of Chromium (VI) is one of the most efficient factors on adsorption field. Figure 6.9a shows the variation of initial Chromium (VI) concentration from 5 to 70 mg/L at constant parameters such as adsorbent dosage (0.3 g), pH 3, room temperature (25 °C), contact time (10 h) and shaking speed (160 rpm). From this plot we observe the Chromium (VI) removal efficiency nearly same from 5 mg/L to 20 mg/L. After 20 mg/L the removal efficiency starts to decrease. This occurs due to that at lower concentrations of Chromium (VI), the ratio of the initial number of Chromium (IV) ions to the obtainable surface area of the adsorbent is high. Although at higher concentrations of Chromium (VI), the remaining sites of adsorption become lower and then the percentage of removal efficiency of Chromium (VI) decreases which depends on the initial concentration of Chromium (VI). Thus 20 mg/L of chromium (VI) concentration was taken as the optimum concentration for further experiment.

Figure 6.9b demonstrates the effect of adsorbent dosage on the removal of Chromium (VI) from the aqueous solution. We change the adsorbent dosage from 0.15 to 0.35 g/L by keeping other parameters constant such as pH 3, room temperature (25 °C), contact time (10 h) and 160 rpm of shaking speed. In this plot we observed that the removal efficiency of Chromium (VI) increases by increasing the adsorbent dosage because the number of active binding sites

increases by increasing adsorbent dosage [379, 460]. The adsorbent dosage from 0.3 g/L to 0.35 g/L shows the percentage of the removal efficiency remains same. From the above plot it was noticed that the percentage of removal efficiency of Cr (VI) is found to be maximum at 0.3 g of adsorbent dose. 0.3 g of adsorbent dose was selected as optimum dose for further experiments

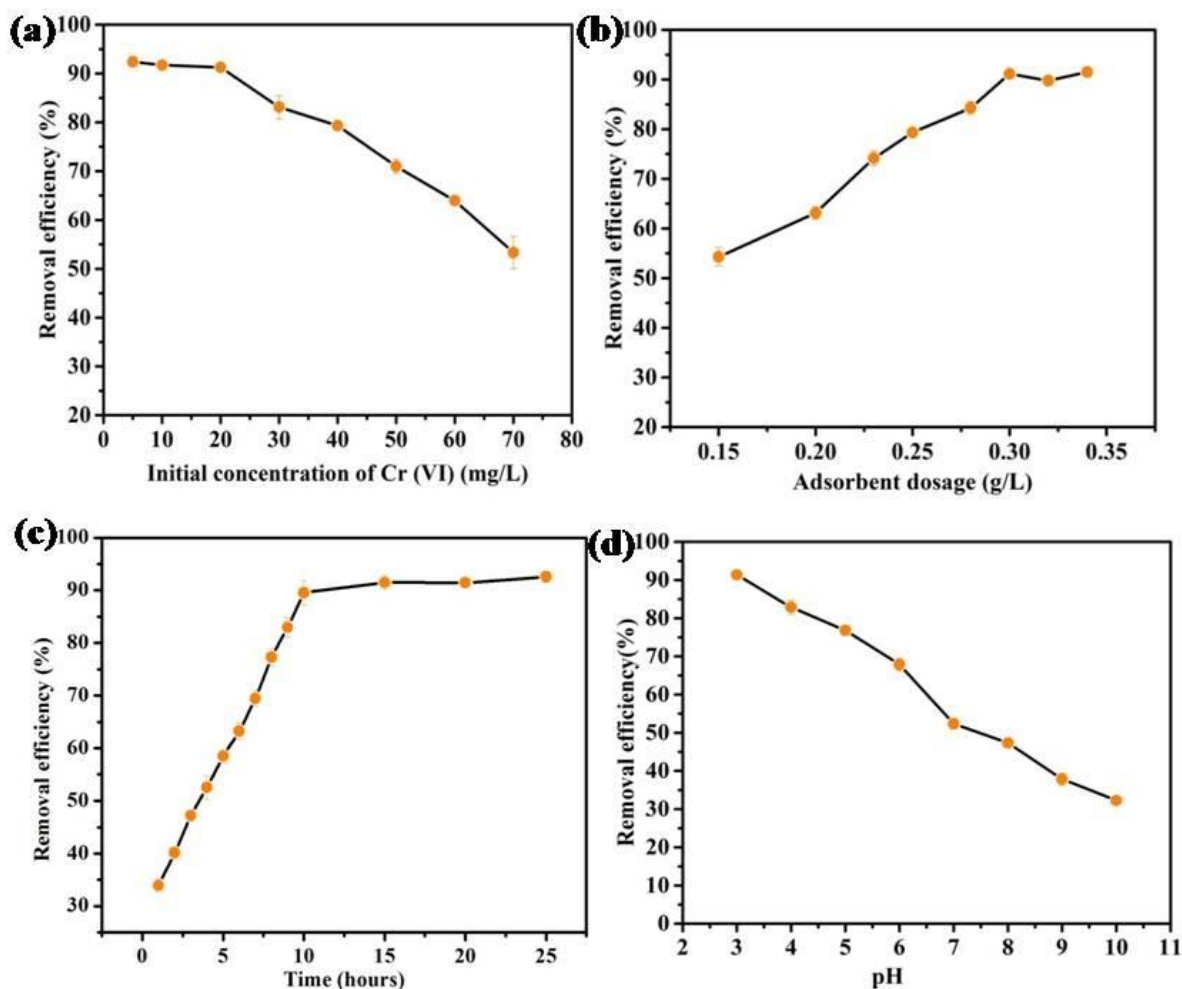


Figure 6.9 (a) the removal of Cr (VI) at different concentrations (b) Effect of adsorbent dosage on Cr (VI) adsorption (c) Effect of time on adsorption of Cr (VI) and (d) Effect of pH on the removal efficiency.

Among all the parameters contact time is one of the most important factors which affects the adsorption capacity of the adsorbent. This is shown in Figure 9c. We varied the contact time from 1 to 25 hours by keeping other parameters constant (pH 3, 20 mg/L Chromium (VI) concentration, adsorbent dose 0.3 g, room temperature (25 °C) and shaking speed 160 rpm). In this plot we observed that 1 to 10 hours of contact time the removal efficiency of Chromium (VI) gradually increases. The maximum adsorption of Chromium (VI) occurred at 10 hours to 25 hours of contact time indicating 91 % of removal efficiency. It occurs due to the availability of maximum numbers of unoccupied surface sites for adsorption process [461]. Thus 10 hours was selected as optimum contact time for further experiments.

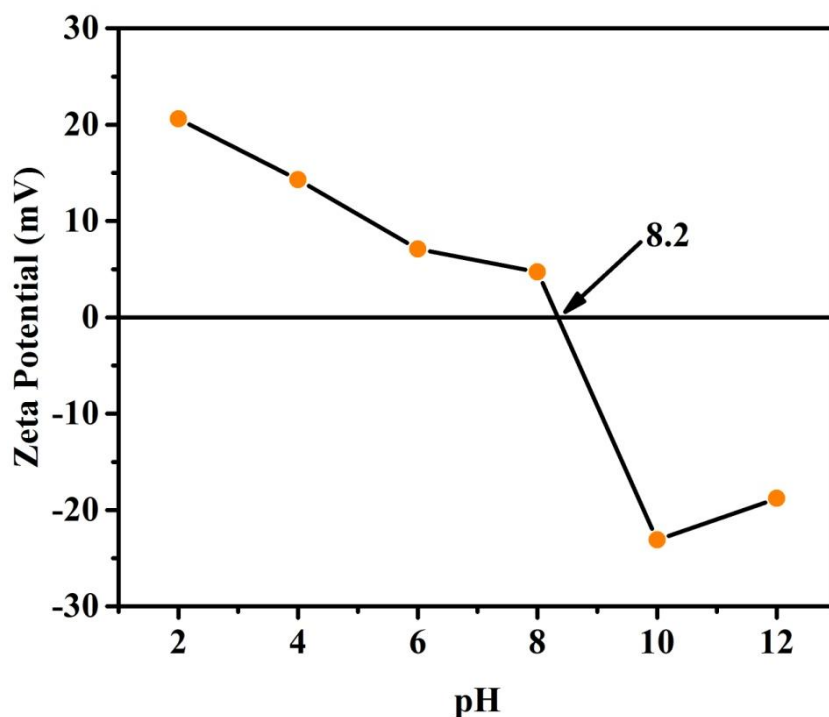


Figure 6.10 Zeta potential plot of GO-Fe₃O₄-APTES.

The effect of pH on the adsorption process is an important parameter and shown in Figure 6.9d. We varied the pH 3 to 10 by keeping other parameters constant such as room adsorbent dose (0.3gm), Initial Chromium (VI) concentration 20 mg/L), temperature (25 °C), contact time (10 hours) and shaking speed (160 rpm). It was observed that at pH 3 the removal efficiency was found to be 91%. After that it significantly decreases up to 34% at pH 10. In acidic medium Chromium (VI) exist as HCrO_4^- , $\text{Cr}_2\text{O}_7^{2-}$ and it is found in form of CrO_4^{2-} above pH 6. Now it is important to find the surface charge of GO-Fe₃O₄-APTES at different pH. Zeta-potential is the best technique to confirm the surface charge of the material. From zeta-potential (Figure 6.9) measurement we found that 8.2 is isoelectric point. The GO-Fe₃O₄-APTES has positive charge at $\text{pH} < 8.2$, so it favors electrostatic attraction[462]. Furthermore, at pH 3 maximum positive charge was observed, that corresponds to strong electrostatic attraction between highly positive charged material and negatively charged chromium ion. Above pH 3, the positive charge decreases so the removal efficiency decreases. Similarly, $\text{pH} > 8.2$ the adsorbent surface becomes negatively charge and hence the material repels negative chromium ion ref. At $\text{pH} < 3$, the removal efficiency decreases because more H^+ ions react with $\text{Cr}_2\text{O}_7^{2-}$ and HCrO_4^- forming $\text{H}_2\text{Cr}_2\text{O}_7$ and H_2CrO_4 which are neutral and could not adsorb[463].

Shaking speed is one of the most important factors which affect the adsorption capacity of the adsorbent. To determine the effect of agitation speed, 80 to 160 rpm of agitation speed was

set to check the adsorption efficiency. Figure 6.11 shows that increasing the speed of agitation from 80 to 160 rpm, the percentage of Chromium (VI) removal efficiency also increases. At 160 rpm of agitation speed maximum adsorption of Chromium (VI) occurs. This is caused due to an increase in the intraparticle diffusion and film diffusivity[464].

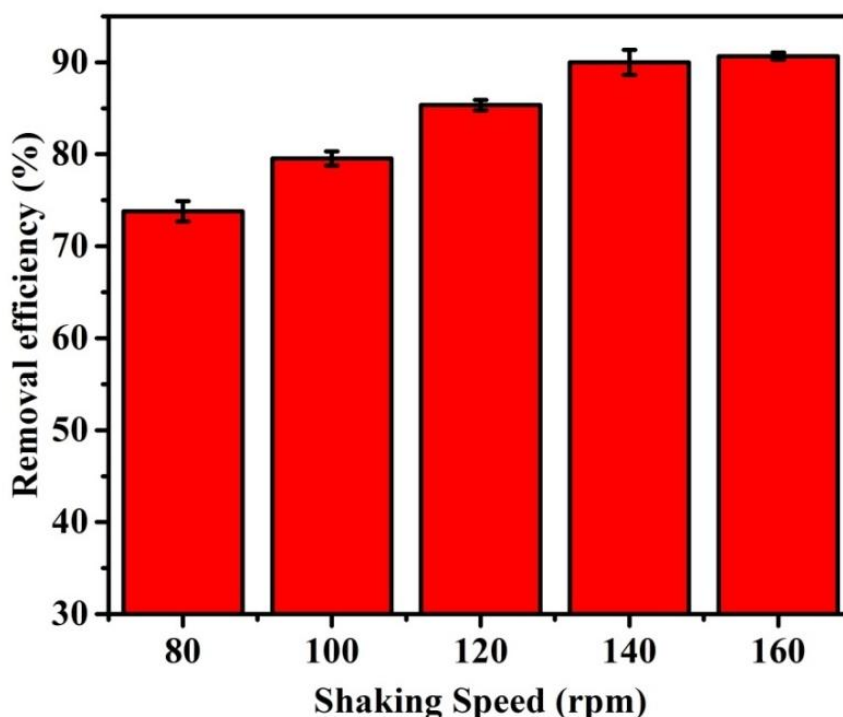


Figure 6.11 Effect of shaking speed on the adsorption of Cr (VI) onGO-Fe₃O₄-APTES.

6.4.3 Adsorption kinetics

Figure 6.12 shows the linear form of Pseudo-first-order, Pseudo-second-order and intra-particle diffusion model for Chromium (VI) adsorption. The computed result which obtained from three models is listed in Table 6.1.comparing to the R^2 value, pseudo-second-order kinetics is well fitted with the Chromium (VI) adsorption [465]. Therefore, this result shows chemisorptions between adsorbent and adsorbate[466]. Intra-particle diffusion model is the best model to identify the adsorption diffusion mechanism. According to this model, if the line passing through origin, then the adsorption process is controlled by intra-particle diffusion, while if the data exhibit multilinear plot but does not pass through origin, then more steps involved the adsorption process [467, 468].Figure 6.12c shows three straight lines which indicate more than one steps are involved in the adsorption mechanism. The first straight line ascribes to outer surface adsorption that means Chromium (VI) diffuses through the solution to the outer adsorbent surface. The middle line corresponds to the gradual adsorption reflecting intra-particle diffusion as the rate-limiting step. The final plateau relates the equilibrium stage and surface adsorption since the diffusion mechanism starts to slow

down and level out[469, 470].From the above results, it could be inferred that the diffusion mechanism was involved in the multi adsorption process.

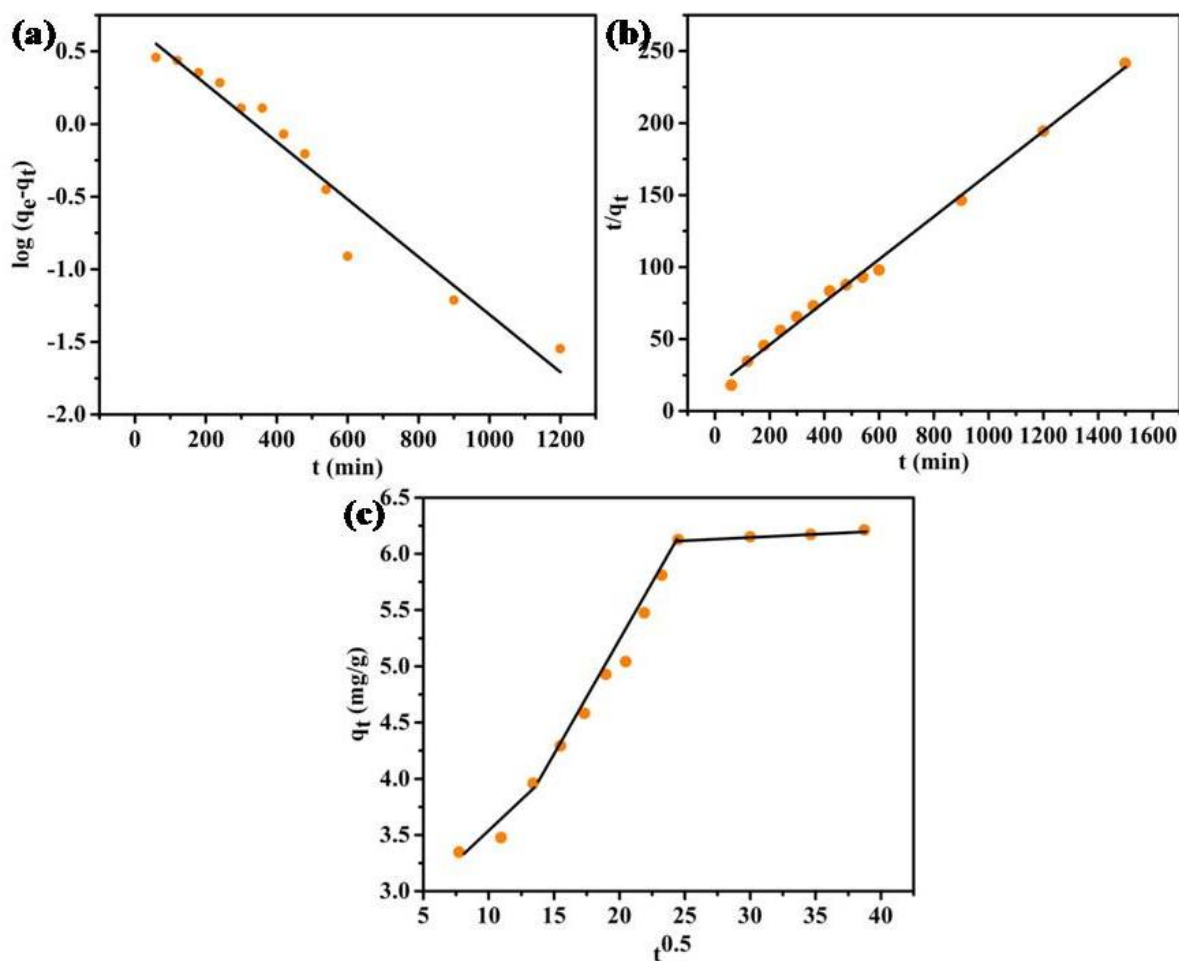


Figure 6.12 (a) Pseudo first-order kinetic model,(b) Pseudo second-order kinetic model and (c) Intraparticle diffusion model for the adsorption of chromium (VI) on GO-Fe₃O₄-APTES

Table 6.1 Kinetic parameters for Chromium (VI) adsorption onGO-Fe₃O₄-APTES powder.

Pseudo-First order Kinetics	Chromium (VI)
q_e (mg/g)	1.956
K_1 (mg/g)	0.0045
R^2	0.95
Pseudo-Second order Kinetics	
q_e (mg/g)	6.744
K_2	0.0013
R^2	0.99
Intraparticle diffusion model	
k_i (L/mg)	0.106
C	2.769
R^2	0.84

6.4.4 Adsorption Isotherm

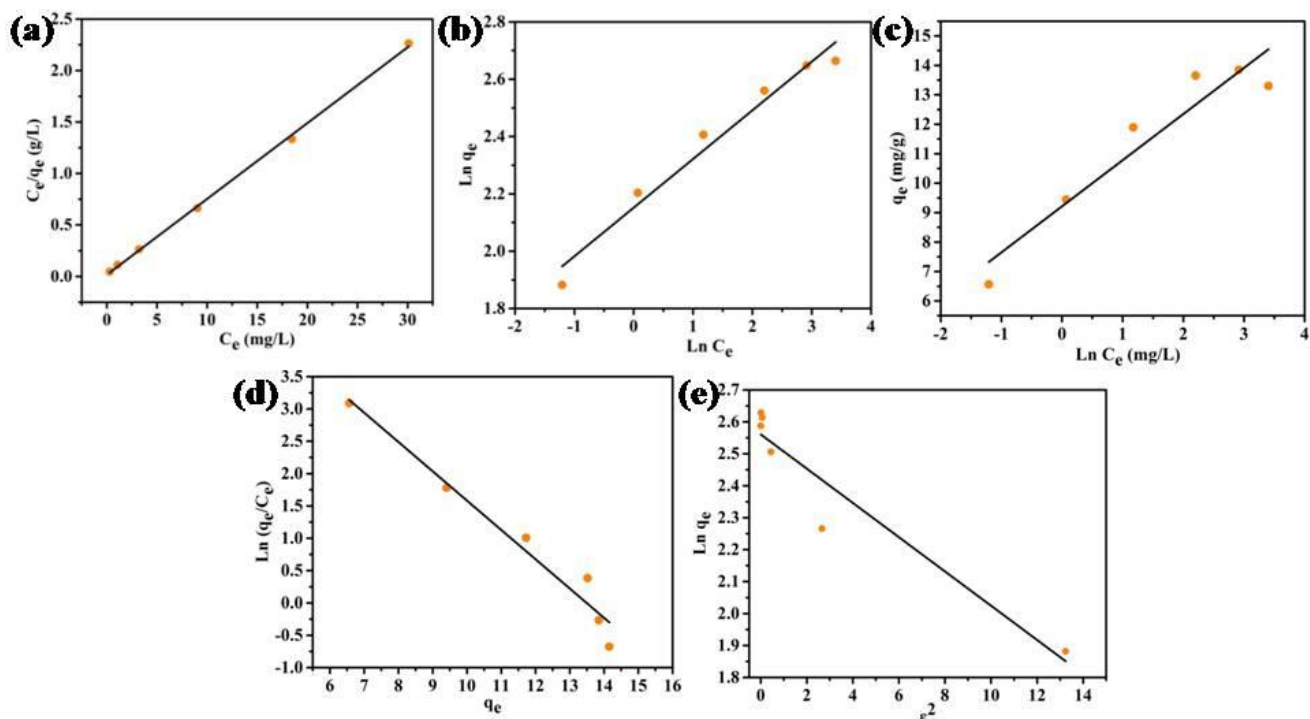


Figure 6.13 (a) Langmuir, (b) Freundlich, (c) Temkin, (d) Elovich and (e) Dubinin-Radushkevich adsorption of Chromium (VI) on GO-Fe₃O₄-APTES.

The adsorption isotherm models such as Langmuir, Freundlich, Temkin, Dubinin-Radushkevich (D-R) and Elovich were selected to define the adsorption process. All isotherm models are demonstrated graphically in Figure 6.13 and the isotherm parameters are listed in Table 6.2. Among five isotherm models, Langmuir isotherm model ($R^2=0.99$) is more appropriate as compared to R^2 value. The Langmuir isotherm model agrees to the formation of monolayer adsorption in between Chromium (VI) on the surface of GO-Fe₃O₄-APTES. The maximum adsorption capacity ($q_m=60.53$) is higher than other reported adsorbent are shown in Table 6.3. The calculated R_L value (0.011) within the range between 0 to 1 which was shown favourable adsorption of Chromium (VI) on GO-Fe₃O₄-APTES[455]. From Freundlich isotherm model it was observed that the value of $1/n$ is 0.169, which is less than 1. It Shows favorable adsorption of adsorbate and adsorbent[471]. Temkin isotherm model is favorable for adsorption of Chromium (VI) because it shows smaller value of Temkin constant ($B_1=1.56$)[472].

6.4.5 Influence of co-existing ion

The studies on the Chromium (VI) removal were observed in the presence of different ions such as Sulphate, Phosphate, carbonate, bicarbonate, fluoride, nitrate, and chloride, which is shown in Fig12. The adsorption procedure was carried out in presence of these ions keeping other parameters constant i.e. adsorbent dosage 0.3g, initial Chromium (VI) concentration 20

mg/L, pH of the solution is 3, shaking speed 160 rpm and an optimum time 10 hours. About 20 ml of each anion having a concentration of 20 mg/L was added to the polyethylene bottle and the adsorption efficiency was measured. Carbonate, fluoride, and phosphate had more impact whereas nitrate, chloride, bicarbonate, and sulfate had little impact on the Chromium (VI) adsorption. The more changes were observed due to change in solution pH caused by the anions. The adsorption capacity of Chromium (VI) increased in the order of chloride > nitrate > sulphate > bicarbonate > phosphate > fluoride > carbonate

Table 6.2 Isotherm parameters for the adsorption of chromium (VI) on to GO-Fe₃O₄-APTES powder at room temperature (25 °C).

Langmuir isotherm Parameter	Chromium (VI)
q _m (mg/g)	60.53
b (mg/g)	4.45
R ²	0.99
Freundlich isotherm Parameter	
K _f (L/g)	8.60
n	5.88
R ²	0.96
Temkin isotherm Parameter	
K _T (L/mg)	357.66
B ₁	1.56
R ²	0.90
Dubbin-Radushkevich isotherm parameter	
q _m (mg/g)	12.94
E	3.05
R ²	0.92
Elovich isotherm Parameter	
K _E	236.57
q _m (mg/g)	2.18
R ²	0.88

6.4.6 Reusability of adsorbent

The primary purpose of reusability is to recover the deleted material. This study is a very chief parameter to study the regeneration or effectiveness of the adsorbent. We have noticed that at lower pH maximum adsorption of Chromium (VI) occurs. Hence for the reusability

study higher pH values were needed. Desorption of Chromium (VI) was conducted by washing Chromium (VI) with distilled water and various concentrations of Na₂CO₃, NaHCO₃, and NaOH. The desorption efficiency of H₂O, Na₂CO₃ and NaOH was noticed to be 1%, 83%, 74%, and 92% respectively (Figure 6.15a). Hence for the desorption process 0.5 M of NaOH solution was used. The plot shows desorption of Chromium (VI) having different pH conditions. Some distilled water was used in this experiment to remove undesirable ions present on the surface of the adsorbent (Figure 6.15b). From the plot it was noticed that after 5 cycles, adsorption efficiency decreases up to 51%. This is shown that the reusability of the material was highly efficient.

Table 6.3 Comparison of performance of the proposed method with some previously reported Chromium (VI) adsorption systems

Adsorbent	Langmuir q_{max} (mg/g)	References
Polyethylenimine facilitated ethyl cellulose	36.8	[473]
Graphene oxide montmorillonite nanocomposite	12.86	[474]
Magnetite polyethylenimine-montmorillonite	8.8	[475]
Activated carbon	3.46	[476]
<i>Neurosporacrassa</i> (acetic acid pretreated)	15.8	[477]
Brown coal	50.9	[478]
Olive oil industry waste	13.9	[479]
<i>Fucusvesiculosus</i> (brown algae)	42.7	[480]
<i>Ulva lactuca</i> (green algae)	27.6	[480]
<i>Ulva</i> spp. (green algae)	30.2	[480]
<i>Polysiphonia lanosa</i> (red algae)	45.8	[480]
<i>Palmaria palmate</i> (red algae)	33.8	[480]
Saccharomyces cerevisiae	32.6	[481]
Alternantheraphiloxeroides	17.7	[482]
GO- Fe₃O₄-APTES	60.53	Present study

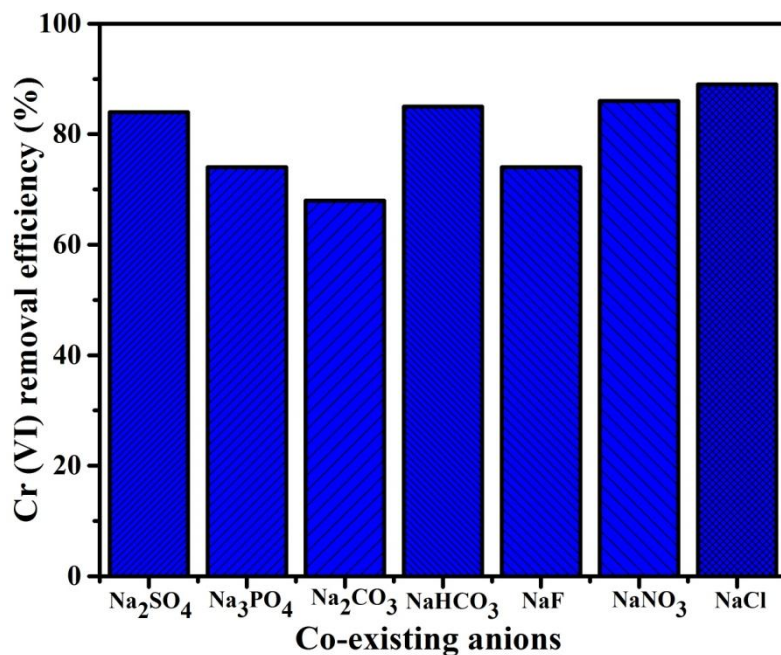


Figure 6.14 Effect of co-existing anions.

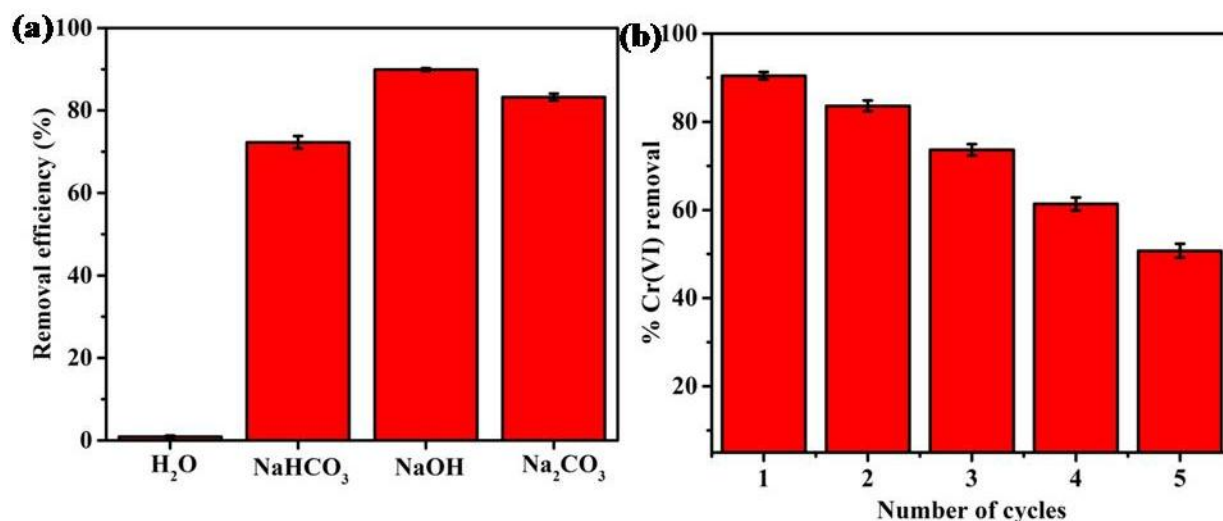


Figure 6.15 Regeneration and reusability of GO-Fe₃O₄-APTES.

6.4.7 Adsorption mechanism

The FT-IR peak of after adsorption of Chromium (VI) on GO-Fe₃O₄-APTES material was shown in Figure A6. Comparing to the FT-IR data of before and after adsorption of chromium (VI), the N-H bending vibration was shifted from 1570 cm⁻¹ to 1577 cm⁻¹ and –CO-NH- was shifted from 1650 cm⁻¹ to 1664 cm⁻¹ with a high intense peak which attributes the bonding between the nitrogen and chromium. The presence of one new peak at 943 cm⁻¹ was ascribing to stretching of Cr-O in CrO₇²⁻ groups[438]. These changes in the FT-IR spectrum after adsorption shows chromium (VI) successfully adsorb the synthesized material. The surface morphology of GO-Fe₃O₄-APTES was aggregated after adsorption of chromium

(VI) (Figure A7a,b). The presence of Chromium on the GO-Fe₃O₄-APTES was further confirmed by EDS analysis. Figure A7c shows the EDS mapping of the material after adsorption of chromium (VI). It was clearly seen the chromium adsorbed uniformly on the surface of GO-Fe₃O₄-APTES. Based on the above results, the possible mechanism for Chromium (VI) was the protonated amine groups and hydroxyl groups of GO-Fe₃O₄-APTES by electrostatic interaction (Shown in Figure 6.16).

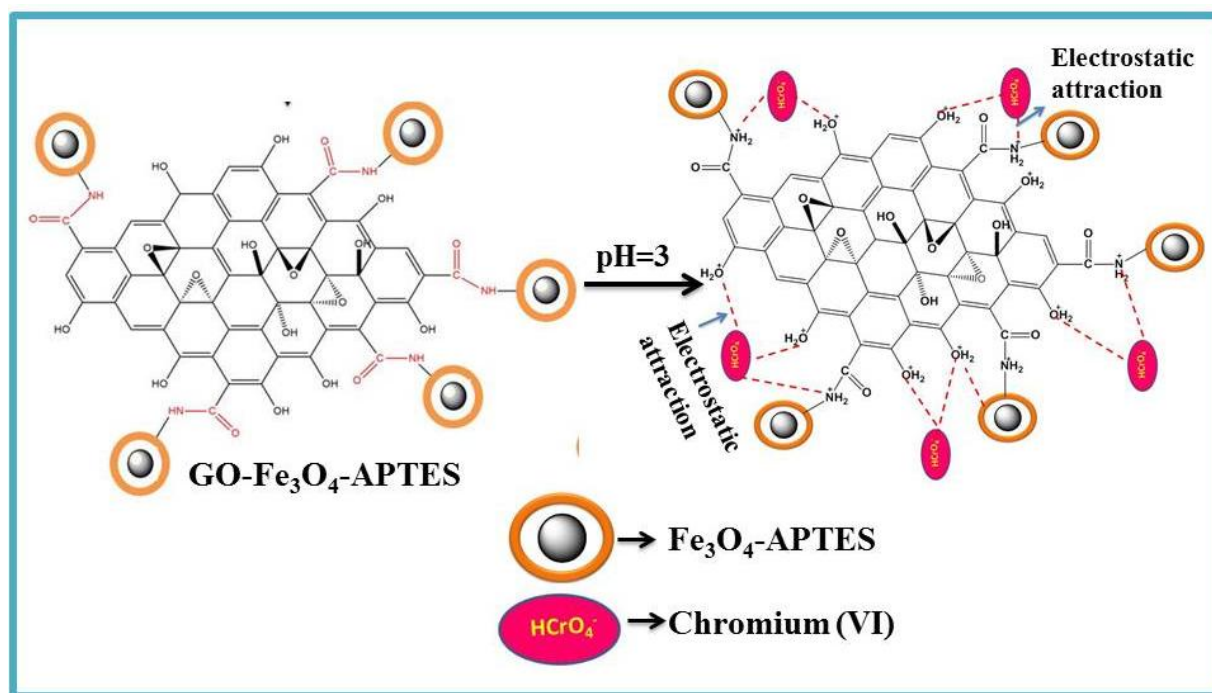


Figure 6.16 Plausible mechanisms for Chromium (VI) removal.

6.4.8 Antibacterial activity

Bactericidal activity of the synthesized material is dependent on the concentration of material and concentration of bacterial cell suspension[459]. Our study includes the initial bacterial load of 10^6 cfu/ml for interaction with GO-Fe₃O₄-APTES. Different concentration of GO-Fe₃O₄-APTES (10, 20, 40, 80, 160 μ g/ml) was treated with bacteria (10^6 cfu/ml) and bacterial growth inhibition was assessed. Disc diffusion assay reveals that the GO-Fe₃O₄-APTES shows the antibacterial activity at 160 μ g/ml and 80 μ g/ml with clear zone of inhibition at 160 μ g/ml but the zone of inhibition is not clearly visible at 20 and 40 μ g/ml against the *E.coli* and *B.subtilis*(Figure 6.17). Antibacterial activity of GO-Fe₃O₄-APTES is dependent on the concentration and time of exposure with the bacteria. Assessment of bacterial growth inhibition by colony count method has suggested that the GO-Fe₃O₄-APTES shows the good antibacterial activity at 160 μ g/ml and its activity decreases gradually with decreasing concentration of the material (Figure 6.18). Growth kinetics study of both the bacteria in the presence as well as in the absence of GO-Fe₃O₄-APTESsuggested that the significant growth inhibition observed in treated one in comparison to control (Figure 6.19).

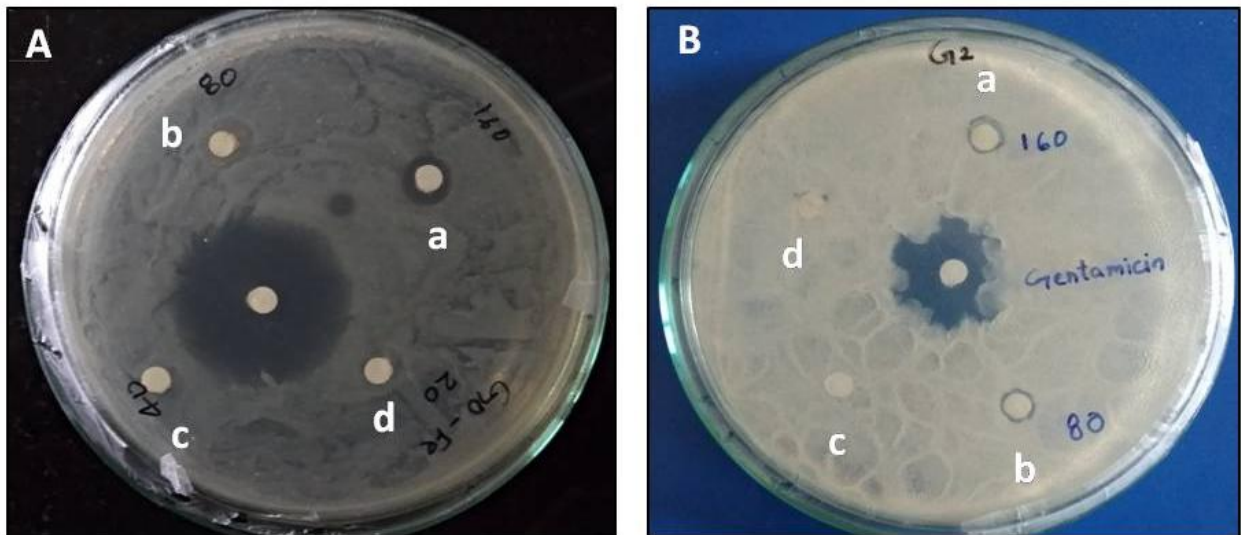


Figure 6.17 Image (A) shows the antibacterial activity of GO-Fe₃O₄-APTES against the *E.coli* at concentration 160 µg/ml (a) with a clear zone of inhibition but the zone of inhibition is not clearly visible at 80, 40, 20 µg/ml shown in b,c,d respectively. Image (B) shows the antibacterial activity of GO-Fe₃O₄-APTES against *B. subtilis* at concentration 160 µg/ml (a) and 80 µg/ml (b) with clear zone of inhibition but the zone of inhibition is not clearly visible at 40, 20 µg/ml shown in c,d respectively. At middle shows the clear zone of inhibition for gentamicin against both the bacteria.

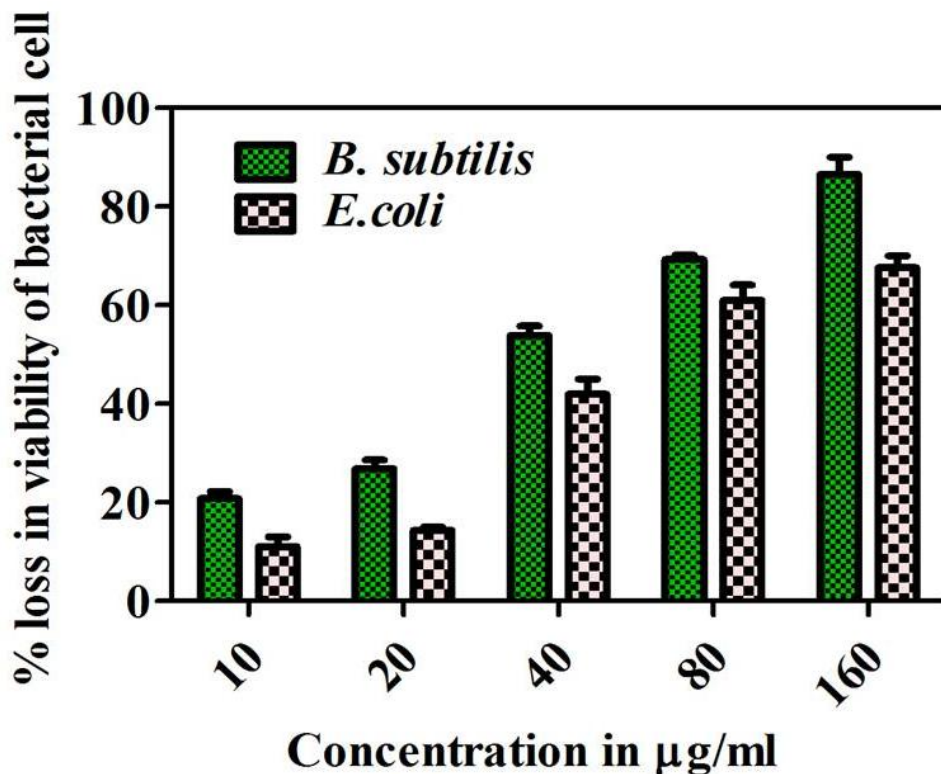


Figure 6.18 Shows the Concentration-dependent effect of GO-Fe₃O₄-APTES, when 10, 20, 40, 80, 160 µg/ml of GO-Fe₃O₄-APTES was incubated with *E.coli* and *B. subtilis* for 6 hours. Percentage viability of bacteria at varying concentration of GO-Fe₃O₄-APTES was measured.

The proposed mechanism of antibacterial activity is supported by an increase in reactive oxygen species (ROS) generation at higher concentration 160 $\mu\text{g/ml}$ and it gradually decreases with decreasing concentration of the prepared material. To quantify the ROS generation the bacteria were treated with DCFDA which react with the ROS and produces the green fluorescence which is measured by the Fluorimeter (Figure 6.20).

Higher the fluorescence intensity higher is the amount of ROS generated from the bacteria in presence of GO- Fe_3O_4 -APTES. ROS generated from the bacteria get mixed with the culture media which shows the fluorescence in presence of DCFDA. Bacteria show the ROS production in stress condition which could be observed in the control batch which is not treated with GO- Fe_3O_4 -APTES. FESEM study also reveals the change in membrane integrity of bacteria with alteration in its morphology (Figure A8 and A9).

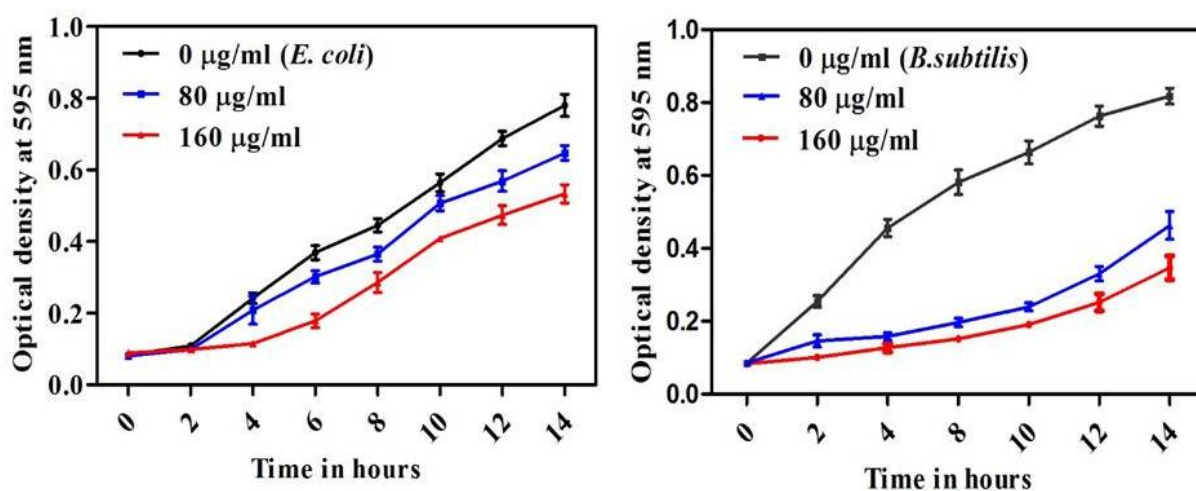


Figure 6.19 Growth of *E. coli* and *B. subtilis* in the presence of GO- Fe_3O_4 -APTES at concentration 160 and 80 $\mu\text{g/ml}$ in varying interval of time.

Both gram-positive and gram-negative bacteria show variation in the toxicity with respect to GO- Fe_3O_4 -APTES bactericidal activity. In case of gram-negative bacteria (*E. coli*) peptidoglycan layer is protected by an outer layer composed of lipopolysaccharide which helps to protect the bacteria from the chemical exposure[483]. Thus the bacterial death was less in *E. coli* in comparison to gram-positive bacteria (*B. subtilis*). Direct contact of graphene material with the bacteria[426] increases oxidative stress[484] as the main mechanism responsible for bacterial growth inhibition and including this the iron oxide itself causes the increased oxidative stress[485]. Increased oxidative stress is also responsible for the release of hydroxyl radical which bind to the carbonyl group of peptide linkage in the bacterial cell membrane which distorts the structure of cell membrane[486] (Figure A9b). It is also reported that the bacterial cell membrane gets ruptured when it comes in contact with

GO[487]. The GO binds to the water molecule by the help of carbonyl group and free radical sites and thus form the colloidal solution which enhances the easy accessibility of material to interact with the bacteria[488, 489].

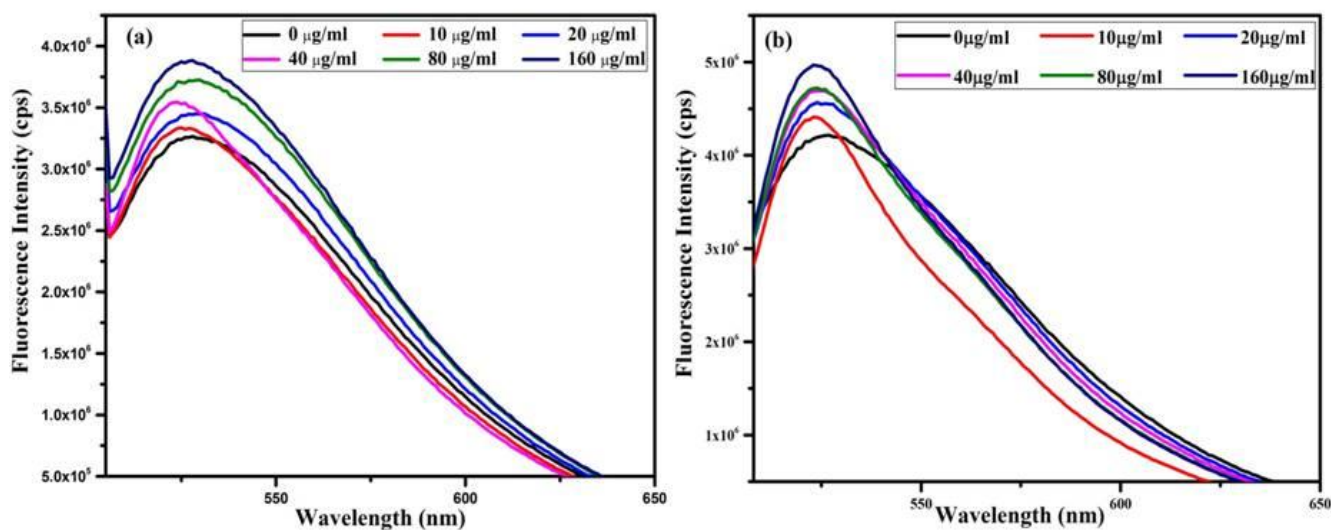


Figure 6.20 GO-Fe₃O₄-APTES induced ROS generation in (a) *E.coli* and (b) *B. subtilis*. Fluorescence intensity shows the ROS generation at different concentration of GO-Fe₃O₄-APTES. Higher fluorescence intensity indicates the excess generation of ROS.

6.5 Summary

Fe₃O₄-APTES was successfully fabricated on GO through organic transformation reaction followed by co-precipitation method. The functionalization, formation, morphology of the material, magnetic properties and surface area were characterized by FTIR, XRD, FE-SEM, TEM, HRTEM, Raman and BET technique. The synthesized GO-Fe₃O₄-APTES is a unique adsorbent for Chromium (VI). Experimental results revealed that the removal efficiency was pH-dependent and higher removal efficiency occurs at pH 3. Pseudo-second-order kinetics model was best fit for the adsorption process and shows chemisorptions. Langmuir isotherm is best fit for Chromium (VI) adsorption on GO-Fe₃O₄-APTES with an adsorption capacity of 60.5 mg/g at room temperature (25°C). It has shown that the coexisting ions had no significant impact on adsorption efficiency. The adsorbed chromium could be effectively washed from the adsorbent into the solution using 0.5 M of NaOH. It can be concluded that GO-Fe₃O₄-APTES material has got good reusable ability. GO-Fe₃O₄-APTES has shown inhibitory effect on the growth of *E.coli* and *B.subtilis*.

Chapter 7

7. Conclusion and Scope of Future Work

7.1 Conclusion

In this research work, we have successfully prepared iron oxide and iron oxide-based nanomaterials such as Fe₃O₄-TSPED-Tryptophan, Fe₃O₄-GG, Fe₃O₄-APTES-EDTA and GO-Fe₃O₄-APTES using precipitation process. The formation, structure, phase, shape, size, morphology, surface area, magnetic properties and adsorption studies of the prepared iron oxide and iron oxide-based materials have been analysed by various techniques such as: FT-IR, XRD, TEM, FE-SEM, VSM, BET surface area, TGA, Zeta potential, Raman and UV-Vis Spectroscopy techniques. The synthesized nanomaterials were used as adsorbents for toxic organic dye (Congo red) and heavy metals (Pb²⁺, Cd²⁺, Ni²⁺, Co²⁺, Cu²⁺, Cr⁺⁶). The following major conclusions have been drawn from this study.

- Fe₃O₄ nanoparticles were synthesized using chemical co-precipitation method. The advantage of this process is because of the high surface area (approximately 220 m²/g). The synthesized materials were used as effective adsorbents with easy separation using an external magnetic field (Ms= 71 emu/g).
- The Fe₃O₄-TSPED-Tryptophan was synthesized and used for the removal of Congo red dye from aqueous solution. The average particle size was found to be 47 nm with surface area 138.7 m²/g. The maximum adsorption capacity was observed as 183.15 mg/g.
- The Guar-gum coated Fe₃O₄ nanocomposite was synthesized using glutaraldehyde as a cross-linker. The Fe₃O₄-GG was observed as a novel adsorbent for Congo red dye from aqueous solution. The diameter of the nanocomposites was measured as 15 nm with high surface area found to be 158 m²/g. The maximum adsorption capacity was shown as 60.24 mg/g.
- Fe₃O₄ nanoparticles modified with hexadentate ligand (EDTA) were synthesized using APTES as a cross-linker. The Fe₃O₄-APTES-EDTA was proved to be a good adsorbent for removal of heavy metals (Pb²⁺, Cd²⁺, Ni²⁺, Co²⁺, Cu²⁺) with maximum adsorption capacity (q_{max}) 11.31, 13.88, 7.64, 4.86, 78.67 mg/g.
- The GO-Fe₃O₄-APTES was successfully synthesized using organic transformation reaction followed by co-precipitation method. The spherical particle of Fe₃O₄-APTES was successfully modified on the graphene oxide layer. The GO-Fe₃O₄-APTES was

experimentally found to be an excellent adsorbent towards Chromium (VI) with maximum adsorption capacity (q_{\max}) 60.53 mg/g.

- All the adsorption process follows Langmuir isotherm model and pseudo-second-order kinetic model.
- All the synthesized materials can be reusable and have good maximum adsorption capacity compare to other existing adsorbents.
- Fe_3O_4 -TSPED-Tryptophan and $\text{GO-Fe}_3\text{O}_4$ -APTES were tested against Gram-negative (*E. coil*) and Gram-positive (*B. subtilis*) bacteria to prove their antibacterial properties.

7.2 Scope of Future Work

Based on the findings of the present work, the following points are considered to be the future scope:

- New and novel magnetic nanomaterials involving other elements will be synthesized and subsequently will be applied in adsorption of heavy metals as well as hazardous organic pollutants in more and cheaper efficiency.
- Application of different bio-char (potato peel, green pea peel, red algae, and sugarcane baggage) modified magnetic-based iron oxide nanoparticle towards wastewater treatment.
- Along with the heavy metals and organic hazardous contaminants, removal of radioactive metals from water bodies will also be carried out by the novel nanomaterials.
- Possible application of the magnetic nanomaterial towards the degradation of organic dyes along with their adsorption.
- Impact of the synthesized nanomaterials on different proteins will be studied with respect to the stability, kinetics, and dynamics of the later along with the cytotoxicity investigations.
- Development of a versatile water filter for the removal of inorganic and organic contaminants for field application.

Bibliography

- [1] H. Perlman, Water Science for Schools, USGS, (1996) 98-99. <http://ga.water.usgs.gov/edu/earthwherewater.html>.
- [2] N. Savage, M.S. Diallo, Nanomaterials and water purification: Opportunities and challenges, *J. Nanoparticle Res.*, 7 (2005) 331-342.
- [3] J. Mateo-Sagasta, S.M. Zadeh, H. Turrall, Water pollution from agriculture: a global review, *Food Agric. Organ, United Nations*, (2017) 35. <http://www.fao.org/33/a-i7754e.pdf>.
- [4] J. Savedge, Water pollution: Causes, effects, and solutions, (2017) <https://www.thoughtco.com/water-pollution-causes-effects-and-solutions-1140786>.
- [5] Worlds top ten most polluted river, (2018) <https://www.conserve-energy-future.com/most-polluted-rivers-world.php>.
- [6] M. Bhaumik, A. Maity, V.V. Srinivasu, M.S. Onyango, Enhanced removal of Cr(VI) from aqueous solution using polypyrrole/Fe₃O₄ magnetic nanocomposite, *J. Hazard. Mater.*, 190 (2011) 381-390.
- [7] G. Cao, L. Su, X. Zhang, H. Li, Hydrothermal synthesis and catalytic properties of α - and β -MnO₂ nanorods, *Mater. Res. Bull.*, 45 (2010) 425-428.
- [8] M. Yang, J. He, Fine tuning of the morphology of copper oxide nanostructures and their application in ambient degradation of methylene blue, *J. Colloid Interface Sci.*, 355 (2011) 15-22.
- [9] P.C. Nagajyoti, K.D. Lee, T.V.M. Sreekanth, Heavy metals, occurrence and toxicity for plants: A review, *Environ. Chem. Lett.*, 8 (2010) 199-216.
- [10] X. Liu, J. Wu, J. Xu, Characterizing the risk assessment of heavy metals and sampling uncertainty analysis in paddy field by geostatistics and GIS, *Environ. Pollut.*, 141 (2006) 257-264.
- [11] O. Abollino, M. Aceto, M. Malandrino, C. Sarzaninia, E. Mentasti, Adsorption of heavy metals on Na-montmorillonite. Effect of pH and organic substances, *Water Res.*, 37 (2003) 1619-1627.
- [12] K.P. Singh, D. Mohan, V.K. Singh, A. Malik, Studies on distribution and fractionation of heavy metals in Gomti river sediments - A tributary of the Ganges, India, *J. Hydrol.*, 312 (2005) 14-27.
- [13] N. Kundu, M. Panigrahi, S. Tripathy, S. Munshi, M. Powell, B. Hart, Geochemical appraisal of fluoride contamination of groundwater in the Nayagarh District of Orissa, India. *Environmental Geology*, 41 (2002) 451-460.
- [14] K. Brindha, R. Rajesh, R. Murugan, L. Elango, Fluoride contamination in groundwater in parts of Nalgonda District, Andhra Pradesh, India. , *Environ. Monit. Assess.*, 172 (2011) 481-492.
- [15] J. Hussain, I. Hussain, K.C. Sharma, Fluoride and health hazards: Community perception in a fluorotic area of central Rajasthan (India): An arid environment., *Environ. Monit. Assess.*, 162 (2010) 1-14.
- [16] A.M. Fan, V.E. Steinberg, Health implications of nitrate and nitrite in drinking water: an update on methemoglobinemia occurrence and reproductive and developmental toxicity, *Regul. Toxicol. Pharmacol.*, 23 (1996) 35-43.
- [17] M. Yusuf, F.M. Elfghi, S.A. Zaidi, E.C. Abdullah, M.A. Khan, Applications of graphene and its derivatives as an adsorbent for heavy metal and dye removal: a systematic and comprehensive overview, *RSC Adv.*, 5 (2015) 50392-50420.

- [18] C. Zhang, L. Wu, Y. Luo, H. Zhang, P. Christie, Identifying sources of soil inorganic pollutants on a regional scale using a multivariate statistical approach: Role of pollutant migration and soil physicochemical properties, *Environ. Pollut.*, 151 (2008) 470-476.
- [19] P. Zhuang, M.B. McBride, H. Xia, N. Li, Z. Li, Health risk from heavy metals via consumption of food crops in the vicinity of Dabaoshan mine South China, *Sci. Total. Environ.*, 407 (2009) 1551-1561.
- [20] X. Wang, T. Sato, B. Xing, S. Tao, Health risks of heavy metals to the general public in Tianjin, China via consumption of vegetables and fish, *Sci. Total. Environ.*, 350 (2005) 28-37.
- [21] S. Khan, Q. Cao, Y.M. Zheng, Y.Z. Huang, Y.G. Zhu, Health risks of heavy metals in contaminated soils and food crops irrigated with wastewater in Beijing, China, *Environ. Pollut.*, 152 (2008) 686-692.
- [22] M. Ahmaruzzaman, Industrial wastes as low-cost potential adsorbents for the treatment of wastewater laden with heavy metals, *Adv Colloid Interface Sci*, 166 (2011) 36-59.
- [23] A. Demirbas, Heavy metal adsorption onto agro-based waste materials: A review, *J. Hazard. Mater.*, 157 (2008) 220-229.
- [24] J.f. Peng, Y.h. Song, P. Yuan, X.y. Cui, G.l. Qiu, The remediation of heavy metals contaminated sediment., *J. Hazard. Mater.*, 161 (2009) 633-640.
- [25] H. Qdais, H. Moussab, Removal of heavy metals from wastewater by membrane processes : a comparative study., *Desalination*, 164 (2004) 105-110.
- [26] A. Dabrowski, Z. Hubicki, P. Podkościelny, E. Robens, Selective removal of the heavy metal ions from waters and industrial wastewaters by ion-exchange method, *Chemosphere*, 56 (2004) 91-106.
- [27] M.M. Matlock, B.S. Howerton, D.A. Atwood, Chemical Precipitation of Lead from Lead Battery Recycling Plant Wastewater, *Ind. Eng. Chem. Res.*, 41 (2002) 1579-1582.
- [28] M.H. Wong, Ecological restoration of mine degraded soils , with emphasis on metal contaminated soils., *Chemosphere*, 50 (2003) 775-780.
- [29] D. Park, Y.S. Yun, J.H. Jo, J.M. Park, Biosorption process for treatment of electroplating wastewater containing Cr(VI): Laboratory-scale feasibility test., *Ind. Eng. Chem. Res.*, 45 (2006) 5059-5065.
- [30] O.S. Amuda, I.A. Amoo, Coagulation/flocculation process and sludge conditioning in beverage industrial wastewater treatment., *J. Hazard. Mater.*, 141 (2007) 778-783.
- [31] O.S. Amuda, A. Alade, Coagulation/flocculation process in the treatment of abattoir wastewater., *Desalination*, 196 (2006) 22-31.
- [32] F. Renault, B. Sancey, P.M. Badot, G. Crini, Chitosan for coagulation/flocculation processes - An eco-friendly approach, *Eur. Polym. J.*, 45 (2009) 1337-1348.
- [33] H. Ali, E. Khan, M. Anwar, Phytoremediation of heavy metals - Concepts and applications., *Environ. Chem.*, 91 (2013) 869-881.
- [34] S.S. Ahluwalia, D. Goyal, Microbial and plant derived biomass for removal of heavy metals from wastewater., *Bioresour. Technol.*, 98 (2007) 2243-2257.
- [35] I. Ali, V.K. Gupta, Advances in water treatment by adsorption technology. , *Nat. Protoc.*, 1 (2007) 2661-2667.
- [36] S.H. Lin, R.S. Juang, Heavy metal removal from water by sorption using surfactant-modified montmorillonite, *J. Hazard. Mater.*, 92 (2002) 315-326.
- [37] W.S.W. Ngah, M.A.K. M.Hanafiah, Removal of heavy metal ions from wastewater by chemically modified plant wastes as adsorbents: A review., *Bioresour Technol.*, 99 (2008) 3935-3948.
- [38] Y.S. Ho, W.T. Chiu, C.S. Hsu, C.T. Huang, Sorption of lead ions from aqueous solution using tree fern as a sorbent., *Hydrometallurgy*, 73 (2004) 55-61.
- [39] S.E. Bailey, T.J. Olin, R.M. Bricka, D.D.A. Adrain, review of potentially low-cost adsorbents for heavy metals., *Water Res.*, 33 (1999) 2469-2479.

- [40] K. Kadirvelu, K. Thamaraiselvi, C. Namasivayam, Removal of heavy metal from industrial wastewater by adsorption onto activated carbon prepared from an agricultural solid waste., *Bioresour. Technol.*, 76 (2001) 63-65.
- [41] S. Babel, Low-cost adsorbents for heavy metals uptake from contaminated water: a review, *J. Hazard. Mater.*, 97 (2003) 219-243.
- [42] B. Yu, Y. Zhang, A. Shukla, S. Shukla, K. Dorris, The removal of heavy metal from aqueous solutions by sawdust adsorption-removal of copper, *J. Hazard. Mater.*, 80 (2000) 33-42.
- [43] E. Erdem, N. Karapinar, R. Donat, The removal of heavy metal cations by natural zeolites, *J. Colloid Interface Sci.*, 280 (2004) 309-314.
- [44] D. Sud, G. Mahajan, M.P. Kaur, Agricultural waste material as potential adsorbent for sequestering heavy metal ions from aqueous solutions - A review, *Bioresour Technol.*, 99 (2008) 6017-6027.
- [45] B. Yu, Y. Zhang, A. Shukla, S.S. Shukla, K.L. Dorris, The removal of heavy metals from aqueous solutions by sawdust adsorption-removal of lead and comparison of its adsorption with copper., *J. Hazard. Mater.*, 84 (2001) 83-94.
- [46] S. Mandal, A. Kunhikrishnan, N. S.Bolan, H. Wijesekara, R. Naidu, Application of Biochar Produced From Biowaste Materials for Environmental Protection and Sustainable Agriculture Production, *Environmental material and waste*, (2016) 73-89.
- [47] D.J. Lapworth, N. Baran, M.E. Stuart, R.S. Ward, Emerging organic contaminants in groundwater: A review of sources, fate and occurrence., *Environ. Pollut.*, 163 (2012) 287-303.
- [48] A. Pal, K.Y.H. Gin, A.Y.C. Lin, M. Reinhard, Impacts of emerging organic contaminants on freshwater resources: Review of recent occurrences, sources, fate and effects, *Sci. Total Environ.*, 408 (2010) 6062-6069.
- [49] T.C. Schmidt, L. Zwank, M. Elsner, M. Berg, R.U. Meckenstock, S.B. Haderlein, Compound-specific stable isotope analysis of organic contaminants in natural environments: A critical review of the state of the art, prospects, and future challenges. , *Anal. Bioanal. Chem.*, 378 (2004) 283-300.
- [50] Q.-Y. Cai, C.-H. Mo, Q.-T. Wu, Q.-Y. Zeng, A. Katsoyiannis, Occurrence of organic contaminants in sewage sludges from eleven wastewater treatment plants, China, *Chemosphere* 68 (2007) 1751-1762.
- [51] G. Balasubramanian, D.D. Dionysiou, M.T. Suidan, I. Baudin, J.M. L  n  , Evaluating the activities of immobilized TiO₂ powder films for the photocatalytic degradation of organic contaminants in water, *Appl. Catal. B. Environmen.*, 47 (2004) 73-84.
- [52] H.M. Pinheiro, E. Touraud, O. Thomas, Aromatic amines from azo dye reduction: Status review with emphasis on direct UV spectrophotometric detection in textile industry wastewaters. , *Dyes Pigm.* , 61 (2004) 121-139.
- [53] P.A. Carneiro, G.A. Umbuzeiro, D.P. Oliveira, M.V.B. Zanoni, Assessment of water contamination caused by a mutagenic textile effluent/dyehouse effluent bearing disperse dyes. , *J. Hazard. Mater.*, 174 (2010) 694-699.
- [54] E. Forgacs, T. Cserh  ti, G. Oros, Removal of synthetic dyes from wastewaters: A review., *Environ Int.*, 30 (2004) 953-971.
- [55] S. Srivastava, R. Sinha, D. Roy, Toxicological effects of malachite green *Aqua. Toxicol.*, 66 (2004) 319-329.
- [56] J.W. Lee, S.P. Choi, R. Thiruvengatachari, W.G. Shim, H. Moon, Evaluation of the performance of adsorption and coagulation processes for the maximum removal of reactive dyes, *Dyes Pig.*, 69 (2006) 196-203.
- [57] T. Robinson, G. McMullan, R. Marchant, P. Nigam, Remediation of dyes in textile effluent: A critical review on current treatment technologies with a proposed alternative. , *Bioresour. Technol.*, 77 (2001) 247-255.

- [58] N. Adhoum, L. Monser, Decolourization and removal of phenolic compounds from olive mill wastewater by electrocoagulation, *Chem. Eng. Process.*, 43 (2004) 1281-1287.
- [59] M. Uğurlu, A. Gürses, C. Doğar, M. Yalçın, The removal of lignin and phenol from paper mill effluents by electrocoagulation, *J. Environ. Manage.*, 87 (2008) 420-428.
- [60] M.M. Emamjomeh, M. Sivakumar, Review of pollutants removed by electrocoagulation and electrocoagulation/flotation processes., *J. Environ. Manage.*, 90 (2009) 1663-1679.
- [61] O. Abdelwahab, N. K. Amin, E.S.Z. El-Ashtouky, Electrochemical removal of phenol from oil refinery wastewater, *J. Hazard. Mater.*, 163 (2009) 711-716.
- [62] N. Modirshahla, M.A. Behnajady, S.M.-A.J.o.H. Materials, Investigation of the effect of different electrodes and their connections on the removal efficiency of 4-nitrophenol from aqueous solution by electrocoagulation, *J. Hazard. Mater.*, 154 (2008) 778-786.
- [63] P. Sharma, H. Kaur, M. Sharma, V. Sahore, A review on applicability of naturally available adsorbents for the removal of hazardous dyes from aqueous waste, *Environ. Monit. Assess.*, 183 (2011) 151-195.
- [64] R.L. Tseng, F.C. Wu, R.S. Juang, Liquid-phase adsorption of dyes and phenols using pinewood-based activated carbons, *Carbon*, 41 (2003) 487-495.
- [65] G. Annadurai, R.S. Juang, D.J. Lee, Use of cellulose - based wastes for adsorption of dyes from aqueous solutions, *J. Hazard. Mater.*, 92 (2002) 263-274.
- [66] K. Lin, J. Pan, Y. Chen, R. Cheng, X. Xu, Study the adsorption of phenol from aqueous solution on hydroxyapatite nanopowders., *J. Hazard. Mater.*, 161 (2009) 231-240.
- [67] G. Crini, Studies on adsorption of dyes on beta-cyclodextrin polymer, *Bioresour. Technol.*, 90 (2003) 193-198.
- [68] N. Modirshahla, M.A. Behnajady, S. Mohammadi-Aghdam, Investigation of the effect of different electrodes and their connections on the removal efficiency of 4-nitrophenol from aqueous solution by electrocoagulation., *J. Hazard. Mater.*, 154 (2008) 778-786.
- [69] U.I. Gaya, A.H. Abdullah, Heterogeneous photocatalytic degradation of organic contaminants over titanium dioxide: A review of fundamentals, progress and problems., *J. Photochem. Photobiol. C*, 9 (2008) 1-12.
- [70] L. Zou, Y. Luo, M. Hooper, E. Hu, Removal of VOCs by photocatalysis process using adsorption enhanced TiO₂-SiO₂ catalyst., *Chemical Engineering and Processing: Process Intensification* 45 (2006) 959-964.
- [71] B. Armagan, O. Ozdemir, M. Turan, M.S. Celik, Clay mineral process for colour removal of textile wastewater, *J. Environ. Sci. Hlth. Part A Toxic Hazard Subst Environ*, 38 (2003) 2251-2258.
- [72] J. Hizal, R. Apak, Modeling of copper (II) and lead (II) adsorption on kaolinite-based clay minerals individually and in the presence of humic acid, *J. Colloid Interface Sci.*, 243 (2001) 1-13.
- [73] H.M. Asfour, O. Fadali, M.M. Nassar, M.S. El-Geundi, Equilibrium studies on adsorption of basic dyes on hardwood, *J. Chem. Technol. Biotechnol.*, (1985) 21-27.
- [74] Y.S. Ho, G. McKay, Kinetic models for the sorption of dye from aqueous solution by wood, *Trans IChemE*, 76 (1998) 183-191.
- [75] V.K. Gupta, I. Ali, V.K. Saini, Removal of rhodamine B, fast green and methylene blue from wastewater using red mud - an aluminum industry waste, *Ind Engg Chem Res*, 43 (2004) 740-747.
- [76] S. Netpradit, P. Thiravetyan, S. Towprayoons, Application of waste metal hydroxide sludge for adsorption of azo reactive dyes, *Water Res.*, 37 (2003) 763-772.
- [77] M.P. Elizalde-Gonzalez, A.A. Peláez-cid, Removal of textile dyes from aqueous solution by adsorption on biodegradable wastes, *Environ. Technol.*, 24 (2003) 821-829.
- [78] K. Kadirvelu, M. Kavipriya, C. Karthika, M. Radhika, N. Vennilamani, S. Pattabhi, Utilization of various agricultural wastes for activated carbon preparation and application for the removal of dyes and metal ions from aqueous solution, *Bior. Tech.*, 87 (2003) 129-132.

- [79] G.M. Walkar, L. Hansen, J.A. Hanna, S.J. Allen, Kinetics of a reactive dye adsorption onto Dolomitic Sorbents, *Wat. Res.*, 37 (2003) 2081-2089.
- [80] R. Mosteo, M. Ormad, P. Goñi, J. Rodríguez-Chueca, A. García, A. Clavel, Identification of pathogen bacteria and protozoa in treated urban wastewaters discharged in the Ebro River (Spain): water reuse possibilities, *Water Science and Technology*, 68 (2013) 575-583.
- [81] G. WHO, The world health report 2002: reducing risks, promoting healthy life, (2002).
- [82] W. WHO, WHO estimates of the global burden of foodborne diseases: foodborne disease burden epidemiology reference group 2007–2015, Geneva, Switzerland, (2015).
- [83] G.J. Bonde, Bacterial indication of water pollution, in: *Advances in aquatic microbiology*, Elsevier, 1977, pp. 273-364.
- [84] A.W. Hoadley, B.J. Dutka, Bacterial Indicators/health Hazards Associated with Water: A Symposium; Chicago, Ill., 28-29 June 1976, ASTM International, 1977.
- [85] S.D. Rayasam, I. Ray, K.R. Smith, L.W. Riley, Extraintestinal Pathogenic *Escherichia coli* and Antimicrobial Drug Resistance in a Maharashtrian Drinking Water System, *The American journal of tropical medicine and hygiene*, (2019).
- [86] K.E.El-Gayar, Isolation, identification and characterization of *Bacillus subtilis* from tap water, *Asian Journal of Microbiology, Biotechnology & Environmental Sciences Paper abbreviation*, 19 (2017) 817-830.
- [87] O. Ostensvik, C. From, B. Heidenreich, K. O'sullivan, P. Granum, Cytotoxic *Bacillus* spp. belonging to the *B. cereus* and *B. subtilis* groups in Norwegian surface waters, *Journal of applied microbiology*, 96 (2004) 987-993.
- [88] M.M. Arjmand, A. Rezaee, S. Nasser, S.S. Eshraghi, Removing *Bacillus subtilis* spores from drinking water using a bipolar electrochemical method, *International Journal of Electrochemical Science*, 11 (2016) 10080-10086.
- [89] Z. Jian, Y. Bai, Y. Chang, J. Liang, J. Qu, Removal of micropollutants and cyanobacteria from drinking water using $KMnO_4$ pre-oxidation coupled with bioaugmentation, *Chemosphere*, 215 (2019) 1-7.
- [90] C. Amor, E. De Torres-Sociás, J.A. Peres, M.I. Maldonado, I. Oller, S. Malato, M.S. Lucas, Mature landfill leachate treatment by coagulation/flocculation combined with Fenton and solar photo-Fenton processes, *Journal of Hazardous Materials*, 286 (2015) 261-268.
- [91] E.I. Unuabonah, R. Nöske, J. Weber, C. Günter, A. Taubert, New micro/mesoporous nanocomposite material from low-cost sources for the efficient removal of aromatic and pathogenic pollutants from water, *Beilstein journal of nanotechnology*, 10 (2019) 119-131.
- [92] Y. Fang, C. Xing, S. Zhan, M. Zhao, M. Li, H. Liu, A polyoxometalate-modified magnetic nanocomposite: a promising antibacterial material for water treatment, *Journal of Materials Chemistry B*, 7 (2019) 1933-1944.
- [93] C. Santhosh, A. Malathi, E. Dhaneshvar, A. Bhatnagar, A.N. Grace, J. Madhavan, Iron Oxide Nanomaterials for Water Purification, in: *Nanoscale Materials in Water Purification*, Elsevier, 2019, pp. 431-446.
- [94] P.K. Gautam, A. Singh, K. Misra, A.K. Sahoo, S.K. Samanta, Synthesis and applications of biogenic nanomaterials in drinking and wastewater treatment, *Journal of environmental management*, 231 (2019) 734-748.
- [95] M.H.D.A. Farahani, V. Vatanpour, Polymer/Carbon Nanotubes Mixed Matrix Membranes for Water Purification, in: *Nanoscale Materials in Water Purification*, Elsevier, 2019, pp. 87-110.
- [96] D. Morantes, E. Muñoz, D. Kam, O. Shoseyov, Highly Charged Cellulose Nanocrystals Applied as A Water Treatment Flocculant, *Nanomaterials*, 9 (2019) 272.

- [97] J. Wang, Y. Liu, L. Tang, X. Ren, G. Zeng, J. Zhu, Mesoporous Carbon-Based Enzyme Biocatalyst for Aquatic Recalcitrant Pollutant Treatment, in: *Nanohybrid and Nanoporous Materials for Aquatic Pollution Control*, Elsevier, 2019, pp. 103-124.
- [98] M. Liu, M. Zhang, R. Hao, T. Du, T. Li, Y. Li, Disinfection byproduct formation and toxicity of graphene oxide in water treatment system, *Chemosphere*, 217 (2019) 68-75.
- [99] D. Huang, J. Wu, L. Wang, X. Liu, J. Meng, X. Tang, C. Tang, J. Xu, Novel insight into adsorption and co-adsorption of heavy metal ions and an organic pollutant by magnetic graphene nanomaterials in water, *Chemical Engineering Journal*, 358 (2019) 1399-1409.
- [100] G. Zhang, M. Zhou, Z. Xu, C. Jiang, C. Shen, Q. Meng, Guanidyl-functionalized graphene/polysulfone mixed matrix ultrafiltration membrane with superior permselective, antifouling and antibacterial properties for water treatment, *Journal of colloid and interface science*, 540 (2019) 295-305.
- [101] C. Martinez-Boubeta, K. Simeonidis, Magnetic Nanoparticles for Water Purification, in: *Nanoscale Materials in Water Purification*, Elsevier, 2019, pp. 521-552.
- [102] W. Hu, C. Peng, W. Luo, M. Lv, X. Li, D. Li, Q. Huang, C. Fan, Graphene-based antibacterial paper, *ACS nano*, 4 (2010) 4317-4323.
- [103] H.M. Hegab, A. ElMekawy, L. Zou, D. Mulcahy, C.P. Saint, M. Ginic-Markovic, The controversial antibacterial activity of graphene-based materials, *Carbon*, 105 (2016) 362-376.
- [104] J. Zhu, S. Wei, L. Zhang, Y. Mao, J. Ryu, N. Haldolaarachchige, D.P. Young, Z. Guo, Electrical and dielectric properties of polyaniline–Al₂O₃ nanocomposites derived from various Al₂O₃ nanostructures, *J. Mater. Chem.*, 21 (2011) 3952-3959.
- [105] J.C. Love, L.A. Estroff, J.K. Kriebel, R.G. Nuzzo, G.M. Whitesides, Self-assembled monolayers of thiolates on metals as a form of nanotechnology, *Chem. Rev.*, 105 (2005) 1103-1169.
- [106] A.S. Edelstein, R.C. Cammarata, *Nanomaterials: synthesis, properties and applications*, Second Edition, CRC Press, New York (01-Jan-1998).
- [107] M. Farre, K. Gajda-Schranz, L. Kantiani, D. Barcelo, Ecotoxicity and analysis of nanomaterials in the aquatic environment, *Anal. Bioanal. Chem.*, 393 (2009) 81-95.
- [108] K. Yoshimatsu, L. Ye, J. Lindberg, I.S. Chronakis, Selective molecular adsorption using Electrospun nanofiber affinity membranes, *Biosens. Bioelect.*, 23 (2008) 1208-1215.
- [109] F. Perreault, A.F.d. Faria, M. Elimelech, Environmental applications of graphene-based nanomaterials, *Chem. Soc. Rev.*, 44 (2015) 5861-5896.
- [110] M. Fernandez-Garcia, A. Martinez-Arias, J.C. Hanson, J.A. Rodriguez, Nanostructured oxides in chemistry: characterization and properties, *Chem. Rev.*, 104 (2004) 4063-4104.
- [111] G. Oskam, Metal oxide nanoparticles: synthesis, characterization and application, *J. Sol-Gel Sci. Techn.*, 37 (2006) 161-164.
- [112] L. Vayssieres, On the design of advanced metal oxide nanomaterials, *Int. J. of Nanotechnology*, 1 (2004) 1-40
- [113] M. Zhang, *Nonaqueous synthesis of metal oxide nanoparticles and their surface*, Ph.D. University of New Orleans, (2008) Print.
- [114] K.R. Reddy, W. Park, B.C. Sin, J. Noh, Y. Lee, Synthesis of electrically conductive and superparamagnetic monodispersed iron oxide-conjugated polymer composite nanoparticles by in situ chemical oxidative polymerization, *J. Colloid Interface Sci.*, 335 (2009) 34-39.
- [115] J. Zhu, K.Y.S. Ng, D. Deng, Micro single crystals of hematite with nearly 100% exposed 104 Facets: Preferred etching and lithium storage, *Cryst. Growth Des.*, 14 (2014) 2811-2817.
- [116] H. Xu, X. Wang, L. Zhang, Selective preparation of nanorods and micro-octahedrons of Fe₂O₃ and their catalytic performances for thermal decomposition of ammonium perchlorate, *Powder Technol.*, 5 (2008) 176-180.

- [117] M. Mohapatra, S. Anand, Synthesis and applications of nano-structured iron oxides/hydroxides - A review, *Int. J. Eng. Sci. Technol.*, 2 (2010) 127-146.
- [118] C. Gregor, M. Hermanek, D. Jancik, J. Pechousek, J. Filip, J. Hrbac, R. Zboril, The effect of surface area and crystal structure on the catalytic efficiency of Iron(III) oxide nanoparticles in hydrogen peroxide decomposition, *Eur. J. Inorg. Chem.*, 2010 (2010) 2343-2351.
- [119] X. Chen, Z. Zhang, Z. Qiu, C. Shi, X. LiLi, A facile biomolecule-assisted approach for fabricating α -Fe₂O₃ nanowires in solution, *Solid State Commun.*, 140 (2006) 267-269
- [120] G.Y. Zhang, Y. Feng, Y.Y. Xu, D.Z. Gao, Y.Q. Sun, Controlled synthesis of mesoporous α -Fe₂O₃ nanorods and visible light photocatalytic property, *Mater. Res. Bull.*, 47 (2012) 625-630.
- [121] L. Tan, J. Xu, X. Xue, Z. Lou, J. Zhu, e.a. A. Baig, Multifunctional nanocomposite Fe₃O₄ @SiO₂-mPD/SP for selective removal of Pb(II) and Cr(VI) from aqueous solutions, *RSC Adv.*, 4 (2014) 45920-45929.
- [122] R. Akhbarizadeh, M.R. Shayestefar, E. Darezereshki, Competitive removal of metals from wastewater by maghemite nanoparticles: A comparison between simulated wastewater and AMD, *Mine. Water Environ.*, 33 (2014) 89-96.
- [123] L. Tan, J. Xu, X. Xue, Z. Lou, J. Zhu, e.a. A. Baig, Multifunctional nanocomposite Fe₃O₄ @SiO₂-mPD/SP for selective removal of Pb(II) and Cr(VI) from aqueous solutions, *RSC Adv.*, 4 (2014) 45920-45929.
- [124] A.F. Ngomsik, A. Bee, D. Talbot, G. Cote, Magnetic solid-liquid extraction of Eu(III), La(III), Ni(II) and Co(II) with maghemite nanoparticles, *Sep. Purif. Technol.*, 86 (2012) 1-8.
- [125] A.Z.M. Badruddoza, Z.B.Z. Shawon, M.T. Rahman, K.W. Hao, K. Hidajat, M.S. Uddin, Ionically modified magnetic nanomaterials for arsenic and chromium removal from water, *Chem. Eng. J.*, 225 (2013) 607-615.
- [126] Y. Lei, F. Chen, Y. Luo, L. Zhang, Three-dimensional magnetic graphene oxide foam/Fe₃O₄ nanocomposite as an efficient absorbent for Cr(VI) removal, *J. Mater. Sci. Total Environ.*, 49 (2014) 4236-4245.
- [127] M. Rahim, M.R.H.M. Haris, Application of biopolymer composites in arsenic removal from aqueous medium: A review, *J. Radiat. Res. Appl. Sci.*, 8 (2015) 255-263.
- [128] J. Sun, X. Li, Q. Zhao, J. Ke, D. Zhang, Novel V₂O₅/BiVO₄/TiO₂ Nanocomposites with High Visible-Light-Induced Photocatalytic Activity for the Degradation of Toluene, *J. Phys. Chem. C*, 118 (2014) 10113–10121.
- [129] M. Mahmoudi, A. Simchi, M. Imani, Recent advances in surface engineering of superparamagnetic iron oxide nanoparticles for biomedical applications, *J. Iran. Chem. Soc.*, 7 (2010) S1-S27.
- [130] C. Pascal, J.L. Pascal, F. Favier, M.L.E. Moubtassim, C. Payen, Electrochemical synthesis for the control of γ -Fe₂O₃ nanoparticle size. morphology, microstructure, and magnetic behavior, *Chem. Mater.*, 11 (1999) 141-147.
- [131] K.V.P.M. Shafi, A. Ulman, Y. Xingzhong, N.-L. Yang, C. Estournès, e.a. H. White, Sonochemical synthesis of functionalized amorphous iron oxide nanoparticles, *Langmuir*, 17 (2001) 5093-5097.
- [132] Y. Lu, Y. Yin, B.T. Mayers, Y. Xia, Modifying the surface properties of superparamagnetic iron oxide nanoparticles through A Sol–Gel approach, *Nano Lett.*, 2 (2002) 183-186.
- [133] C.M. Bautista, O. Bomati-Miguel, D.P.M. Morales, C.J. Serna, S. Veintemillas-Verdaguer, Surface characterisation of dextran-coated iron oxide nanoparticles prepared by laser pyrolysis and coprecipitation, *J. Magn. Mater.*, 293 (2005) 20-27.
- [134] S. Ge, X. Shi, K. Sun, C. Li, C. Uher, J.R. Baker, M.M.B. Holl, B.G. Orr, Facile Hydrothermal Synthesis of Iron Oxide Nanoparticles with Tunable Magnetic Properties, *J. Phys. Chem. C* 31 (2009) 13593-13599.

- [135] P.L. Hariani, M. Faizal, R. Marsi, D. Setiabudidaya, Synthesis and Properties of Fe₃O₄ Nanoparticles by Co-precipitation Method to Removal Procion Dye, *Int. J. Environ. Sci. Technol.*, 4 (2013) 336-340.
- [136] M. Unni, A.M. Uhl, S. Savliwala, B.H. Savitzky, R. Dhavalikar, N. Garraud, D.P. Arnold, L.F. Kourkoutis, J.S. Andrew, C. Rinaldi, Thermal Decomposition Synthesis of Iron Oxide Nanoparticles with Diminished Magnetic Dead Layer by Controlled Addition of Oxygen, *ACS Nano*, 11 (2017) 2284–2303.
- [137] C.N.R. Rao, A. Müller, *The chemistry of nanomaterials*, A.K. Cheetham (Eds.), Wiley-VCH, Weinheim, 3rd Reprint, 1 (2005).
- [138] F. Yazdani, M. Seddigh, Magnetite nanoparticles synthesized by co-precipitation method: The effects of various iron anions on specifications, *Mater. Chem. Phys.*, 184 (2016) 318-323.
- [139] J. Xu, J. Sun, Y. Wang, J. Sheng, F. Wang, M. Sun, Application of iron magnetic nanoparticles in protein immobilization, *Molecules*, 19 (2014) 11465-11486.
- [140] S.J. Iyengar, M. Joy, C.K. Ghosh, S. Dey, R.K. Kotnalad, S.K. Ghosh, Magnetic, X-ray and Mössbauer studies on magnetite/maghemite core-shell nanostructures fabricated through an aqueous route†, *RSC Adv.*, 2 (2014) 64919-64929.
- [141] M.E. Compeán-Jasso, F. Ruiz, J.R. Martínez, A. Herrera-Gómez, Magnetic properties of magnetite nanoparticles synthesized by forced hydrolysis, *Mater. Lett.*, 62 (2008) 4248-4250.
- [142] B. Tang, L. Yuan, T. Shi, L. Yu, Y. Zhu, Preparation of nano-sized magnetic particles from spent pickling liquors by ultrasonic-assisted chemical co-precipitation, *J. Hazard. Mater.*, 163 (2009) 1173-1178.
- [143] Z. Wu, J. Wu, H. Xiang, M. Chun, K. Lee, Organosilane-functionalized Fe₃O₄ composite particles as effective magnetic assisted adsorbents, *Colloids Surf A Physicochem. Eng. Asp.*, 279 (2006) 167-174.
- [144] J. Safari, Z. Zarnegar, Ultrasonic activated efficient synthesis of chromenes using amino-silane modified Fe₃O₄ nanoparticles: A versatile integration of high catalytic activity and facile recovery, *J. Mol. Struct.*, 1072 (2014) 53-60.
- [145] Y. Xu, K. Sheng, C.L. Shi, Self-Assembled Graphene Hydrogel via a One-Step Hydrothermal Process, *ACS Nano*, 4 (2010) 4324-4330.
- [146] K. Golka, S. Kopps, Z.W. Myslak, Carcinogenicity of azo colorants: influence of solubility and bioavailability, *Toxicol. Lett.*, 151 (2004) 203-210.
- [147] N. Bao, Y. Li, Z.T. Wei, G.B. Yin, J.J. Niu, Adsorption of dyes on hierarchical mesoporous TiO₂ fibers and its enhanced photocatalytic properties, *J. Phys. Chem.*, 115 (2011) 5708-5719.
- [148] A.A. Juwarkar, S.K. Singh, A. Mudhoo, A comprehensive overview of elements in bioremediation, *Rev. Environ. Sci. Bio.*, 9 (2010) 215-288.
- [149] H.M. Asfour, O. Fadali, M.M. Nassar, M.S. El-Geundi, Equilibrium studies on adsorption of basic dyes on hardwood, *J. Chem. Technol. Biotechnol.*, 35 (1985) 21-27.
- [150] C. Namasivayam, N. Muniasamy, K. Gayatri, M. Rani, K. Ranganathan, Removal of dyes from aqueous solutions by cellulosic waste orange peel *Bioresour. Technol.*, 57 (1996) 37-43.
- [151] A.K. Goswami, S.J. Kulkarni, S.K. Dharmadhikari, P.E. Patil, Fly ash as low cost adsorbent to remove dyes, *Inter. J. Scientific Res. and Manag.*, 5 (2014) 842-845.
- [152] A. Ahemad, B. Hameed, N. Aziz, Adsorption of direct dye on palm ash: kinetic and equilibrium modelling, *J. Hazard. Mater.*, 141 (2007) 70-76.
- [153] S. Sonal, A. Singh, B.K. Mishra, Decolorization of reactive dye Remazol Brilliant Blue R by zirconium oxychloride as a novel coagulant: optimization through response surface methodology, *Water Sci. Technol.*, 78 (2018) 379-389.

- [154] I. Arslan-Alaton, G. Tureli, T. Olmez-Hanci, Treatment of azo dye production wastewaters using Photo-Fenton-like advanced oxidation processes: Optimization by response surface methodology, *J. Photochem. Photobiol. A*, 202 (2009) 142–153.
- [155] E. Demirbas, M.Z. Nas, Batch kinetic and equilibrium studies of adsorption of Reactive Blue 21 by fly ash and sepiolite, *Desalination*, 243 (2009) 8-21.
- [156] A. Sergi, F. Shemirani, M. Alvandb, A. Tajbakhshian, Graphene oxide magnetic nanocomposites for the preconcentration of trace amounts of malachite green from fish and water samples prior to determination by fiber optic-linear array detection spectrophotometry, *Anal. Methods*, 6 (2014) 7744-7751.
- [157] Y.S. Ho, G. McKay, Kinetic models for the sorption of dye from aqueous solution by wood, *Trans. Int. Chem. Eng.*, 76 (1998) 183-191.
- [158] S. Nethaji, A. Sivasamy, G. Thennarasu, S. Saravanan, Adsorption of Malachite Green dye onto activated carbon derived from *Borassus aethiopum* flower biomass, *J. Hazard. Mater.*, 181 (2010) 271-280.
- [159] P. Frid, S.V. Anisimov, N. Popovic, Congo red and protein aggregation in neurodegenerative diseases, *Brain Res. Rev.*, 53 (2007) 135-160.
- [160] R. Gopinathan, J. Kanhere, J. Banerjee, Effect of malachite green toxicity on non target soil organisms, *Chemosphere*, 120 (2015) 637-644.
- [161] A.N. Ejhieh, M. Khorsandi, Photodecolorization of Eriochrome Black T using NiSP zeolite as a heterogeneous catalyst, *J Hazard. Mater.*, 176 (2010) 629-637.
- [162] M. Jiang, X. Jin, X. Lu, Z. Cheng, Adsorption of Pb (II), Cd (II), Ni (II) and Cu (II) onto natural kaolinite clay, *Desalination*, 252 (2010) 33-39.
- [163] A. Gürses, C. Doğar, M.Yalcin, M. Açikyildiz, R. Bayrak, S. Karaca, The adsorption kinetics of the cationic dye, methylene blue, onto clay, *J. Hazard. Mater.*, 131 (2006) 217-228.
- [164] C. Allegre, P. Moulin, M. Maisseu, F. Charbit, Treatment and reuse of reactive dyeing effluents, *J. Membr. Sci.*, 269 (2006) 15-34.
- [165] J.C. Duan, Q. Lu, R.W. Chen, Y.Q. Duan, L.F. Wang, L. Gao, S.Y. Pan, Synthesis of a novel flocculant on the basis of crosslinked Konjac glucomannangraftpolyacrylamide- co-sodium xanthate and its application in removal of Cu²⁺ ion, *Carbohydr. Polym.*, 80 (2010) 436-441.
- [166] J. Hizal, R. Apak, Modeling of copper (II) and lead (II) adsorption on kaolinite-based clay minerals individually and in the presence of humic acid, *J. Colloid Interface Sci.*, 243 (2001) 1-13.
- [167] V.K. Gupta, D. Mohan, S. Sharma, M. Sharma, Removal of basic dyes (rhodamine B and methylene 20 blue) from aqueous solutions using bagasse fly ash, *Sep. Sci. Technol.*, 35 (2003) 2097-2113.
- [168] T. Viraraghavan, K.R. Ramakrishna, Fly ash for colour removal from synthetic dye solutions, *Water Quality Res. J. Can.*, 34 (1999) 505-517.
- [169] K.P. Yadava, B.S. Tyagi, V.N. Singh, Effect of temperature on the removal of lead(II) by adsorption on China clay and wollastonite, *J. Chem. Technol. Biotechnol.*, 51 (1991) 47-60.
- [170] K.K. Panday, G. Prasad, V.N. Singh, Copper (II) removal from aqueous solutions by fly ash, *Water Res.*, 19 (1985) 869.
- [171] G.P. Damasmahapatra, T.K. Pal, A.K. Bhadra, B. Bhattacharya, *Sep. Sci. Technol.*, 31 (1996) 2001.
- [172] M. Villaescusa, N. Miralles, Heavy metal uptake from aqueous solution by cork and yohimbe bark wastes, *J. Chem. Technol. Biotechnol.*, 75 (2000) 812-816.
- [173] B. Acemioglu, M.H. Alma, A.R. Demirkiran, Removal of Zn(II) and Pb(II) ions by calabrian pine bark wastes, *Jour. Chem. Soc. Pak.*, 26 (2004) 82-89.
- [174] Y.S. Ho, G. McKay, Sorption of dye from aqueous solution by peat, *Chem. Eng. J.*, 70 (1998) 115-124.

- [175] R. Gundogan, B. Acemioglu, M.H. Alma, Copper (II) adsorption from aqueous solution by herbaceous peat, *J. Colloid Interface Sci.*, 269 (2004) 303-309.
- [176] V.K. Gupta, Suhas, I. Ali, V.K. Saini, Removal of rhodamine B, fast green and methylene blue from wastewater using red mud - an aluminum industry waste, *Ind. Engg. Chem. Res.*, 43 (2004) 740-747.
- [177] M. Hirata, N. Kawasaki, T. Nakamura, K. Motsumoto, M. Kabayama, T. Tamura, S. Tanada, Adsorption of dyes onto carbonaceous materials produced from coffee grounds by microwave treatment, *J. Colloid Inter. Sci.*, 254 (2002) 7-22.
- [178] N.K. Lazaridis, T.D. Karapantsios, D. Georgantas, Kinetic analysis for the removal of a reactive dye from aqueous onto hydrotalcite by adsorption, *Water Res.*, 37 (2003) 3023-3033.
- [179] J.K. Sahoo, A. Kumar, J. Rath, T. Mohanty, P. Dash, H. Sahoo, Guar gum-coated iron oxide nanocomposite as an efficient adsorbent for Congo red dye, *Desalin. Wat. Treat.*, 95 (2017) 342-354.
- [180] L. Wang, A.Q. Wang, Adsorption characteristics of Congo Red onto the chitosan/montmorillonite nanocomposite, *J. Hazard. Mater.*, 147 (2007) 979-985.
- [181] I. Safarik, L.F.T. Rego, M. Borovska, E. Mosiniewicz-Szablewska, F. Weyda, M. Safarikova, New magnetically responsive yeast-based biosorbent for the efficient removal of water-soluble dyes, *Enzyme and Microbial Tech.*, 40 (2007) 1551-1556.
- [182] L. Zhou, C. Gao, W. Xu, Magnetic Dendritic Materials for Highly Efficient Adsorption of Dyes and Drugs, *App. Mat. & Inte.*, 2 (2010) 1483-1493.
- [183] N.A. Oladoja, A.K. Akinlabi, Congo red biosorption on palm kernel seed coat., *Ind. Eng. Chem. Res.*, 48 (2009) 6188-6196.
- [184] C. Namasivayam, D. Kavitha, Removal of Congo Red from water by adsorption onto activated carbon prepared from coir pith an agricultural solid waste, *Dyes and Pigments*, 54 (2002) 47-58.
- [185] N. Kannan, M. Meenakshisundaram, Adsorption of congo red on various activated carbons A Comparative Study, *Water Air Soil Pollut.*, 138 (2002) 289-305.
- [186] Z. Wu, J. Wu, H. Xiang, M.-S. Chun, K. Lee, Organosilane-functionalized Fe₃O₄ composite particles as effective magnetic assisted adsorbents, *Colloids Surf. A*, 279 (2006) 167-174.
- [187] A. Ebrahiminezhad, Y. Ghasemi, S. Rasoul-Amini, J. Barar, S. Davarana, Preparation of novel magnetic fluorescent nanoparticles using amino acids, *Colloids Surf. B Biointerfaces*, 102 (2013) 534-539.
- [188] S.M. Dizaj, F. Lotfipour, M. Barzegar-Jalali, M.H. Zarrintan, K. Adibkia, Antimicrobial activity of the metals and metal oxide nanoparticles, *Materials Science and Engineering: C*, 44 (2014) 278-284.
- [189] C. Buzea, I.I. Pacheco, K. Robbie, Nanomaterials and nanoparticles: sources and toxicity, *Biointerphases*, 2 (2007) MR17-MR71.
- [190] J.T. Seil, T.J. Webster, Antimicrobial applications of nanotechnology: methods and literature, *International journal of nanomedicine*, 7 (2012) 2767.
- [191] G. Mohammadi, H. Valizadeh, M. Barzegar-Jalali, F. Lotfipour, K. Adibkia, M. Milani, M. Azhdarzadeh, F. Kiafar, A. Nokhodchi, Development of azithromycin-PLGA nanoparticles: Physicochemical characterization and antibacterial effect against *Salmonella typhi*, *Colloids and Surfaces B: Biointerfaces*, 80 (2010) 34-39.
- [192] Y. Li, Z. Chen, N. Gu, In vitro biological effects of magnetic nanoparticles, *Chinese science bulletin*, 57 (2012) 3972-3978.
- [193] D. Malwal, P. Gopinath, Efficient adsorption and antibacterial properties of electrospun CuO-ZnO composite nanofibers for water remediation, 321 (2017) 611-621.
- [194] R.D. Waldron, Infrared Spectra of Ferrites, *Phys. Rev.*, 99 (1955) 1727-1735.

- [195] M. Yamaura, R. Camilo, L. Sampaio, M. Macêdo, M. Nakamura, H. Toma, Preparation and characterization of (3-aminopropyl)triethoxysilane-coated magnetite nanoparticles, *J. Magn. Magn. Mater.*, 279 (2004) 210-217.
- [196] M. Ma, Y. Zhang, W. Yu, H. Shen, H. Zhang, N. Gu, Preparation and characterization of magnetite nanoparticles coated by amino silane, *Colloids Surf. A*, 212 (2003) 219-226.
- [197] L.D. White, C.P. Tripp, Reaction of (3-Aminopropyl)dimethylethoxysilane with Amine Catalysts on Silica Surfaces, *J. Colloid Interface Sci.*, 232 (2000) 400-407.
- [198] Z. Xu, Q. Liu, J.A. Finch, Silanation and stability of 3-aminopropyl triethoxy silane on nanosized superparamagnetic particles: I. Direct silanation, *Appl. Surf. Sci.*, 120 (1997) 269-278.
- [199] A. Ebrahiminezhad, Y. Ghasemi, S. Rasoul-Amini, J. Barar, S. Davarana, Preparation of novel magnetic fluorescent nanoparticles using amino acids, *Colloids Surf. B*, 102 (2013) 534-539.
- [200] T. Tang, H. Fan, S. Ai, R. Han, Y. Qiu, Hemoglobin (Hb) immobilized on amino-modified magnetic nanoparticles for the catalytic removal of bisphenol A, *Chemosphere*, 83 (2011) 255-264.
- [201] S. ÇAKIR, E. BİÇER, Synthesis, spectral characterization and electrochemistry of vanadium(v) complex with tryptophan, *J. Chil. Chem. Soc.*, 55 (2010) 236-239.
- [202] Z. Wang, H. Zhu, X. Wang, F. Yang, X. Yang, One-pot green synthesis of biocompatible arginine-stabilized magnetic nanoparticles, *Nanotech.*, 20 (2009) 456-606.
- [203] J.K. Sahoo, A. Kumar, L. Rout, J. Rath, P. Dash, H. Sahoo, An investigation of heavy metal adsorption by hexa-dentate ligand-modified magnetic nanocomposites, *Sep. Sci. Technol.*, 53 (2007) 863-876.
- [204] J.Y. Park, E.S. Choi, M.J. Baek, G.H. Lee, Colloidal stability of amino acid coated magnetite nanoparticles in physiological fluid, *Mater. Lett.*, 63 (2009) 379-381.
- [205] H. Shi, L. Tan, Q. Du, X. Chen, L. Li, T. Liu, C. Fu, H. Liua, X. Meng, Green synthesis of Fe₃O₄ nanoparticles with controlled morphologies using urease and their application in dye adsorption, *Dalton Trans.*, 43 (2014) 12474-12479.
- [206] Z. Li, L. Wei, M.Y. Gao, H. Lei, One-Pot Reaction to Synthesize Biocompatible Magnetite Nanoparticles, *Adv. Mater.*, 17 (2005) 1001-1005.
- [207] B. Feng, R.Y. Hong, L.S. Wang, L. Guo, H.Z. Li, J. Ding, Y. Zheng, D.G. Wei, Synthesis of Fe₃O₄/APTES/PEG diacid functionalized magnetic nanoparticles for MR imaging, *Colloids Surf. A*, 328 (2008) 52-59.
- [208] G.F. Goya, T.S. Berquo, F.C. Fonseca, M.P. Morales, Static and dynamic properties of spherical magnetite nanoparticles, *J. Appl. Phys.*, 94 (2003) 3520-3528.
- [209] B. Feng, R.Y. Hong, L.S. Wang, L. Guo, H.Z. Li, J. Ding, Y. Zheng, D.G. Wei, Synthesis of Fe₃O₄/APTES/PEG diacid functionalized magnetic nanoparticles for MR imaging, *Colloids Surf. A*, 328 (2008) 52-59.
- [210] Z.Y. Ma, Y.P. Guan, H.Z. Liu, Synthesis and characterization of micron-sized monodisperse superparamagnetic polymer particles with amino groups, *J. Polym. Sci. Part A Polym. Chem.*, 43 (2005) 3433-3439.
- [211] H. Su, Z. Ye, N. Hmidi, R. Subramanian, Carbon nanosphere-iron oxide nanocomposites as high-capacity adsorbents for arsenic removal, *RSC Adv.*, 7 (2017) 36138-36148.
- [212] Y. Liang, N. Guo, L. Li, L. R, G. Ji, S. Gan, Preparation of porous 3D Ce-doped ZnO microflowers with enhanced photocatalytic performance, *RSC Adv.*, 5 (2015) 59887-59894.
- [213] G. Bharath, R. Madhu, S.-M. Chen, V. Veeramani, D. Mangalaraja, N. Ponpandian, Solvent-free mechanochemical synthesis of graphene oxide and Fe₃O₄-reduced graphene oxide nanocomposites for sensitive detection of nitrite, *J. Mater. Chem. A*, 3 (2015) 15529-15539.

- [214] M. Foroughi-Dahr, H. Abolghasemi, M. Esmaili, A. Shojamoradi, H. Fatoorehchi, Adsorption Characteristics of Congo Red from Aqueous Solution onto Tea Waste, *Chem. Eng. Commun.*, 202 (2015) 181-193.
- [215] I.D. Mall, V.C. Srivastava, G.V. A.Kumar, I.M. Mishra, Characterization and utilization of mesoporous fertilizer plant waste carbon for adsorptive removal of dyes from aqueous solution, *Colloids Surf. A*, 278 (2006) 175-187.
- [216] L. Zhou, R. Johnson, T. Habteyes, H. Guo, Adsorption of methylene blue and its Ndemethylated derivatives on the (111) face of coinage metals: the importance of dispersion interactions, *J. Chem. Phys.*, 146 (2017) 1647011-1647017.
- [217] C. Namasivayam, R.T. Yamuna, Removal of Congo Red from aqueous solutions by biogas waste slurry, *J. Chem. Technol. Biotechnol.*, 53 (1992) 153-157.
- [218] H.-Y. Zhu, Y.-Q. Fu, R. Jiang, J.-H. Jiang, L. Xiao, G.-M. Zeng, S.-L. Zhao, Y. Wang, Adsorption removal of congo red onto magnetic cellulose/Fe₃O₄/activated carbon composite: Equilibrium, kinetic and thermodynamic studies, *Chem. Eng. J.*, 173 (2011) 494-502.
- [219] C. Namasivayam, D.J.S.E. Arasi, Removal of congo red from wastewater by adsorption onto waste red mud, *Chemosphere*, 34 (1997) 401-417.
- [220] K.S. Chou, J.C. Tsai, C.T. Lo, The adsorption of Congo red and vacuum pump oil by rice hull ash, *Bioresour. Technol.*, 78 (2001) 217-219.
- [221] M. Arakha, S. Pal, D. Samantarrai, T.K. Panigrahi, B.C. Mallick, K. Pramanik, B. Mallick, S. Jha, Antimicrobial activity of iron oxide nanoparticle upon modulation of nanoparticle-bacteria interface, *Scientific reports*, 5 (2015) 14813.
- [222] S. Hong, Y. Chang, I. Rhee, Chitosan-coated ferrite (Fe₃O₄) nanoparticles as a T2 contrast agent for magnetic resonance imaging, *J. Korean Phys. Soc.*, 56 (2010) 868-873.
- [223] J. Borchering, J. Baltrusaitis, H. Chen, L. Stebounova, C.-M. Wu, G. Rubasinghege, I.A. Mudunkotuwa, J.C. Caraballo, J. Zabner, V.H. Grassian, Iron oxide nanoparticles induce *Pseudomonas aeruginosa* growth, induce biofilm formation, and inhibit antimicrobial peptide function, *Environmental Science: Nano*, 1 (2014) 123-132.
- [224] S. Chatterjee, A. Bandyopadhyay, K. Sarkar, Effect of iron oxide and gold nanoparticles on bacterial growth leading towards biological application, *Journal of Nanobiotechnology*, 9 (2011) 34.
- [225] S. Ahmad, M.A. Farrukh, M. Khan, M. Khaleeq-ur-Rahman, M.A. Tahir, Synthesis of iron oxide–tin oxide nanoparticles and evaluation of their activities against different bacterial strains, *Can. Chem. Trans*, 2 (2014) 122-133.
- [226] K.Golka, S.Kopps, Z.W.Myslak, Carcinogenicity of azo colorants: influence of solubility and bioavailability, *Toxicol. Lett.*, 151 (2004) 203-210.
- [227] N.Bao, Y.Li, Z.T. Wei, G.B. Yin, J.J. Niu, Adsorption of dyes on hierarchical mesoporous TiO₂ fibers and its enhanced photocatalytic properties, *J. Phys. Chem. C*, 115 (2011) 5708–5719.
- [228] G.R. Chaudhary, P. Saharan, A. Kumar, S.K. mehta, S. Mor, A. umar, Adsorption Studies of Cationic, Anionic and Azo-Dyes via Monodispersed Fe₃O₄ Nanoparticles, *J. Nanosci. Nanotech.*, 13 (2013) 3240-3245.
- [229] P. Frid, S.V. Anisimov, N. Popovic, Congo red and protein aggregation in neurodegenerative diseases, *Brain Research Reviews*, 53 (2007) 135-160.
- [230] S. Chatterjee, M. W. Lee, S.H. Woo, Adsorption of congo red by chitosan hydrogel beads impregnated with carbon nanotubes, *Bior. Tech.*, 101 (2010) 1800-1806.
- [231] A.N. Ejhieh, M. Khorsandi, Photodecolorization of Eriochrome Black T using NiSP zeolite as a heterogeneous catalyst, *J Hazard Mater*, 176 (2010) 629-637.
- [232] M. Jiang, X. Jin, X. Lu, Z. Cheng, Adsorption of Pb (II), Cd (II), Ni (II) and Cu (II) onto natural kaolinite clay, *Desalination*, 252 (2010) 33-39.

- [233] B. Galan, D. Castaneda, I. Ortiz, Integration of ion exchange and non-dispersive solvent extraction processes for the separation and concentration of Cr(VI) from ground waters, *J. Hazard. Mater.*, 152 (2008) 795–804.
- [234] J.C. Duan, Q. Lu, R.W. Chen, Y.Q. Duan, L.F. Wang, L. Gao, S.Y. Pan, Synthesis of a novel flocculant on the basis of crosslinked Konjac glucomannan graft polyacrylamide-co-sodium xanthate and its application in removal of Cu²⁺ ion, *Carbohydrate Polymers*, 80 (2010) 436-441.
- [235] A. Gürses, C. Doğar, M. Yalcin, M. Açıkyıldız, R. Bayrak, S. Karaca, The adsorption kinetics of the cationic dye, methylene blue, onto clay, *J. Hazard. Mater.*, 131 (2006) 217-228.
- [236] H.-Y. Shu, C.R. Huang, M.C. Chang, Decolorization of mono-azo dyes in wastewater by advanced oxidation process: A case study of acid red 1 and acid yellow 23, *Chemosphere*, 29 (1994) 2597-2607.
- [237] H.-Y. Zhu, Y.-Q. Fu, R. Jiang, J. Yao, L. Xiao, G.-M. Zeng, Novel magnetic chitosan/poly(vinyl alcohol) hydrogel beads: Preparation, characterization and application for adsorption of dye from aqueous solution, *Bior. Tech.*, 105 (2012) 24-30.
- [238] N.A. Oladoja, A.K. Akinlabi, Congo red biosorption on palm kernel seed coat, *Ind. Eng. Chem. Res.*, 48 (2009) 6188–6196.
- [239] I. Safarika, L.F.T. Regoc, M. Borovskaa, E. Mosiniewicz-Szablewskae, F. Weydab, M. Safarikovaa, New magnetically responsive yeast-based biosorbent for the efficient removal of water-soluble dyes, *Enzyme and Microbial Tech.*, 40 (2007) 1551-1556.
- [240] L. Wang, A. Wang, Adsorption characteristics of Congo Red onto the chitosan/montmorillonite nanocomposite, *J. Hazard. Mater.*, 147 (2007) 979-985.
- [241] V.K. Gupta, D. Mohan, S. Sharma, M. Sharma, Removal of basic dyes (rhodamine B and methylene 20 blue) from aqueous solutions using bagasse fly ash, *Sep Sci Technol.*, 35 (2003) 2097-2113.
- [242] M.P. Elizalde-Gonzalez, A.A.P.-Cid, Removal of textile dyes from aqueous solution by adsorption on biodegradable wastes, *Environ. Technol.*, 24 (2003) 821-829.
- [243] B. Acemioglu, A. Samil, M.H. Alma, R. Gundogan, Copper(II) removal from aqueous solution by organosolv lignin and its recovery, *J. Appl. Polym. Sci.*, (2003) 1573-1541.
- [244] N. Kannan, M. Meenakshisundaram, Adsorption of Congo Red on Various Activated Carbons. A Comparative Study, *Water Air Soil Pollut.*, 138 (2002) 289-305.
- [245] C. Namasivayam, R.T. Yamuna, Removal of congo red from aqueous solutions by biogas waste slurry, *J. Chem. Technol. Biotechnol.*, 53 (1992) 153-157.
- [246] A. Fornara, P. Johansson, K. Petersson, S. Gustafsson, J. Qin, E. Olsson, D. Ilver, A. Krozer, M. Muhammed, C. Johansson, Tailored Magnetic Nanoparticles for Direct and Sensitive Detection of Biomolecules in Biological Samples, *Nano Lett.*, 8 (2008) 3423-3428.
- [247] E.H. Kim, H.S. Lee, B.K. Kwak, B.K. Kim, Synthesis of ferrofluid with magnetic nanoparticles by sonochemical method for MRI contrast agent, *Magn. Mater.*, 289 (2005) 328-330.
- [248] M.C. Urbina, S. Zinoveva, T. Miller, C.M. Sabliov, W.T. Monroe, C.S.S.R. Kumar, Investigation of Magnetic Nanoparticle-Polymer Composites for Multiple-controlled Drug Delivery, *J. Phys. Chem. C*, 112 (2008) 11102-11108.
- [249] S.J. Son, J. Reichel, B. He, M. Schuchman, S.B. Lee, Magnetic Nanotubes for Magnetic-Field-Assisted Bioseparation, Biointeraction, and Drug Delivery, *J. Am. Chem. Soc.*, 127 (2005) 7316-7317.
- [250] K. Wu, T. Liu, W. Xue, X. Wang, Arsenic(III) oxidation/adsorption behaviors on a new bimetal adsorbent of Mn-oxide-doped Al oxide, *Chemical Engineering Journal*, 192 (2012) 343–349.

- [251] Y. Masue, R.H. Loeppert, T.A. Kramer, Arsenate and arsenite adsorption and desorption behavior on co-precipitated aluminum: iron hydroxides, *Environmental Science and Technology*, 41 (2007) 837–842.
- [252] N.A. Travlou, G.Z. Kyzas, N.K. Lazaridis, E.A. Deliyanni, Functionalization of Graphite Oxide with Magnetic Chitosan for the Preparation of a Nanocomposite Dye Adsorbent, *Langmuir*, 29 (2013) 1657-1668.
- [253] L. Ai, M. Li, L.L. 2011, Adsorption of methylene blue from aqueous solution with activated carbon/cobalt ferrite/alginate composite beads: kinetics, isotherms, and thermodynamics., *J. Chem. Eng. Data*, 56 (2011) 3475–3483.
- [254] S. Liu, L. Zhang, J. Zhou, J. Xiang, J. Sun, J. Guan, Fiberlike Fe₂O₃ Macroporous Nanomaterials Fabricated by Calcinating Regenerate Cellulose Composite Fibers, *Chem. Mater.*, 20 (2008) 3623-3628.
- [255] R.Q. Long, R.T. Yang, Carbon Nanotubes as Superior Sorbent for Dioxin Removal, *J. Am. Chem. Soc.*, 123 (2001) 2058-2059.
- [256] L. Yan, P.R. Chang, P.W. Zheng, X. Ma, Preparation and characterization of starch-grafted multiwall carbon nanotube composites, *Carbohydr. Polym.*, 84 1378-1383.
- [257] J.L. Gong, B. Wang, G. M. Zeng, C. P. Yang, C. G. Niua, Q. Y. Niua, W. J. Zhou, Y. Liang, Removal of cationic dyes from aqueous solution using magnetic multi-wall carbon nanotube nanocomposite as adsorbent, *J. Hazard. Mater.*, 164 (2009) 1517-1522.
- [258] Y. Xie, D. Qian, D. Wu, X. Ma, Magnetic halloysite nanotubes/iron oxide composites for the adsorption of dyes, *Chem. Eng. J.*, 168 (2011) 959-963.
- [259] J. Kramer, R.K. Prud'homme, P. Wiltzius, P. Mirau, S. Knoll, Comparison of galactomannan crosslinking with organotitanates and borates, *Colloid and Polymer Sci.*, 266 (1988) 145-155.
- [260] C. Montgomery, A. Bunger, J. McLennan, R. Jeffrey, *Fracturing Fluid Components. In Effective and Sustainable Hydraulic Fracturing*, INTECH Publishing, (2013).
- [261] L.W. Teufel, J.A. Clark, *Hydraulic Fracture Propagation in Layered Rock: Experimental Studies of Fracture Containment*, *Soc. Pet. Engr. J.*, 24 (1984) 19-32.
- [262] H. Sun, L. Cao, L. Lu, Magnetite/reduced graphene oxide nanocomposites: One step solvothermal synthesis and use as a novel platform for removal of dye pollutants, *Nano Res.*, 4 (2011) 550-562.
- [263] S. Zhan, Y. Yang, Z. Shen, J. Shan, Y. Li, S. Yang, D. Zhu, Efficient removal of pathogenic bacteria and viruses by multifunctional amine-modified magnetic nanoparticles, *J. Hazard. Mater.*, 274 (2014) 115-123.
- [264] J.K. Sahoo, J. Rath, P. Dash, H. Sahoo, EDTA functionalized magnetic nanoparticle as a multifunctional adsorbent for Congo red dye from contaminated water, *AIP Conference Proceedings*, 1832 (2017).
- [265] C. Fringant, I. Tvaroska, K. Mazeau, M. Rinaudo, J. Desbrieres, Hydration of alpha-maltose and amylose: molecular modelling and thermodynamics study, *Carbohydr. Res.*, 278 (1995) 27–41.
- [266] M. Kacurakova, A. Ebringerova, J. Hirsch, Z. Hromadkova, Infrared study of arabinoxylans, *J. Sci. Food Agr.*, 66 (1994) 423–427.
- [267] M.F. Abdullah, S.K. Ghosh, S. Basu, A. Mukherjee, Cationic guar gum orchestrated environmental synthesis for silver nano-bio composite films, *Carbohydr. Polym.*, 134 (2015) 30-37.
- [268] H. Shi, L. Tan, Q. Du, X. Chen, L. Li, T. Liu, C. Fu, H. Liua, X. Meng, Green synthesis of Fe₃O₄ nanoparticles with controlled morphologies using urease and their application in dye adsorption, *Dalt. Trans.*, 43 (2014) 12474-12479.
- [269] K. Rajendran, S. Sen, Effect of capping agent on antimicrobial activity of nanoparticles *Der Pharmacia Lettre*, 7 (11) (2015) 37-42.

- [270] B. Feng, R.Y. Hong, L.S. Wang, L. Guo, H.Z. Li, J. Ding, Y. Zhenge, D.G. Weif, Synthesis of Fe₃O₄/APTES/PEG diacid functionalized magnetic nanoparticles for MR imaging, *Colloids and Surfaces A: Physicochem. Eng. Aspects*, 328 (2008) 52-59.
- [271] A. Turpin, Y.V. Loiko, A. Peinado, A. Lizana, J. Campos, T.K. Kalkandjiev, J. Mompart3, Polarization tailored novel vector beams based on conical refraction, *Phy. Optics*, (2014).
- [272] G.J. Copelloa, A.M. Mebert, M. Raineri, M.P. Pesenti, L.E. Diaz, Removal of dyes from water using chitosan hydrogel/SiO₂ and chitin hydrogel/SiO₂ hybrid materials obtained by the sol-gel method, *J. Hazard. Mater.*, 186 (2011) 932-939.
- [273] S. Ghorai, A. Sinhamahpatra, A. Sarkar, A.B. Panda, S. Pal, Novel biodegradable nanocomposite based on XG-g-PAM/SiO₂: Application of an efficient adsorbent for Pb²⁺ ions from aqueous solution, *Bior. Tech.*, 119 (2012) 181-190.
- [274] Y.A. Shchipunov, T.Y. Karpenko, Hybrid Polysaccharide-Silica Nanocomposites Prepared by the Sol-Gel Technique, *Langmuir*, 20 (2004) 3882-3887.
- [275] Y. Liang, N. Guo, L. Li, R. Li, G. Ji, S. Gan, *RSC Adv.*, 5 (2015).
- [276] H. Shi, L. Tan, Q. Du, X. Chen, L. Li, T. Liu, C. Fu, H. Liua, X. Meng, Green synthesis of Fe₃O₄ nanoparticles with controlled morphologies using urease and their application in dye adsorption, *Dalt. Trans.*, 43 (2014) 12474.
- [277] L.C. S. Pirillo, M. L. Ferreira, E. H. Rueda Removal of Fluorescein using different iron oxides as adsorbents: Effect of pH, *Spectrochim. Acta A*, 71 (2008) 636-643.
- [278] M.L.F. S. Pirillo, E. H. Rueda Adsorption of Alizarin, Eriochrome Blue Black R, and Fluorescein Using Different Iron Oxides as Adsorbents, *Ind. Eng. Chem. Res.*, 46 (2007) 8255-8263.
- [279] G. Crini, P.M. Badot, Application of chitosen, a natural aminopoly-saccharide for dye removal from aqueous solution by adsorption process using batch studies, *Prog. Polym. Sci.*, 33 (2008) 399-447.
- [280] N. Sakkayawonga, P. Thiravetyana, W. Nakbanpoteb, Adsorption mechanism of synthetic reactive dye wastewater by chitosan, *J. Colloid Interface Sci.*, 286 (2005) 36-42.
- [281] L. Wang, A. Q.Wang, Adsorption characteristics of Congo Red onto the chitosan/montmorillonite nanocomposite, *J. Hazard. Mater.*, 147 (2007) 979-985.
- [282] G. Mckay, Y.S. Ho, The sorption of lead ions on peat *Water Res.*, 33 (1999) 578-584.
- [283] A. Kausar, H. Nawaz, G. Mackinnon, Cost Effective Adsorption of Aluminium and Iron from Synthetic and Real Wastewater by Rice Hull Activated Carbon, *American J. Anal. Chem.*, 111 (2013) 124-133.
- [284] M.K. Sahu, R.K. Patel, Removal of safranin-O dye from aqueous solution using modified red mud: kinetics and equilibrium studies, *RSC Adv.*, 5 (2015) 78491-78501.
- [285] L. Wang, A. Wang, Adsorption characteristics of Congo Red onto the chitosan/montmorillonite nanocomposite, *J. Hazard. Mater.*, 147 (2007) 979-985.
- [286] N.A. Oladoja, A.K. Akinlabi, Congo red biosorption on palm kernel seed coat., *Ind. Eng. Chem. Res.*, 48 (2009.) 6188-6196.
- [287] H. Zhu, M. Zhang, Y. Liu, L. Zhang, R. Han, Study of congo red adsorption on to chitosen coated magnetic iron oxide in batch mode, *Desalin. Water Treat.*, 37 (2012) 46-54.
- [288] A.A. Juwarkar, S.K. Singh, A. Mudhoo, A comprehensive overview of elements in bioremediation, *Rev. Environ. Sci.*, (2010) 215-288.
- [289] F.L. Fu, Q.J. Wang, Removal of heavy metal ions from wastewaters: A review, 92 (2011) 407-418.
- [290] M.M. Matlock, B.S. Howerton, D.A. Atwood, Chemical precipitation of heavy metals from acid mine drainage, *Water Res.*, 36 (2002) 4757-4764.
- [291] P. Venkateswaran, A.N. Gopalakrishnan, K. Palanivelu, Di(2- ethylhexyl)phosphoric acid-coconut oil supported liquid membrane for the separation of copper ions from copper plating wastewater, *J. Environ. Sci.* , 19 (2007) 1446-1453.

- [292] M.G.d. Fonseca, M.M.d. Oliveira, L.N.H. Arakaki, J.G.P. Espinola, C. Airoidi, Natural vermiculite as an exchanger support for heavy cations in aqueous solution, *J. Colloid Interface Sci.*, 285 (2005) 50–55.
- [293] S.H. Hasan, P. Srivastava, Batch and continuous biosorption of Cu²⁺ by immobilized biomass of *Arthrobacter* sp., *J. Environ. Manage.*, 90 (2009) 3313–3321.
- [294] C.L. Lai, S.H. Lin, Electrocoagulation of chemical mechanical polishing (CMP) wastewater from semiconductor fabrication, *Chem. Eng. J.*, 95 (2003) 205–211.
- [295] T.Mohammadi, A.Moheb, M. Sadrzadeh, A. Razmi, Modeling of metal ion removal from wastewater by electrodialysis, *Sep. Purif. Technol.*, 41 (2005) 73–82.
- [296] M.M. Rao, D.K. Ramana, K. Seshaiyah, M.C. Wang, S.W.C. Chien, Removal of copper and cadmium from the aqueous solutions by activated carbon derived from *Ceiba pentandra* hulls, *J. Hazard. Mater.*, 166 (2009) 1006–1013.
- [297] P. Solanki, V. Gupta, R. Kulshrestha, *Chem. Eur. J.*, 7 (2010) 1200–1207.
- [298] S.H. Lin, R.S. Juang, Adsorption of phenol and its derivatives from water using synthetic resins and low-cost natural adsorbents, *Journal of Environmental Management*, 90 (2009) 1336–1349.
- [299] G.B. Cai, G.X. Zhao, X.K. Wang, S.H. Yu, Synthesis of Polyacrylic Acid Stabilized Amorphous Calcium Carbonate Nanoparticles and Their Application for Removal of Toxic Heavy Metal Ions in Water, *J. Phys. Chem. C*, 114 (2010) 12948–12954.
- [300] F. Fu, H. Zeng, Q. Cai, R. Qiu, J. Yu, Y. Xiong, Effective removal of coordinated copper from wastewater using a new dithiocarbamate-type supramolecular heavy metal precipitant, *Chemosphere*, 69 (2007) 1783–1789.
- [301] M.S. Mauter, M. Elimelech, Environmental Applications of Carbon-Based Nanomaterials, *Environ. Sci. Technol.*, 42 (2008) 5843–5859.
- [302] L.E. Macaskie, I.P. Mikheenko, P. Yong, K. Deplanche, A.J. Murray, M. Paterson-Beedle, V.S. Coker, C.I. Pearce, R. Cutting, R.A.D. Patrick, D. Vaughan, G.v.d. Laan, J.R. Lloyd, Today's wastes, tomorrow's materials for environmental protection, *Hydrometallurgy*, 104 (2010) 483–487.
- [303] T. Pradeep, Anshup, Noble metal nanoparticles for water purification: A critical review, *Thin Solid Films*, 517 (2009) 6441–6478.
- [304] J.P. Ruparelia, S.P. Dutttagupta, A.K. Chatterjee, S. Mukherji, Potential of carbon nanomaterials for removal of heavy metals from water, *Desalination*, 232 (2008) 145–156.
- [305] X. Huang, A. Schmucker, J. Dyke, S.M. Hall, J. Retrum, B. Stein, N. Remmes, D.V. Baxter, B. Dragnea, L.M. Bronstein, Magnetic nanoparticles with functional silanes: evolution of well-defined shells from anhydride containing silane, *J. Mater. Chem.*, 19 (2009) 4231–4239.
- [306] M.R. Gao, J. Jiang, S.H. Yu, *Small*, 8 (2012) 1961–2124.
- [307] Y.L. Dong, H.G. Zhang, Z.U. Rahman, L. Su, X.J. Chen, J. Hu, X.G. chen, Graphene oxide–Fe₃O₄ magnetic nanocomposites with peroxidase-like activity for colorimetric detection of glucose, *Nanoscale*, 4 (2012) 3969–3976.
- [308] H.B. Wu, J.S. Chen, H.H. Hng, X.W. Lou, Nanostructured metal oxide-based materials as advanced anodes for lithium-ion batteries, *Nanoscale*, 4 (2012) 2526–2542.
- [309] J.M. Patete, X. Peng, C. Koenigsmann, B.K. Y. Xu, S.S. Wong, Viable methodologies for the synthesis of high-quality nanostructures, *Green Chem*, 13 (2011) 482–519.
- [310] L.H. Shen, J.F. Bao, D. Wang, Y.X. Wang, Z.W. Chen, L. Ren, X. Zhou, X.B. Ke, M. Chen, A.Q. Yang, One-step synthesis of monodisperse, water-soluble ultra-small Fe₃O₄ nanoparticles for potential bioapplication, *Nanoscale*, 5 (2013) 2133–2141.
- [311] X.A. Fan, J. Guan, Z. Li, F. Mou, G. Tong, W. Wang, One-pot low temperature solution synthesis, magnetic and microwave electromagnetic properties of single-crystal iron submicron cubes, *J. Mater. Chem.*, 20 (2010) 1676–1682.
- [312] K. Kalantari, M.B. Ahmad, H.R.F. Masoumi, K. Shameli, M. Basri, R. Khandanlou, Rapid and high capacity adsorption of heavy metals by Fe₃O₄/montmorillonite

- nanocomposite using response surface methodology: Preparation, characterization, optimization, equilibrium isotherms, and adsorption kinetics study, *J Taiwan Inst. Chem. Eng.*, 49 (2015) 192-198.
- [313] K. Kalantari, M.B. Ahmad, H.R.F. Masoumi, K. Shameli, M. Basri, R. Khandanlou, Rapid Adsorption of Heavy Metals by Fe₃O₄/Talc Nanocomposite and Optimization Study Using Response Surface Methodology, *Int. J. Mol. Sci.*, 15 (2014) 12913-12927.
- [314] P. Bhunia, G. Kim, C. Baik, H. Lee, A strategically designed porous iron–iron oxide matrix on graphene for heavy metal adsorption, *Chem. Commun*, 48 (2012) 9888-9890.
- [315] F. Mi, X. Chen, Y. Ma, S. Yin, F. Yuan, H. Zhang, Facile synthesis of hierarchical core–shell Fe₃O₄@MgAl–LDH@Au as magnetically recyclable catalysts for catalytic oxidation of alcohols, *Chem. Commun*, 47 (2011) 12804–12806.
- [316] L.H. Shen, J.F. Bao, D. Wang, Y.X. Wang, Z.W. Chen, L. Ren, X. Zhou, X.B. Ke, M. Chen, A.Q. Yang, *Nanoscale*, 5 (2013) 2133-2141.
- [317] Y. Liu, L. Zhou, Y. Hu, C. Guo, H. Qian, F. Zhang, X.W. Lou, Magnetic-field induced formation of 1D Fe₃O₄/C/CdS coaxial nanochains as highly efficient and reusable photocatalysts for water treatment, *J. Mater. Chem.*, 21 (2011) 18359-18364.
- [318] Y. Wang, S. Wang, H. Niu, Y. Ma, T. Zeng, Y. Cai, Z. Meng, Preparation of polydopamine coated Fe₃O₄ nanoparticles and their application for enrichment of polycyclic aromatic hydrocarbons from environmental water samples, *J. Chromatogr*, 20 (2013) 20-26.
- [319] D. Zhang, C. Lu, Y. Ni, Z. Xu, W. Zhang, A novel 3-D chiral polyoxovanadate architecture based on breaking high symmetry of spherical [V₁₅O₃₆Cl]₈₂ cluster, *CrystEngComm*, 15 (2013) 4593-4596.
- [320] H. Shi, L. Tan, Q. Du, X. Chen, L. Li, T. Liu, C. Fu, H. Liu, X. Meng, Green synthesis of Fe₃O₄ nanoparticles with controlled morphologies using urease and their application in dye adsorption, *Dalton Trans.*, 43 (2014) 12474–12479.
- [321] W. Fan, W. Gao, C. Zhang, W.W. Tjiu, J. Pan, T. Liu, Hybridization of graphene sheets and carbon-coated Fe₃O₄ nanoparticles as a synergistic adsorbent of organic dyes, *J. Mater. Chem.*, 22 (2012) 25108-25115.
- [322] X. Li, S. Song, X. Wang, D. Liu, H. Zhang, Self-assembled 3D flower-like hierarchical Fe₃O₄/KxMnO₂ core–shell architectures and their application for removal of dye pollutants, *CrystEngComm*, 14 (2012) 2866-2870.
- [323] L.P. Zhu, N.C. Bing, L.L. Wang, H.Y. Jin, G.H. Liao, L.J. Wang, Self-assembled 3D porous flowerlike α -Fe₂O₃ hierarchical nanostructures: Synthesis, growth mechanism, and their application in photocatalysis, *Dalton Trans.*, 41 (2012) 2959-2965.
- [324] G. Xie, P. Xi, H. Liu, F. Chen, L. Huang, Y. Shi, F. Hou, Z. Zeng, C. Shao, J. Wang, A facile chemical method to produce superparamagnetic graphene oxide–Fe₃O₄ hybrid composite and its application in the removal of dyes from aqueous solution, *J. Mater. Chem.*, 22 (2012) 1033–1039.
- [325] X. Wang, Y. Zhong, T. Zhai, Y. Gao, S. Chen, Y. Ma, J. Yao, Y. Bando, D. Golberg, Multishelled Co₃O₄- Fe₃O₄ hollow spheres with even magnetic phase distribution: Synthesis, magnetic properties and their application in water treatment, *J. Mater. Chem.*, 21 (2011) 17680-17687.
- [326] B. Geng, F. Zhan, H. Jiang, Y. Guo, Z. Xing, Egg albumin as a nanoreactor for growing single-crystalline Fe₃O₄ nanotubes with high yields, *Chem. Commun.*, (2008) 5773-5775.
- [327] K.C. Chin, G.L. Chong, C.K. Poh, L.H. Van, C.H. Sow, J. Lin, A.T.S. Wee, Large-Scale Synthesis of Fe₃O₄ Nanosheets at Low Temperature, *J. Phys. Chem. C*, 111 (2007) 9136-9141.
- [328] X. Li, Z. Si, Y. Lei, J. Tang, S. Wang, S. Su, S. Song, L. Zhao, H. Zhang, Direct hydrothermal synthesis of single-crystalline triangular Fe₃O₄ nanoprisms, *CrystEngComm*, 12 (2010) 2060–2063.

- [329] P.K. Jal, S. Patel, B.K. Mishra, Chemical modification of silica surface by immobilization of functional groups for extractive concentration of metal ions, *Talanta*, 62 (2004) 1005–1028.
- [330] K. Sharma, S. Mittal, M. Koel, Analysis of trace amounts of metal ions using silica-based chelating resins: a green analytical method, *Crit. Rev. Anal. Chem.*, 33 (2003) 183–198.
- [331] T. Seshadri, A. Kettrupt, Synthesis and characterization of silica gel ionexchanger bearing 2-amino-1-cyclopentene-1-dithio-carboxylic acid (ACDA) as chelating compound, *Fresen. Z. Anal. Chem.*, 310 (1982) 1–5.
- [332] D.E. Leyden, G.H. Luttrell, Preconcentration of trace metals using chelating groups immobilized via silylation, *Anal. Chem.*, 47 (1975) 1612–1617.
- [333] M. Martinez, N. Miralles, S. Hidalgo, N. Fiol, I. Villaescusa, J. Poch, Removal of lead(II) and cadmium(II) from aqueous solutions using grape stalk waste, *J. Hazard. Mater.*, 133 (2006) 203–211.
- [334] E. Repo, J.K. Warchol, T.A. Kurniawan, M.E.T. Sillanpaa, Adsorption of Co(II) and Ni(II) by EDTA- and/or DTPA-modified chitosan: kinetic and equilibrium modeling, *Chem. Eng. J.*, 161 (2010) 73–82.
- [335] O.K. Junior, L.V.A. Gurgel, R.P.d. Freitas, L.F. Gil, Adsorption of Cu (II), Cd (II), and Pb (II) from aqueous single metal solutions by mercerized cellulose and mercerized sugarcane bagasse chemically modified with EDTA dianhydride (EDTAD), *Carbohydr. Polym.*, 77 (2009) 643–650.
- [336] L.Y. Wang, I.Q. Yang, Y.F. Li, Y. Zhang, X.J. Ma, Z.F. Ye, Study on adsorption mechanism of Pb(II) and Cu(II) in aqueous solution using PS-EDTA resin, *Chem. Eng. J.*, 163 (2010) 364–372.
- [337] E. Repo, T.A. Kurniawan, J.K. Warchol, M.E.T. Sillanpaa, Removal of Co(II) and Ni(II) ions from contaminated water using silica gel functionalized with EDTA and/or DTPA as chelating agents, *J. Hazard. Mater.*, 171 (2009) 1071–1080.
- [338] M.A. Hughes, E. Rosenherg, Characterization and applications of poly-acetate modified silica polyamine composites, *Sep. Sci. Technol.*, 42 (2007) 261–283.
- [339] J.X. Yu, M. Tong, X.M. Sun, B.H. Li, Enhanced and selective adsorption of Pb²⁺ and Cu²⁺ by EDTAD-modified biomass of baker's yeast, *Bioresour. Technol.*, 99 (2008) 2588–2593.
- [340] Z.G. Xiong, L.L. Zhang, J.Z. Ma, X.S. Zhao, Photocatalytic degradation of dyes over graphene-gold nanocomposites under visible light irradiation, *Chem. Commun.*, 46 (2010) 6099–6101.
- [341] M. Yamaura, R.L. Camilo, L.C. Sampaio, M.A. Macêdo, M. Nakamura, H.E. Toma, Preparation and characterization of (3-aminopropyl)triethoxysilane-coated magnetite nanoparticles, *J. Magn. Mater.*, 279 (2004) 210–217.
- [342] B. Feng, R.Y. Hong, L.S. Wang, L. Guo, H.Z. Li, J. Ding, Y. Zheng, D.G. Wei, Synthesis of Fe₃O₄/APTES/PEG diacid functionalized magnetic nanoparticles for MR imaging, *Colloid Surface A*, 328 (2008) 52–59.
- [343] M. Yamaura, R.L. Camilo, L.C. Sampaio, M.A. Macedo, M. Nakamura, H.E. Toma, Preparation and characterization of (3-aminopropyl) triethoxysilane-coated magnetite nanoparticles, 279 (2004) 210–217.
- [344] L. Jiang, F. Li, J. Feng, P. Wang, Q. Liu, Y. Li, Y. Dong, Q. Wei, *RSC Adv.*, 6 (2016) 24373–24380.
- [345] S. Bruni, F. Cariati, M. Casu, A. Lai, A. Musinu, G. Piccaluga, S. Solinas, IR and NMR study of nanoparticle-support interactions in a Fe₂O₃-SiO₂ nanocomposite prepared by a Sol-gel method, *Nanostruct. Mater.*, 11 (1999) 573–586.
- [346] L. Guang-She, L. Li-Ping, R. Smith, H. Inomata, Characterization of the dispersion process for NiFe₂O₄ nanocrystals in a silica matrix with infrared spectroscopy and electron paramagnetic resonance, *J. Mol. Struct.*, 560 (2001) 87–93.

- [347] L. Jiang, F. Li, J. Feng, P. Wang, Q. Liu, Y. Li, Y. Dong, Q. Wei, *RSC Adv.*, 6 (2016) 24373–24380.
- [348] X. Wang, S. Zhang, J. Li, J. Xub, X. Wang, *Inorg. Chem. Front.*, Fabrication of Fe/Fe₃C@porous carbon sheets from biomass and their application for simultaneous reduction and adsorption of uranium(VI) from solution, 1 (2014) 641-648.
- [349] M.J. Nasab, A.R. Kiasat, Multifunctional Fe₃O₄@nSiO₂@mSiO₂/Pr-Imi-NH₂·Ag core-shell microspheres as highly efficient catalysts in the aqueous reduction of nitroarenes: improved catalytic activity and facile catalyst recovery, *RSC Adv.*, 6 (2016) 41871-41877.
- [350] S.P. Schwaminger, P.F. García, G.K. Merck, F.A. Bodensteiner, S. Heissler, S. Günther, S. Berensmeier, Nature of Interactions of Amino Acids with Bare Magnetite Nanoparticles, *J. Phys. Chem. C*, 119 (2015) 23032–23041.
- [351] S. Yu, G.M. Chow, Carboxyl group (–CO₂H) functionalized ferrimagnetic iron oxide nanoparticles for potential bio-applications, *J. Mater. Chem.*, 14 (2004) 2781-2786.
- [352] G.F. Goya, T.S. Berquo, F.C. Fonseca, M.P. Morales, Static and dynamic magnetic properties of spherical magnetite nanoparticles, *J. Appl. Phys.*, 94 (2003) 3520–3528.
- [353] S. Zeng, Y. Cao, W. Sang, T. Li, N. Gan, L. Zheng, Enrichment of Polychlorinated Biphenyls from Aqueous Solutions Using Fe₃O₄ Grafted Multiwalled Carbon Nanotubes with Poly Dimethyl Diallyl Ammonium Chloride, *Int. J. Mol. Sci.*, 13 (2012) 6382-6398.
- [354] E.C.S. Santos, T.C.d. Santos, R.B. Guimarães, L. Ishida, R.S. Freitas, C.M. Ronconi, Guanidine-functionalized Fe₃O₄ magnetic nanoparticles as basic recyclable catalysts for biodiesel production, *RSC Adv.*, 5 (2015) 48031-48038.
- [355] M. Bloemen, W. Brullot, T.T. Luong, N. Geukens, A. Gils, T. Verbiest, Improved functionalization of oleic acid-coated iron oxide nanoparticles for biomedical applications, *J Nanopart Res.*, 14 (2012) 1100-1110.
- [356] S. Mosivand, I. Kazeminezhad, Functionalization and characterization of electrocrystallized iron oxide nanoparticles in the presence of β-cyclodextrin, *CrystEngComm.*, 18 (2016) 417-426.
- [357] Y. Liang, N. Guo, L. Li, R. Li, G. Ji, S. Gan, Preparation of porous 3D Ce-doped ZnO microflowers with enhanced photocatalytic performance, *RSC Adv.*, 5 (2015) 59887-59894.
- [358] J. Guo, X. Zhang, H. Gu, Y. Wang, X. Yag, D. Ding, J. Long, S. Tadakamalla, Q. Wang, M.A. Khan, J. Liu, X. Zhang, B.L. Weeks, L. Sun, D.P. Young, S.W. and, Z. Guo, Reinforced magnetic epoxy nanocomposites with conductive polypyrrole nanocoating on nanomagnetite as a coupling agent, *RSC Adv.*, 4 (2014) 36560–36572.
- [359] S. Venkateswarlu, M. Yoon, Core-Shell Ferromagnetic Nanorod Based on Amine Polymer Composite (Fe₃O₄@DAPF) for Fast Removal of Pb(II) from Aqueous Solutions, *ACS Appl. Mater. Interfaces.*, 7 (2015) 25362–25372.
- [360] S. Zhang, X. Chen, C. Gu, Y. Zhang, J. Xu, Z. Bian, D. Yang, N. Gu, The Effect of Iron Oxide Magnetic Nanoparticles on Smooth Muscle Cells, *Nanoscale Res. Lett.*, 4 (2009) 70-77.
- [361] A. Zirino, S. Yamamoto, A pH-dependent model for the chemical speciation of copper, zinc, cadmium and lead in seawater. , *Limnol. Oceanogr.*, 17 (1972) 661-671.
- [362] A. Shahzad, W. Miran, K. Rasool, M. Nawaz, J. Jang, S.R. Lim, D.S. Lee, Heavy metals removal by EDTA-functionalized chitosan graphene oxide nanocomposites, *RSC Adv.*, 7 (2017) 9764–9771.
- [363] X.-j. Yang, L. Yang, L. Dong, X.-l. Long, W.-k. Yuan, Kinetics of the [Fe(III)-EDTA]⁻ Reduction by Sulfite under the Catalysis of Activated Carbon, *Energy Fuels*, 25 (2011) 4248–4255.
- [364] B. Tawabini, S. Al-Khaldi, M. Atieh, M. Khaled, Removal of mercury from water by multi-walled carbon nanotubes, *Water Sci. Technol.*, 61 (2010) 591-598.

- [365] K. Pyrzynska, Sorption of Cd(II) onto carbon-based materials—a comparative study, *Microchim. Acta.*, 169 (2010) 7-13.
- [366] A. Kausar, H. Nawaz, G. Mackinnon, Equilibrium, kinetic and thermodynamic studies on the removal of U(VI) by low cost agricultural waste, *Colloids Surf., B*, 111 (2013) 124–133.
- [367] S. Chowdhury, R. Mishra, P. Kushwaha, P. Saha, Removal of safranin from aqueous solutions by NaOH-treated rice husk: thermodynamics, kinetics and isosteric heat of adsorption, *Asia-Pac. J. Chem. Eng.*, 7 (2012) 236–249.
- [368] S.F. Hou, S.J. Su, M.L. Kasner, P. Shah, K. Patel, C. Madarang, Formation of highly stable dispersions of silane-functionalized reduced graphene oxide, *Chem. Phys. Lett.*, 501 (2010) 68.
- [369] K. Kadirvelu, C.F. -Brasquet, P.L. Cloirec, Removal of Cu(II), Pb(II), and Ni(II) by Adsorption onto Activated Carbon Cloths, *Langmuir*, 16 (2000) 8404–8409.
- [370] M. Babazadeh, R. H.-Khanmiria, J. Abolhasania, E. G.-Kalhora, A. Hassanpour, Solid phase extraction of heavy metal ions from agricultural samples with the aid of a novel functionalized magnetic metal–organic framework, *RSC Adv.*, 5 (2015) 19884-19892.
- [371] F. Gao, H. Gu, H. Wang, X. Wang, B. Xiang, Z. Guob, Magnetic amine-functionalized polyacrylic acidnanomagnetite for hexavalent chromium removal from polluted water, *RSC Adv.*, 5 (2015) 60208-60219.
- [372] T. Mayer-Gall, K. Opwis, J.S. Gutmann, Polyvinylamine modified polyester fibers – innovative textiles for the removal of chromate from contaminated groundwater, *J. Mater. Chem. A*, 3 (2015) 386-394.
- [373] R. Mukherjee, P. Bhunia, S. De, Long term filtration modelling and scaling up of mixed matrix ultrafiltration hollow fiber membrane: a case study of chromium(VI) removal, *Journal of Membrane Science*, 570–571 (2019) 204-214.
- [374] H. Gu, H. Lou, D. Ling, B. Xiang, Z. Guo, Polystyrene Controlled Growth of Zerovalent Nanoiron/Magnetite on a Spongelike Carbon Matrix towards Effective Cr(VI) Removal from Polluted Water., *RSC Adv.*, 6 (2016) 110134–110145.
- [375] F. Gao, H. Gu, H. Wang, X. Wang, B. Xiang, Z. Guo, Magnetic Amine-Functionalized Polyacrylic Acid-Nanomagnetite for Hexavalent Chromium Removal from Polluted Water *RSC Adv*, 5 (2015) 60208–60219.
- [376] Z. Zhang, H. Luo, X. Jiang, Z. Jiang, C. Yang, Synthesis of reduced graphene oxide-montmorillonite nanocomposite and its application in hexavalent chromium removal from aqueous solutions, *RSC Adv*, 5 (2015) 47408–47417.
- [377] M. Costa, Toxicity and Carcinogenicity of Cr(VI) in Animal Models and Humans, *Crit. Rev. Toxicol* 27 (1997) 431–442.
- [378] A.E. Nogueira, A.S. Giroto, A.B.S. Neto, C. Ribeiro, CuO Synthesized by Solvothermal Method as a High Capacity Adsorbent for Hexavalent Chromium, *Colloids Surf., A* 498 (2016) 161–167.
- [379] Z.-n. Huang, X.-l. Wang, D.-s. Yang, Adsorption of Cr(VI) in Wastewater Using Magnetic Multi-Wall Carbon Nanotubes *Water Sci. Eng.*, 8 (2015) 226–232.
- [380] A.M. Muliwa, T.Y. Leswif, M.S. Onyango, A. Maity, Magnetic Adsorption Separation (MAS) Process: An Alternative Method of Extracting Cr(VI) from Aqueous Solution Using Polypyrrole Coated Fe₃O₄nanocomposites., *Sep. Purif. Technol.*, 158 (2016) 250–258.
- [381] J. Wang, K. Pan, Q. He, B. Cao, Polyacrylonitrile/Polypyrrole Core/Shell Nanofiber Mat for the Removal of Hexavalent Chromium from Aqueous Solution. , *J. Hazard. Mater.*, 244–245 (2013) 121–129.
- [382] L.A. Rodrigues, L.J. Maschio, R.E.d. Silva, M.L.C.P.d. Silva, Adsorption of Cr(VI) from Aqueous Solution by Hydrous Zirconium Oxide., *J. Hazard. Mater.*, 173 (2010) 630–636.

- [383] Y. Zeng, H. Woo, G. Lee, J. Park, Removal of chromate from water using surfactant modified Pohang clinoptilolite and Haruna chabazite, *Desalination*, 257 (2010) 102–109.
- [384] N. Sankararamkrishnan, A. Dixit, L. Iyengar, R. Sanghi, Removal of hexavalent chromium using a novel cross linked xanthated chitosan, *Bioresour. Technol.*, 97 (2006) 2377–2382.
- [385] Z. Wu, X. Yuan, G. Zeng, L. Jiang, H. Zhong, Y. Xie, H. Wang, X. Chen, H. Wang, Highly Efficient Photocatalytic Activity and Mechanism of $\text{Yb}^{3+}/\text{Tm}^{3+}$ codoped In_2S_3 from Ultraviolet to near Infrared Light towards Chromium (VI) Reduction and Rhodamine B Oxydative Degradation., *Appl. Catal. B* 225 (2018) 8–21.
- [386] J.Y. Zheng, X. Wang, W. Li, Z. Cao, H. Wang, C. Zhang, W.-G. Song, Y. Ma, J. Yao, Cubic nickel frames: one-pot synthesis, magnetic properties and application in water treatment, *Cryst. Eng. Comm* 14 (2012) 7616–7620.
- [387] S. Rengaraj, C.K. Joo, Y. Kim, J. Yi, Kinetics of removal of chromium from water and electronic process wastewater by ion exchange resins: 1200H 1500H and IRN97H, *J. Hazard. Mater.*, 102 (2003) 257–275.
- [388] S. Rengaraj, K.H. Yeon, S.H. Moon, Removal of chromium from water and wastewater by ion exchange resins, *J. Hazard. Mater.*, 87 (2001) 273–287.
- [389] M. Tan, X. Liu, W. Li, H. Li, Enhancing Sorption Capacities for Copper(II) and Lead(II) under Weakly Acidic Conditions by l-Tryptophan-Functionalized Graphene Oxide, *J. Chem. Eng. Data* 60 (2015) 1469–1475.
- [390] A. Hafez, S. El-Mariharawy, Design and performance of the two-stage/two-pass RO membrane system for chromium removal from tannery wastewater, *Desalination*, 165 (2004) 141–151.
- [391] Z. Modrzejewska, W. Kaminski, Separation of Cr(VI) on chitosan membranes, *Ind. Eng. Chem. Res.*, 38 (1999) 4946–4950.
- [392] S. Tunali, I.K. ve, T. Akar, Chromium(VI) biosorption characteristics of *Neurospora crassa* fungal biomass *Miner. Eng* 18 (2005) 681–689.
- [393] A. Sari, M. Tuzen, O.D.U. zlu, M. Soylak, Biosorption of Pb(II) and Ni(II) from aqueous solution by lichen (*Cladonia furcata*) biomass, *Biochem. Eng. J.*, 37 (2007) 151–158.
- [394] A. Sari, M. Tuzen, M. Soylak, Adsorption of Pb(II) and Cr(III) from aqueous solution on celtek clay, *J. Hazard. Mater. B* 141 (2007) 258–263.
- [395] M. Yusuf, M.A. Khan, M. Otero, E.C. Abdullah, M. Hosomi, A. Terada, S. Riya, Synthesis of CTAB intercalated graphene and its application for the adsorption of AR265 and AO7 dyes from water, *J. Colloid Interface Sci.*, 493 (2017) 51–61.
- [396] H. Wang, X. Yuan, Y. Wu, X. Chen, L. Leng, H. Wang, H. Li, G. Zeng, Facile Synthesis of Polypyrrole Decorated Reduced Graphene Oxide- Fe_3O_4 magnetic Composites and Its Application for the Cr(VI) Removal, *Chem. Eng. J* 262 (2015) 597–606.
- [397] V.K. Gupta, S. Agarwal, T.A. Saleh, Chromium removal by combining the magnetic properties of iron oxide with adsorption properties of carbon nanotubes *Water Res.*, 45 (2011) 2207–2212.
- [398] D. Park, Y.-S. Yun, D.S. Lee, J.M. Park, Optimum condition for the removal of Cr (VI) or total Cr using dried leaves of *pinus densiflora*, *Desalination*, 271 (2011) 309–314.
- [399] Z. Li, Q. Tang, T. Katsumi, X. Tang, T. Inui, S. Imaizumi, Leaf char: an alternative adsorbent for Cr(III), *Desalination*, 264 (2011) 70–77.
- [400] E. Kilic, J. Font, R. Puigb, S.C. Olak, D. C, Elik, Chromium recovery from tannery sludge with saponin and oxidative remediation, *J. Haz. Mat.*, 185 (2011) 456–462.
- [401] K.R. Reddy, K.P. Lee, A.I. Gopalan, Self-assembly approach for the synthesis of electro-magnetic functionalized Fe_3O_4 /polyaniline nanocomposites: Effect of dopant on the properties, *Colloids and Surfaces A: Physicochemical and Engineering Aspects*, 320 (2008) 49–56.

- [402] K.R. Reddy, K.P. Lee, J.Y. Kim, Y. Lee, Self-Assembly and Graft Polymerization Route to Monodispersed $\text{Fe}_3\text{O}_4@\text{SiO}_2$ —Polyaniline Core–Shell Composite Nanoparticles: Physical Properties, *J. Nanosci. Nanotechnol.*, 8 (2008) 5632–5639.
- [403] F. Mi, X. Chen, Y. Ma, S. Yin, F. Yuan, H. Zhang, Facile synthesis of hierarchical core–shell $\text{Fe}_3\text{O}_4@\text{MgAl-LDH}@Au$ as magnetically recyclable catalysts for catalytic oxidation of alcohols, *Chemical Communicable*, 47 (2011) 12804–12806.
- [404] L.H. Shen, J.F. Bao, D. Wang, Y.X. Wang, Z.W. Chen, L. Ren, X. Zhou, X.B. Ke, M. Chen, A.Q. Yang, One-step synthesis of monodisperse, watersoluble ultra-small Fe_3O_4 nanoparticles for potential bioapplication., *Nanoscale* 5 (2013) 2133–2141.
- [405] M.R. Gao, J. Jiang, S.H. Yu, Solution-based synthesis and design of late transition metal chalcogenide materials for oxygen reduction reaction (ORR), *Small*, 8 (2012) 1961–2124.
- [406] Y.L. Dong, H.G. Zhang, Z.U. Rahman, L. Su, X.J. Chen, J. Hu, X.G. Chen, Graphene oxide– Fe_3O_4 magnetic nanocomposites with peroxidase-like activity for colorimetric detection of glucose, *Nanoscale*, 4 (2012) 3969–3976.
- [407] J. Mu, B. Chen, Z. Guo, M. Zhang, Z. Zhang, P. Zhang, C. Shao, Y. Liu, Highly dispersed Fe_3O_4 nanosheets on one-dimensional carbon nanofibers: synthesis, formation mechanism, and electrochemical performance as supercapacitor electrode materials., *Nanoscale*, 3 (2011) 5034–5040.
- [408] H.B. Wu, J.S. Chen, H.H. Hng, X.W. Lou, Nanostructured metal oxide-based materials as advanced anodes for lithium-ion batteries, *Nanoscale*, 4 (2012) 2526–2542.
- [409] J.M. Patete, X. Peng, C. Koenigsmann, Y. Xu, B. Karn, S.S. Wong, Viable methodologies for the synthesis of high-quality nanostructures, *Green Chemistry*, 13 (2011) 482–519.
- [410] Y. Liu, L. Zhou, Y. Hu, C. Guo, H. Qian, F. Zhang, X.W. Lou, Magnetic-field induced formation of 1D $\text{Fe}_3\text{O}_4/\text{C}/\text{CdS}$ coaxial nanochains as highly efficient and reusable photocatalysts for water treatment *Journal of Materials Chemical*, 21 (2011) 18359–18364.
- [411] Y. Wang, S. Wang, H. Niu, Y. Ma, T. Zeng, Y. Cai, Z. Meng, Preparation of polydopamine coated Fe_3O_4 nanoparticles and their application for enrichment of polycyclic aromatic hydrocarbons from environmental water samples. , *Journal of Chromatography*, 20 (2013) 20–26.
- [412] D. Zhang, C. Lu, Y. Ni, Z. Xu, W. Zhang, A novel 3-D chiral polyoxovanadate architecture based on breaking high symmetry of spherical $[\text{V}_{15}\text{O}_{36}\text{Cl}]_{82}$ cluster, *Crystal Engineering Commission*, 15 (2013) 4593–4596.
- [413] P. Bhunia, G. Kim, C. Baik, H. Lee, A strategically designed porous iron–iron oxide matrix on graphene for heavy metal adsorption. , *Chemical Communicable*, 48 (2012) 9888–9890.
- [414] L. Ai, J. He, Y. Wang, C. Wei, J. Zhan, Aerosol-assisted in situ synthesis of iron–carbon composites for the synergistic adsorption and reduction of Cr(VI), *RSC Adv.*, 6 (2016) 56108-56115.
- [415] S. Kumar, M. Umar, A. Saifi, S. Kumar, S. Augustine, S. Srivastava, B. D.Malhotra, Electrochemical paper based cancer biosensor using iron oxide nanoparticles decorated PEDOT:PSS, *Anal. Chim. Acta*, 1056 (2019) 135-145.
- [416] J. Zhu, S. Wei, H. Gu, S.B. Rapole, Q. Wang, Z. Luo, N. Haldolaarachchige, D.P. Young, Z. Guo, One-Pot Synthesis of Magnetic Graphene Nanocomposites Decorated with Core@Double-Shell Nanoparticles for Fast Chromium Removal. , *Environ. Sci. Technol.*, 46 (2012) 977–985.
- [417] L.P. Lingamdinne, J.R. Koduru, Y.L. Choi, Y.Y. Chang, J.K. Yang, Studies on Removal of Pb(II) and Cr(III) Using Graphene Oxide Based Inverse Spinel Nickel Ferrite Nano-Composite as Sorbent, *Hydrometallurgy*, 165 (2016) 64–72.

- [418] C. He, Z. Yang, J. Ding, Y. Chen, X. Tong, Y. Li, Effective Removal of Cr(VI) from Aqueous Solution by 3-Aminopropyltriethoxysilane-Functionalized Graphene Oxide, *Colloids Surf.A* 520 (2017) 448–458.
- [419] M.R. Das, Synthesis of silver nanoparticles in an aqueous suspension of graphene oxide sheets and its antimicrobial activity, *Colloids and Surfaces B: Biointerfaces*, 83 (2011) 16-22.
- [420] Q. Bao, D. Zhan, P. Qi, Synthesis and characterization of silver nanoparticle and graphene oxide nanosheet composites as a bactericidal agent for water disinfection, *Journal of colloid and interface science*, 360 (2011) 463-470.
- [421] Z. Liu, J.T. Robinson, X. Sun, H. Dai, PEGylated nanographene oxide for delivery of water-insoluble cancer drugs, *Journal of the American Chemical Society*, 130 (2008) 10876-10877.
- [422] H. Chen, M.B. Müller, K.J. Gilmore, G.G. Wallace, D. Li, Mechanically strong, electrically conductive, and biocompatible graphene paper., *Advanced Materials*, 20 (2008) 3557-3561.
- [423] M. Premanathan, K. Karthikeyan, K. Jeyasubramanian, G. Manivannan, Selective toxicity of ZnO nanoparticles toward Gram-positive bacteria and cancer cells by apoptosis through lipid peroxidation, *Nanomedicine: Nanotechnology, Biology and Medicine*, 7 (2011) 184-192.
- [424] X. Sun, Z. Liu, K. Welsher, J.T. Robinson, A. Goodwin, S. Zaric, H. Dai, Nano-graphene oxide for cellular imaging and drug delivery, *Nano research*, 1 (2008) 203-212.
- [425] A. Nath, A. Das, L. Rangan, A. Khare, Bacterial inhibition by Cu/Cu₂O nanocomposites prepared via laser ablation in liquids *Science of Advanced Materials*, 4 (2012) 106-109.
- [426] O. Akhavan, E. Ghaderi, Toxicity of graphene and graphene oxide nanowalls against bacteria, *ACS nano* 4(2010) 5731-5736.
- [427] C.D. Vecitis, K.R. Zodrow, S. Kang, M. Elimelech, Electronic-structure-dependent bacterial cytotoxicity of single-walled carbon nanotubes, *ACS nano*, 4 (2010) 5471-5479.
- [428] S. Liu, T.H. Zeng, M. Hofmann, E. Burcombe, J. Wei, R. Jiang, J. Kong, Y. Chen, Antibacterial activity of graphite, graphite oxide, graphene oxide, and reduced graphene oxide: membrane and oxidative stress *ACS nano*, 5 (2011) 6971-6980.
- [429] M.R. Das, R.K. Sarma, R. Saikia, V.S. Kale, M.V. Shelke, P. Sengupta, Synthesis of silver nanoparticles in an aqueous suspension of graphene oxide sheets and its antimicrobial activity, *Colloids and Surfaces B: Biointerfaces*, 83 (2011) 16-22.
- [430] Q. Bao, D. Zhang, P. Qi, Synthesis and characterization of silver nanoparticle and graphene oxide nanosheet composites as a bactericidal agent for water disinfection, *Journal of colloid and interface science*, 360 (2011) 463-470.
- [431] D. Zhang, X. Liu, X. Wang, Green synthesis of graphene oxide sheets decorated by silver nanoprisms and their anti-bacterial properties, *Journal of inorganic biochemistry*, 105 (2011) 1181-1186.
- [432] X. Fan, W. Peng, Y. Li, X. Li, S. Wang, G. Zhang, F. Zhang, Deoxygenation of exfoliated graphite oxide under alkaline conditions: a green route to graphene preparation, *Advanced Materials*, 20 (2008) 4490-4493.
- [433] K.S. Novoselov, A.K. Geim, S.V. Morozov, D. Jiang, Y. Zhang, S.V. Dubonos, I.V. Grigorieva, Electric Field Effect in Atomically Thin Carbon Films, *Science* 306 (2004) 666-669.
- [434] S. Stankovich, D.A. Dikin, G.H.B. Dommett, K.M. Kohlhaas, E.J. Zimney, E.A. Stach, R.D. Piner, S.T. Nguyen, R.S. Ruoff, Graphene-based composite materials, *Nature*, 442 (2006) 282-286.
- [435] S. Watcharotone, D.A. Dikin, S. Stankovich, R. Piner, I. Jung, G.H.B. Dommett, G. Evmenenko, S.E. Wu, S. FChen, C.P.Liu, S.T. Nguyen, R.S. Ruoff, Graphene– silica composite thin films as transparent conductors *Nano letters* 7(2007) 1888-1892.

- [436] X. Wang, S. Yu, J. Jin, H. Wang, N.S. Alharbi, A. Alsaedi, T. Hayat, X. Wang, Application of graphene oxides and graphene oxide-based nanomaterials in radionuclide removal from aqueous solutions, *Science bulletin*, 61 (2016) 1583-1593.
- [437] L.A. Carvalho, J.D. Ardisson, R.M. Lago, M.D. Vargas, M.H. Araujo, Reactive Porous Composites for Chromium(VI) Reduction Applications Based on Fe/Carbon Obtained from Post-Consumer PET and Iron Oxide†, *RSC Adv*, 5 (2015) 97248–97255.
- [438] B.M. Weckhuysen, I.E. Wachs, R.A. Schoonheydt, *Surface Chemistry and Spectroscopy of Chromium in Inorganic Oxides*, *Chem. Rev.*, 96 (1996) 3327-3349.
- [439] J.K. Sahoo, S.K. Paikra, M. Mishra, H. Sahoo, Amine functionalized magnetic iron oxide nanoparticles: Synthesis, antibacterial activity and rapid removal of Congo red dye, *J. mol. Liq.*, 282 (2019) 428-440.
- [440] S. Verma, H.P. Mungse, N. Kumar, S. Choudhary, S.L. Jain, B. Sain, O.P. Khatri, Graphene oxide: An efficient and reusable carbocatalyst for aza-Michael addition of amines to activated alkenes, *Chem. Commun*, 47 (2011) 12673–12675.
- [441] M. Liu, T. Wen, X. Wu, C. Chen, J. Hu, J. Li, X. Wang, Synthesis of Porous Fe₃O₄ Hollow Microspheres/Graphene Oxide Composite for Cr(vi) Removal, *Dalt. Trans*, 42 (2013) 14710–14717.
- [442] S. Mohan, V. Kumar, D.K. Singh, S.H. Hasan, Synthesis and Characterization of RGO/ZrO₂ Nanocomposite for Enhanced Removal of Fluoride from Water: Kinetics, Isotherm, and Thermodynamic Modeling and Its Adsorption Mechanism, *RSC Adv* 6(2016) 87523–87538.
- [443] R.D. Waldron, *Infrared Spectra of Ferrites*, *Phys. Rev* 99 (1955) 1727.
- [444] M. Ma, Y. Zhang, W. Yu, H. Shen, H. Zhang, N. Gu, Preparation and characterization of magnetite nanoparticles coated by amino silane, *Colloids Surf. A* 212 (2003) 219-226.
- [445] L. Guang-She, L. Li-Ping, R.L.S. Jr, H. Inomata, Characterization of the dispersion process for NiFe₂O₄ nanocrystals in a silica matrix with infrared spectroscopy and electron paramagnetic resonance, *J. Molec. Struct.* , 560 (2001) 87-93.
- [446] S. Bruni, F. Cariati, M. Casu, A. Lai, A. Musinu, G. Piccaluga, S. Solinas, IR and NMR study of nanoparticle-support interactions in a Fe₂O₃-SiO₂ nanocomposite prepared by a Sol-gel method, *NanoStructured Mater*, 11 (1999) 573-586.
- [447] Z. Xu, Q. Liu, J.A. Finch, Silanation and stability of 3-aminopropyl triethoxy silane on nanosized superparamagnetic particles: I. Direct silanation, *Appl. Surf. Sci*, 120 (1997) 269-278.
- [448] L.D. White, C.P. Tripp, Reaction of (3-Aminopropyl)dimethylethoxysilane with Amine Catalysts on Silica Surfaces, *J. Colloid Interface Sci*, 232 (2000) 400-407.
- [449] W. Hou, B. Tang, L. Lu, J. Sun, J. Wang, C. Qin, L. Dai, Preparation and Physico-Mechanical Properties of Amine-Functionalized Graphene/Polyamide 6 Nanocomposite Fiber as a HighPerformance Material, *RSC Adv*, 4 (2014) 4848–4855.
- [450] B. Dehghanzad, M.K.R. Aghjeh, O. Rafeie, A. Tavakoli, A.J. Oskooie, Synthesis and Characterization of Graphene and Functionalized Graphene via Chemical and Thermal Treatment Methods *RSC Adv*, 6 (2016) 3578–3585.
- [451] D. Zhao, X. Gao, C. Wu, R. Xie, S. Feng, C. Chen, Facile Preparation of Amine Functionalized Graphene Oxide Decorated with Fe₃O₄ nanoparticles for the Adsorption of Cr(VI), *Appl. Surf. Sci*, 384 (2016) 1–9.
- [452] M. Heidarizad, S.S. Şengör, Synthesis of Graphene Oxide/ Magnesium Oxide Nanocomposites with High-Rate Adsorption of Methylene Blue, *J. Mol. Liq*, 224 (2016) 607–617.
- [453] X. Yang, C. Chen, J. Li, G. Zhao, X. Ren, X. Wang, Graphene oxide-iron oxide and reduced graphene oxide-iron oxide hybrid materials for the removal of organic and inorganic pollutants, *RSC Adv*, 2 (2012) 8821-8826.

- [454] M. Heidarizad, S.S. Şengör, Synthesis of Graphene Oxide/ Magnesium Oxide Nanocomposites with High-Rate Adsorption of Methylene Blue., *J. Mol. Liq* 224 (2016) 607–617.
- [455] S.K. Sahoo, G. Hota, Surface Functionalization of GO with MgO/MgFe₂O₄ Binary Oxides : A Novel Magnetic Nanoadsorbent for Removal of Fluoride Ions, *J. Environ. Chem. Eng.*, 6 (2018) 2918–2931.
- [456] D. Yang, Chemical analysis of graphene oxide films after heat and chemical treatments by X-ray photoelectron and Micro-Raman spectroscopy., *Carbon* 47 (2009) 145–152.
- [457] D. Zhao, X. Gao, C. Wu, R. Xie, S. Feng, C. Chen, Facile Preparation of Amino Functionalized Graphene Oxide Decorated with Fe₃O₄ nanoparticles for the Adsorption of Cr(VI), *Appl. Surf. Sci.*, 384 (2016) 1–9.
- [458] Y. Lin, S. Xu, J. Li, Fast and Highly Efficient Tetracyclines Removal from Environmental Waters by Graphene Oxide Functionalized Magnetic Particles, *Chem. Eng. J.*, 225 (2013) 679–685.
- [459] D. Dinda, S.K. Saha, Sulfuric Acid Doped Poly Diaminopyridine/Graphene Composite to Remove High Concentration of Toxic Cr(VI). *J. Hazard. Mater.* , 291 (2015) 93–101.
- [460] Z. Wu, H. Zhong, X. Yuan, H. Wang, L. Wang, X. Chen, G. Zeng, Y. Wu, Adsorptive Removal of Methylene Blue by Rhamnolipid-Functionalized Graphene Oxide from Wastewater, *Water Res.* , 67 (2014) 330–344.
- [461] D.K. Singh, V. Kumar, S. Mohan, S.H. Hasan, Polylysine Functionalized Graphene Aerogel for the Enhanced Removal of Cr(VI) through Adsorption: Kinetic, Isotherm, and Thermodynamic Modeling of the Process., *J. Chem. Eng. Data* 62 (2017) 1732–1742.
- [462] C. He, Z. Yang, J. Ding, Y. Chen, X. Tong, Y. Li, Effective Removal of Cr(VI) from Aqueous Solution by 3-Aminopropyltriethoxysilane-Functionalized Graphene Oxide., *Colloids Surf. A* 520 (2017) 448–458.
- [463] G. Lan, X. Hong, Q. Fan, B. Luo, P. Shi, X. Chen, Removal of Hexavalent Chromium in Wastewater by Polyacrylamide Modified Iron Oxide Nanoparticle, *J. Appl. Polym. Sci.* , 131 (2014) 40945–40955.
- [464] G.L. Dotto, L.A.A. Pinto, Adsorption of food dyes acid blue 9 and food yellow 3 onto chitosan: Stirring rate effect in kinetics and mechanism, *J. Hazard. Mater.*, 187 (2011) 164–170.
- [465] S. Pourbeyram, Effective Removal of Heavy Metals from Aqueous Solutions by Graphene Oxide–Zirconium Phosphate (GO–Zr-P) Nanocomposite, *Ind. Eng. Chem.*, 55 (2016) 5608-5617.
- [466] F.C. Wu, R. L.Tseng, R.S. Juang, Enhanced abilities of highly swollen chitosan beads for color removal and tyrosinase immobilization, *J. Hazard. Mater.*, 81 (2001) 167-177
- [467] H. Chaudhuri, S. Dash, A. Sarkar, Single-Step Room-Temperature in Situ Syntheses of Sulfonic Acid Functionalized SBA-16 with Ordered Large Pores: Potential Applications in Dye Adsorption and Heterogeneous Catalysis, *Ind. Eng. Chem. Res.* , 56 (2017) 2943–2957.
- [468] H. Chaudhuri, S. Dash, R. Gupta, D.D. Pathak, A. Sarkar, Room-Temperature In-Situ Design and Use of Graphene Oxide-SBA-16 Composite for Water Remediation and Reusable Heterogeneous Catalysis, *Chemistry Select*, 2 (2017) 1835-1842.
- [469] S. Chowdhury, P. Saha, Sea shell powder as a new adsorbent to remove Basic Green 4 (Malachite Green) from aqueous solutions: equilibrium, kinetic and thermodynamic studies, *Chemical Engineering Journal*, 164 (2010) 168–177.
- [470] P.D. Saha, S. Chakraborty, S. Chowdhury, Batch and continuous (fixed-bed column) biosorption of crystal violet by *Artocarpus heterophyllus* (jackfruit) leaf powder, *Colloids and Surfaces B*, 92 (2012) 262–270.
- [471] A. Kausar, H. Nawaz, G. Mackinnon, Equilibrium, kinetic and thermodynamic studies on the removal of U(VI) by low cost agricultural waste, *Colloids Surf. A*, 111 (2013) 124-133.

- [472] K.K.H. Choy, G.M. Kay, J.F. Porter, Sorption of acid dyes from effluents using activated carbon, *Resour. Conserv. Recycl.*, 27 (1999) 57–71.
- [473] B. Qiu, J. Guo, X. Zhang, D. Sun, H. Gu, Q. Wang, H. Wang, X. Wang, X. Zhang, B.L. Weeks, Z. Guo, S. Wei, Polyethylenimine Facilitated Ethyl Cellulose for Hexavalent Chromium Removal with a Wide pH Range, *ACS Appl. Mater. Interfaces* 6(2014) 19816–19824.
- [474] Z. Zhang, H. Luo, X. Jiang, Z. Jiang, C. Yang, Synthesis of reduced graphene oxide-montmorillonite nanocomposite and its application in hexavalent chromium removal from aqueous solutions, *RSC Adv.*, 5 (2015) 47408–47417.
- [475] I. Larraza, M. Lo´pez-Go´nzalez, T. Corrales, G. Marcelo, Hybrid materials: Magnetite–Polyethylenimine–Montmorillonite, as magnetic adsorbents for Cr(VI) water treatment, *J. Colloid Interface Sci.*, 385 (2012) 24–33.
- [476] K. Selvi, S. Pattabhi, K. Kadirvelu, Removal of Cr(VI) from aqueous solution by adsorption onto activated carbon, *Bioresour. Technol.*, 80 (2001) 87–89.
- [477] S. Tunali, I.K. ve, T. Akar, Chromium(VI) biosorption characteristics of *Neurospora crassa* fungal biomass *Miner. Eng.*, 18 (2005) 681–689.
- [478] F. Gode, E. Pehlivan, Chromium(VI) adsorption by brown coals *Energy Source* 28 (2006) 447–457.
- [479] E. Malkoc, Y. Nuhoglu, M. Dundar, Adsorption of chromium(VI) on pomace—an olive oil industrywaste: batch and column studies *J. Hazard. Mater.* , 138 (2006) 142–151.
- [480] V. Murphy, H. Hughes, P. McLoughlin, Comparative study of chromium biosorption by red, green and brown seaweed biomass, *Chemosphere*, 70 (2008) 1128–1134.
- [481] A.O. zer, D.O. zer, Comparative study of the biosorption of Pb(II), Ni(II) and Cr(VI) ions onto *S. cerevisiae*: determination of biosorption heats *J. Hazard. Mater.* , 100 (2003).
- [482] X.S. Wang, Y. Qin, Removal of Ni(II), Zn(II) and Cr(VI) from aqueous solution by *Alternanthera philoxeroides* biomass, *J. Hazard. Mater.*, 138 (2006) 582–588.
- [483] M.L. Chen, Z.D. Meng, L. Zhu, J.G. Choi, C.Y. Park, S.C. Lee, D.S. Hong, J.G. Lee, W.K. Jang, W.C. Oh, Dispersion stability of metal (oxide)-graphene nanofluids with electrical and thermal properties., *Sci. Adv. Mater.*, 3 (2011) 887-892.
- [484] Y. Chang., S.T. Yang, J.H. Liu, E. Dong, Y. Wang, A. Cao, Y. Liu, H. Wang, In vitro toxicity evaluation of graphene oxide on A549 cells, *Toxicol. Lett.*, 200 (2011) 201-210.
- [485] M. Arakha, D.S. S. P, T.K. Panigrahi, B.C. Mallick, K. Pramanik, B. Mallick, S. Jha, Antimicrobial activity of iron oxide nanoparticle upon modulation of nanoparticle-bacteria interface, *Sci. Rep.*, 14813 (2015).
- [486] M. Valko, D. Leibfritz, J. Moncol, M.T.D. Cronin, M. Mazur, J.Telser, Free radicals and antioxidants in normal physiological functions and human disease, *Int. J. Biochem. Cell Biol.*, 39 (2007) 44-84.
- [487] W. Hu, C. Peng, W. Luo, M. Lv, X. Li, D. Li, Q. Huang, C. Fan, Graphene-Based Antibacterial Paper, *ACS Nano* 4(2010) 4317-4432.
- [488] K. Krishnamoorthy, N. Umasuthan, R. Mohan, J. Lee, S.J. Kim, Antibacterial Activity of Graphene Oxide Nanosheets, *Sci. Adv. Mater.*, 4 (2012) 1111-1117.
- [489] S. Park, R.S. Ruoff, Chemical methods for the production of graphenes, *Nat. Nanotechnol.*, 4 (2009) 217-224.

Appendices

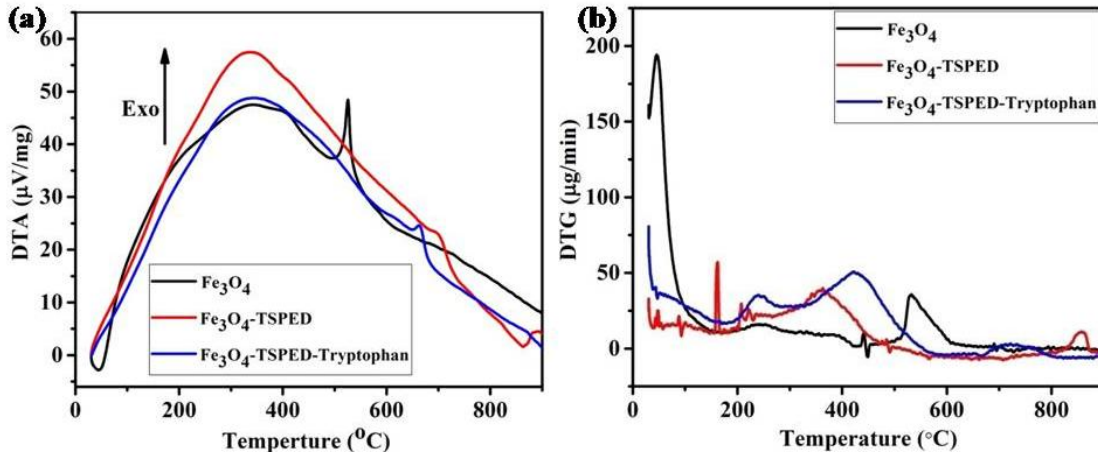


Figure A1 DTA and DTG curve of Fe₃O₄, Fe₃O₄-TSPED and Fe₃O₄-TSPED-Tryptophan

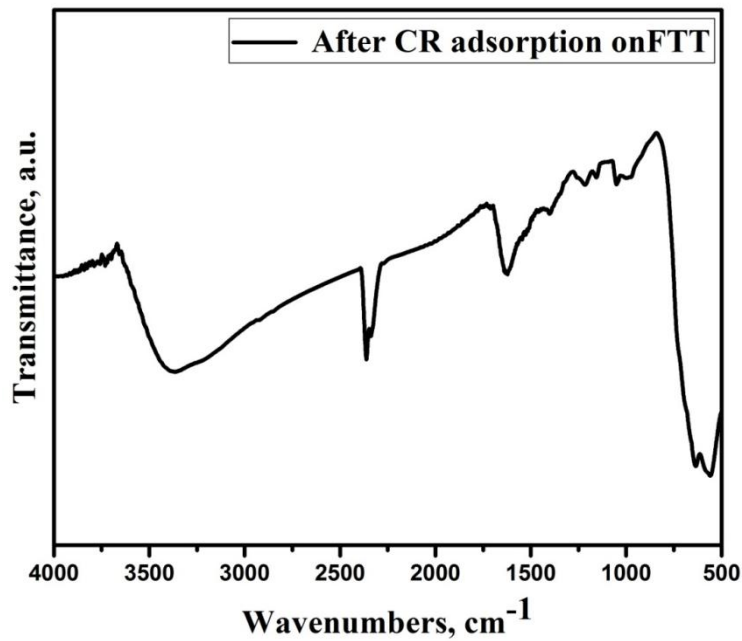


Figure A2 FT-IR spectrum of FTT after CR adsorption.

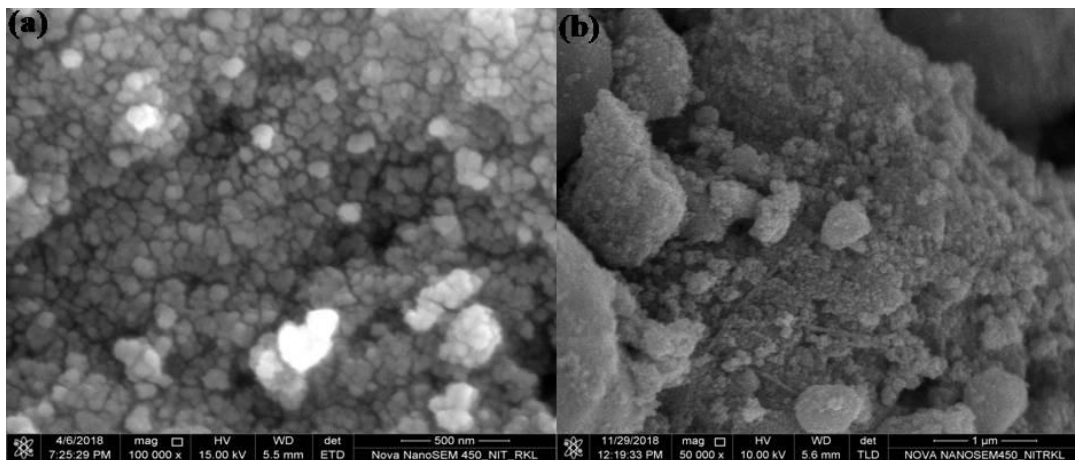


Figure A3 FE-SEM image of FTT nanocomposite (a) before adsorption and (b) after CR adsorption.

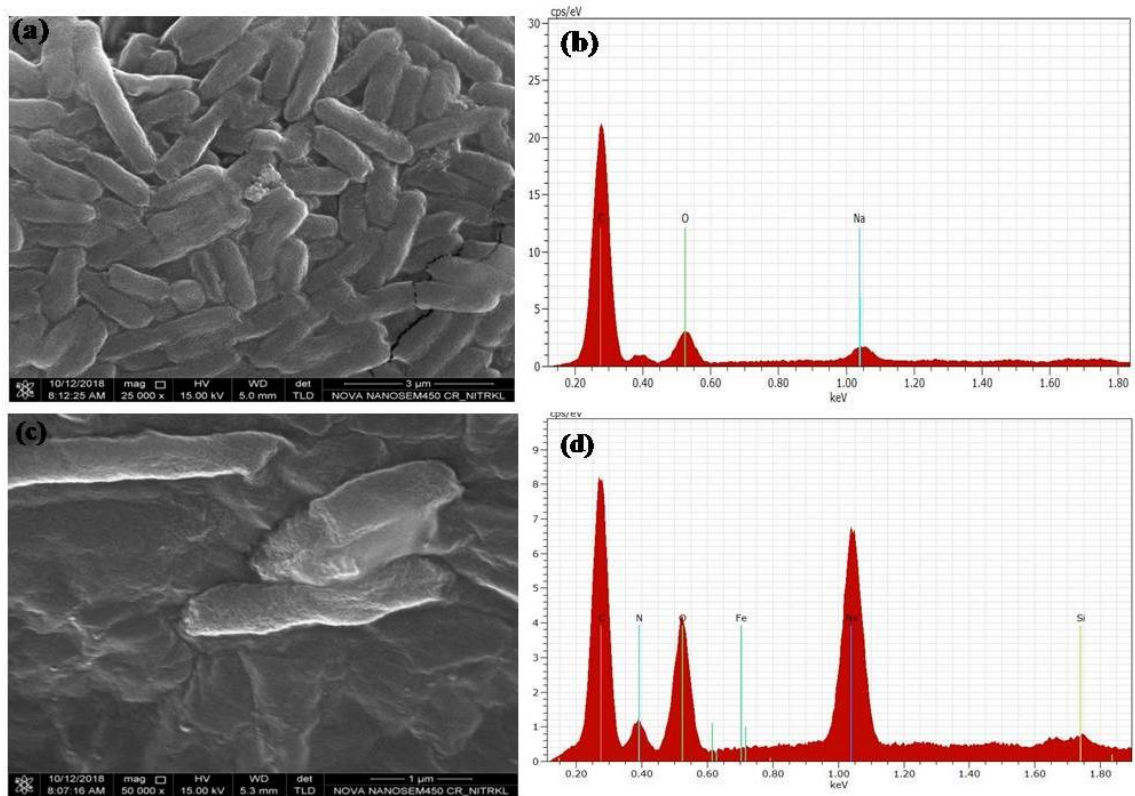


Figure A4 FE-SEM micrograph showing the alteration in bacterial cell membrane morphology where (a) represent the *E.coli* control image (b) represent the EDX spectrum of *E.coli* surface, in the same way (c) represent the FTT treated *E. coli* and (d) shows the EDX spectrum of FTT treated *E.coli*.

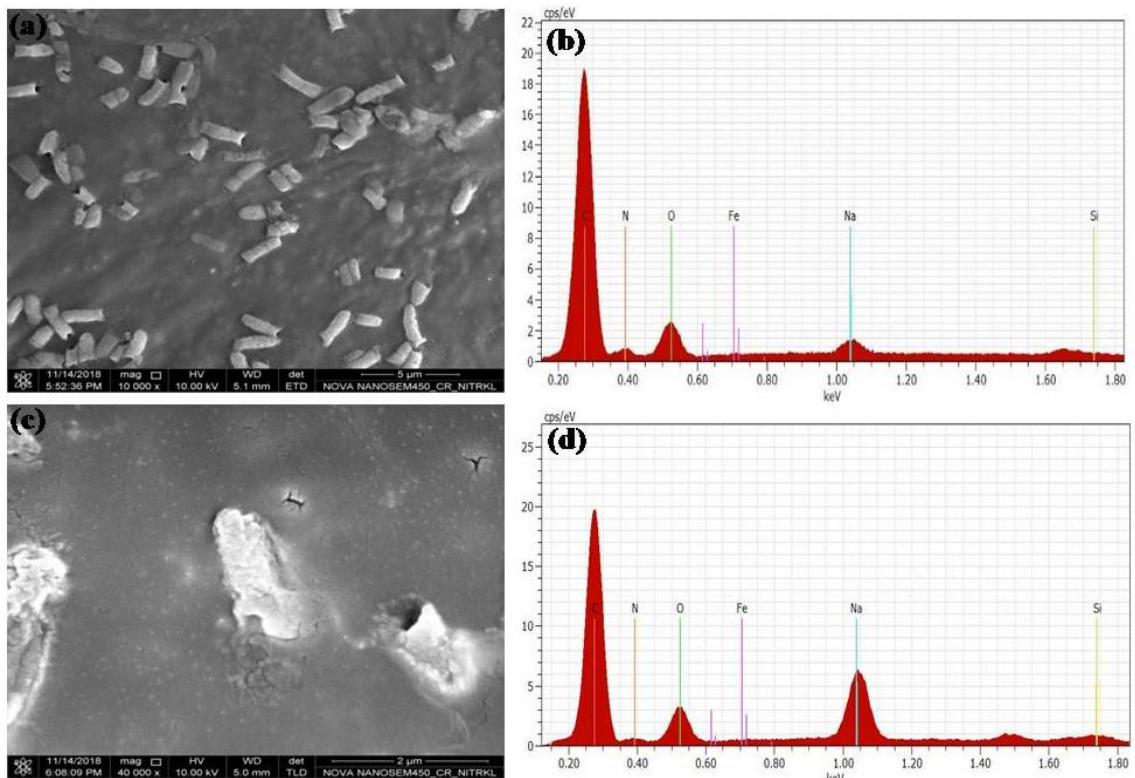


Figure A5 FE-SEM micrograph showing the alteration in bacterial cell membrane morphology where (a) represent the *B.subtilis* control image and (b) represent the EDX spectrum of bacterial surface (c) represent the FTT treated *B. subtilis* and (d) shows the EDX spectrum of FTT treated *B.subtilis*.

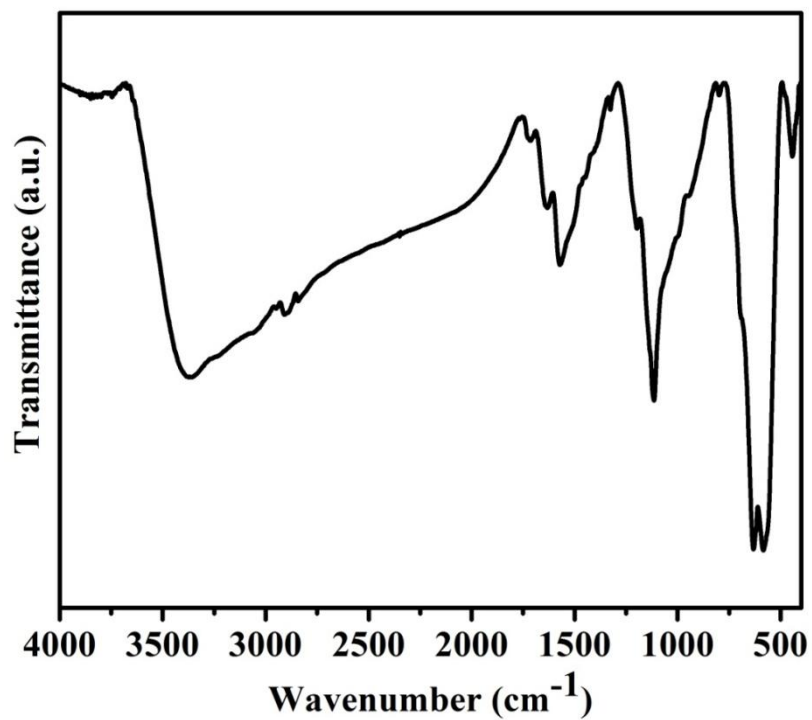


Figure A6 FT-IR spectrum of GO-Fe₃O₄-APTES after Cr (VI) adsorption.

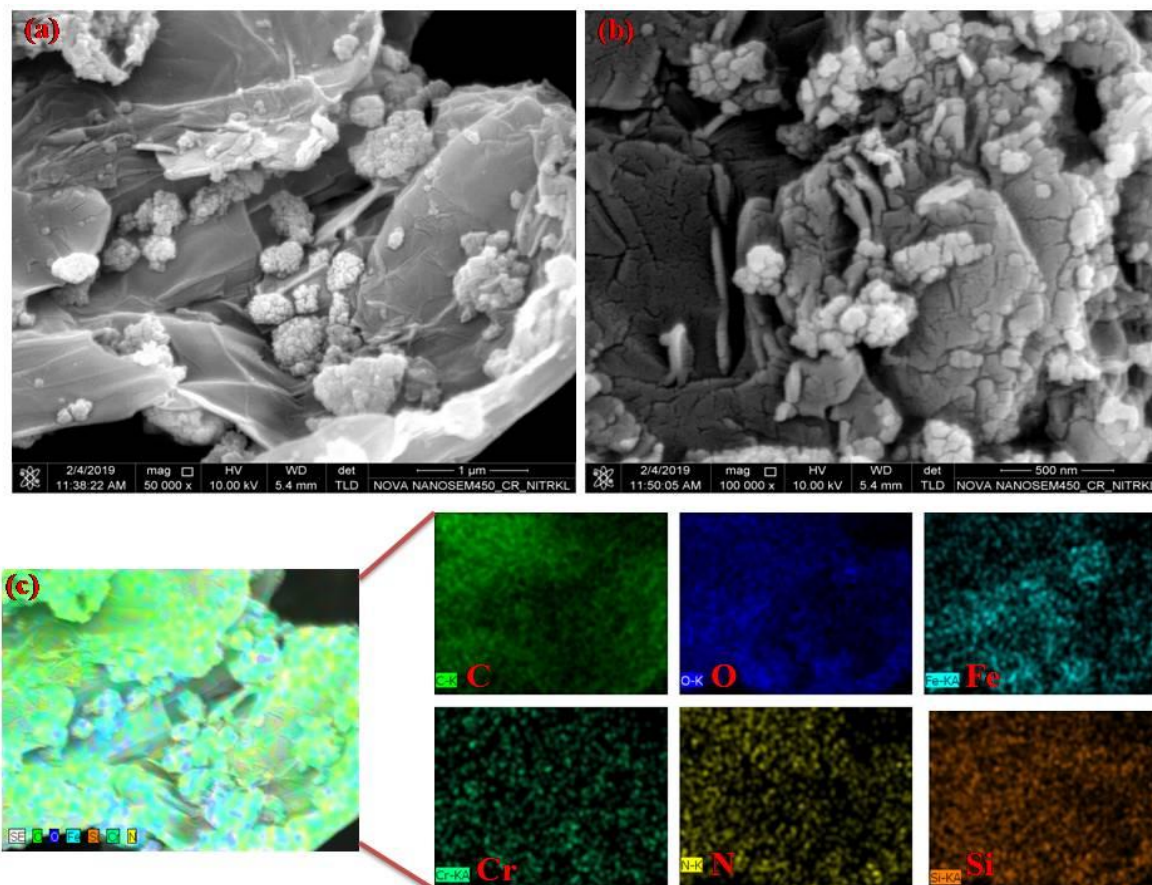


Figure A7 FE-SEM image of after adsorption of Chromium (VI) (a) 1000 nm, (b) 500 nm resolution and (c) EDS mapping.

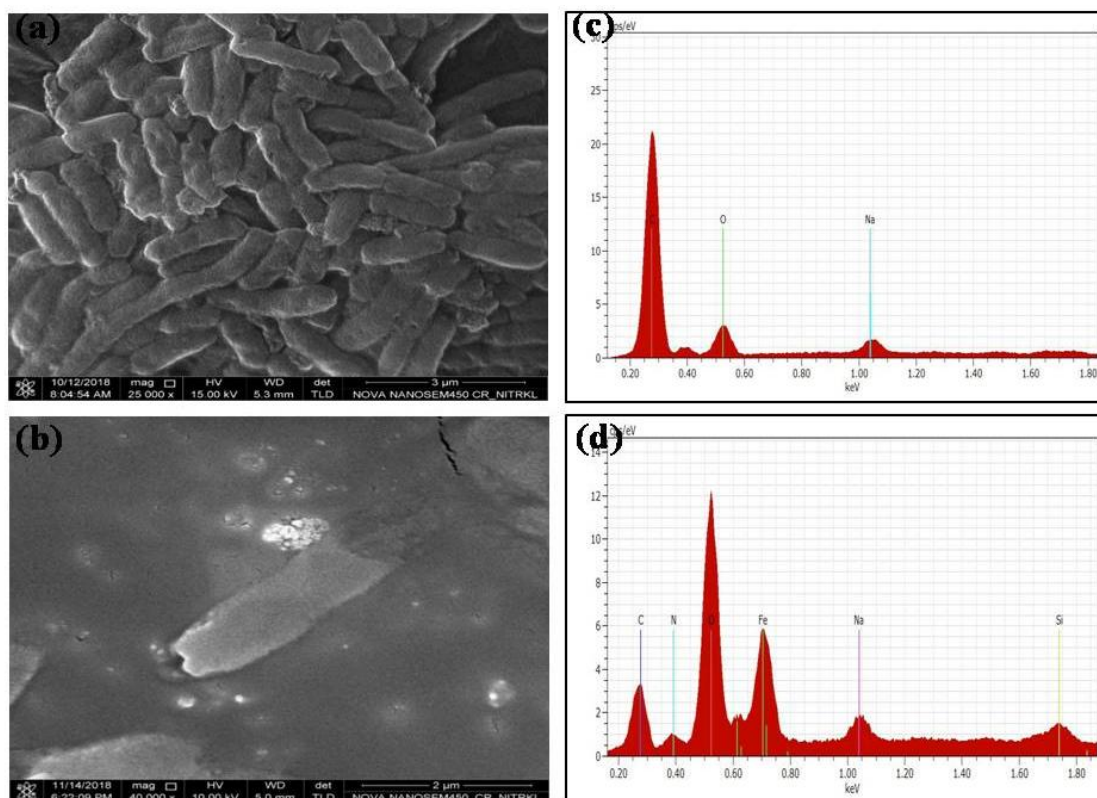


Figure A8 Antibacterial activity of GO-Fe₃O₄-APTES against *E.coli*, where (a) is FESEM image of *E.coli* and (b) is the *E.coli* treated with GO-Fe₃O₄-APTES, (c) is the EDS analysis showing the elements in bacteria and (d) is the element deposited in bacteria after GO-Fe₃O₄-APTES treatment.

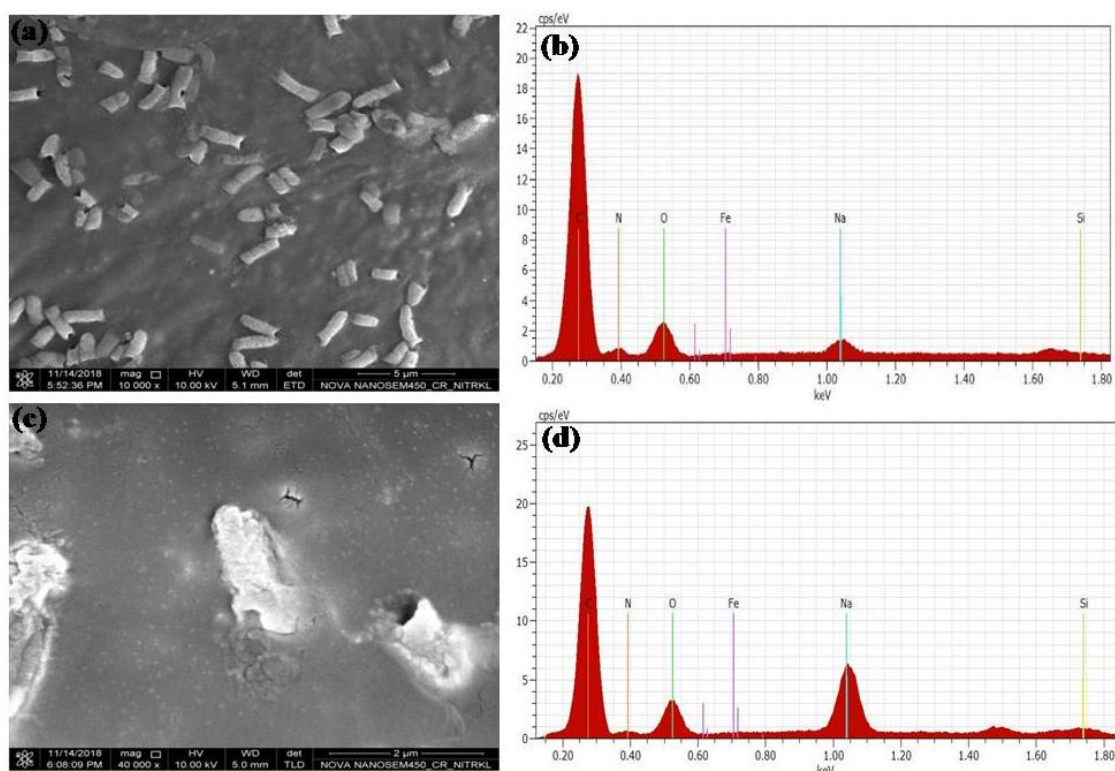


Figure A9 Antibacterial activity of GO-Fe₃O₄-APTES against *B. subtilis*, where (a) is FESEM image of *B. subtilis* and (b) is the *B. subtilis* treated with GO-Fe₃O₄-APTES, (c) is the EDS analysis showing the elements in bacteria and (d) is the element deposited in bacteria after GO-Fe₃O₄-APTES treatment.

Dissemination

Publications: Manuscript

1. **J. K. Sahoo**, S. K. Paikra, M. Mishra and H Sahoo* Amine functionalized magnetic iron oxide nanoparticles: Synthesis, antibacterial activity and rapid removal of Congo red dye. *Journal of Molecular Liquids*, 282 (2019) 428-440.
2. **J. K. Sahoo**, M. Konar. J. Rath, D. Kumar and H Sahoo* Hexagonal strontium ferrite: Cationic dye adsorption and antibacterial activity. *Separation Science and Technology* 2019 <https://doi.org/10.1080/01496395.2019.1577267>.
3. **J. K. Sahoo**, A. Kumar, L. Rout, J. Rath, P. Dash* and H. Sahoo*, An investigation of heavy metal adsorption by hexa-dentate ligand-modified magnetic nanocomposites, *Separation Science and Technology*, 53 (2017) 863-876.
4. **J. K. Sahoo**, A. Kumar, J. Rath, T. Mohanty, P. Dash and H. Sahoo*, Guar gum-coated iron oxide nanocomposite as an efficient adsorbent for Congo red dye, *Desalination and Water Treatment*, 95 (2017) 342-354.
5. **J. K. Sahoo**, J. Rath, P. Dash and H. Sahoo*, EDTA functionalized magnetic nanoparticle as a multifunctional adsorbent for Congo red dye from contaminated water. *AIP Conference Proceeding* **1832**, (2017) 050087.
6. **J. K. Sahoo**, M. Konar. D. Kumar and H Sahoo*, Magnetic Hydroxyapatite Nanocomposite: Impact on Eriochrome black-T removal and Antibacterial activity. 2019, *Journal of Molecular Liquids* 294 (2019) 11596.
7. M. Konar, **J. K. Sahoo**, and H Sahoo*, Impact of Bone Extracellular Matrix Mineral Based Nanoparticles on Structure, Stability and Activity of Bone Morphogenetic Protein 2 (BMP 2), 2018, *Journal of Photochemistry & Photobiology, B*, 198 (2019) 111563.

Submitted/Under Review

1. **J. K. Sahoo**, S. K. Paikra, A. Baliarsingh, D. Panda, S. Rath, M. Mishra and H Sahoo*, Surface functionalization of graphene oxide using amino silane magnetic nanocomposite for Cr (VI) removal and bacterial treatment. (Submitted to Journal)
2. **J. K. Sahoo**, B Barik, P. Dash, S. K. Sahoo, N. K. Sethy, H. Sahoo* Spatial distribution of uranium and associated water quality parameters in Sundergarh district of Odisha. (Conference Proceeding)
3. J. bag, S. Mukherjee, **J. K. Sahoo**, K. S. Tung, H. Sahoo and M. Mishra* Sex-dependent neurotoxic and behavioural teratogenic effect of guar gum coated Fe₃O₄ nanocomposites on *Drosophila melanogaster*. (Revision submitted)

Book chapter

1. L. Satish, S. Millan, **J. K. Sahoo**, G. Chakraborty, L. Swain, S. Mishra, H. Sahoo, Renaissance of Bioremediation: Degradation of Environmental Pollutants. *Environ. Sci. & Engg.* 2017, Studium Press LLC, USA. ISBN: 1-62699-096-4. SERIES ISBN: 1-62699-088-3.

Work shop and Conferences

- December 3-5, 2014** Work shop titled “**Generation Of National Database On Uranium In Drinking Water**” Bhabha Atomic Research Center, Mumbai.
- December 24-25, 2016** Oral presentation titled “**An Investigation of Heavy Metals Adsorption by Hexadentate Ligand Modified Magnetic Nanocomposite**” Conference of Odisha Chemical Society, KIIT university, BBSR, Odisha.
- December 26-30, 2016** Poster presentation titled “**EDTA functionalized magnetic nanoparticle as a multifunctional adsorbent for Congo red dye from contaminated water**” in 61st DAE Solid State Physics Symposium, KIIT university, BBSR, Odisha.
- December 18- 20, 2017** Poster presentation titled “**Rapid removal of Eriochrome black-T using magnetic hydroxyapatite nanoparticles and its antibacterial activity**” National conference 22nd Biennial Conference of the Indian Photobiology Society, NIT, Rourkela.
- October 30-31, 2018** Oral Presentation titled “**Novel synthesis of Fe₃O₄-TSPED-Tryptophan nanocomposite for removal of Congo red dye from aqueous solution**” International conference on synthetic potent molecule and its application (ICSPMIA-2018), SMIT, Sikkim.
- December 12-14, 2018** Poster presentation titled “**Novel synthesis of amine functionalized magnetic iron oxide nanoparticles for rapid removal of Congo red dye and antibacterial properties**” National conference on Advance materials for energy and environmental application (AMEEA-2018), NIT Rourkela.

Vitae

Mr. Jitendra Kumar Sahoo was born in 7th June 1992 at Khurda district of Odisha, India. He completed his Bachelor of Science (B.Sc.) in Chemistry (Honours) from Pranatha (Autonomous) college, Khurda, which is affiliated to Utkal University, Odisha, in 2012 and obtained his Master of Science (M.Sc.) in Chemistry from Berhampur University, Berhampur in June 2014. Then he joined as a Ph.D. scholar at the National Institute of Technology, Rourkela in November 2014, in Department of Chemistry under supervision of Dr. Harekrushna Sahoo and co-supervision of Dr. Priyabrat Dash. He has submitted Ph.D. thesis in May 2019. His area of research interest includes synthesis of novel functionalized nanomaterials and application towards inorganic and organic contaminants, and antibacterial activity.

